Autonomous Swarm Navigation

Dissertation

zur Erlangung des akademischen Grads eines

Doktor der Ingenieurwissenschaften
(Dr.-Ing.)

der Technischen Fakultät
der Christian-Albrechts-Universität zu Kiel

vorgelegt von

Siwei Zhang

Kiel, Dezember 2019

Tag der Einreichung: 30.12.2019
Tag der Disputation: 17.06.2020

Berichterstatter: Prof. Dr.-Ing. Peter Adam Hoeher
Prof. Dr.-Ing. Jörn Thielecke

Preface

The work presented in this thesis is the outcome of my research conducted at the German Aerospace Center (DLR). My journey at DLR began in April 2010, when I started working on cooperative positioning. Two years later, this topic had evolved into Mars swarm navigation, the fascinating topic I have enjoyed since then.

First of all, I want to express my special thanks to Prof. Peter Adam Hoeher from the Kiel University, for providing me a chance to pursue my doctoral degree, and for the enjoyable and inspiring discussions. Secondly, I am very grateful to Prof. Jörn Thielecke from the University Erlangen-Nuremberg, for being interested in the work and evaluating it as the co-referee. Additionally, I am sincerely grateful to Prof. Uwe Carsten Fiebig, for offering me a great working position at his department to explore such a fantastical topic. A very special thank belongs to my group leader Dr. Armin Dammann, who has been always there for encouragement and in-depth scientific discussion. His outside-the-box thinking has inspired me way beyond research. Furthermore, I am thankful to all DLR colleagues and students, particularly, Ronald, Thomas Jost, Wei, Robert, Stephan, Christian, Michael, Markus, Dmitriy, Thomas Wiedemann, Benjamin, Christoph, Ibrahim, Erik and Tsung-Huan, for their supports and numerous productive discussions. I would like to specially thank Emanuel for providing experimental data to validate my work. In addition, I an grateful to the project partners of WHERE2, VaMEx, VaMEx-CoSMiC, HIGHTS and ARCHES, for the fruitful collaborations. A special thank belongs to Prof. Henk Wymeersch, for the illuminating discussions during my visit to the Chalmers University of Technology.

Finally, I would like to express my deepest thanks to my family. My parents have been very supportive to my decision of pursuing a PhD. My wife Qiufeng has always been my side, with close to infinite patience, throughout my almost a decade long doctoral study. Our adorable little daughter Vanessa occasionally pretended to be attracted by my work, which has motivated me to continue and finish the journey. Without their endless encouragement, this thesis would not have been possible.

Wessling, December 2019

Abstract

Robotic swarm systems attract increasing attention in a wide variety of applications, where a multitude of self-organized robotic entities collectively accomplish sensing or exploration tasks. Compared to a single robot, a swarm system offers advantages in terms of exploration speed, robustness against single point of failures, and collective observations of spatio-temporal processes.

Autonomous swarm navigation, including swarm self-localization, the localization of external sources, and swarm control, is essential for the success of an autonomous swarm application. However, as a newly emerging technology, a thorough study of autonomous swarm navigation is still missing.

In this thesis, we systematically study swarm navigation systems, particularly emphasizing on their collective performance, which distinguishes them from traditional navigation systems. The general theory of swarm navigation as well as an in-depth study on a specific swarm navigation system proposed for future Mars exploration missions are covered. First, a generic swarm navigation system is formally defined. Then, the theoretic potential of swarm self- and source localization is investigated. The theoretical findings are then used for swarm localization and control algorithm design and validation.

Concerning swarm localization, a decentralized algorithm dubbed *direct particle filtering for decentralized network localization (DiPNet)* is proposed. DiPNet achieves a near-optimal performance with low complexity for a dense swarm network.

Regarding swarm control, a position-aware swarm control concept is proposed. The swarm is aware of not only the position estimates and the estimation uncertainties of itself and the sources, but also the potential motions to enrich position information. As a result, the swarm actively adapts its formation to improve localization performance, without losing track of other objectives, such as goal approaching and collision avoidance.

The autonomous swarm navigation concept described in this thesis is verified for a specific Mars swarm exploration system. More importantly, this concept is generally adaptable to an extensive range of swarm applications.

Zusammenfassung

Robotische Schwarmsysteme werden zunehmend für Anwendungen in Betracht gezogen, bei denen eine Vielzahl von selbstorganisierten Roboter-Einheiten gemeinsam Mess- oder Explorationsaufgaben durchführen. Im Vergleich zu einem einzelnen Roboter bietet ein Schwarmsystem Vorteile in Bezug auf die Explorationsgeschwindigkeit, die Robustheit gegenüber „Single Point of Failures“ und die gemeinsame Beobachtung von räumlich und zeitlich varianten Prozessen.

Die autonome Schwarmnavigation, einschließlich der Selbstlokalisierung im Schwarm, der Lokalisierung externer Quellen, und der Schwarmregelung ist für den Erfolg einer autonomen Schwarm-Anwendung unerlässlich. Da es sich um eine neuartige Technologie handelt, fehlt jedoch noch eine gründliche, theoretische Betrachtung.

In dieser Arbeit untersuchen wir systematisch Schwarmnavigationssysteme, wobei wir ein besonderes Augenmerk auf ihre kollektive Leistung legen. Dies unterscheidet sie von herkömmlichen Navigationssystemen. Es werden sowohl die allgemeine Theorie der Schwarmnavigation, als auch eine detaillierte Studie eines spezifischen Schwarmnavigationssystems, das für zukünftige Mars Explorationsmissionen vorgeschlagen wird, behandelt. Zunächst wird ein generisches Schwarmnavigationssystem formal definiert. Anschließend wird die Selbst- und Quellenlokalisierung hergeleitet und das theoretische Potenzial untersucht. Die theoretischen Ergebnisse werden dann für die Schwarmnavigation und das Design und die Validierung des Regelungsalgorithmus verwendet.

Bezüglich der Schwarmlokalisierung wird ein dezentraler Algorithmus mit dem Namen „Direct Particle Filtering for Decentralized Network Localization“ (DiPNet) vorgeschlagen. Für ein dichtes Schwarmnetzwerk arbeitet DiPNet, trotz geringer Komplexität, nahe am Optimum.

Hinsichtlich der Schwarmregelung wird ein Konzept vorgeschlagen, welches die Positionierung einbezieht. Der Schwarm berücksichtigt dabei nicht nur die Positionsschätzungen und Schätzunsicherheiten seiner Teilnehmer und der Quellen, sondern auch mögliche Bewegungen, welche einen Gewinn von Positionsinformationen ermöglichen. Der Schwarm passt daher seine Formation aktiv an um die Lokalisierungsleistung zu verbessern, ohne andere Aufgaben wie Zielannäherung und Kollisionsvermeidung aus den Augen zu verlieren.

Das in dieser Arbeit beschriebene Konzept zur autonomen Schwarmnavigation wird für bestimmtes Schwarmexplorationssystem für den Mars verifiziert. Das vorgestellte Konzept kann jedoch an eine Vielzahl von Schwarmanwendungen angepasst werden.

Contents

Chapter 1

Introduction

1.1 Autonomous Robotic Swarms

In nature, swarm behavior refers to grouping of numerous biological entities, for example bird flocking (like in Figure 1.1), mammal herding, insect swarming or fish schooling [1]. Each entity, or agent, follows simple interaction rules based on the observation of its surrounding [2]. Yet the whole swarm acts as a single organ with emerging global situation awareness and collective behaviors, such as immigrating, foraging or escaping from predators [3, 4].

Autonomous robotic swarms, analogous to biological swarms in nature, are self-organized multi-agent systems composed of a crowd of collaborative artificial entities [5, 6, 7, 8]. Robotic swarm systems attract increasing attention in sensing and exploration applications, e.g. for search and rescue [9], environmental monitoring [10], and extraterrestrial missions [11, 12, 5, 13]. The size of a robotic swarm, referred to either its cardinality or its collective aperture's size, varies depending on the applications. The cardinality, i.e. the number of agents in the swarm, differs from a few dozens in laboratory demonstrations [14, 15] to a few thousands in National Aeronautics and Space Administration (NASA)'s envisioned deep space exploration missions [5, 16, 17]. The collective aperture, i.e. the collective area covered by the swarm, has also a wide range of size, from nanometer scale for nano-swarms implanted inside the human body [18], to a few hundred meters for planetary surface swarm sensing and exploration in both terrestrial [19] and extraterrestrial applications [12], and to hundreds of kilometers for orbital applications with a satellite swarm [5].

Compared to a single robot used in state-of-the-art exploration such as the Curiosity [20], a swarm offers various advantages. First, the exploration efficiency increases due to collaboration [5]. Second, the inherent system redundancy avoids single point of

Figure 1.1. *A flock of birds recorded in Sylt, Germany, 2014.*

failures that could jeopardize the whole mission [21]. Last but not least, a spread-out swarm can be collectively seen as a distributed sensor array with dynamically adaptable sensing aperture and resolution. Spatio-temporal processes generated from some physical phenomena, for example luminous, radio frequency (RF), acoustic, gas and seismic emissions [8, 13], can be observed by the swarm at multiple spatial points simultaneously. These observations enhance the environmental cognition and situation awareness of the swarm. The situation awareness, especially position awareness is essential for autonomous exploration missions. The implication of *position awareness* is threefold with three gradually increasing awareness levels:

1) Awareness of position estimates;

2) Awareness of position estimation uncertainties;

3) Awareness of potential motions to enrich position information.

The three position awareness levels are closely related to autonomous swarm navigation, which will be introduced in Section 1.2. Humans only need to interact with an autonomous swarm by high-level abstract mission objectives, such as search for life forms, water, mineral resources or gas releasing sources. It is up to the swarm itself to decide the minutiae of an efficient exploration strategy, based on its cognition of the surrounding [22].

A radio-based swarm system for future Mars exploration missions is taken as an application example for investigation in this thesis, which is illustrated in Figure 1.2. A swarm of rovers autonomously drive from the mission base (upper left) to an exploration area (lower right), where a gas source may be present. Agents in the swarm observe

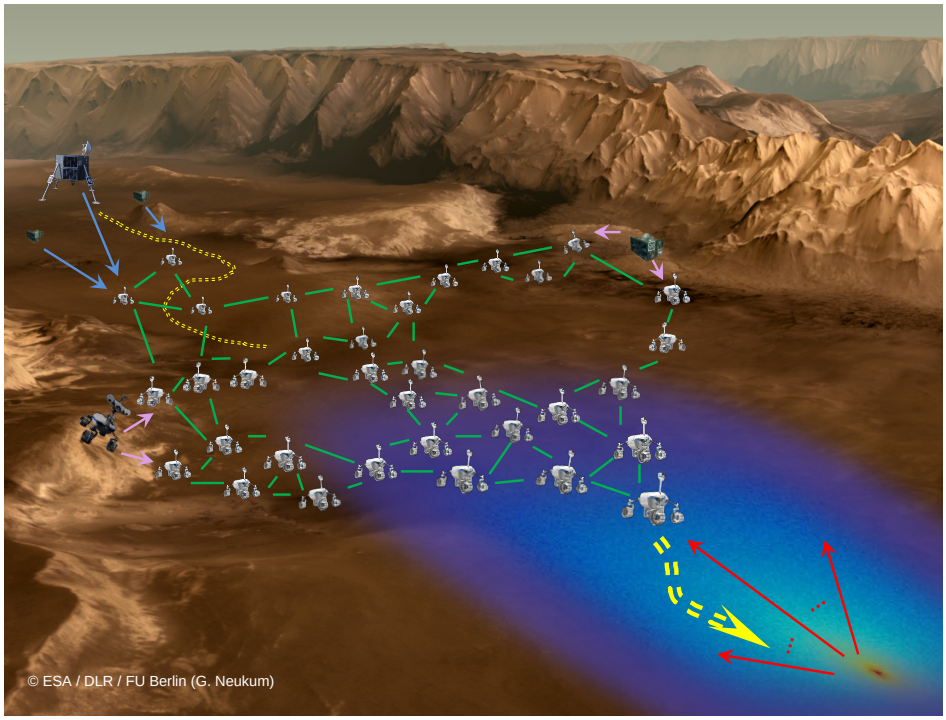

Figure 1.2. *A radio-based swarm system for future Mars exploration missions: The swarm autonomously drives from the landing site to an exploration area, where a gas source may be present. The green lines and arrows with various colors indicate observation link between entities.*

RF signals from a lander, three static probes, a mobility incapacitated rover and other agents. Agents also measure the concentration of gas, emitted from the gas source. The swarm exploits these observations for localization and to navigate itself towards the area of interest.

All the entities are considered as isotropic point emitters when they send out signals, such as RF signals and gas, into the environment. Besides agents in the swarm, whose positions are unknown and controllable, there are two general types of entities considered in this thesis. An entity external to the swarm with a known position is referred to as a beacon, such as the lander and the static probes close to the mission base. An external entity with an unknown position is referred to as a source, for example the mobility incapacitated rover and the static prob in the middle, and the gas emitter. The different entities in the considered system are shown in Figure 1.3. Formal definitions of the entities will be introduced in Chapter 2 and illustrated in Figure 2.1.

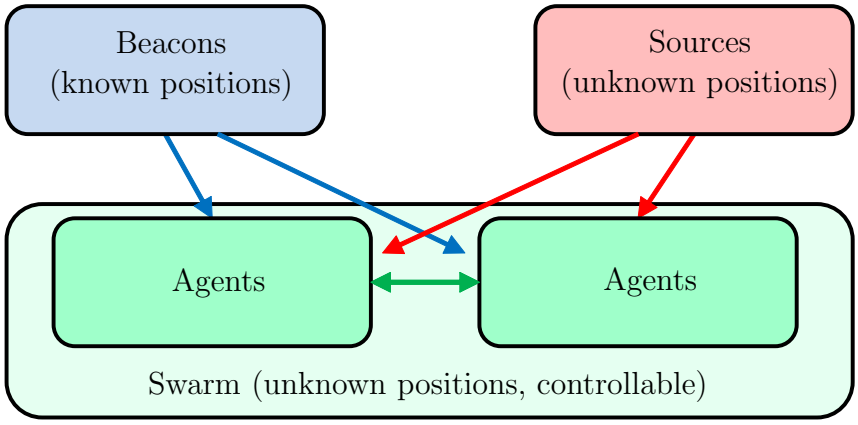

Figure 1.3. *Different entities of the swarm system shown in Figure 1.2: Arrows indicate signals propagating from the emitters to the observers.*

1.2 Autonomous Swarm Navigation

Autonomous navigation is essential for a swarm system, where the swarm aims to answer by itself the questions of

1) Where am I?

2) Where shall I go?

The answers to these two questions correspond to two interconnected research topics, namely *swarm localization* and *swarm control*.

There is limited literature in swarm navigation than in the closely related topics such as multi-agent navigation and network navigation. Even though, the distinction between swarms and classic multi-agent systems is vague, we define a swarm as a multi-agent system with (1) a large cardinality, (2) computational decentralization with low complexity, and (3) self-organized mobility with collective behaviors, and focus on the impacts of these unique properties on swarm navigation.

1.2.1 Swarm Localization

Localization is a classical problem in signal processing, where the geometrical relationship of a group of objects is determined by, for example, distance and angular related observations between objects. Swarm localization includes problems such as estimating (1) agent's relative position with respect to (w.r.t.) the swarm, (2) the swarm's position w.r.t. an external coordinate system, and (3) environmental features' positions w.r.t. the swarm or/and the external coordinate system. Environmental features can generally be active points emitting signals, passive points interacting with environment,

like scatterers in radar applications, or functions like profiles of certain fields. In this thesis, we only consider point emitters as examples of environmental features. Swarm localization is closely related to the topics such as network localization, relative localization, cooperative positioning, cooperative simultaneous localization and mapping (SLAM) [23], simultaneous localization and tracking (SLAT) [24, 25], simultaneous localization and synchronization (SLAS) [26], wireless sensor network (WSN) localization and tracking, etc. Intensive research has been conducted in these topics. From theory, fundamental limits of localization-related problems are addressed with the help of mathematical tools in estimation and detection theory such as Fisher information (FI)/Cramér-Rao bound (CRB) [27, 28, 29] and different variants of Bayesian bound (BB) [30, 31]. In practice, numerous localization algorithms have been developed, which can be categorized as centralized/decentralized, Bayesian/non-Bayesian and low complexity/high resolution algorithms [32, 33]. However, in distinction to classical localization, swarm localization emphasizes on the collective behavior and possesses the following four unique properties.

1.2.1.1 Multi-Level Perspectives

For most of the classical localization problems, a global coordinate system is externally specified. Especially due to the development of global navigation satellite systems (GNSSs) [34, 35], the geographic coordinate system and the Earth-centered, Earth-fixed (ECEF) system are widely employed for localization. Precise geodesic measurements of ground stations are exploited to determine a globally unified coordinate system, like the world geodetic system 1984 (WGS84) for global positioning system (GPS). In most GNSS-based localization applications, global coordinate systems are considered without any uncertainty. For swarm exploration scenarios, an external coordinate system is not always available. The swarm localization problem is formulated according to the original definition of localization, i.e. determining the geometrical relationship among objects. Multiple levels of perspectives can be employed to describe swarm localization, depending on the applications.

1) Micro-Level

   In micro-level, or agent-centric perspective, the geometry of the local network around an agent, including the agent itself, its neighboring agents and its environmental surroundings, is estimated. The agent-centric view is favorable for designing decentralized swarm localization algorithm and for applying the low-level control such as collision-avoidance to the agent.

2) Meso-Level

In meso-level, or swarm-centric perspective, the "shape" of the swarm, i.e. the geometrical relationships among all agents or a subset of agents are estimated. In addition, the relative positions of point sources w.r.t. the swarm are jointly estimated by the observations of agents. In the meso-level perspective, the swarm is viewed as a single organ. The swarm-centric view is in favor when the swarm collective behaviors and performance are under investigation.

3) Macro-Level

In macro-level, or global perspective, sufficient number of swarm's observations are connected to an external global coordinate system. Therefore, the swarm and the external sources' positions w.r.t. this global coordinate system can be determined. The macro-level perspective is appropriate when a mission is designed with a global coordinate system, which car be defined by pre-deployed nodes at known positions, also known as (a.k.a.) beacons, or priorly acquired environment maps.

1.2.1.2 Dense Network with Scalable Topology

By definition, a swarm is composed of a multitude of agents, which are able to conduct inter-agent communications and measurements through agent-to-agent (A2A) links. The agents form a large-scale meshed network, which is advantageous in estimating not only the positions of agents and external sources, but also additional parameters, such as clock offset and drift, parameters of an observation model and signal propagation model. In tracking mode, parameters like agents' heading, velocity and acceleration can also be estimated through the meshed network. The swarm network's topology is configurable by adapting the communication and measurement protocols and resource assignment. For a swarm of $|\mathcal{A}|$ agents, the total number of A2A links scales from the order of $\mathcal{O}(|\mathcal{A}|)$ when agents are only connected within their close proximity, to the order of $\mathcal{O}(|\mathcal{A}|^2)$ when the measurement coverage of agents is comparable to the collective aperture size of the swarm. The notation $|\cdot|$ denotes the cardinality of a set, and $\mathcal{A}$ denotes the set of all agents in a swarm. As a comparison, the number of unknown agents' parameters is in the order of $\mathcal{O}(|\mathcal{A}|)$. Therefore, the swarm network's topology can be configured, such that arbitrary properly designed agent parameter estimation problems are over-determined, hence solvable. Similarly, an external source is connected with the swarm by source-to-agent (S2A) links, forming a star network with the external source as the central hub. The number of observations on the source is in the order of $\mathcal{O}(|\mathcal{A}|)$, which is often much larger than the number of unknown parameters of the source. Hence, the source parameter estimation problems are in general solvable as well. As a result, a dense swarm network is suitable for simultaneous localization

and any other parameter determination (SLAX), which is a generalization of a class of problems, including the above mentioned cooperative SLAM, SLAT, SLAS, etc. For classical localization systems like GNSS, the number of independent observations are essential. Contrarily, for swarm localization, we can evaluate the performance at $|\mathcal{A}|\rightarrow \infty$ asymptotics, where only the collective aperture and the underlying observation model play essential roles. Another factor to be considered in swarm network's topology design is the limitation on total resources in the network, such as RF spectrum, transmit power, time slot, etc. Finding a favorable trade-off between the number of established links and the amount of resource, allocated per link, is challenging.

1.2.1.3 Decentralized Localization Algorithm in Real-time

Typically, agents in a swarm move in condensed formations, which demands accurate position estimates in real-time, for example to avoid collision. Besides, in order to exploit the scalability of a swarm, decentralized localization algorithm executed at each agent is preferable. In addition, even though the swarm localization as a whole is a high dimensional complex problem, the execution on single agent should remain relatively simple. Therefore, it is crucial to design a decentralized swarm localization algorithm, achieving a high accuracy with low complexity.

1.2.1.4 Coupling with Swarm Control

Another unique feature of swarm localization is the potential benefit of coupling with the swarm mobility. Firstly, an agent is aware of the control commands employed to itself, which can be utilized for self-localization. Secondly, each agent decides its own mobility. Hence, the agent is capable of moving to a desired position, so that the whole swarm is in an advantageous formation for localization.

1.2.2 Swarm Control

Swarm control is another essential component of swarm navigation, where the swarm decides on its own where to go according to certain objectives. First of all, the swarm decides for a common direction to move according to mission objectives, such as approaching to the mission base, a water or gas source, mineral resource, biological signature, etc. Second, the swarm is controlled according to formation optimization objectives, to improve, for example the observation quality of the swarm or external source's position. Last but not least, there are some critical objectives act as constraints, such as collision avoidance, minimally tolerated agent position uncertainty, energy and physical mobility limitations, etc.

Multi-agent control [36, 37, 38, 39, 40] is a research topic closely related to swarm control, and has been intensively investigated. A key focus of multi-agent control is formation control. The goal is to achieve and maintain a stable formation as close as possible to a predefined target formation, or according to a target group geometry relationship. Another focus of multi-agent control is to cooperatively accomplish some abstract functionalities, such as maximizing the coverage, task assignment, path planning, etc. Other multi-agent control schemes exist as well. One example is the nature-inspired flocking algorithm [41], which acts according to the three heuristic rules of swarming proposed in [2], i.e. cohesion (stay close to each other), separation (avoid collisions) and alignment (match velocity).

Precise position or relative geometrical information is assumed for most of the multi-agent controls. The uncertainty in position information is often overlooked. Some formation control schemes do include this information but in a tolerance-base [42, 43, 44], i.e. to evaluate the effectiveness of the controller with the presence of position uncertainty.

Very few studies have been conducted in controlling multi-agent systems to improve the knowledge of position. In [45], formation is controlled to guarantee the rigidity of the agent network, which neglected the impacts of measurement quality. In [46], linear state transition and measurement models are assumed, both distorted by additive white Gaussian noise (AWGN). With this simplified model, the covariance matrix obtained from a Kalman filter (KF) is exploited to achieve preferable swarm formations for both self- and source localization. In [25] a Bayesian framework was proposed, supporting only a few agents due to the high complexity.

A signal processing theoretical view of swarm control is still missing. We propose position-aware swarm control, where the swarm possesses all three levels of position awareness and applies information seeking control. In this way, the swarm is able to actively compose formations, which enhances the localization accuracy or guarantees the accuracy to meet mission objectives. The full position awareness is especially crucial for autonomous swarm systems.

The overview of the swarm navigation system considered in this thesis are summarized in Figure 1.4.

1.3 Contributions of the Thesis

As we can see from Section 1.2, swarm navigation is an interdisciplinary topic, involving many aspects of research. In this thesis, we concentrate on the signal processing perspective of swarm navigation, including swarm self- and source localization, as well as

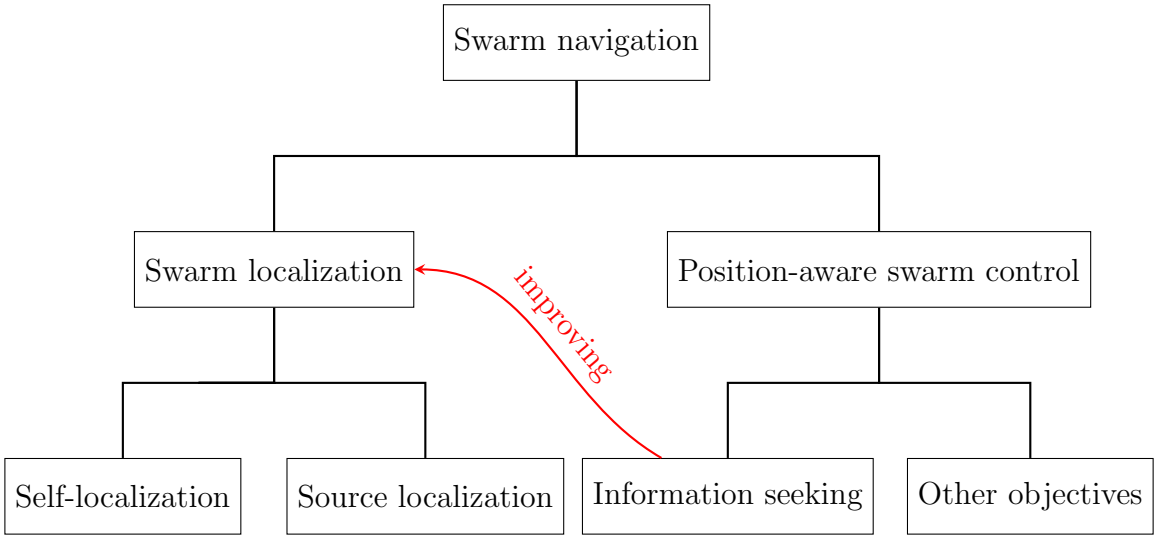

Figure 1.4. *Swarm navigation system breakdown diagram.*

swarm control to improve localization performance. Three aspects in swarm navigation are under investigation, namely (1) potential of swarm localization, (2) decentralized swarm localization algorithms, and (3) position-aware swarm control. With these aspects, we aim to cover both general swarm navigation theory and an in-depth study on a specific swarm navigation system proposed for future Mars exploration missions as illustrated in Figure 1.2. On the one hand, we introduce a formal generic swarm navigation framework, which includes general theory as well as system design and analysis methodologies suitable for a wide variety of swarm applications. On the other hand, we apply the general theory to the particular Mars swarm exploration system. Agents observe the RF signals from other agents, beacons and RF sources, and the gas signals from the gas source, and utilize these signals for navigation.

The main contribution of this thesis is threefold, corresponding to the three aspects to be addressed:

1) From the theoretic aspect, a unified formal definition for swarm navigation systems is introduced. Based on this definition, theoretical analysis on the potential and constraints of swarm localization is provided. Both swarm self-localization and external source localization are investigated. For swarm self-localization, we focus on the network localizability with limited RF resource. The trade-off between number of A2A links and amount of RF resource allocated per link is studied. For external source localization, the swarm is collectively considered as a distributed array with a large aperture. We investigate the impacts of swarm's aperture on source localization with different types of observations. Particularly, in many applications external sources are located in the near field of the swarm's aperture. Hence, the curvature of

the spherical signal front is observable to the swarm. By estimating the signal curvature of arrival (CoA), not only the source angular information, but also distance information can be inferred. A low complexity CoA based source localization algorithm expressed in closed-form is derived, which employs the exact CoA formula. The proposed algorithm outperforms the traditional Fresnel approximation-based near field source localization algorithms. Additionally, the mutual enhancement of swarm self- and source localization is addressed. Precise swarm position information is required for source localization. By collectively observing a source, the swarm's position information is further enriched. Specific to RF signals, the potential of joint self- and source localization with a mixture of symbol delay and carrier phase processing is investigated.

2) From the algorithmic aspect, we focus on the design of decentralized low-complexity algorithms for swarm localization. Most of the network localization algorithms apply a two-step approach, i.e. distance estimation (ranging) and position estimation (localization). In two-step approaches, the location information contained in the RF signal is not fully exploited, since the two steps are usually optimized separately. Unpredictable propagation conditions, for example the multipath and non-line-of-sight (NLOS) propagation, are the main source of error in two-step localization. We exploit the high density feature of the swarm and propose a localization algorithm dubbed direct particle filtering for decentralized network localization (DiPNet). An agent's position is directly estimated from the received signal waveform, incorporating location uncertainty of neighboring nodes, with a low complexity multi-link fusion scheme. We prove that the multipath and NLOS effects on DiPNet become insignificant for dense networks, due to the multi-link collective processing. Therefore, DiPNet achieves a near-optimal performance with low complexity, which is particularly attractive for realtime swarm self-localization. Both simulations and experiments have been conducted to verify the superior performance of DiPNet over traditional two-step approaches.

3) From the swarm control aspect, we utilize the theoretical findings in swarm localization and introduce a position-aware swarm control concept. The core component of position-aware swarm control is information seeking. A swarm exploits the third level of position awareness to reduce the position uncertainties of itself and the sources. The position information qualities are quantified by the FI and Bayesian information (BI), which are utilized by the swarm to formulate the information seeking objectives. Having derived analytically the closed-form expressions of the information gradients, the information seeking control commands can be generated

efficiently, which is particularly attractive for the control of a large-scale swarm. With the proposed concept, the total position information, or its partitions, can be flexibly chosen as either cost functions or constraints of the swarm control problem, depending on the applications. As a result, the swarm actively adapts its formation to improve localization performance of itself as well as the external point sources, without losing track of other mission objectives. Unlike the traditional formation control, where a target formation is given, the position-aware swarm control results swarm formations, which are justifiably preferable for navigation purpose. The proposed position-aware swarm control concept can be employed to different phases of swarm exploration missions, such as exploration area approaching, external source searching, and returning to the mission base after exploration. More importantly, it can be generalized to a wide variety of swarm applications.

1.4 Structure of the Thesis

Despite of the logical interconnections, the three swarm navigation aspects, namely the theoretical analysis, localization algorithm design and swarm control, are relatively independent from each other. Accordingly, the thesis is structured by these three aspects. Each chapter focuses on one individual aspect, including background study, main contributions, results and discussion.

The rest of this thesis is structured as follows. In Chapter 2, a formal definition of swarm navigation systems is introduced. In Chapter 3, theoretical potential of swarm localization is investigated. In Chapter 4, the DiPNet algorithm for swarm self-localization is proposed and followed by an analysis of its robustness against propagation effects. In Chapter 5, the concept of position-aware swarm control is introduced. Multiple examples are provided to demonstrate the employment of this concept to different phases of swarm exploration missions. In Chapter 6, conclusions of the thesis are drawn. Extensive mathematical derivations are stored in Appendix C, in order to improve the readability of the main text. Complementary materials are provided in the appendices as well, including a list of acronyms and abbreviations in Appendix A, a list of mathematical notations in Appendix B, and a list of own publications in Appendix D.

The thesis structure is depicted in Figure 1.5 to provide an intuitive overall impression of the thesis. Each circle illustrates the amount of theoretical contribution versus the load of numerical and experimental validation in each technical chapter. The circle size represents the volume of that chapter.

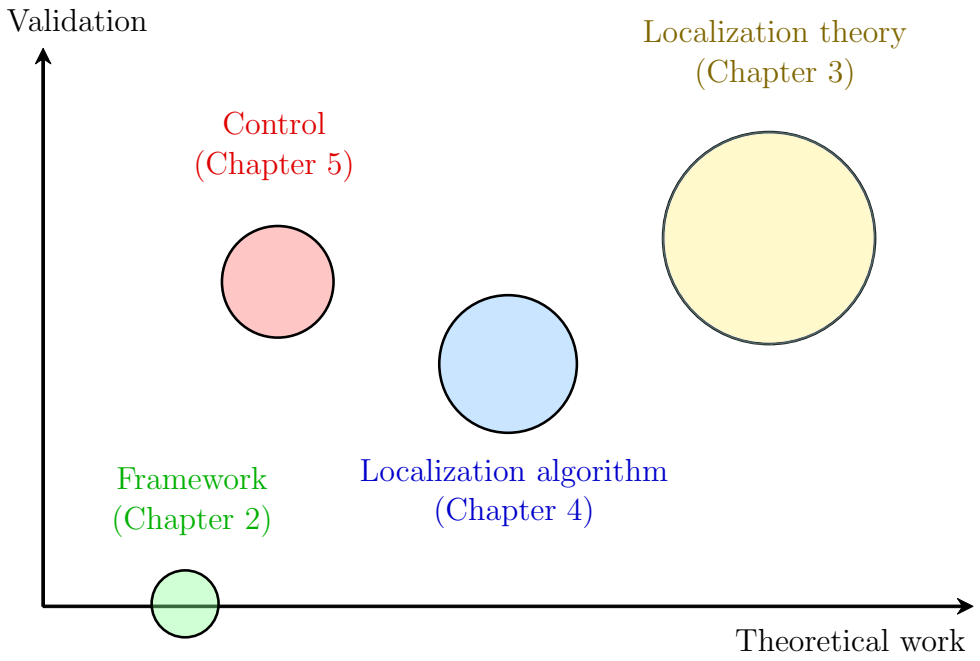

Figure 1.5. *Overview of the thesis structure: Each circle illustrates the amount of theoretical work versus the load of numerical and experimental validation in each technical chapter. The circle size represents the volume of that chapter.*

Chapter 2

A Formal Definition of Swarm Navigation

As we have already seen in Chapter 1, swarm navigation is an emerging interdisciplinary topic, involving physical signal processing, localization, Bayesian estimation, network and graph theory, control theory, etc. It is important to define a unified formal definition of swarm navigation systems before diving into particular aspects.

2.1 Extended Swarm Network

In this thesis we consider an extended swarm network in two-dimensional (2D) space, for example the Mars swarm exploration system introduced in Figure 1.2. Different entities of the example swarm network are illustrated in Figure 2.1 and formally defined in Section 2.1-2.5.

A generic node $\mathbb{a}_u \in \mathcal{V}$ with an index u in the network located at point P_u is either an agent within the agent set $\mathcal{A}$, an external source within the source set $\mathcal{S}$ or a beacon within the beacon set $\mathcal{B}$. Throughout the thesis, the index u preferably indicates a generic node, or an agent which receives a signal. The index v preferably indicates a node which transmits a signal. The complete node set in the network is defined as $\mathcal{V} = \mathcal{A} \cup \mathcal{S} \cup \mathcal{B}$. The coordinates, a.k.a. positions, of nodes are defined by the different coordinate systems under investigation. The collection of all agents' positions is referred to as the swarm's formation. In applications such as environmental feature mapping and path planning, the coordinates, $\mathbf{p}_u^{\mathbb{G}} = \text{vec}\{x_u^{\mathbb{G}}, y_u^{\mathbb{G}}\}$, w.r.t. a pre-defined global Cartesian coordinate system $\mathbb{G}$ are crucial. The vectorization operator $\text{vec}\{\cdots\}$ arranges elements into a column vector. The coordinate system $\mathbb{G}$ is often spanned by multiple beacons. In some other applications, for example, swarm formation estimation and source observation, an alternative swarm-level Cartesian coordinate system $\mathbb{C}$ with the origin at the swarm centroid is beneficial for analysis. The coordinates of node $\mathbb{a}_u$ become $\mathbf{p}_u^{\mathbb{C}} = \text{vec}\{x_u^{\mathbb{C}}, y_u^{\mathbb{C}}\}$. When the angular and distance information

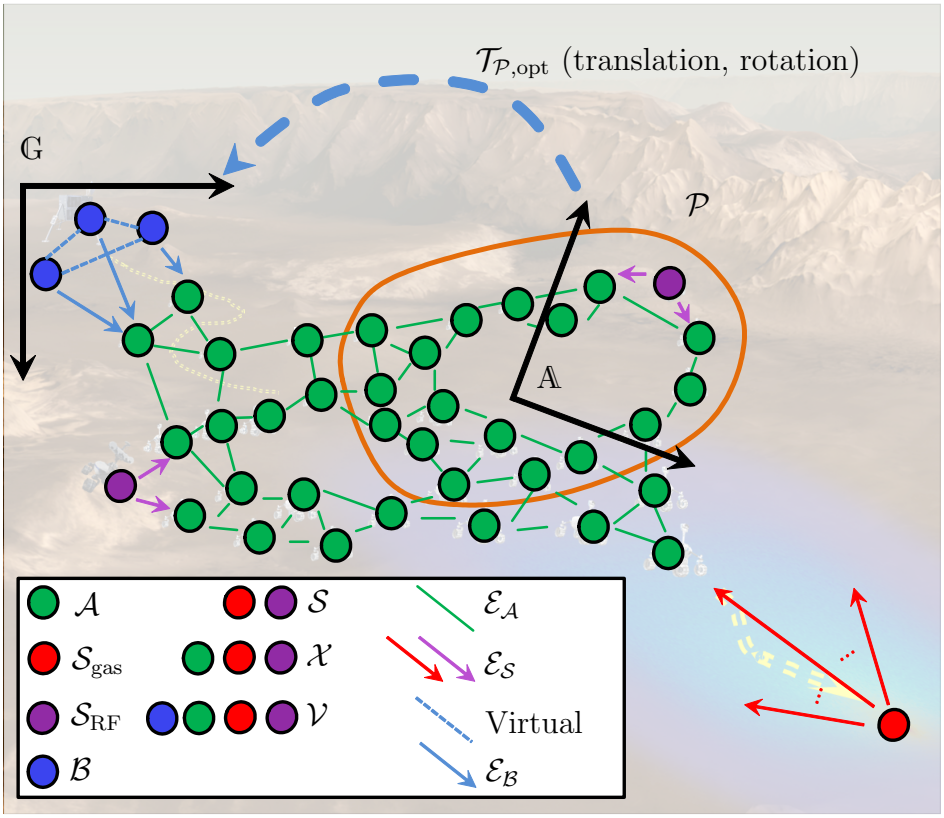

Figure 2.1. *Graph representation and different entities of the swarm system example shown in Figure 1.2: Agents, a gas source, RF sources and beacons, are illustrated as green, red, magenta and blue dot(s), respectively. Different links are shown with lines and arrows. Dashed arrow on the top indicates the transformation from an arbitrary swarm coordinate system $\mathbb{A}$ to the global coordinate system $\mathbb{G}$.*

between the source and the swarm are investigated individually, the swarm-level polar coordinate system $\mathbb{P}$, corresponding to $\mathbb{C}$, is preferable. In that case, the coordinates of the node $\mathbb{o}_u$ are denoted as $\mathbf{p}_u^{\mathbb{P}} = \text{vec}\{d_u^{\mathbb{P}}, \theta_u^{\mathbb{P}}\}$. If the coordinate system under investigation is previously specified, the superscript is often omitted for simplicity, where the coordinates of the node $\mathbb{o}_u$ are denoted as $\mathbf{p}_u$. A state vector of $\mathbb{o}_u$ is denoted as $\mathbf{x}_u = \text{vec}\{\mathbf{p}_u, \mathbf{a}_u\}$, including the coordinates $\mathbf{p}_u$ and other generic parameters $\mathbf{a}_u$, a.k.a. nuisance parameters. These parameters, e.g. clock offset, carrier phase offset or signal propagation parameters, maybe unknown and need to be jointly estimated together with the node's coordinates. The three types of nodes, i.e. beacons, sources and agents, are distinguished as follows.

1) Beacons

   A beacon $\mathbb{o}_u \in \mathcal{B}$ is a node with perfectly known global coordinates $\mathbf{p}_u^{\mathbb{G}}$ and nuisance parameters. The states of all beacons are $\mathbf{x}_{\mathcal{B}} = \text{vec}\{\mathbf{x}_u : \forall \mathbb{o}_u \in \mathcal{B}\}$. Beacons are static infrastructures, for example fixed RF transmitters at the mission base, which span the global coordinate system. The beacons are synchronized to each other and their clocks represent the system clock. A beacon $\mathbb{o}_u \in \mathcal{B}$ continuously emits a signal $s_u(t)$, which is exploited by the swarm for localization in the global coordinate system. In the context of cooperative and network localization, a beacon is also referred to as an anchor in literature, e.g. [32].

2) Sources

   A source $\mathbb{o}_u \in \mathcal{S}$ is an external node whose state $\mathbf{x}_u$ is unknown and of interest to the swarm. As in the swarm exploration example introduced in Chapter 1, a source can either be a static unit emitting RF signals, which is observed by the swarm as signals of opportunity, or an environmental point source that shall be localized by the swarm, e.g. a gas diffusion source. For this example, the set of sources $\mathcal{S}$ can be further divided into the set of RF sources $\mathcal{S}_{\text{RF}}$ and a set of gas sources $\mathcal{S}_{\text{gas}}$. Similar to beacons, the emitted signal from source $\mathbb{o}_u \in \mathcal{S}$ is generically denoted as $s_u(t)$. The states of all sources are represented as $\mathbf{x}_{\mathcal{S}} = \text{vec}\{\mathbf{x}_u : \forall \mathbb{o}_u \in \mathcal{S}\}$.

3) Agents

   Actively controlled agents are the core components of a swarm. An agent $\mathbb{o}_u \in \mathcal{A}$ emits a signal $s_u(t)$ and receives the signals $r_{uv}(t)$ emitted from other nodes $\mathbb{o}_v \in \mathcal{V}$ through unidirectional links $\mathbb{e}_{uv}$. Measurements like range, containing geometric relationship between $\mathbb{o}_u$ and $\mathbb{o}_v$ can be extracted from the received signals and are generically denoted as $\mathbf{z}_{uv}$. Links in the swarm network can be classified according to the origin of the signal. Agent $\mathbb{o}_u$ communicates and conducts measurements

with a neighboring agent $\mathbb{a}_v \in \mathcal{A}_u$ by an A2A link $\mathbb{e}_{uv} \in \mathcal{E}_{\mathcal{A},u} \subset \mathcal{E}_{\mathcal{A}}$. The set of neighboring agents $\mathcal{A}_u$ of $\mathbb{a}_u$ is defined for example by the measurement coverage of agents. The A2A link sets of agent $\mathbb{a}_u$ and of the network are defined as $\mathcal{E}_{\mathcal{A},u}$ and $\mathcal{E}_{\mathcal{A}}$, respectively. Additionally, agent $\mathbb{a}_u$ receives signals transmitted from an beacon $\mathbb{a}_v \in \mathcal{B}$ or a source $\mathbb{a}_v \in \mathcal{S}$ within the observation ranges of the beacon-to-agent (B2A) link $\mathbb{e}_{uv} \in \mathcal{E}_{\mathcal{B},u} \subset \mathcal{E}_{\mathcal{B}}$ and S2A link $\mathbb{e}_{uv} \in \mathcal{E}_{\mathcal{S},u} \subset \mathcal{E}_{\mathcal{S}}$. The B2A and S2A link sets of agent $\mathbb{a}_u$ and of the network are denoted as $\mathcal{E}_{\mathcal{B},u}$, $\mathcal{E}_{\mathcal{S},u}$, $\mathcal{E}_{\mathcal{B}}$ and $\mathcal{E}_{\mathcal{S}}$, respectively. The collective link sets of agent $\mathbb{a}_u$ and the network are $\mathcal{E}_u = \mathcal{E}_{\mathcal{A},u} \cup \mathcal{E}_{\mathcal{B},u} \cup \mathcal{E}_{\mathcal{S},u}$ and $\mathcal{E}_0 = \mathcal{E}_{\mathcal{A}} \cup \mathcal{E}_{\mathcal{B}} \cup \mathcal{E}_{\mathcal{S}}$. Agent $\mathbb{a}_u$ exploits the received signals collected from links $\mathcal{E}_u$ and the state information of its neighbors to estimate its own state $\mathbf{x}_u$. At the same time the agents jointly estimate the states of the sources $\mathbf{x}_{\mathcal{S}}$. The states of all agents are represented as $\mathbf{x}_{\mathcal{A}} = \text{vec}\{\mathbf{x}_u : \forall \mathbb{a}_u \in \mathcal{A}\}$. The measurement collection of agent $\mathbb{a}_u$ is denoted as $\mathbf{z}_u = \text{vec}\{\mathbf{z}_{uv} : \forall \mathbb{a}_v \in \mathcal{V}_u\}$. The total measurements in the swarm is defined as $\mathbf{z} = \text{vec}\{\mathbf{z}_u : \forall \mathbb{a}_u \in \mathcal{A}\}$.

Agents and sources are collectively denoted as the nodes with unknown parameters $\mathbb{a}_u \in \mathcal{X} = \mathcal{A} \cup \mathcal{S}$ and the set $\mathcal{X}$ is referred to as the unknown node set. The states of all unknown nodes are $\mathbf{x} = \text{vec}\{\mathbf{x}_{\mathcal{A}}, \mathbf{x}_{\mathcal{S}}\}$. The total states of the whole network are $\mathbf{x}_{\mathcal{V}} = \text{vec}\{\mathbf{x}_{\mathcal{B}}, \mathbf{x}\}$. While the explicit assignment of nodes to different sets is fixed, nodes can nevertheless take different implicit roles during a mission. An agent who is not moving for a while can accumulate precise absolute position information and can thus act as a quasi-beacon to other agents. Vice versa, an agent outside of the swarm or a remote beacon can be considered as a source to the swarm, when relative positions of nodes are of interest.

2.2 Graph Representation of Swarm Localization

We utilize graph theory to unify the swarm localization problem formulation, consisting the cases of anchor-free where available beacons are insufficient to span a global coordinate system, and anchor-based with sufficient number of beacons to define the global coordinate system $\mathbb{G}$. The swarm observation network can be interpreted as a framework $\mathcal{F}_0 = (\mathcal{G}_0, \mathbf{p}^{\mathbb{G}})$ with an underlying directed graph $\mathcal{G}_0 = (\mathcal{V}, \mathcal{E}_0)$, where nodes are interpreted as the vertices and measurement links as edges. The superscript $\mathbb{G}$ of coordinates is omitted for global coordinate system. The swarm observation network can be extended to an undirected graph with the same vertices $\mathcal{V}$ and undirected edges $\mathcal{L}_0 = \{\mathbb{l}_{uv} : \forall u < v, \mathbb{e}_{uv} \text{ or } \mathbb{e}_{vu} \in \mathcal{E}_0\}$. In order to incorporate the beacons in the formulation, we extend $\mathcal{L}_0$ with a virtual beacon-to-beacon (B2B) link set $\mathcal{L}_{\mathcal{B}} = \{\mathbb{l}_{uv} : \forall u < v, \mathbb{a}_u \text{ and } \mathbb{a}_v \in \mathcal{B}\}$ without measurement to completely connect all

the beacons, i.e. the new edge set is $\mathcal{L} = \mathcal{L}_0 \bigcup \mathcal{L}_\mathcal{B}$. The extended graph and framework become $\mathcal{G} = (\mathcal{V}, \mathcal{L})$ and $\mathcal{F} = (\mathcal{G}, \mathbf{p})$, respectively. In anchor-free case, positions of nodes w.r.t. $\mathbb{G}$ are not observable. Only the 'shape' of the network can be observed. The framework can be estimated subject to (s.t.) rigid affine transformations $\mathcal{T}(\hat{\mathbf{p}})$ including translations and rotations, where $\hat{\mathbf{p}}$ is the estimated position vector of nodes. Theoretically, there exists a flipping ambiguity for the 'shape' estimate. However, it is not a continuous transformation in 2D, thus excluded from discussion. In practice, the flipping ambiguity can be eliminated by initial information or tacking. The objective of network localization is to find a framework $\hat{\mathcal{F}} = (\mathcal{G}, \hat{\mathbf{p}})$, with nodes' coordinates $\hat{\mathbf{p}}$, whose 'shape' is as 'similar' as possible to the original one $\mathcal{F}$, given all the observations $\mathbf{z}$. In some applications, only nodes belong to a certain node subset $\mathcal{V}_\mathcal{P} = \mathcal{X}_\mathcal{P} \bigcup \mathcal{B}_\mathcal{P}$, including a subset of agents $\mathcal{A}_\mathcal{P}$, sources $\mathcal{S}_\mathcal{P}$ and beacons $\mathcal{B}_\mathcal{P}$, and $\mathcal{X}_\mathcal{P} = \mathcal{A}_\mathcal{P} \bigcup \mathcal{S}_\mathcal{P}$, are considered for localization and control. Through this thesis $\mathcal{P}$ is used to denote an unspecific set. A sub-framework $\mathcal{F}_\mathcal{P} = (\mathcal{G}_\mathcal{P}, \mathbf{p}_\mathcal{P})$ is defined with corresponding positions $\mathbf{p}_\mathcal{P}$, graph $\mathcal{G}_\mathcal{P} = (\mathcal{V}_\mathcal{P}, \mathcal{L}_\mathcal{P})$ and edge set $\mathcal{L}_\mathcal{P}$. Hence, the objective of swarm localization can be generally written as minimizing the shape difference $\varepsilon(\tilde{\mathcal{F}}_\mathcal{P}, \mathcal{F}_\mathcal{P})$ between sub-frameworks $\tilde{\mathcal{F}}_\mathcal{P} = (\mathcal{G}_\mathcal{P}, \mathbf{q}_\mathcal{P})$ and $\mathcal{F}_\mathcal{P}$. Given the total measurements $\mathbf{z}$, the swarm localization problem can be formally stated as

$$\hat{\mathbf{p}}_\mathcal{P} = \arg\min_{\mathbf{q}_\mathcal{P}} \ \varepsilon(\mathbf{q}_\mathcal{P}, \mathbf{p}_\mathcal{P}). \tag{2.1}$$

The cost function $\varepsilon(\mathbf{q}_\mathcal{P}, \mathbf{p}_\mathcal{P})$ describes the shape difference of the two sub-frameworks and can be defined as either the average shape difference $\varepsilon_{\tilde{\mathcal{F}}_\mathcal{P}}$ or as framework distance root mean square error (RMSE) $\varepsilon_{\hat{\mathbf{d}}_\mathcal{P}}$. Prior to the definition of $\varepsilon_{\tilde{\mathcal{F}}_\mathcal{P}}$, we need to define the position error vector after an affine transformation $\mathcal{T}_\mathcal{P}(\mathbf{q}_\mathcal{P})$ as

$$\boldsymbol{\varepsilon}_{\mathcal{T}_\mathcal{P}(\mathbf{q}_\mathcal{P})} \triangleq \mathcal{T}_\mathcal{P}(\mathbf{q}_\mathcal{P}) - \mathbf{p}_\mathcal{P}. \tag{2.2}$$

The notation $\triangleq$ denotes the definition and is read as 'is defined as'. The average shape difference is a direct metric to assess the 'similarity' of these two sub-frameworks and is defined as

$$\varepsilon_{\tilde{\mathcal{F}}_\mathcal{P}} \triangleq \sqrt{\frac{1}{|\mathcal{X}_\mathcal{P}|} \|\boldsymbol{\varepsilon}_{\mathcal{T}_{\mathcal{P},\mathrm{opt}}(\mathbf{q}_\mathcal{P})}\|^2}, \tag{2.3}$$

where the optimal affine transformation $\mathcal{T}_{\mathcal{P},\text{opt}}$ is the affine transformation, which leads to the minimum position estimation RMSE [47], constrained on beacons' positions, i.e.

$$\mathcal{T}_{\mathcal{P},\text{opt}} = \arg\min_{\mathcal{T}_{\mathcal{P}}} \|\boldsymbol{\varepsilon}_{\mathcal{T}_{\mathcal{P}}(\mathbf{q}_{\mathcal{P}})}\|^2 \tag{2.4}$$

$$\text{s.t.} \quad \mathcal{T}_{\mathcal{P}}(\mathbf{q}_u) = \mathbf{p}_u, \quad \forall \mathbb{o}_u \in \mathcal{B}_{\mathcal{P}}. \tag{2.5}$$

The notation $\|\cdot\|$ denotes the Frobenius norm of a scalar, a vector or a matrix, distinguished from the notation $|\cdot|$, which exclusively denotes the cardinality of a set. The optimal affine transformation aligns an arbitrary Cartesian coordinate system $\mathbb{A}$ to $\mathbb{G}$. For the anchor-based case, $\mathbb{A}$ and $\mathbb{G}$ are identical. The term $\boldsymbol{\varepsilon}_{\mathcal{T}_{\mathcal{P},\text{opt}}(\mathbf{q}_{\mathcal{P}})}$ is referred to as the shape difference.

The cost function $\varepsilon(\mathbf{q}_{\mathcal{P}}, \mathbf{p}_{\mathcal{P}})$ can also be defined by an indirect metric dubbed framework distance RMSE $\varepsilon_{\hat{\mathbf{d}}_{\mathcal{P}}}$, which compares the distance differences of every node pairs, even if there are no measurements between the pairs. Since beacons' positions are known, the virtual B2B link set $\mathcal{L}_{\mathcal{B}}$ is excluded. We define the considered link set $\mathcal{L}_{\text{all}}$, which describes a fully connected network, except the B2B pairs, i.e. $\mathcal{L}_{\text{all}} = \{\mathbb{l}_{uv} : \forall u < v,\ \mathbb{o}_u \text{ and } \mathbb{o}_v \in \mathcal{P},\ \mathbb{l}_{uv} \notin \mathcal{L}_{\mathcal{B}}\}$. The framework distance RMSE is defined as

$$\varepsilon_{\hat{\mathbf{d}}_{\mathcal{P}}} = \sqrt{\frac{\|\boldsymbol{\varepsilon}_{\hat{\mathbf{d}}_{\mathcal{P}}}\|^2}{|\mathcal{L}_{\text{all}}|}}, \tag{2.6}$$

where $\boldsymbol{\varepsilon}_{\hat{\mathbf{d}}_{\mathcal{P}}} = \text{vec}\{\varepsilon_{uv} : \forall\ \mathbb{l}_{uv} \in \mathcal{L}_{\text{all}}\}$, and $\varepsilon_{uv} = \|\hat{d}_{uv} - d_{uv}\|$ are the absolute difference between the node pair distances $\hat{d}_{uv} = \|\mathbf{q}_u^{\mathbb{A}} - \mathbf{q}_v^{\mathbb{A}}\|$ and $d_{uv} = \|\mathbf{p}_u - \mathbf{p}_v\|$ of sub-frameworks $\tilde{\mathcal{F}}_{\mathcal{P}}$ and $\mathcal{F}_{\mathcal{P}}$. The framework distance RMSE compares the distance differences of every node pairs, including the non-connected pairs, and does not require optimal transformation. The two metrics are not identical. However, for a generic large-scale sub-framework, both of the metrics capture the shape difference between the two sub-frameworks. Often, the average shape difference $\varepsilon_{\tilde{\mathcal{F}}_{\mathcal{P}}}$ in (2.3) is preferable for formal navigation problem formulation, whereas the framework distance RMSE $\varepsilon_{\hat{\mathbf{d}}_{\mathcal{P}}}$ in (2.6) is preferable for performance evaluation. If the measurements are the distances between nodes, the localizability of the sub-framework $\mathcal{F}_{\mathcal{P}}$ is analogous to the rigidity of the corresponding mechanical bar-joint framework. Hence, the localizability of a extended swarm network can be equivalently described by the rigidity theory from mechanics [48], which is discussed in Chapter 3.

As we can see, the extended swarm network is a complex system composed of heterogeneous entities. For the swarm system example shown in Figure 1.2, the graph

representation and different entities are illustrated in Figure 2.1 to visualize the introduced formal swarm navigation definition.

2.3 Swarm Dynamics and Position-Aware Control

Having defined the entities and sets, we have a look at the dynamics and control model of the agents. In many applications, the temporal evolution of the network state is of interest, instead of a snapshot of the current state. One example is Bayesian tracking, where temporal coherency of the state is exploited to improve the current state estimation. Another example is swarm control, where a control command is applied to the swarm for spatial transition. We use the superscripts $(-)$ to denote variables at the previous time step, and $(+)$ at the current step. Moreover, $(0:-)$ and $(0:+)$ indicate all previous time steps up to the last step and the current step, respectively.

Bayes' theorem is often applied for estimation problems with dynamics or more generally with *a-priori* information. A Bayesian estimator treats states $\mathbf{x}^{(+)}$ as random variables and estimates them from the *a posteriori* probability density function (pdf) $p(\mathbf{x}^{(+)}|\mathbf{z}^{(+)})$, which incorporates the *a priori* pdf $p(\mathbf{x}^{(+)})$ and the observation likelihood function $p(\mathbf{z}^{(+)}|\mathbf{x}^{(+)})$ by Bayes' rule

$$p\left(\mathbf{x}^{(+)}|\mathbf{z}^{(+)}\right) \propto p\left(\mathbf{x}^{(+)}\right) p\left(\mathbf{z}^{(+)}|\mathbf{x}^{(+)}\right). \tag{2.7}$$

With a state transition model and the first-order Markov assumption, the Bayesian estimation framework can be extended to an *a posteriori* filtered density $p\left(\mathbf{x}^{(+)}|\mathbf{z}^{(1:+)}\right)$ recursively with sequential measurements as

$$p\left(\mathbf{x}^{(+)}|\mathbf{z}^{(1:+)}\right) \propto p\left(\mathbf{z}^{(+)}|\mathbf{x}^{(+)}\right) p\left(\mathbf{x}^{(+)}|\mathbf{z}^{(1:-)}\right) \tag{2.8}$$

$$= p\left(\mathbf{z}^{(+)}|\mathbf{x}^{(+)}\right) \int p\left(\mathbf{x}^{(+)}|\mathbf{x}^{(-)}\right) p\left(\mathbf{x}^{(-)}|\mathbf{z}^{(1:-)}\right) \, \mathrm{d}\, \mathbf{x}^{(-)}. \tag{2.9}$$

Equation (2.9) is the foundation of recursive Bayesian tracking algorithms such as different variants of KFs and particle filters (PFs). The derivation of (2.9) is well known and can be found in [49, 50]. Once the *a posteriori* filtered density $p(\mathbf{x}^{(+)}|\mathbf{z}^{(1:+)})$ is acquired, a point estimate of the states can be obtained in a minimum mean square error (MMSE) or maximum *a posteriori* (MAP) manner.

Agents collaborate in the sense of actively adapting their positions so that the emerging swarm formation is optimized according to certain mission objectives. In our

example, these objectives include e.g. minimizing the position uncertainty of the swarm and external sources, i.e. information seeking, approaching to an area of interest, and avoiding collision. In this thesis, we mainly consider measurements that provide geometric information between nodes. The dynamic parameters of agent such as velocity, acceleration and heading are not included in the state. An extension to the dynamic state space is straightforward as shown in [51]. The transition of the agent's position in the global coordinate system $\mathbb{G}$ between two consecutive time steps is described by movement model

$$\mathbf{p}_u^{(+)} = f(\mathbf{p}_u^{(-)}, \mathbf{b}_u) + \boldsymbol{\omega}_{\mathbf{p}_u}, \quad \forall \mathbb{o}_u \in \mathcal{A}. \tag{2.10}$$

As an example in this thesis, we consider the following movement model [37]

$$\mathbf{p}_u^{(+)} = \mathbf{p}_u^{(-)} + \mathbf{b}_u + \boldsymbol{\omega}_{\mathbf{p}_u}, \quad \forall \mathbb{o}_u \in \mathcal{A}, \tag{2.11}$$

i.e. the control command $\mathbf{b}_u$ is directly applied to the 2D position of the agent. This control command is constrained by a maximum step size $b_{\max}$, i.e. $\mathbf{b}_u \in \mathcal{U} = \{\mathbf{b}_u : \forall \|\mathbf{b}_u\| \leq b_{\max}\}$. In other words, the spatial movement between two time steps is limited. In addition, the control command is disturbed by additive Gaussian noise, i.e.

$$\boldsymbol{\omega}_{\mathbf{p}_u} \sim \mathcal{N}(\mathbf{0}, \mathbf{Q}_{\mathbf{p}_u}(\mathbf{b}_u)), \quad \forall \mathbb{o}_u \in \mathcal{A}. \tag{2.12}$$

The Gaussian noise has zero mean and its covariance is a function of the control command $\mathbf{b}_u$, e.g.

$$\mathbf{Q}_{\mathbf{p}_u}(\mathbf{b}_u) = \sigma^2 \|\mathbf{b}_u\| \otimes \mathbf{I}_{2\times 2}, \quad \forall \mathbb{o}_u \in \mathcal{A}, \tag{2.13}$$

where σ^2 is the variance of noise normalized to step size, $\otimes$ denotes the Kronecker product, and $\mathbf{I}_{n\times n}$ denotes identity matrix with dimension n. This movement model reflects the fact that if the traveled distance, i.e. the magnitude of the control command, is large, so is the disturbance employed on this control. This is a realistic assumption for a high level movement model of a robot whose low level controller is based on odometry suffering from drift. For notation simplicity, we combine the control commands of all agents to $\mathbf{b}_{\mathcal{A}} = \text{vec}\{\mathbf{b}_u : \forall \mathbb{o}_u \in \mathcal{A}\}$, and denote the collective feasible control set as $\mathcal{U}_{\mathcal{A}}$. An extension to a more sophisticated movement model would not change the overall approach presented in this thesis. The considered swarm dynamic model allow us to focus on demonstrating the concept of applying estimation theory to swarm control. The transition of a generic parameter $[\mathbf{x}]_l$ other than agents' position, i.e. the nuisance parameter of an arbitrary node, or the coordinate of a non-agent node, is modeled similarly with a Gaussian process noise with small variance σ_l^2. Particularly $\sigma_l^2 = 0$ represents a special case of static state. The covariance of the complete state space of

the swarm is given by the diagonal matrix $\mathbf{Q}(\mathbf{b}_{\mathcal{A}})$, aggregating the diagonal elements of $\mathbf{Q}_{\mathbf{p}_u}(\mathbf{b}_u), \quad \forall \mathbb{o}_u \in \mathcal{A}$, and σ_l^2 for all other parameters.

Position-aware control aims to optimize the swarm formation to meet the aforementioned objectives. The objectives can be formulated as either cost functions, referred to as the $f-$type objectives, or as constraints, referred to as the $h-$type objectives. The information seeking can be employed as both types, i.e. either actively minimizing position uncertainties, or maintaining the uncertainties below a certain tolerated value $\varepsilon_{\max}$. In general, the information seeking as a cost function, can be combined with other high level mission objective like goal approaching, denoted as $f_{\mathrm{m}}(\mathbf{b}_{\mathcal{A}})$, with weighting factor w_{p} for information seeking and w_{m} for other cost functions, respectively. Besides, additional constraints like the collision avoidance function $h_{c,uv}(d_{uv}, d_{\min})$, with minimum tolerated distance between nodes $d_{\min}$ will be discussed in Section 5.5. The feasible control command set $\mathcal{U}_{\mathcal{A}}$ can be interpreted acts as a constraint as well. However, since it acts on the travel distance instead of direction, we consider it separately from the other constraints. To put these criteria into a formal formulation, a desired control command $\mathbf{b}_{\mathcal{A}}$ is generally defined as the one, which mostly efficiently reducing the estimation error of sub-framework $\mathcal{F}_{\mathcal{P}_f}$ and other potential mission cost function $f_{\mathrm{m}}(\mathbf{b}_{\mathcal{A}})$, while constrained on the estimation error of the sub-framework $\mathcal{F}_{\mathcal{P}_h}$, collision avoidance, and other potential constraints, i.e.

$$\underset{\mathbf{b}_{\mathcal{A}} \in \mathcal{U}_{\mathcal{A}}}{\text{minimize}} \quad w_{\mathrm{p}} \varepsilon(\hat{\mathbf{p}}_{\mathcal{P}_f}^{(+)}, \mathbf{p}_{\mathcal{P}_f}^{(+)}) + w_{\mathrm{m}} f_{\mathrm{m}}(\mathbf{b}_{\mathcal{A}}), \tag{2.14}$$

$$\text{s.t.} \quad \varepsilon_{\max} - \varepsilon(\hat{\mathbf{p}}_{\mathcal{P}_h}^{(+)}, \mathbf{p}_{\mathcal{P}_h}^{(+)}) \geqslant 0, \tag{2.15}$$

$$h_{c,uv}(d_{uv}, d_{\min}) \geqslant 0, \quad \forall \mathbb{l}_{uv} \in \mathcal{L}_{\text{all}}, \tag{2.16}$$

$$\vdots$$

The information seeking objective function $\varepsilon(\hat{\mathbf{p}}_{\mathcal{P}}^{(+)}, \mathbf{p}_{\mathcal{P}}^{(+)})$ depends on the new agents' positions, i.e. is a function of the control command $\mathbf{b}_{\mathcal{A}}$ as expressed in (2.11). The sub-frameworks $\mathcal{P}_f$ and $\mathcal{P}_h$, as well as the weights w_{p} and w_{m} can be chosen flexibly according to applications. For information seeking, individual weight can be assigned to each node. Variants of objective functions can be defined according to the employed signal processing models, for example the Bayesian and non-Bayesian models, which will be discussed in details in Chapter 5.

2.4 Signals and Observations in Swarm

Different types of physical emission processes can be modeled with partial differential equations (PDEs), such as the wave equation for RF, seismic and acoustic waves, and the diffusion equation for gas and heat diffusion. If the emission area of the physical process is small enough, it can be approximated as a point emitter, such as an external source, a beacon or another agent. We only focus on the isotropic point emitter case, where the distance information between the observing agent and the emitter can be extracted from either the intensity-based signal features like the received amplitude of RF signals [52], or the concentration of gas signals [53], or the propagation time based signal features like carrier phase [54, 55] and symbol delay [56, 57, 58, 59] of RF signals. Note, that non-geometrical information such as proximity and fingerprint can be exploited for localization as well. However, these techniques either provide insufficient accuracy or require a database, which are not suitable for swarm navigation and excluded from the discussion. In general, localization approaches with RF signals could be directly adapted to acoustic source localization tasks [60, 61]. Instead of RF signals, acoustic waves are received by microphone arrays in order to estimate or track unknown sound sources. Similarly, range related observations can be exploited in seismic applications to find sources of tremors or earthquakes. For example, seismic source is localized in [62] based on time difference of arrival (TDoA) observations obtained from synchronous sensor networks. Even for other physical phenomena like airborne dispersion of gas, it is possible to find range related observations that indicate the geometrical relationship between the swarm and an emission source. The most evident observations is the gas concentration that is decreasing with the distance to the source [63, 53]. For gas source localization, one can also find other statistic features of the gas signal, e.g. variance [64] or bouts [65], that correlate with the relative distance to the source. We unify different signal observations by introducing a general signal model for fields generated by point sources in Section 2.4.1. Observation models with RF signal, derived from the wave equation, are discussed in details in Section 2.4.2 and Section 2.4.3, which are the main observation models assumed for the swarm application in this thesis. To demonstrate the signal model's generality, an observation of gas diffusion, derived from the diffusion equation, is briefly introduced in Section 2.4.4.

2.4.1 Generic Signal Model

The spatial-temporal process exploited for swarm navigation can be often described by a PDE. The solution of the PDE is normally a function of position and time, which we referred to as the signal model, indicating the signal observable at certain position

and time.

For a general case we assume a node $\mathbb{o}_v \in \mathcal{V}_u$, emitting a continuous signal $s_v(t)$. An agent $\mathbb{o}_u \in \mathcal{A}$ observes this continuous signal as

$$r_{uv}(t) = s_{uv}(\mathbf{x}_{uv}, t) + \epsilon_{uv}(t), \quad 0 \leq t < T_o \tag{2.17}$$

through link $\mathbb{e}_{uv}$. The term $s_{uv}(\mathbf{x}_{uv}, t)$ contains the emitted signal, propagation effects as well as position-related information about nodes $\mathbb{o}_u$ and $\mathbb{o}_v$, where $\mathbf{x}_{uv} \triangleq \text{vec}\{\mathbf{x}_u, \mathbf{x}_v\}$. As (2.17) is general, $s_{uv}(\mathbf{x}_{uv}, t)$ can be either real or complex valued depending on the underlying physics. For real $s_{uv}(\mathbf{x}, t)$, the additive noise $\epsilon_{uv}(t)$ is a white process [66] with a power spectral density (PSD) of $N_0/2$. In the complex-valued case we have $\epsilon_{uv}(t) = \Re[\epsilon_{uv}(t)] + \jmath\Im[\epsilon_{uv}(t)]$ with the real, denoted with the real value operator $\Re[\cdot]$, and imaginary parts, denoted with the imaginary value operator $\Im[[\cdot]$, being white processes with a PSD of $N_0/2$. The letter $\jmath$ denotes the imaginary unit. As $\epsilon_{uv}(t)$ is zero-mean, $s_{uv}(\mathbf{x}_{uv}, t)$ represents the mean of $r_{uv}(t)$.

Particularly for radial signals, i.e. the signals sent out from isotropic point emitters and homogeneously propagating into the environment, the signal fronts are spherical. Hence, the received signal depends only on the emitter-to-receiver distance and time. Therefore, the geometric relationship of the emitter and receiver is solely embedded in distance-related signal features.

The signal features $\mathbf{g}_{uv} = \mathbf{g}(d_{uv}, \mathbf{a}_u, \mathbf{a}_v)$ are expressed as real-valued functions of real-valued nuisance parameters $\mathbf{a}_u, \mathbf{a}_v$ and distance d_{uv}. Both signal feature functions and nuisance parameters are determined by the underlying physical models. Often in practice, discrete received signals $\mathbf{r}_{uv} = \text{vec}\{r_{uv}(iT_{\text{sa}}) : i = 1, \cdots, N\}$ are obtained, which are sampled from the continuous signal $r_{uv}(t)$ at N time instants with a sampling period T_{sa}.

2.4.2 Generic RF Signals

RF propagation is described by the spherical wave equation

$$\frac{\partial^2 dE(P,t)}{\partial d^2} = \frac{1}{c^2}\frac{\partial^2 dE(P,t)}{\partial t^2}, \tag{2.18}$$

which can be derived from the Maxwell equations for a three-dimensional (3D) observation point P at time t, with distance d between observation point and the emitter, the speed of light c and electric field $E(P,t)$ [54, p. 465]. Equation (2.18) holds for electric fields $E(P,t)$ when the medium of propagation is homogeneous and non-dispersive. Considering signals sent from a point emitter, the generic solution to (2.18) is of the

form

$$E(P,t) = \frac{1}{d}\, s_+(t - d/c) + \frac{1}{d} s_-(t + d/c), \tag{2.19}$$

where $s_+(t)$ and $s_-(t)$ are two arbitrary functions. We are only interested in the outward traveling wave $1/d s_+(t - d/c)$, i.e. the signal traveling from the emitter into environment. Particularly, for a RF point emitter $\mathbb{t}_v$, the outward traveling wave can be modeled as

$$d^{-1} s_+(t - d/c) = d^{-1} A_v e^{\jmath\omega(t-d/c)} s_v(t - d/c), \tag{2.20}$$

with the transmit power A_v^2 and the normalized transmitted baseband signal $s_v(t)$ modulated onto a carrier $e^{\jmath\omega t}$ with carrier frequency f and $\omega = 2\pi f$. A receiver $\mathbb{t}_u$ at distance d_{uv} from the emitter would observe the down converted and low-pass filtered baseband signal (multiplication by $e^{-\jmath\omega t}$) within the observation interval $0 < t < T_o$ as

$$r_{uv}(t) = \underbrace{\overbrace{A_v d_{uv}^{-\frac{\gamma}{2}}}^{A_{uv}} e^{-\jmath\omega(\overbrace{d_{uv} - \delta_{uv} - \phi_{uv}}^{\Phi_{uv}})/c)}}_{\alpha_{uv}} \underbrace{\overbrace{s_v(t - (\underbrace{d_{uv} - \delta_{uv}}_{\tau_{uv}})/c)}^{\tilde{s}_{uv}(t)}}_{s_{uv(t)}} + \epsilon(t). \tag{2.21}$$

The path-loss exponent γ equals to two for free-space propagation and larger than two if the propagation path is (partially) obstructed. As oscillators in transmitter and receiver are not synchronized we have a clock offset $\delta_{uv} = \delta_u - \delta_v$ in addition to the propagation, with δ_v and δ_u denoting the clock offsets of the transmitter and receiver, w.r.t. a system clock, respectively. Additional phase offsets $\phi_{uv} = \phi_u - \phi_v$ can be present, e.g. due to phase-locked loops (PLLs) in the transceiver chain. The phase offsets of the transmitter and receiver, w.r.t. a system phase are denoted as ϕ_v and ϕ_u, respectively. The additive noise $\epsilon(t)$ is circularly-symmetric complex normally distributed with a PSD $N_0/2$ for real and imaginary components, respectively. Since we are interested in the geometric information contained in the signal, both symbol delay τ_{uv} and carrier phase Φ_{uv} are in units of meters. For simplicity we assume that the carrier frequency offset and clock drift have already been compensated.

It can be observed that the position information can be extracted from either received signal magnitude A_{uv}, symbol delay τ_{uv} and carrier phase Φ_{uv}, which are functions of distance between transceivers d_{uv} and nuisance parameters, i.e. A_v, γ, δ_{uv}, ϕ_{uv}. If these additional parameters are known, direct range measurements can be obtained, for example, by received signal strength (RSS) from magnitude A_{uv} or time of arrival (ToA) from symbol delay τ_{uv}. Ranging directly from the carrier phase is difficult due to short wavelength. However, with appropriate infrastructure and ini-

tialization, ranging with carrier phase is possible, similar to the real-time kinematic (RTK) service in GNSSs. If both forward and backward links are available, symbol delays from both directions can be combined to the round trip time (RTT) observation. The clock offsets δ_{uv} and δ_{vu} cancel each other out, so that an equivalent direct ranging can be obtained. In the case of general unknown nuisance parameters, measurements at spatially separated points are collected by agents. Essentially, distance differences between transceivers are exploited for joint localization and parameter estimation. For magnitude and symbol delay, differential received signal strength (DRSS) and TDoA are utilized for localization, respectively. For carrier phase, traditional angle of arrival (AoA) measurement from the phase difference of arrival (PDoA) observation with plane-wave model contains only the angular information between nodes. The CoA measurement adopts the spherical-wave model, which includes both distance and angular information [67].

For the transmitted baseband signal $s_v(t)$, orthogonal frequency-division multiplexing (OFDM) modulation scheme is assumed as an example for discussion, which is widely employed in communications, e.g. in wireless local area network (WLAN), long-term evolution (LTE) and intelligent transport systems (ITS)-G5, as well as foreseen in 5^{th} generation mobile networks (5G). An OFDM signal $s_v(t)$ transmitted from $\mathbb{a}_v$ is expressed as

$$s_v(t) = \frac{1}{\sqrt{N}} \sum_{n \in \mathcal{N}_v} S_n e^{\jmath \omega_{sc} n t}, \tag{2.22}$$

where $\omega_{sc} = 2\pi f_{sc}$, f_{sc} is the subcarrier spacing, n is the subcarrier index, and S_n is the information symbol carried by the n^{th} subcarrier. The subcarriers employed for RF observation are in general a subset of the total subcarriers, i.e. $\mathcal{N}_v \subseteq \{-\frac{N-1}{2}, \cdots, \frac{N-1}{2}\}$. We assume an odd number N of total subcarriers, without loss of generality.

In a realistic scenario, the signal is not only distorted by AWGN, but also affected by the propagation channel. For line-of-sight (LOS) scenarios, the signal propagates along the LOS path and some additional paths, referred to as multipath components (MPCs). Whereas for NLOS scenarios, the signal is solely received via the MPCs. The observation model defined in (2.21) considered only a single path, i.e., the LOS path. This model is mainly assumed within the thesis, which allows us to concentrate on the main topics of swarm navigation. One exception is in Chapter 4, where the impacts of unpredictable propagation conditions on the proposed DiPNet algorithm is explicitly investigated, and the RF observation model in (2.21) is extended with multipath/NLOS propagation. A generic path component l is defined by its complex amplitude $\alpha_{uv,l} = A_{uv,l} e^{\jmath \omega \phi_{uv,l}/c}$, with a magnitude $A_{uv,l}$ and a phase $\phi_{uv,l}$, and the total propagation delay $\tau_{uv,l} = d_{uv,0} + \delta_{uv,l} + b_{uv}$, which includes the LOS distance $d_{uv,0}$, the

NLOS delay b_{uv} and the path's delay δ_l additional to the potential LOS path delay all with units of meters. The NLOS delay b_{uv} is positive for NLOS scenarios and zero for LOS scenarios. The LOS path is denoted with index 0, i.e. $\delta_{uv,0} = 0$. NLOS scenarios are included by setting $\alpha_{uv,0} = 0$. The clock offsets are assumed to be compensated with the RTT technique already. The received signal can be generally written as the superposition of the potential LOS path and L MPCs distorted by the AWGN $\epsilon_{uv}(t)$ as

$$r_{uv}(t) = \sum_{l=0}^{L} \alpha_{uv,l}\ s_v(t - \tau_{uv,l}/c) + \epsilon_{uv}(t). \tag{2.23}$$

2.4.3 Heterogeneous RF Signals in Swarm

Two types of RF signals are employed by the swarm. The first one is with a higher carrier frequency like $f_c = 5.2\,\text{GHz}$ and $\omega_c = 2\pi f_c$, and a larger bandwidth like $B_c = 37\,\text{MHz}$, aiming for short distance communications and intra-swarm measurements, i.e. on A2A links. The second one is with a much lower carrier frequency like $f_s = 20\,\text{MHz}$ and $\omega_s = 2\pi f_s$, and a smaller bandwidth like $B_s = 1\,\text{KHz}$, which is suitable for long distance communications and beacon/RF source to swarm measurements, i.e. on B2A and S2A links. For the three different RF link classes, namely A2A, B2A and S2A links, we consider three specific types of signal models derived from (2.21).

1) A2A links

   For a specific A2A link $\mathbb{e}_{uv} \in \mathcal{E}_\mathcal{A}$, agent $\mathbb{v}_v$ transmits a signal $s_v(t)$ modulated onto a carrier with carrier frequency f_c. The signal is received by agent $\mathbb{v}_u$ and down-converted to baseband. The received signal in baseband can then be expressed by

   $$r_{uv}(t) = \alpha_{uv}\, s_v(t - (d_{uv} - \delta_u + \delta_v)/c) + \epsilon_{uv}(t), \tag{2.24}$$

   where α_{uv} is the unknown complex signal amplitude, considered as a nuisance parameter. For the A2A links we mainly consider the position information extracted from the symbol delay. Particularly, if the A2A links are always symmetric, i.e. $\mathbb{e}_{uv} \in \mathcal{E}_\mathcal{A}$ if and only if (i.f.f.) $\mathbb{e}_{vu} \in \mathcal{E}_\mathcal{A}$, the clock offsets from both links cancel out. Hence (2.24) can be equivalently expressed with $-\delta_u + \delta_v = 0$. In this case, distance can be directly estimated from ToA.

2) B2A links

   The second type is the B2A links included in $\mathcal{E}_\mathcal{B}$. Signals are emitted by beacons near the mission base. The lower carrier frequency $f_s \ll f_c$ is suitable for guiding the

swarm within a wider area. Beacons' clock offsets δ_v and phase offsets ϕ_v are set to zero and assumed to be known. Due to the lower carrier frequency we assume that in this case the position information contained in the carrier phase can be exploited in addition to the symbol delay. In order to extract geometric information from the phase, it is essential to assume that the phase offset from the agent's receiving frontend is coherent to its clock offset. This assumption is valid explicitly for low RFs if the carrier phase, for example from the PLL or direct sampling, are adjusted to be aligned with its own clock. Hence, the receiver's phase offset fulfills $\phi_u = \delta_u$. In the end, the phase offset in the transceiver chain becomes $\phi_{uv} = \delta_u$. A signal transmitted by beacon $\mathbb{a}_v$ and received by agent $\mathbb{a}_u$ is defined in baseband as

$$r_{uv}(t) = A_{uv} e^{-\jmath\omega_s(d_{uv}-\delta_u)/c}\, s_v(t - (d_{uv} - \delta_u)/c) + \epsilon_{uv}(t). \tag{2.25}$$

For sufficient number of beacons, the positions of agents in the global coordinate system $\mathbb{G}$ can be estimated from symbol delays with the TDoA observations. In addition, by exploiting the carrier phase, the AoA or CoA measurements can be applied to estimate agents' angle or position in $\mathbb{G}$. In the case of insufficient number of beacons, the position of agents in $\mathbb{G}$ is not observable. However, if the swarm's formation is already estimated with A2A links, w.r.t. its own coordinate system $\mathbb{C}$, the beacons' positions in $\mathbb{C}$ can be estimated reversely, with range difference, AoA or CoA measurements. In this case, the beacons are similar to an external RF source. One application of this technique is returning to mission base, where insufficient number of beacons are deployed, which will be discussed in Chapter 5.

3) S2A links

The third link type under consideration is S2A links included in $\mathcal{E}_{\mathcal{S}}$, where signals are emitted from external RF sources. Similar to the B2A signals, they have a low carrier frequency $f_s \ll f_c$. Similar to (2.25), we assume the receiver's carrier phase is aligned with its clock, i.e. $\phi_u = \delta_u$. A signal transmitted by source $\mathbb{a}_v$ and received by agent $\mathbb{a}_u$ is described by

$$r_{uv}(t) = A_{uv} e^{-\jmath\omega_s(d_{uv}-\delta_u+\phi_v)/c} s_v(t - (d_{uv} - \delta_u + \delta_v)/c) + \epsilon_{uv}(t). \tag{2.26}$$

The difference to (2.25) is that in contrast to the beacons, the clocks of the RF sources are not synchronized to the system. Therefore the unknown clock offset and phase offset δ_v and ϕ_v has to be estimated jointly as nuisance parameters. Similarly symbol delays and carrier phase can be exploited with range difference, AoA or CoA method for source localization, w.r.t. $\mathbb{C}$ or $\mathbb{G}$, depending on whether

the number of beacons is sufficient.

2.4.4 Gas Diffusion

Gas diffusion process can be described by PDEs, referred to as the diffusion equations [68]. The gas concentration can be observed by swarm and utilized for gas source localization. In [53], sophisticated gas diffusion models have be investigated. In this thesis, we consider a single gas source $\mathbb{o}_v \in \mathcal{S}_{\text{gas}}$ at point P_v with radial diffusion. Planar isotropic diffusion in steady state is assumed, which corresponds to the diffusion of material with a density heavier than the surrounding atmosphere. With this model, similar as described in [68, p. 69], the diffusion equation simplifies to an ordinary differential equation (ODE), which depends only on the source distance d, and expressed as

$$-\kappa\left(\frac{\partial^2 C(d)}{\partial d^2}+\frac{1}{d}\frac{\partial C(d)}{\partial d}\right)=h_s(d),\quad d\in\mathbb{R}_+, \tag{2.27}$$

where κ is the diffusion coefficient and $h_s(d)$ is a source function. We define the source function as $h_s(d)=\eta\cdot(1-\sigma_H(d/R_0-1))$ with σ_H indicating a Heaviside step function. The source function describes a disc with a significantly small radius of, for example $R_0=1\,\text{m}$, which can be considered as a point in the ground, with an emission rate η. As a boundary condition, we assume that the concentration reaches 0 at a distance $d_{\max}$ from the source. In addition we consider $\frac{\partial C(d)}{\partial d}|_{d=0}=0$. The solution of the ODE in (2.27) is derived together with my colleague Thomas Wiedemann, and expressed as

$$\begin{cases} \dfrac{\eta}{2\kappa}\left(\dfrac{R_0^2}{2}-\dfrac{d^2}{2}+R_0^2\ln d_{\max}-R_0^2\ln R_0\right), & 0<d<R_0 \quad (2.28a)\\ \dfrac{\eta R_0^2}{2\kappa}\left(\ln d_{\max}-\ln d\right), & R_0<d<d_{\max}. \quad (2.28b)\end{cases}$$

For source localization we are interested in the second case $R_0 < d < d_{\max}$, i.e. the concentration outside the source. We can rewrite the concentration from the gas source $\mathbb{o}_v \in \mathcal{S}_{\text{gas}}$ at agent $\mathbb{o}_u \in \mathcal{A}$ within an observation window $0 < t < T_o$ as

$$s_{uv}(\mathbf{x}_{uv},t)=C(d_{uv})=\underbrace{\frac{\eta R_0^2}{2\kappa}\ln d_{\max}}_{a_{\text{g}}}-\underbrace{\frac{\eta R_0^2}{2\kappa}}_{b_{\text{g}}}\ln d_{uv}. \tag{2.29}$$

As can be seen from (2.29), the gas concentration has two nuisance parameters, namely the scaling parameter a_{g} and the exponent parameter b_{g}, employed to the distance, which has a similar expression as the magnitude observation of a RF source in (2.21). With the gas diffusion model and a Gaussian assumption on the sensor noise, the

received signal at $\mathbb{o}_u$ is given as

$$r_{uv}(t) = s_{uv}(\mathbf{x}_{uv}, t) + \epsilon_{uv}(t), \tag{2.30}$$

with $\epsilon_{uv}(t)$ being AWGN. With the gas source model under consideration, we assume either there is only one gas source, or there exist multiple separable sources, e.g. with different types of gas. This assumption circumvents the necessity to distinguish between the received concentration of different emission sources in the diffusion process. There are also possibilities as discussed in [69] to localize multiple gas sources with same type.

2.5 Generic terminologies in Swarm Localization

To avoid ambiguities, the terminologies used in this thesis for problem statement of swarm localization are listed as follows. A node with index u belonging to node set $\mathcal{P}$, is denoted as $\mathbb{o}_u \in \mathcal{P}$. The node is located at a point in space independent to coordinate system as P_u. In a particular coordinate system $\mathbb{A}$, the node possesses coordinates $\mathbf{p}_u^{\mathbb{A}}$, which is referred to as the position of that node. The process of acquiring the node's position estimate $\hat{\mathbf{p}}_u^{\mathbb{A}}$ is referred to as localization. A list of these terminologies can be found in Table 2.1.

Table 2.1. *Terminologies in swarm localization problem statement.*

Node index	**Node**	**Node set**	**Point in space**	**Coordinate system**	**Coordinates (position)**	**Position estimate (localization)**
u	$\mathbb{o}_u$	$\mathcal{P}$	P_u	$\mathbb{A}$	$\mathbf{p}_u^{\mathbb{A}}$	$\hat{\mathbf{p}}_u^{\mathbb{A}}$

The terminologies used in the swarm localization signal processing chain are defined as follows. An agent first receives continuous or sampled signals, e.g. RF and gas signals. Signals are generically denoted with the letter $\mathbf{r}$. Features of the signals, generically denoted with the letter $\mathbf{g}$, are the physical quantities in the signal model, which contain geometrical relationship between the emitter and the receiver. As particularly for an isotropic point source, the signal features can be represented as functions of emitter-to-receiver distance and nuisance parameters, and classified into two categories, namely the intensity based, and the propagation time based features. The intensity based features include, e.g. amplitude of RF signals, and concentration of gas signals. The propagation time based features are only observable for time variant signals, such as the carrier phase and symbol delay of RF signals. In the case of known nuisance parameters, the signal features solely depend on the distance. Whereas in presence of unknown nuisance parameters, the signal features are expressed as joint functions of

Table 2.2. *Terminologies in signal processing chain of swarm localization.*

Terminology	**Examples**
Received signals ($\mathbf{r}$)	continuous $r_{uv}(t)$, sampled $\mathbf{r}_{uv}$
Signal features ($\mathbf{g}$)	amplitude A_{uv}, phase Φ_{uv}, symbol delay τ_{uv}, gas concentration C_{uv}
Observations	RSS, DRSS, PoA, PDoA, ToA, TDoA, RTT, observed concentration
Measurements ($\mathbf{z}$)	range, range difference, AoA, AoD, CoA, sampled signal $\mathbf{r}_{uv}$(for direct localization)
States ($\mathbf{x}$)	positions of nodes (parameters of interest) $\mathbf{p}_{\mathcal{X}}$, nuisance parameters: $A_v, \gamma, \delta_{uv}, \phi_{uv}, a_{\mathrm{g}}, b_{\mathrm{g}}$
Evaluation metrics ($\boldsymbol{\varepsilon}$)	covariance, variance, RMSE, (average) framework shape difference: $(\varepsilon_{\tilde{\mathcal{F}}_{\mathcal{P}}})$, $\boldsymbol{\varepsilon}_{\mathcal{T}_{\mathcal{P},\mathrm{opt}}(\mathbf{q}_{\mathcal{P}})}$, framework distance error and RMSE: $\boldsymbol{\varepsilon}_{\hat{\mathbf{d}}_{\mathcal{P}}}$, and $\varepsilon_{\hat{\mathbf{d}}_{\mathcal{P}}}$

distance and nuisance parameters. Observations are obtained by the receivers, linked to the signal features, and contaminated by noise. Observations can be clustered into two categorizes according to the presence of nuisance parameters. Without nuisance parameter, direct observations are obtained at each receiver, e.g. RSS, phase of arrival (PoA), ToA and the observed gas concentration. With nuisance parameters, indirect observations combing the ones at multiple receivers are obtained, e.g. DRSS, PDoA, TDoA and observed gas concentration difference. The observations are transferred to geometrical inference between nodes,such as range, pseudo-range, range difference, AoA, angle of departure (AoD), CoA, etc., referred to as measurements, generically denoted with the letter $\mathbf{z}$. In an exceptional case of direct localization in Chapter 4, the sampled received signal $\mathbf{r}_{uv}$ is directly treated as measurements. The direct localization scheme has a benefit of preserving more information from the signal for localization, which will be discussed in Chapter 4. States, generically denoted with the letter $\mathbf{x}$, including the parameters of interest like nodes' positions and the nuisance parameters, can be then estimated from the measurements. Finally, the performance of swarm localization is evaluated by the metrics, generically denoted with the letter $\boldsymbol{\varepsilon}$, such as covariance, variance, RMSE, (average) framework shape difference and framework distance error and RMSE. A summary of the terminologies in the signal processing chain is listed in Table 2.2.

Chapter 3

Theoretical Aspects of Swarm Localization

With the formal framework introduced in Chapter 2, we are able to theoretically investigate the potential, constraints and geometrical interpretations of swarm localization. In estimation theory, a variety of mathematical tools have been introduced to reveal some specific characteristics of parameter estimation problems. Among those tools, estimation performance bounds directly indicate the best possible statistical performance of arbitrary estimators given the system model, which can be utilized in a wide range of applications, such as system analysis and optimization, estimator design, etc. Especially, the CRB and its variations are widely used for both swarm localization and position-aware swarm control in the thesis. We briefly introduce the CRB, posterior Cramér-Rao bound (PCRB) and Ziv-Zakai bound (ZZB), which are relevant to the thesis, in Section 3.1. In Section 3.2, the FI contained in the swarm observations is derived. We also discuss the choice an of optimal swarm coordinate system $\mathbb{C}$, when the number of beacons is insufficient. For swarm self-localization, in Section 3.3 we focus on the network localizability and limited RF resource effects. In Section 3.4, we look into the geometrical interpretation of source localization with different types of nuisance parameters and introduce the concept of CoA based source localization. In Section 3.5, the potential of swarm joint self- and source localization is analyzed. The results in Section 3.6 evaluate the potential performance of swarm localization.

3.1 Lower Bounds for Parameter Estimation

3.1.1 Cramér-Rao Bound

The theory of FI and CRB is one of the most widely used tools in statistical signal processing for system analysis/design, estimator benchmark, etc., due to its simplistic expression. The CRB has been intensively discussed e.g. in [70, 27, 71]. In many

estimation problems, parameters $\mathbf{x}$ to be estimated are considered as unknown deterministic variables. Discrete observations $\mathbf{z}$ are distorted with random noise and linked to the parameters with a likelihood function $p(\mathbf{z};\mathbf{x})$. The Fisher information matrix (FIM) $\mathbf{I}_\mathbf{x}$ quantifies the 'information' contained in $\mathbf{z}$ about $\mathbf{x}$, and is defined as [27, p. 44]

$$\mathbf{I}_\mathbf{x} = -\mathbb{E}_\mathbf{z}\left[\triangle_\mathbf{x}^\mathbf{x} \ln p(\mathbf{z};\mathbf{x})\right], \tag{3.1}$$

with the notations of the first and second order partial derivatives $\nabla_\mathbf{a}$ and $\triangle_\mathbf{a}^\mathbf{b} \triangleq \nabla_\mathbf{a}\nabla_\mathbf{b}^T$. If $\mathbf{I}_\mathbf{x}$ is full rank, and the regularity condition holds, i.e.

$$\mathbb{E}_\mathbf{z}\left[\nabla_\mathbf{x} \ln p(\mathbf{z};\mathbf{x})\right] = \mathbf{0}, \tag{3.2}$$

the CRB, defined as the inverse of the FIM, bounds from below the covariance matrix $\mathrm{cov}[\hat{\mathbf{x}}]$ of any unbiased estimates $\hat{\mathbf{x}}$, i.e.

$$\mathrm{cov}[\hat{\mathbf{x}}] \succcurlyeq \mathrm{CRB}[\mathbf{x}] \triangleq \mathbf{I}_\mathbf{x}^{-1}. \tag{3.3}$$

The expression $\mathbf{A} \succcurlyeq \mathbf{B}$ reads as '$\mathbf{A}$ is more positive semidefinite than $\mathbf{B}$', meaning $\mathbf{A}-\mathbf{B}$ is a positive semidefinite matrix, i.e. $\mathbf{A}-\mathbf{B} \succcurlyeq \mathbf{0}$. The CRB can be alternatively expressed as a lower bound for the variance of any unbiased individual estimate $[\hat{\mathbf{x}}]_l$, i.e.

$$\mathrm{var}\left[[\hat{\mathbf{x}}]_l\right] \geq \mathrm{CRB}[\mathbf{x}]_{l,l}. \tag{3.4}$$

Cases of singular FIM are discussed in [72], where constraints may be added to the problem, so that a meaningful CRB can be derived. In our swarm navigation application, if the swarm network is not localizable, the position FIM will be singular. A singular position FIM is also expected when the number of beacons is insufficient. For example, if there is only one beacon, the coordinate system can be rotated around that beacon, which leads to a rank one deficiency. Both singularity cases will be discussed in Section 3.3.

The theory of FI and CRB is extended to general Gaussian observations in [27, p. 47], discrete complex-valued observations in [27, p. 525], continuous real-valued observations with approximation in limits in [27, p. 55], and with the Karhunen-Loéve expansion in [70, p. 275] and [71, p. 332]. In Section 3.2 we derive the FI for swarm localization from continuous complex-valued observations like RF signals. Besides of swarm localization, the CRB is also applied in FI seeking swarm control in Section 5.3, where the formation is optimized, to gain maximal position information with a snapshot

of observations.

Often we are interested in the estimation bound of a parameter subset $\mathbf{x}_1$, where $\mathbf{x} = \text{vec}\{\mathbf{x}_1, \mathbf{x}_2\}$. The total FIM can be divided into sub-matrices as

$$\mathbf{I}_{\mathbf{x}} = \begin{pmatrix} \mathbf{I}_{\mathbf{x}_1} & \mathbf{I}_{\mathbf{x}_1,\mathbf{x}_2} \\ \mathbf{I}_{\mathbf{x}_2,\mathbf{x}_1} & \mathbf{I}_{\mathbf{x}_2} \end{pmatrix}, \tag{3.5}$$

where $\mathbf{I}_{\mathbf{x}_1}$ is the FIM of $\mathbf{x}_1$ when the complementary set of parameter $\mathbf{x}_2$ is perfectly known. The terms $\mathbf{I}_{\mathbf{x}_1,\mathbf{x}_2}$ and $\mathbf{I}_{\mathbf{x}_2,\mathbf{x}_1}$ represent the correlation between variables $\mathbf{x}_1$ and $\mathbf{x}_2$. When $\mathbf{x}_2$ is unknown, the CRB of $\mathbf{x}_1$ can be equivalently formulated by the so-called equivalent Fisher information matrix (EFIM) [73] $\tilde{\mathbf{I}}_{\mathbf{x}_1}$ according to the Schur complement

$$\text{cov}_{\mathbf{z};\mathbf{x}}[\hat{\mathbf{x}}_1] \succcurlyeq \text{CRB}[\mathbf{x}_1] = \tilde{\mathbf{I}}_{\mathbf{x}_1}^{-1} \triangleq \Big(\mathbf{I}_{\mathbf{x}_1} - \underbrace{\mathbf{I}_{\mathbf{x}_1,\mathbf{x}_2}\mathbf{I}_{\mathbf{x}_2}^{-1}\mathbf{I}_{\mathbf{x}_2,\mathbf{x}_1}}_{\triangleq \mathbf{D}_{\mathbf{x}_2 \to \mathbf{x}_1}}\Big)^{-1}, \tag{3.6}$$

where the term $\mathbf{D}_{\mathbf{x}_2 \to \mathbf{x}_1}$ represents the information degradation of $\mathbf{x}_1$ from the uncertainty in $\mathbf{x}_2$. The Schur complement also plays an important role in the derivation of PCRB, where the parameters $\mathbf{x}$ are considered as random variables and estimated incorporating *a-priori* information, the current and historical observations.

3.1.2 Posterior Cramér-Rao Bound

As mentioned in Section 2.3, the parameters of interest $\mathbf{x}$ are often assumed to be random variables, in order to systematically incorporate historical or *a-priori* information in Bayesian estimators. One example of a Bayesian estimator is the DiPNet algorithm proposed in Chapter 4. In this case, the PCRB of $\mathbf{x}^{(+)}$, a.k.a. Bayesian Cramér-Rao bound (BCRB), is introduced analogously to the classic CRB, to lower bound the mean square error (MSE) of any Bayesian estimates $\text{cov}_{\mathbf{x}^{(+)}|\mathbf{z}^{(+)}}[\hat{\mathbf{x}}^{(+)}]$, i.e.

$$\text{cov}_{\mathbf{x}^{(+)}|\mathbf{z}^{(+)}} \succcurlyeq \text{PCRB}[\mathbf{x}^{(+)}] \triangleq \left(\mathbf{J}_{\mathbf{x}}^{(+)}\right)^{-1}. \tag{3.7}$$

The Bayesian information matrix (BIM) of $\mathbf{x}^{(+)}$ can be defined from the joint pdf $p(\mathbf{z}^{(+)}, \mathbf{x}^{(+)})$ as [74, p. 5]

$$\mathbf{J}_{\mathbf{x}}^{(+)} = \mathbb{E}_{\mathbf{x}^{(+)}}\Big[- \triangle_{\mathbf{x}^{(+)}}^{\mathbf{x}^{(+)}} \ln p(\mathbf{x}^{(+)}) + \underbrace{\mathbb{E}_{\mathbf{z}^{(+)}|\mathbf{x}^{(+)}}\Big[- \triangle_{\mathbf{x}^{(+)}}^{\mathbf{x}^{(+)}} \ln p(\mathbf{z}^{(+)}|\mathbf{x}^{(+)})\Big]}_{\mathbf{I}_{\mathbf{x}}^{(+)}}\Big], \tag{3.8}$$

where $\mathbf{I}_{\mathbf{x}^{(+)}}$ is the information from the current measurements $\mathbf{z}^{(+)}$ with a similar expression as the FIM $\mathbf{I}_{\mathbf{x}}$ in the non-Bayesian case. The BIM can be expressed recursively as [31]

$$\mathbf{J}_{\mathbf{x}^{(+)}} = \mathbf{D}_{22} - \mathbf{D}_{21}(\mathbf{J}_{\mathbf{x}^{(-)}} + \mathbf{D}_{11})^{-1}\mathbf{D}_{12}, \tag{3.9}$$

where

$$\mathbf{D}_{11} = \mathbb{E}_{\mathbf{x}^{(-)},\mathbf{x}^{(+)}}\left[-\triangle^{\mathbf{x}^{(-)}}_{\mathbf{x}^{(-)}} \ln p\left(\mathbf{x}^{(+)}|\mathbf{x}^{(-)}\right)\right], \tag{3.10}$$

$$\mathbf{D}_{12} = \mathbb{E}_{\mathbf{x}^{(-)},\mathbf{x}^{(+)}}\left[-\triangle^{\mathbf{x}^{(+)}}_{\mathbf{x}^{(-)}} \ln p\left(\left(\mathbf{x}^{(+)}|\mathbf{x}^{(-)}\right)\right] = \mathbf{D}_{21}^{T}, \tag{3.11}$$

$$\mathbf{D}_{22} = \mathbb{E}_{\mathbf{x}^{(-)},\mathbf{x}^{(+)}}\left[-\triangle^{\mathbf{x}^{(+)}}_{\mathbf{x}^{(+)}} \ln p\left(\left(\mathbf{x}^{(+)}|\mathbf{x}^{(-)}\right)\right] + \mathbb{E}_{\mathbf{x}^{(+)}}\left[\mathbf{I}_{\mathbf{x}^{(+)}}\right]. \tag{3.12}$$

The PCRB is also applied in Bayesian information seeking swarm control in Section 5.4, where the formation is optimized to gain maximal position information, taking all historical information into account.

3.1.3 Ziv-Zakai Bound

The CRB and its variants essentially evaluate the curvature of the log-likelihood function at its peak, therefore do not take detection errors into account. The ZZB [75] and its variations combine the detection probability and the estimation accuracy, which are MSE lower bounds tighter than CRB. In this thesis, only the ZZB for scalar parameter estimation is relevant. For a scalar random variable x with a uniform *a-priori* pdf in the state space $[0, X]$, the MSE of estimate $\hat{x}$ is lower bounded by

$$\mathrm{MSE}[\hat{x}] \geq \mathrm{ZZB}[x] \triangleq \int_0^X G\left(\frac{1}{X}\int_0^{X-\delta} P_{\min}(\chi, \chi+\delta)\mathrm{d}\chi\right)\delta \ \mathrm{d}\delta, \tag{3.13}$$

where $G(\cdot)$ is a valley-filling function, and $P_{\min}(\theta, \theta+h)$ is the minimum error probability from likelihood ratio test [74, p. 55]. In Section 3.3, the scalar ZZB is utilized to analyze the ToA/RTT based distance estimation performance [76], especially with RF resource limitation. A ZZB modified CRB (ZCRB) incorporates the detection error in observation model with ZZB, which is used for swarm self-localization analysis and position-aware swarm control in Chapter 5. The ZZB is extended to multi-parameter estimation in [77] and adapted to localization applications in [78, 79, 80]. However, due to the high complexity of multiple integrals, the vector ZZB cannot be readily used for large-scale swarm localization, therefore, is excluded from this thesis.

3.2 Fisher Information in Swarm Observations

Now we assume that for all links in the extended swarm network $\mathbb{e}_{uv} \in \mathcal{E}_0$ a total of $|\mathcal{E}_0|$ different signals $\mathbf{r}(t) = \text{vec}\{r_{uv}(t) : \mathbb{e}_{uv} \in \mathcal{E}_0\}$ defined by the generic model (2.17) are received. The information contained in all these signals regarding the parameter vector $\mathbf{x}$ can then be quantified by the FIM $\mathbf{I}_{\mathbf{x}}$

$$\mathbf{I}_{\mathbf{x}} = \frac{2}{N_0}\Re\Big\{\sum_{\mathbb{e}_{uv}\in\mathcal{E}_0}\int_0^{T_o} \nabla_{\mathbf{x}} s_{uv}^*(t)\nabla_{\mathbf{x}^T} s_{uv}(t)\mathrm{d}t\Big\}. \tag{3.14}$$

Equation (3.14) can be obtained by modifying the proof for real-valued continuous signals [70, p. 275] and complex-valued discrete signals [27, p. 525], and is detailed in Appendix C.1. By the chain rule of derivatives, the signal features $\mathbf{g}_{uv}$ preserve all the information about $\mathbf{x}$ contained in the complex-valued continuous signal. The FIM of the state in (3.14) can be rewritten as

$$\mathbf{I}_{\mathbf{x}} = \sum_{\mathbb{e}_{uv}\in\mathcal{E}_0} \nabla_{\mathbf{x}}\mathbf{g}_{uv}^T\mathbf{I}_{\mathbf{g}_{uv}}\nabla_{\mathbf{x}^T}\mathbf{g}_{uv}, \tag{3.15}$$

where $\mathbf{I}_{\mathbf{g}_{uv}}$ is the FIM of the signal features $\mathbf{g}_{uv}$ from the received signal $r_{uv}(t)$ [81, 71] expressed as

$$\mathbf{I}_{\mathbf{g}_{uv}} \triangleq \frac{2}{N_0}\Re\left\{\int_0^{T_o} \nabla_{\mathbf{g}_{uv}} s_{uv}^*(t)\nabla_{\mathbf{g}_{uv}^T} s_{uv}(t)\mathrm{d}t\right\}. \tag{3.16}$$

For a one-dimensional signal feature g_{uv}, the FI is denoted as $\iota_{g_{uv}}$. Especially, if the signal feature is distance, $\iota_{g_{uv}}$ is also referred to as ranging information intensity (RII) in [73]. Following the definition in Section 2.4.1, (3.14) is valid for both real and complex valued $s_{uv}(t)$. For a gas source, the signal feature is the concentration defined in **??**, i.e. $g_{uv} = C(d_{uv})$. The FI becomes $\iota_{g_{uv}} = {}^2/_{N_0}$. For a RF source the distance information is embedded in the signal features, amplitude A_{uv}, phase Φ_{uv} and symbol delay τ_{uv}, i.e. $\mathbf{g}_{uv} = \text{vec}\{A_{uv}, \Phi_{uv}, \tau_{uv}\}$. As observed in Section 2.4.4, the gas diffusion model has a similar expression as the RF amplitude model in logarithm domain. We therefore only discuss the FI contained in continuous complex-valued RF signals $r_{uv}(t)$.

For RF signal the integrand in (3.16) can be represented as

$$\begin{aligned}
&\nabla_{\mathbf{g}_{uv}} s^*_{uv}(t)\ \nabla_{\mathbf{g}^T_{uv}} s_{uv}(t) \\
&= \begin{bmatrix} \|\tilde{s}_{uv}(t)\|^2 & \jmath A_{uv}\|\tilde{s}_{uv}(t)\|^2\omega_v/c & A_{uv}\tilde{s}^*_{uv}(t)\frac{\partial \tilde{s}_{uv}(t)}{\partial \tau_{uv}} \\ -\jmath A_{uv}\|\tilde{s}_{uv}(t)\|^2\omega_v/c & A^2_{uv}\|\tilde{s}_{uv}(t)\|^2\omega_v^2/c^2 & -\jmath A^2_{uv}\tilde{s}^*_{uv}(t)\frac{\partial \tilde{s}_{uv}(t)}{\partial \tau_{uv}}\omega_v/c \\ A_{uv}\tilde{s}_{uv}(t)\frac{\partial \tilde{s}^*_{uv}(t)}{\partial \tau_{uv}} & \jmath A^2_{uv}\tilde{s}_{uv}(t)\frac{\partial \tilde{s}^*_{uv}(t)}{\partial \tau_{uv}}\omega_v/c & A^2_{uv}\|\frac{\partial \tilde{s}_{uv}(t)}{\partial \tau_{uv}}\|^2 \end{bmatrix},
\end{aligned} \tag{3.17}$$

with the carrier frequency f_v and $\omega_v = 2\pi f_v$ Considering the $N_0 \to 0$ and $T_o \to \infty$ asymptotics [71], we can have

$$\int_0^{T_o} \|\tilde{s}_{uv}(t)\|^2 \mathrm{d}t = \int_{-\infty}^{\infty} \|S(f)\|^2 \mathrm{d}f \triangleq {}^{\|\bar{S}_{uv}\|^2}\!/_{A^2_{uv}}, \tag{3.18}$$

with the received signal energy $\|\bar{S}_{uv}\|^2$.

$$\begin{aligned}
&\int_0^{T_o} \tilde{s}_{uv}(t)\frac{\partial \tilde{s}_{uv}(t)^*}{\partial \tau_{uv}}\mathrm{d}t \\
&= \int_{-\infty}^{\infty}\int_{-\infty}^{\infty} \jmath 2\pi f_2 S(f_2)S^*(f_1)/c \int_0^{T_o} e^{\jmath 2\pi (f_2-f_1)(t-\tau_{uv}/c)}\mathrm{d}t\mathrm{d}f_1\mathrm{d}f_2 \\
&= \int_{-\infty}^{\infty}\int_{-\infty}^{\infty} \jmath 2\pi f_2 S(f_2)S^*(f_1)/c e^{\jmath 2\pi (f_2-f_1)(T_o/2-\tau_{uv}/c)} \underbrace{\int_{-T_o/2}^{T_o/2} e^{\jmath 2\pi (f_2-f_1)t'}\mathrm{d}t'}_{=\delta(f_1-f_2)} \mathrm{d}f_1\mathrm{d}f_2 \\
&= \jmath \int_{-\infty}^{\infty} 2\pi f \|S(f)\|^2/c \mathrm{d}f \triangleq \jmath G_v \|\bar{S}_{uv}\|^2/(A^2_{uv}c),
\end{aligned} \tag{3.19}$$

with the centroid of the spectrum G_v, and

$$\int_0^{T_s} \left\|\frac{\partial \tilde{s}_{uv}(t)}{\partial \tilde{\tau}_{uv}}\right\|^2 \mathrm{d}t = \int_{-\infty}^{\infty} 4\pi^2 f^2 \|S(f)\|^2/c^2 \mathrm{d}f \triangleq {}^{\beta_v^2\|\bar{S}_{uv}\|^2}\!/_{A^2_{uv}c^2}, \tag{3.20}$$

where β_v is the root-mean-square signal bandwidth, or β_v^2 the effective bandwidth. The transformed FIM can be expressed as

$$\mathbf{I}_{\mathbf{g}_{uv}} = 2N\ \mathrm{SNR}_{uv} \begin{bmatrix} A_{uv}^{-2} & 0 & 0 \\ 0 & \omega_v^2/c^2 & -G_v\omega_v/c^2 \\ 0 & -G_v\omega_v/c^2 & \beta_v^2/c^2 \end{bmatrix}. \tag{3.21}$$

The signal to noise ratio (SNR) is defined as the total energy ratio between the signal and the noise, referred to as the input SNR

$$\mathrm{SNR}_{uv} = {}^{\|\bar{S}_{uv}\|^2}\!/_{N_0 N}, \tag{3.22}$$

which is proportional to $d^{-\gamma}$ as indicated in (2.21). Additionally, if we assume a symmetric spectrum, i.e. $G_v = 0$, the matrix $\mathbf{I}_{\mathbf{g}_{uv}}$ becomes diagonal, with the FIs of amplitude $\iota_{A_{uv}}$, phase $\iota_{\Phi_{uv}}$ and symbol delay $\iota_{\tau_{uv}}$ along the diagonal, i.e.

$$\mathbf{I}_{\mathbf{g}_{uv}} = \mathrm{diag}\{\iota_{A_{uv}}, \iota_{\Phi_{uv}}, \iota_{\tau_{uv}}\}. \tag{3.23}$$

The diagonalization operator $\mathrm{diag}\{\cdot\}$ arranges the elements (scalers, vectors or matrices) into the diagonal of a matrix. The diagonal FIM of $\mathbf{g}_{uv}$ is optimal in the sense of maximizing the information of Φ_{uv} and τ_{uv}, according to the Schur complement in (3.6). Additionally, the contributions of amplitude, phase and symbol delay to the state FIM $\mathbf{I}_{\mathbf{x}}$ can be assessed independently in this case. In this thesis, $G_v = 0$ is generally assumed, which can be achieved by waveform design.

If the nuisance parameters, i.e. $A_v, \gamma, \delta_{uv}, \phi_{uv}, \delta_{uv}$ are known, the distance between transceivers d_{uv} can be directly estimated from the signal features $\mathbf{g}_{uv}$, which is commonly referred to as *ranging*. Utilizing the diagonal property of $\mathbf{I}_{\mathbf{g}_{uv}}$, the RII, $\iota_{d_{uv}}$, of different ranging techniques can be evaluated by transferring $\mathbf{I}_{\mathbf{g}_{uv}}$, or its diagonal elements, back to distance, i.e.

$$\mathrm{var}[\hat{d}_{uv}] \geq \mathrm{CRB}[d_{uv}] = \iota_{d_{uv}}^{-1} = \left(\sum_{l \in \mathcal{I}_{uv}} \iota_{d_{uv}}^{[\mathbf{g}_{uv}]_l} \right)^{-1} \triangleq \left(\sum_{l \in \mathcal{I}_{uv}} \frac{\partial [\mathbf{g}_{uv}]_l}{\partial d_{uv}} [\mathbf{I}_{\mathbf{g}_{uv}}]_{l,l} \frac{\partial [\mathbf{g}_{uv}]_l}{\partial d_{uv}} \right)^{-1}, \tag{3.24}$$

where $\iota_{d_{uv}}^{[\mathbf{g}_{uv}]_l}$ is the distance FI in the signal features $[\mathbf{g}_{uv}]_l$ and $\mathcal{I}_{uv}$ is the index set of the considered signal features.

1) RSS

Distance between transceivers can be extracted from the RSS, given the transmit power and the path-loss exponent. The distance FI $\iota_{d_{uv}}^{\mathrm{RSS}}$ and CRB with RSS observation can be written as

$$\mathrm{CRB}^{\mathrm{RSS}}[d_{uv}] = (\iota_{d_{uv}}^{\mathrm{RSS}})^{-1} = \left(2\mathrm{SNR}_{uv} A_{uv}^{-2} \left(\frac{\partial A_{uv}}{\partial d_{uv}} \right)^2 \right)^{-1} = \frac{2 d_{uv}^2}{\gamma N \ \mathrm{SNR}_{uv}}. \tag{3.25}$$

For free space path-loss, i.e. $\gamma = 2$, and $\mathrm{SNR}_{uv} \propto d^{-2}$, besides the impact of SNR, the distance CRB with RSS observation increases, in addition, quadratically with

distance d_{uv}. In reality, the performance of RSS-based ranging is sensitive to the propagation model mismatch, even though intensive research has been conducted to it.

2) ToA

Symbol delay can be exploited for distance estimation in a ToA manner, with the distance FI $\iota_{d_{uv}}^{\mathrm{ToA}}$ and CRB expressed as

$$\mathrm{CRB}^{\mathrm{ToA}}[d_{uv}] = (\iota_{d_{uv}}^{\mathrm{ToA}})^{-1} = \frac{c^2}{2\beta_v^2 N \ \mathrm{SNR}_{uv}}. \tag{3.26}$$

Hence, the variance of distance estimation is inversely proportional to the effective bandwidth β_v^2 and the SNR. In practice, the clock offset may affect the ToA based observation. Synchronization or a multi-way ranging protocol needs to be implemented to eliminate the effects of clock offset. The effective bandwidth is determined by the PSD function of the baseband signal, which can be maximized by waveform optimization. ToA-based ranging is robust against model mismatch and relatively simple for implementation. Therefore, it is widely considered through investigation, particularly in swarm self-localization topics, such as system design [82, 83], distributed algorithm design [51, 84] and formation control [85].

3) PoA

Carrier phase can also be exploited for distance estimation, with the FI and CRB defined similarly to the ToA case, i.e.

$$\mathrm{CRB}^{\mathrm{PoA}}[d_{uv}] = (\iota_{d_{uv}}^{\mathrm{PoA}})^{-1} = \frac{c^2}{2\omega_v^2 N \ \mathrm{SNR}_{uv}}. \tag{3.27}$$

Hence, the variance of distance estimation is inversely proportional to the square of the angular carrier frequency ω_v^2 and the SNR. It can be seen that the PoA bound possesses a same tendency as the ToA bound. The ratio ω_v^2/β_v^2 indicates the gain of using PoA in comparison with ToA. However, in practice, PoA-based ranging is more difficult due to integer ambiguities, or phase wrapping. In addition, coherent transceivers need to be implemented. PoA-based ranging requires an accurate initialization, or tracking. It is used in, for example, the RTK service of GNSS.

4) All three features

Fundamentally, if the amplitude, symbol delay and carrier phase are jointly ex-

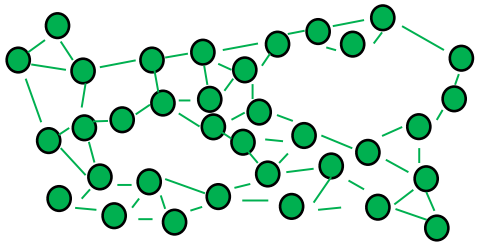

Figure 3.1. *Graph representation of swarm self-localization: Green dots and lines indicate agents and A2A links, respectively.*

ploited for ranging, a joint ranging CRB can be derived as

$$\mathrm{CRB}^{\mathrm{RF}}[d_{uv}] = (\iota^{\mathrm{RF}}_{d_{uv}})^{-1} = (\iota^{\mathrm{RSS}}_{d_{uv}} + \iota^{\mathrm{ToA}}_{d_{uv}} + \iota^{\mathrm{PoA}}_{d_{uv}})^{-1} = \frac{c^2}{2N\ \mathrm{SNR}_{uv}(\gamma c^2 d^{-2}/4 + \beta_v^2 + \omega_v^2)}, \tag{3.28}$$

which follows from (3.21) being diagonal.

In the presence of unknown nuisance parameters, distance information cannot be extracted solely from a single link. However, by collaboration among agents, distance between transceivers can be estimated jointly with the nuisance parameters, which will be discussed with the swarm source localization in Section 3.4.

3.3 Swarm Self-Localization

We investigate an anchor-free self-localization case illustrated in Figure 3.1, i.e. $\mathcal{V} = \mathcal{X} = \mathcal{P} = \mathcal{A}$. Only the ranging measurements from the ToA observation are exploited. The impacts of swarm's formation and connectivity on self-localization are discussed in detail. First of all, the swarm self-localization performance depends on the formation of the swarm. Second, for a swarm with fixed formation $\mathbf{p}_{\mathcal{A}}$, the connectivity condition is adaptable by modifying the measurement coverage assumption, which also affects the localization performance. In practice, the measurement coverage can be changed by either changing the transmit power or link selection according to the receive power. The connectivity has to be sufficiently high to guarantee a unique localization solution. However, due to the limits on total RF resource, e.g. power and bandwidth, increasing measurement coverage leads to reducing resources allocated to each link in order to guarantee orthogonal channel accesses. As a consequence, the ranging measurements are erroneous, which leads to a poor self-localization performance.

3.3.1 Swarm Self-Localizability

As discussed before, with the absence of nuisance parameters, the swarm's position information is solely embedded in the distance between agents. In this case, the swarm network can be analogously interpreted as a bar-joint framework and its localizability is addressed fundamentally by the rigidity theory [48]. A framework is rigid, if none of the vertices can move continuously without changing at least one edge length. For a generic framework $\mathcal{F}_\mathcal{A} = (\mathcal{G}_\mathcal{A}, \mathbf{p}_\mathcal{A})$, if it can be smoothly transformed into another framework $\tilde{\mathcal{F}}_\mathcal{A} = (\mathcal{G}_\mathcal{A}, \mathbf{q}_\mathcal{A})$ with agents position $\mathbf{q}_\mathcal{A} \neq \mathbf{p}_\mathcal{A}$ and all the edge distances $\mathbf{d}_\mathcal{A} = \text{vec}\{\mathbf{d}_{uv} : \forall \mathbb{l}_{uv} \in \mathcal{L}_0\}$ keep constant during the transformation, we can state

$$\|\mathbf{p}_u - \mathbf{p}_v\|^2 = \text{const.}, \quad \forall \mathbb{l}_{uv} \in \mathcal{L}_0. \tag{3.29}$$

Taking the derivative of (3.29), we can get

$$(\mathbf{p}_u - \mathbf{p}_v)^T (\dot{\mathbf{p}}_u - \dot{\mathbf{p}}_v) = 0, \quad \forall \mathbb{l}_{uv} \in \mathcal{L}_0. \tag{3.30}$$

$\dot{\mathbf{p}}_u$ is a virtual velocity of agent $\mathbb{o}_u$. Collecting for all the edges, (3.30) can be rewritten as

$$\mathbf{R}(\mathcal{F}_\mathcal{A})\dot{\mathbf{p}}_\mathcal{A} = \mathbf{0}, \tag{3.31}$$

with $\dot{\mathbf{p}}_\mathcal{A} = \text{vec}\{\dot{\mathbf{p}}_u : \ \forall \mathbb{o}_u \in \mathcal{A}\}$ and $\mathbf{R}(\mathcal{F}_\mathcal{A}) \in \mathbb{R}^{|\mathcal{L}_0| \times 2|\mathcal{A}|}$ is called rigidity matrix of the framework $\mathcal{F}_\mathcal{A}$ expressed as

$$\mathbf{R}(\mathcal{F}_\mathcal{A}) = \begin{array}{c} \\ \vdots \\ i_{uv} \\ \vdots \end{array} \begin{array}{c} \begin{array}{cccccc} \cdots & & 2u{:}2u{+}1 & \cdots & 2v{:}2v{+}1 & \cdots \end{array} \\ \begin{pmatrix} \ddots & & & & & \\ \mathbf{0}^T & (\mathbf{p}_u - \mathbf{p}_v)^T & \mathbf{0}^T & (\mathbf{p}_v - \mathbf{p}_u)^T & \mathbf{0}^T \\ & & & \ddots & \end{pmatrix} \end{array}, \tag{3.32}$$

where i_{uv} is the index of the edge $\mathbb{l}_{uv} \in \mathcal{L}_0$. In 2D, there are 3-degree flexible global motions, 2-degree in translations and 1-degree in rotations, which lead to three groups of non-zero vectors of $\dot{\mathbf{p}}_\mathcal{A}$. Hence, the rank of $\mathbf{R}(\mathcal{F}_\mathcal{A})$ fulfills $\text{rank}[\mathbf{R}(\mathcal{F}_\mathcal{A})] \leq 2|\mathcal{A}|-3$, where the equality holds i.f.f. the framework is rigid. Therefore, to prove the rigidity of a generic framework where no more than two agents are collinear, we can simple check if the rigidity matrix has rank $2|\mathcal{A}|-3$. The rigidity can prevent continuous motion of agents, which means a swarm self-localization algorithm will converge to a solution. However, it does not necessarily mean the solution is unique. One common exception is the folding ambiguity. If an agent $\mathbb{o}_u$ is only connected to two agents $\mathbb{o}_v$ and $\mathbb{o}_w$, then $\mathbb{o}_u$ can be folded along the line of $\mathbb{o}_v$ and $\mathbb{o}_w$ into a new position $\tilde{\mathbf{p}}_u$ which makes the

new formation different from the original. For the uniqueness of the solution, we need to verify the framework is global rigid. It has been proved in [48] that a framework is global rigid if it is 3-connected and redundantly rigid. 3-connected means deleting any less than three vertices, the graph is still connected. Redundantly rigid means removal any one edge, the remaining graph is still generic rigid. Checking a framework's global rigidity is more computational demanding compared with the check of rigidity. Since the folding ambiguity produces isolated local minima, it can be avoided by tracking filters such as extended Kalman filter (EKF) or PF.

The ToA measurements from each link are assumed to be independent. In addition, the ranging information on the bi-directional link is equivalently considered as a single measurement with new ranging information of $\iota_{uv} = \iota_{uv}^{\text{ToA}} + \iota_{vu}^{\text{ToA}}$. The total ranging FIM can be written as $\mathbf{I}_{\mathbf{d}_{\mathcal{L}_0}} = \text{diag}\{\iota_{uv} : \forall\, \mathbb{l}_{uv} \in \mathcal{L}_0\}$. The swarm's position FIM $\mathbf{I}_{\mathbf{p}_\mathcal{A}}$ based on ToA measurements can be written by mapping the ranging FIM $\mathbf{I}_{\mathbf{d}_{\mathcal{L}_0}}$ onto position domain, i.e.

$$\mathbf{I}_{\mathbf{p}_\mathcal{A}} = \mathbf{H}_{\mathcal{L}_0} \mathbf{I}_{\mathbf{d}_{\mathcal{L}_0}} \mathbf{H}_{\mathcal{L}_0}^T, \tag{3.33}$$

with the ranging geometry matrix $\mathbf{H}_{\mathcal{L}_0}$ defined as

$$\mathbf{H}_{\mathcal{L}_0} = \nabla_{\mathbf{p}_\mathcal{A}} \mathbf{d}_{\mathcal{L}_0}^T. \tag{3.34}$$

Theorem 3.3.1 (FIM and rigidity)**.** *The swarm framework $\mathcal{F}_\mathcal{A}$ is rigid, i.f.f.* $\text{rank}\,(\mathbf{I}_{\mathbf{p}_\mathcal{A}}) = 2|\mathcal{A}|-3$.

Proof. Combining (3.32), (3.34) and (3.33), we can rewrite $\mathbf{I}_{\mathbf{p}_\mathcal{A}}$ as

$$\mathbf{I}_{\mathbf{p}_\mathcal{A}} = \mathbf{R}(\mathcal{F}_\mathcal{A})^T \mathbf{I}_{\mathbf{d}_{\mathcal{L}_0}} \cdot \text{diag}\left\{\mathbf{d}_{\mathcal{L}_0}\right\}^{-2} \mathbf{R}(\mathcal{F}_\mathcal{A}). \tag{3.35}$$

Since the measurement links are independent, i.e. $\mathbf{I}_{\mathbf{d}_{\mathcal{L}_0}}$ and $\text{diag}\left\{\mathbf{d}_{\mathcal{L}_0}\right\}^{-2}$ are full rank diagonal matrices with positive real-valued scalars along the diagonal, we have

$$\text{rank}\,(\mathbf{I}_{\mathbf{p}_\mathcal{A}}) = \text{rank}\,(\mathbf{R}(\mathcal{F}_\mathcal{A}))\,. \tag{3.36}$$

Hence the network rigidity can be equivalently checked by the rank of the swarm self-localization FIM $\mathbf{I}_{\mathbf{p}_\mathcal{A}}$. □

3.3.2 Anchor-free Self-Localization CRBs

As discussed before, due to the anchor-free setup, swarm self-localization is often a problem with singularity, where the position FIM is at least rank deficient by three,

corresponding to the global rigid motion of translation (two degree of freedom) and rotation (one degree of freedom). Hence, three linearly independent constraints have to be defined to determine a unique swarm coordinate system $\mathbb{A}$.

3.3.2.1 Position CRB with Baseline Constraints

An intuitive choice of the constraints is to define a baseline B from two agents, for example, constraining $\mathbb{a}_u$ at the origin and $\mathbb{a}_v$ on the positive y-axis. The coordinate system defined by the baseline B is denoted as $\mathbb{B}$. Since the state for baseline $\mathbf{x}_B$, i.e., the coordinates of $\mathbb{a}_u$ and x-coordinate of $\mathbb{a}_v$ is no longer unknown, the position FIM $\mathbf{I}_{\mathbf{p}_\mathcal{A}}$ can be truncated to $\mathbf{I}_{\mathbf{p}_{\mathcal{A}/\mathbf{x}_B}}$, where columns and rows corresponding to the baseline states are removed. If the formation is rigid, the reduced FIM $\mathbf{I}_{\mathbf{p}_{\mathcal{A}/\mathbf{x}_B}}$ will be full rank. Therefore, the CRB of the remaining unknowns can be expressed as

$$\mathrm{CRB}[\mathbf{p}_{\mathcal{A}/\mathbf{x}_B}] = \mathbf{I}^{-1}_{\mathbf{p}_{\mathcal{A}/\mathbf{x}_B}}. \tag{3.37}$$

The total position CRB in $\mathbb{B}$, denoted as $\mathrm{CRB}[\mathbf{p}^{\mathbb{B}}_{\mathcal{A}}]$, can be written by inserting zero column and row vectors to $\mathrm{CRB}[\mathbf{p}_{\mathcal{A}/\mathbf{x}_B}]$ corresponding to $\mathbf{x}_B$.

The coordinate systems defined by baselines are not optimum in the sense of minimizing the position RMSE according to (2.4). Due to the noisy measurements, the choice of baseline will bring additional coordinate system uncertainty. As a consequence, agents at larger distance from the baseline will experience larger localization errors.

3.3.2.2 Position CRB with Group Motion Constraints

As discussed in [47], an optimal coordinate system $\mathbb{C}$ for self-localization can be found by directly constraining the self-localization problem with the three global motions. The optimal constraints are represented by the subspace $\mathbf{U}_\perp = [\mathbf{u}_x, \mathbf{u}_y, \mathbf{u}_r]$, with orthonormal bases of translations in x and y directions $\mathbf{u}_x$ and $\mathbf{u}_y$, and rotation $\mathbf{u}_r$ defined as

$$[\mathbf{u}_x, \mathbf{u}_y] = \frac{1}{\sqrt{|\mathcal{A}|}}\mathbf{1}_{|\mathcal{A}|\times 1} \otimes \mathbf{I}_{2\times 2}, \tag{3.38}$$

$$\mathbf{u}_r = \frac{1}{\|\mathbf{p}_\mathcal{A}\|}\mathrm{vec}\{y_u, -x_u : u = 1, \cdots |\mathcal{A}|\}. \tag{3.39}$$

The base $\mathbf{U}_\perp$ spans the left nullspace of the state space, i.e., the constraints. The orthonormal bases of column space $\mathbf{U}_{||}$ can be determined by the eigenvalue decompo-

sition as

$$\mathbf{I} - \mathbf{U}_{\perp}\mathbf{U}_{\perp}^{T} = [\mathbf{U}_{\shortparallel}, \tilde{\mathbf{U}}_{\perp}] \begin{bmatrix} \mathbf{\Lambda} & \mathbf{0} \\ \mathbf{0} & \mathbf{0} \end{bmatrix} \begin{bmatrix} \mathbf{U}_{\shortparallel}^{T} \\ \tilde{\mathbf{U}}_{\perp}^{T} \end{bmatrix}. \tag{3.40}$$

The total FIM can be projected onto the column space as $\mathbf{U}_{\shortparallel}^{T}\mathbf{I}_{\mathbf{p}_{\mathcal{A}}}\mathbf{U}_{\shortparallel}$ and becomes full-rank. Finally, the position CRB in $\mathbb{C}$ is calculated by inverting the projected FIM and transforming back to the parameter space as

$$\mathrm{CRB}[\mathbf{p}_{\mathcal{A}}^{\mathbb{C}}] = \mathbf{U}_{\shortparallel}\Big(\mathbf{U}_{\shortparallel}^{T}\mathbf{I}_{\mathbf{p}_{\mathcal{A}}}\mathbf{U}_{\shortparallel}\Big)^{-1}\mathbf{U}_{\shortparallel}^{T}. \tag{3.41}$$

Alternatively, the position CRB in $\mathbb{C}$ can be equivalently written as the Moore-Penrose pseudoinverse of $\mathbf{I}_{\mathbf{p}_{\mathcal{A}}}$ [47], i.e.

$$\mathrm{CRB}[\mathbf{p}_{\mathcal{A}}^{\mathbb{C}}] = \mathbf{I}_{\mathbf{p}_{\mathcal{A}}}^{\dagger}. \tag{3.42}$$

The position CRB in $\mathbb{C}$ lower bounds the covariance of shape error defined in (2.4), i.e.

$$\mathrm{cov}[\boldsymbol{\varepsilon}_{\mathcal{T}_{\mathcal{A},\mathrm{opt}}}(\mathbf{q}_{\mathcal{P}})] \succcurlyeq \mathrm{CRB}[\mathbf{p}_{\mathcal{A}}^{\mathbb{C}}], \tag{3.43}$$

or the variance of the average shape difference defined in (2.3), i.e.

$$\mathrm{var}[\varepsilon_{\tilde{\mathcal{F}}_{\mathcal{A}}}] \geq \overline{\mathrm{CRB}}[\mathbf{p}_{\mathcal{A}}] \triangleq \mathrm{Tr}\left[\mathrm{CRB}[\mathbf{p}_{\mathcal{A}}^{\mathbb{C}}]\right]/|\mathcal{A}|, \tag{3.44}$$

where $\overline{\mathrm{CRB}}[\mathbf{p}_{\mathcal{A}}^{\mathbb{C}}]$ is the average position CRB in $\mathbb{C}$. The coordinate system $\mathbb{C}$ is optimum in the sense of eliminating the coordinate system uncertainty, i.e. $\mathrm{Tr}[\mathrm{CRB}[\mathbf{p}_{\mathcal{A}}^{\mathbb{C}}]] \leq \mathrm{Tr}[\mathrm{CRB}[\mathbf{p}_{\mathcal{A}}^{\mathbb{B}}]]$. Therefore, we refer $\mathrm{CRB}[\mathbf{p}_{\mathcal{A}}^{\mathbb{C}}]$ to as the optimal position CRB.

3.3.2.3 Framework Distance CRB

The position CRB with arbitrary constraints can be transferred back to the link distances $\mathbf{d}_{\mathcal{A}} = \mathrm{vec}\{d_{uv} : \forall\, \mathbb{1}_{uv} \in \mathcal{L}_{\mathrm{all}}\}$, with the overall geometry matrix $\mathbf{H}_{\mathcal{A}}$ defined as

$$\mathbf{H}_{\mathcal{A}} = \nabla_{\mathbf{p}_{\mathcal{A}}}\mathbf{d}_{\mathcal{A}}^{T}. \tag{3.45}$$

Theorem 3.3.2 (Framework distance CRB)**.** *For a swarm $\mathcal{A}$ with a position CRB constrained with an arbitrary Cartesian coordinate system $\mathbb{A}$, e.g. $\mathbb{A} \in \{\mathbb{B}, \mathbb{C}\}$, denoted as $\mathrm{CRB}[\mathbf{p}_{\mathcal{A}}^{\mathbb{A}}]$, the distance estimation error in framework can be lower bounded by the*

framework distance CRB denoted as $\mathrm{CRB}[\mathbf{d}_{\mathcal{A}}]$*, or its mean* $\overline{\mathrm{CRB}}[\mathbf{d}_{\mathcal{A}}]$*, i.e.*

$$\mathrm{cov}[\boldsymbol{\varepsilon}_{\hat{\mathbf{d}}_{\mathcal{A}}}] \succcurlyeq \mathrm{CRB}[\mathbf{d}_{\mathcal{A}}] = \mathbf{H}_{\mathcal{A}}^{T}\mathrm{CRB}[\mathbf{p}_{\mathcal{A}}^{\mathbb{A}}]\mathbf{H}_{\mathcal{A}}, \tag{3.46}$$

or

$$\mathrm{var}[\varepsilon_{\hat{\mathbf{d}}_{\mathcal{A}}}] \geq \overline{\mathrm{CRB}}[\mathbf{d}_{\mathcal{A}}] \triangleq \mathrm{Tr}\Big[\mathrm{CRB}[\mathbf{d}_{\mathcal{A}}]\Big]/|\mathcal{L}_{\mathrm{all}}|. \tag{3.47}$$

Proof. Apply the CRB for the transformed parameters [27, p. 45], [86]. □

Theorem 3.3.2 indicates that the framework distance CRB is invariant to the choice of constraints, e.g. either defined by a baseline or group motions. The framework distance CRB assesses self-localization performance in distance, which is the same domain as ranging. Therefore, it can be utilized to evaluate the resource allocation efficiency and the performance gain through collaboration, which will be discussed in Section 3.3.3.

3.3.2.4 Interpretation of CRBs

The position CRBs in an arbitrary Cartesian coordinate system $\mathbb{A}$, denoted as $\mathrm{CRB}[\mathbf{p}_{\mathcal{A}}^{\mathbb{A}}]$ are preferable for investigating the geometrical inference of $\mathbf{p}_u^{\mathbb{A}}$ estimation. For example, we can extract the 2×2 sub-matrix corresponding to the position $\mathbf{p}_u^{\mathbb{A}}$ of agent $\mathbb{a}_u$ from $\mathrm{CRB}[\mathbf{p}_{\mathcal{A}}^{\mathbb{A}}]$

$$\mathrm{CRB}[\mathbf{p}_u^{\mathbb{A}}] = \mathrm{CRB}\left[\mathbf{p}_{\mathcal{A}}^{\mathbb{A}}\right]_{<\mathbf{p}_u^{\mathbb{A}},\mathbf{p}_u^{\mathbb{A}}>}. \tag{3.48}$$

By eigenvalue decomposition, $\mathrm{CRB}[\mathbf{p}_u^{\mathbb{A}}]$ can be interpreted as an ellipse with major axis λ_1 and minor axis λ_2 rotated by the rotation matrix $\boldsymbol{\Phi}(\xi_u)$

$$\mathrm{CRB}[\mathbf{p}_u^{\mathbb{A}}] = \boldsymbol{\Phi}(\xi_u)\begin{pmatrix}\lambda_1^2 & 0\\ 0 & \lambda_2^2\end{pmatrix}\boldsymbol{\Phi}(\xi_u)^{T}. \tag{3.49}$$

The shape and size of the CRB ellipses are firstly affected by the formation of swarm, reflected in the geometry matrix $\mathbf{H}_{\mathcal{L}_0}$. A swarm in open area often intends to form quasi-lattice formations, like in flocking [41], which cover the area of interest homogeneously. Secondly, the CRB ellipses depend on the range information intensity, $\mathbf{I}_{\mathcal{L}_0}$, which is determined by the ranging techniques. Theoretically, for an optimal self-localization algorithm, the performance is independent of the choice of constraints, since the results are transformable upon different constraints. However, the position CRB under the optimal constraints eliminates the coordinate system uncertainty, which

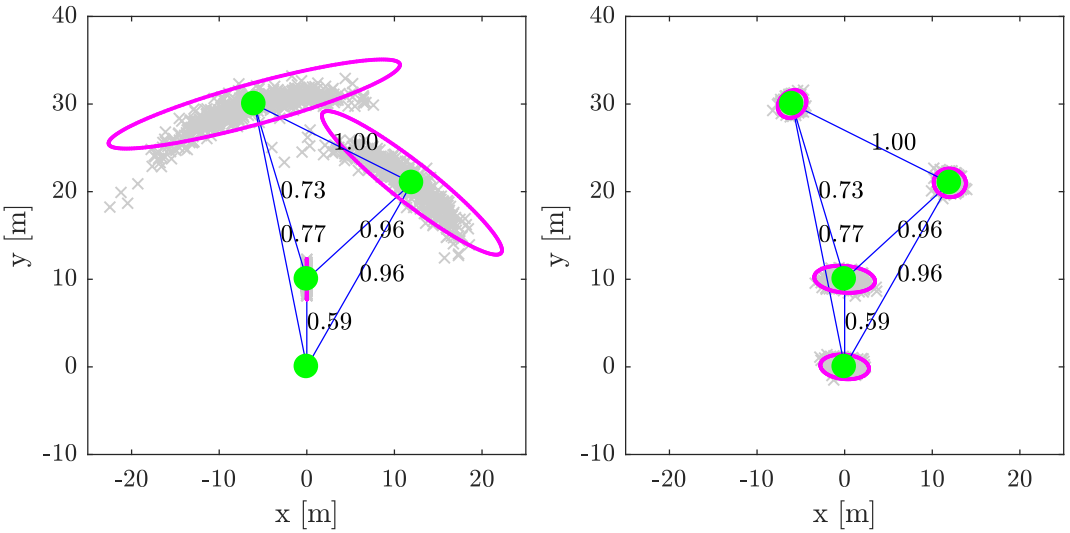

(a) *CRBs with baseline constraints* **(b)** *CRBs with group motion constraints*

Figure 3.2. *Comparison of different self-localization CRBs and the centralized WLS position estimators: The position CRBs of each agent is illustrated with magenta ellipse. The values on A2A links indicate the framework distance CRBs.*

allows us to infer the fundamental property of swarm self-localization. Besides, for sub-optimal algorithms a short baseline may leads to an unstable position estimation. A comparison of different self-localization CRBs is illustrated in Figure 3.2. In Figure 3.2, we also show the performance of a centralized weighted least-square (WLS) position estimator, which is a commonly used maximum likelihood (ML) estimator under Gaussian assumption [33]. The green dots represent agents' positions. 3 σ position CRBs ellipses are illustrated in magenta color. The numbers along the A2A links indicate the distance CRBs from the framework estimate. The ranging observation is assumed to be distorted with Gaussian noise, where the RII of each link is set to $1\,\mathrm{m}^{-2}$. The gray markers are the localization results of 500 numerical simulation runs. The illustration of baseline and group motion constraints are depicted in Figure 3.2a and Figure 3.2b, respectively. The baseline is defined with the position of the agent at the origin and the $x-$coordinate of the agent located on the $y-$axis. As we discussed, the group motion constraints are optimal in the sense of minimizing the position RMSE. With the baseline constraints, the agent further away from the baseline additionally suffers from the coordinate system uncertainty, which leads to a bending, sometimes referred to as a "banana-shape" [87], estimation uncertainty. In this case, neither the CRB ellipse nor second-moment statistics would capture the position uncertainty of the agent. As described in Theorem 3.3.2, the framework distance CRBs, which are shown on each links, are invariant to the choice of constraints, i.e. inherently optimal for evaluating the self-localization performance. Two definitions of optimal CRBs in

(3.43) and (3.46) show the link between the two performance evaluation metrics introduced in Section 2.2, namely the average shape difference $\varepsilon_{\tilde{\mathcal{F}}_\mathcal{P}}$ and the framework distance RMSE $\varepsilon_{\hat{\mathbf{d}}_\mathcal{P}}$.

3.3.3 Self-Localization under RF Resource Limits

A swarm is a dynamic network system with a large-scale and high density. The total RF resources used by the swarm, i.e. total available spectrum, total allowed transmission power, and transmission time, are often limited. The objective of designing a radio access technology (RAT) for a swarm system is to achieve synchronization, communications and precise multi-link ranging among agents with a high update rate. As an example of such a system, a specific RAT is depicted in Figure 3.3, which is designed for the Mars swarm exploration system at German Aerospace Center (DLR) [82]. An OFDM modulation scheme is employed for physical layer (PHY) transmissions due to its flexibility in orthogonal RF resource allocation. For the media access control layer (MAC), a hybrid time-division multiple access (TDMA)-orthogonal frequency-division multiple access (OFDMA) scheme is used. TDMA is used for the first layer, where agents exclusively access the channel in a sequential manner. Inside one TDMA slot, eight OFDM symbols are dedicated for synchronization, ranging and communications. TDMA slots can be assigned in a self-organized fashion, either with traditional detect-and-preserve scheme, or with a more flexible scheme like pulse coupled oscillator (PCO) [82]. The subcarriers are further distributed for simultaneous multi-link two-way ranging. The depicted system applies a frequency division duplexing (FDD) amplify-and-forward ranging with interleaved subcarrier allocation for implementation simplicity as proposed in [88].

3.3.3.1 CRB for Multi-Link Ranging

As a generalization for theoretical analysis of self-localization with limited resource, we assume there exists a subcarrier allocation scheme which allocates $|\mathcal{N}_{uv}|$ out of N subcarriers, for the ranging link $\mathbb{1}_{uv} \in \mathcal{L}_0$. The ratio between the total subcarrier number and the used subcarrier number per link is defined as the resource sharing factor $K_{uv} = {}^{N}/_{|\mathcal{N}_{uv}|}$. If the subcarriers are equally allocated among links, we have $K_{uv} = |\mathcal{L}_0|$ for unicast-based ranging and $K_{uv} = |\mathcal{A}|$ for broadcast-based ranging. For a special case where each occupied subcarrier has an constant energy density, i.e. $\|S(f)\|^2 = \|S\|^2$ and $\|S_n\|^2 = \|S\|^2 f_{\text{sc}} \triangleq \|\tilde{S}\|^2$, the ranging CRB with the OFDM signal can be derived

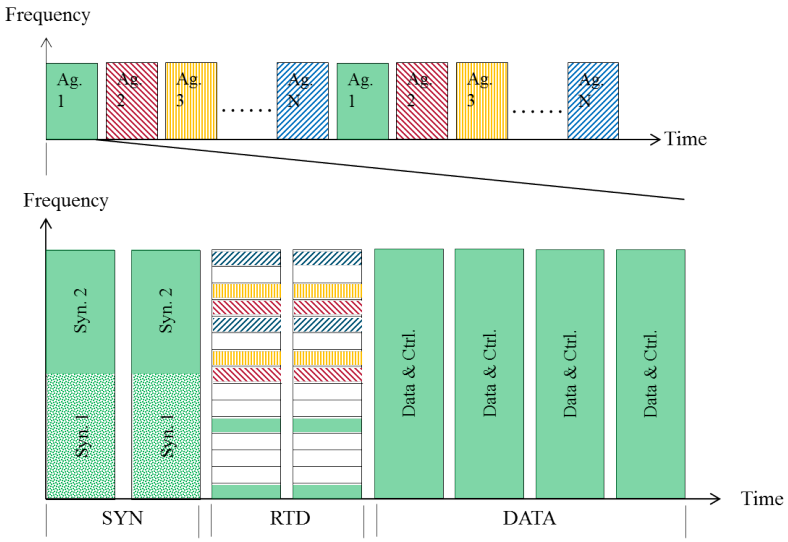

Figure 3.3. *Hybrid TDMA-OFDMA structure of A2A links.*

from (3.26) as

$$\mathrm{CRB}[d_{uv}] = \frac{c^2}{2\omega_{\mathrm{sc}}^2 \ \mathrm{SNR}_{uv} \sum_{n\in\mathcal{N}_{uv}} n^2}. \tag{3.50}$$

Additionally assume each subcarrier is occupied with an equal probability $1/K_{uv}$, i.e.

$$\mathbb{E}\left[\sum_{n\in\mathcal{N}_{uv}} n^2\right] = \frac{1}{K_{uv}} \sum_{n=-\frac{N-1}{2}}^{\frac{N-1}{2}} n^2 = \frac{(N-1)N(N+1)}{12K_{uv}}. \tag{3.51}$$

Lemma 3.3.1 (Multi-Link Ranging CRB)**.** *With randomized orthogonal subcarrier allocation and a fixed power allocated per subcarrier, the ranging CRB can be asymptotically approximated as*

$$\mathrm{CRB}[d_{uv}] \approx \frac{6c^2K_{uv}}{\omega_{\mathrm{sc}}^2 \ \mathrm{SNR}_{uv}(N-1)N(N+1)} = \frac{3c^2K_{uv}}{2\pi^2 B_c^2 N \ \mathrm{SNR}_{uv}} = K_{uv}\mathrm{CRB}_0[d_{uv}], \tag{3.52}$$

hence, the ranging CRB with full subcarrier occupation, $\mathrm{CRB}_0[d_{uv}]$*, scaled by the resource sharing factor* K_{uv}*.*

Proof. Replace the summation in (3.50) with its expectation in (3.51). □

An interpretation of Lemma 3.3.1 is that by randomized subcarrier occupation, the effective bandwidth β_{uv}^2 asymptotically remains the same as the one with full occupation, whereas the SNR is degraded to SNR_{uv}/K_{uv} due to the subcarrier allocation.

3.3.3.2 Collaboration Gain in Self-Localization

For a meshed network like the swarm network under investigation, agents localize themselves collaboratively. There is a gain in network localization obtained through collaboration [32, 28]. The collaboration gain in position domain has been investigated in [28]. As a conclusion, for a fully connected swarm network with a ranging model independent of the number of links, the position CRB of each agent scales as $O(1/|\mathcal{A}|)$. We investigate the collaboration gain in the link distance domain with the framework distance CRB introduced in Theorem 3.3.2, which directly compares the accuracy of ranging from single link and the distance from the framework estimate. In addition, we consider the limited resource effects with both unicast and broadcast ranging schemes. We also assume a fully connected network, i.e. $\mathcal{L}_0 = \mathcal{L}_{\text{all}}$, $\mathbf{d}_{\mathcal{L}_0} = \mathbf{d}_{\mathcal{A}}$ and $\mathbf{H}_{\mathcal{L}_0} = \mathbf{H}_{\mathcal{A}}$. Combining (3.33), (3.42) and (3.47), the averaged framework distance CRB is defined as

$$\begin{aligned}
\overline{\text{CRB}}[\mathbf{d}_{\mathcal{A}}] =& \text{Tr}\left[\mathbf{H}_{\mathcal{A}}^T \left(\mathbf{H}_{\mathcal{A}} \mathbf{I}_{\mathbf{d}_{\mathcal{L}_0}} \mathbf{H}_{\mathcal{A}}^T\right)^{\dagger} \mathbf{H}_{\mathcal{A}}\right] \Big/ |\mathcal{L}_{\text{all}}| \\
=& \text{Tr}\left[\mathbf{I}_{\mathbf{d}_{\mathcal{L}_0}}^{-1/2} \left(\mathbf{H}_{\mathcal{A}} \mathbf{I}_{\mathbf{d}_{\mathcal{L}_0}}^{1/2}\right)^T \left(\mathbf{H}_{\mathcal{A}} \mathbf{I}_{\mathbf{d}_{\mathcal{L}_0}}^{1/2} \left(\mathbf{H}_{\mathcal{A}} \mathbf{I}_{\mathbf{d}_{\mathcal{L}_0}}^{1/2}\right)^T\right)^{\dagger} \mathbf{H}_{\mathcal{A}} \mathbf{I}_{\mathbf{d}_{\mathcal{L}_0}}^{1/2} \mathbf{I}_{\mathbf{d}_{\mathcal{L}_0}}^{-1/2}\right] \Big/ |\mathcal{L}_{\text{all}}| \quad (3.53) \\
=& \text{Tr}\left[\mathbf{I}_{\mathbf{d}_{\mathcal{L}_0}}^{-1} \left(\mathbf{H}_{\mathcal{A}} \mathbf{I}_{\mathbf{d}_{\mathcal{L}_0}}^{1/2}\right)^{\dagger} \mathbf{H}_{\mathcal{A}} \mathbf{I}_{\mathbf{d}_{\mathcal{L}_0}}^{1/2}\right] \Big/ |\mathcal{L}_{\text{all}}|. \quad (3.54)
\end{aligned}$$

To derive (3.54) from (3.53), we utilize the properties of trace and Moore–Penrose inverse of matrix, $\text{Tr}[\mathbf{AB}] = \text{Tr}[\mathbf{BA}]$ and $\mathbf{A}^T(\mathbf{AA}^T)^{\dagger} = \mathbf{A}^{\dagger}$. We apply the singular value decomposition (SVD) to $\mathbf{H}_{\mathcal{A}} \mathbf{I}_{\mathbf{d}_{\mathcal{L}_0}}^{1/2}$

$$\mathbf{H}_{\mathcal{A}} \mathbf{I}_{\mathbf{d}_{\mathcal{L}_0}}^{1/2} = [\mathbf{U}_1, \mathbf{U}_2] \begin{pmatrix} \mathbf{S}_1 & \mathbf{0} \\ \mathbf{0} & \mathbf{0} \end{pmatrix} [\mathbf{V}_1, \mathbf{V}_2]^T. \quad (3.55)$$

With this decomposition, the averaged framework distance CRB can be rewritten as

$$\begin{aligned}
\overline{\text{CRB}}[\mathbf{d}_{\mathcal{A}}] =& \text{Tr}\left[\mathbf{I}_{\mathbf{d}_{\mathcal{L}_0}}^{-1} \mathbf{V}_1 \mathbf{D}_1^{-1} \underbrace{\mathbf{U}_1^T \mathbf{U}_1}_{\mathbf{I}} \mathbf{D}_1 \mathbf{V}_1^T\right] \Big/ |\mathcal{L}_{\text{all}}| \\
=& \text{Tr}\left[\mathbf{I}_{\mathbf{d}_{\mathcal{L}_0}}^{-1} \mathbf{V}_1 \mathbf{V}_1^T\right] \Big/ |\mathcal{L}_{\text{all}}|. \quad (3.56)
\end{aligned}$$

In this thesis, the notations $\mathbf{I}$ and $\mathbf{I}_{n\times n}$ denote identity matrices, whereas $\mathbf{I}_{\mathbf{x}}$ denotes the FIM of state $\mathbf{x}$. If the ranging CRB of each link is a constant σ_ρ^2, which can be achieved by setting $K_{uv} \propto \text{SNR}_{uv}$, a corollary can be readily stated as follows.

Corollary 3.3.1 (Framework Distance CRB with Equal Ranging Accuracy)**.** *For a*

swarm $\mathcal{A}$ with equal ranging CRB, σ_ρ^2, the average framework distance CRB can be expressed as

$$\overline{\mathrm{CRB}}[\mathbf{d}_\mathcal{A}] = {\sigma_\rho^2(2|\mathcal{A}|-3)}/{|\mathcal{L}_{\mathrm{all}}|}. \tag{3.57}$$

Hence, through collaboration, the average distance estimation accuracy is gained by ${|\mathcal{L}_{\mathrm{all}}|}/{2|\mathcal{A}|-3}$.

Proof.

$$\overline{\mathrm{CRB}}[\mathbf{d}_\mathcal{A}] = \mathrm{Tr}\left[\sigma_\rho^2 \mathbf{I}\mathbf{V}_1\mathbf{V}_1^T\right] \Big/ |\mathcal{L}_{\mathrm{all}}| = \sigma_\rho^2 \mathrm{Tr}\left[\mathbf{V}_1\mathbf{V}_1^T\right] \Big/ |\mathcal{L}_{\mathrm{all}}| = \sigma_\rho^2 \mathrm{rank}(\mathbf{V}_1) \Big/ |\mathcal{L}_{\mathrm{all}}|. \tag{3.58}$$

□

For generic cases, with unequal ranging CRBs, the average framework distance CRB can be over-bounded with the following corollary.

Corollary 3.3.2 (Framework Distance CRB with Unequal Ranging Accuracy)**.** *For a swarm $\mathcal{A}$ with unequal ranging CRBs decreasingly sorted as $\sigma_1^2 \geq \sigma_2^2, \cdots, \sigma_{|\mathcal{L}_0|}^2 > 0$, the average framework distance CRB can be over-bounded by*

$$\overline{\mathrm{CRB}}[\mathbf{d}_\mathcal{A}] \leq \frac{1}{|\mathcal{L}_{\mathrm{all}}|} \sum_{l=1}^{2|\mathcal{A}|-3} \sigma_l^2, \tag{3.59}$$

i.e. depending on the $2|\mathcal{A}|-3$ most significant ranging CRBs in the network.

Proof. To prove Corollary 3.3.2, we utilize the trace inequality of any two Hermitian positive semidefinite $n \times n$ matrices $\mathbf{A}$ and $\mathbf{B}$ [89]

$$\mathrm{Tr}[\mathbf{A}\mathbf{B}] \leq \sum_{i=1}^{n} \lambda_i(\mathbf{A})\lambda_i(\mathbf{B}), \tag{3.60}$$

where $\{\lambda_i(\mathbf{X}) : i = 1 \cdots n\}$ are the eigenvalues of $\mathbf{X}$ sorted in non-increasing order. We insert the eigenvalues

$$\begin{aligned} &\{\lambda_l(\mathbf{I}_{\mathbf{d}_{\mathcal{L}_0}}^{-1}) = \sigma_l^2 : l = 1 \cdots \mathcal{L}_0\} \\ &\mathrm{vec}\{\lambda_l(\mathbf{V}_1\mathbf{V}_1^T) : l = 1 \cdots \mathcal{L}_0\} = \mathrm{vec}\{\mathbf{1}_{2|\mathcal{A}|-3}, \mathbf{0}_{\mathcal{L}_0-2|\mathcal{A}|+3}\} \end{aligned} \tag{3.61}$$

into (3.60). The equality in (3.56) can be relaxed to the inequality (3.59). □

Since the swarm network is fully connected, we have $|\mathcal{L}_{\mathrm{all}}| = {|\mathcal{A}|(|\mathcal{A}|-1)}/{2}$. From Corollary 3.3.1 and Corollary 3.3.2, we can observe that for both equal and unequal ranging

CRBs cases, the average framework distance CRBs are reduced to $O(1/|\mathcal{A}|)$ of the ranging CRBs, which is similar as the conclusion about position CRB scaling in [28]. In addition, for unicast ranging schemes, the average framework distance CRBs is in $O(|\mathcal{A}|\mathrm{CRB}_0[d_{uv}])$, i.e. $|\mathcal{A}|$ times worse than ranging performance with all the subcarriers. For broadcast ranging schemes, the average framework distance CRBs is on the order of $O(\mathrm{CRB}_0[d_{uv}])$. Hence, for broadcast ranging, the framework distance estimation of all links are almost as accurate as single link ranging occupying all RF resources, i.e. the degradation due to resource sharing is compensated by the collaboration gain.

According to the CRB analysis in this section, a large-scale network with massive number of simultaneous multi-links is preferable for self-localization, especially for broadcast schemes. However, detection failure effects are excluded with traditional CRB, which makes the analysis over optimistic. Next, we include the detection failures with the help of ZZB.

3.3.3.3 ZZB modified CRB for Self-Localization

CRB is a lower bound of unbiased estimators, which is achievable for high SNR. For our swarm system with multi-link ranging, the SNR can be low due to resource sharing. As a consequence, an estimator may fail to distinguish signal from noise which leads to a severe error. In this case, the CRB is no longer applicable in predicting the performance of estimators. Therefore, we have to take the detection probability into consideration as well, for example by the ZZB defined in (3.13). [56] and [90] derived the ranging ZZB for ultra-wide band (UWB) and multicarrier signals, respectively. We adapt the result in [56] to our signal and the randomized subcarrier allocation scheme. The ranging ZZB of a ranging link with subcarrier set $\mathcal{N}_{uv}$ states

$$\mathrm{ZZB}[d_{uv}] = \frac{c^2}{T_o}\int_0^{T_o} t(T_o - t)Q\left(\sqrt{\mathrm{SNR}_{uv}|\mathcal{N}_{uv}|(1-\rho(t))}\right)\mathrm{d}t, \tag{3.62}$$

where $Q(\cdot)$ is the Gaussian Q-function and $\rho(t)$ is the signal auto-correlation function normalized to one. The ToA is assumed to be uniformly distributed in the *a-priori* searching window $(0, T_o]$. As a Bayesian bound, ZZB treats the distance between agents as a random variable, which is contrary to the deterministic variable assumption of the ranging CRB. The Bayesian and non-Bayesian concepts are not restrictively comparable since they describe a variable from different perspectives. Intuitively speaking, Bayesian concept measures subjectively the *a-posteriori* 'knowledge' about the variable of interest, given the *a-priori* knowledge and the observations. Non-Bayesian concept emphasizes on objectively estimating the variable given the observations. However, in practice the Bayesian concept is often adapted to estimate an objective physical

variable, like distance between agents, since it conveniently combines the *a-priori* information and the observations. In this case, the bounds, e.g. ZZB and CRB, and estimators, e.g. MMSE and ML estimators, from Bayesian and non-Bayesian concepts are often compared. For example as a well known result, the ranging ZZB converges to the ranging CRB for high SNR, since in the high SNR region, the *a-priori* information plays an insignificant role. In the threshold SNR region, the ranging ZZB diverges above the CRB, which is tighter to the ranging MSE since it includes the detection failures. In the low SNR region, the ranging ZZB flattens due to the *a-priori* information, whereas the CRB remains increasing as the SNR decreases. A comparison of ranging ZZB, CRB and estimation RMSEs with different resource sharing factors is illustrated in Figure 3.11 in Section 3.6.1. The CRB discussion in Section 3.3.3.2 is valid for high SNR. However, to investigate the resource limitation effect on self-localization, which is essentially determined by the SNR according to Lemma 3.3.1, we are interested in the whole range of SNRs. We propose a ZCRB, which incorporates the ranging ZZB in position CRB. In order to do so, the ranging model is modified as follows. We consider the A2A distance d_{uv} is a deterministic unknown variable. The starting point τ_o of the searching window $(\tau_o, \tau_o + T_o]$ is assumed by a Bayesian range estimator as uniformly distributed in $({}^{d_{uv}}/_{c} - T_o, {}^{d_{uv}}/_{c}]$. The range estimate ρ_{uv} is modeled as the real distance d_{uv} distorted by a additive noise ϵ_{uv}, i.e.

$$\rho_{uv} = d_{uv} + \epsilon_{uv}. \tag{3.63}$$

The distribution of the noise is generally unknown, which leads to a difficulty to derive the exact position CRB. However, the noise is zero mean since the searching window is symmetric w.r.t. ${}^{d_{uv}}/_{c}$. In addition, the noise variance is tightly bounded from below by the ranging ZZB. It has been proved in [91], that for a parameter estimation problem with an observation distorted by a zero mean noise with fixed variance, the CRB gets its largest value if the noise is Gaussian distributed. We utilize this result and find another ranging model

$$\tilde{\rho}_{uv} = d_{uv} + \tilde{\epsilon}_{uv}, \tag{3.64}$$

where $\tilde{\epsilon}_{uv} \sim \mathcal{N}(0, \mathrm{ZZB}[d_{uv}])$. The position FIM with the virtual ranging $\tilde{\rho}_{uv}$ can be written according to [27] as

$$\check{J}_{\mathbf{p}_\mathcal{A}} = \mathbf{H}_{\mathcal{L}_0} \mathrm{diag}\{\mathrm{ZZB}[d_{uv}] : \mathbb{1}_{uv} \in \mathcal{L}_0\} \mathbf{H}_{\mathcal{L}_0}^T. \tag{3.65}$$

The optimal position CRB corresponding to $\check{I}_{\mathbf{p}_\mathcal{A}}$ is referred to as the position ZCRB, i.e.

$$\mathrm{ZCRB}[\mathbf{p}_\mathcal{A}^{\mathbb{C}}] = \check{I}_{\mathbf{p}_\mathcal{A}}^{\dagger}, \tag{3.66}$$

which is a conservative approximation of the exact position CRB in the optimal coordinate system $\mathbb{C}$. As we can see from (3.62), once the transmitted signal is determined, the ranging ZZB only depends on the SNR, which can be pre-calculated and stored in a lookup table. Then the position ZCRB can be assessed with a low computational effort. The position ZCRB is used to evaluate the connectivity-ranging trade-off in self-localization in Section 3.6.1, and to optimize the swarm formation minimizing position uncertainty in Chapter 5.

3.4 Swarm Source Localization

As next step we are interested in what we can learn from Fisher information for the scenario where a distant point source $\mathbb{o}_v \in \mathcal{S}$ is collectively localized by the swarm $\mathcal{A}$. As introduced in Section 1.2.1, a swarm-centric view is applied with a meso-level Cartesian coordinate system $\mathbb{C}$, i.e. the swarm coordinate system. In order to focus on the source localization problem, we assume the agent states $\mathbf{x}_\mathcal{A}$ are known in this section, i.e. $\mathcal{X} = \mathcal{S}$. Therefore, the choice of the coordinate system will not affect the investigation, unlike swarm self-localization, discussed in Section 3.3. A graph representation of swarm source localization can be found in Figure 3.4.

3.4.1 From Discrete to Continuous Swarm Aperture

Without loosing the generality, we investigate the case where the origin of the coordinate system $\mathbb{C}$ is located at the swarm center and the source $\mathbb{o}_v$ is located at the positive side of the $x-$axis. Source localization can be equivalently seen as two problems, namely determining the AoA θ_v and the distance d_v of the source $\mathbb{o}_v$ w.r.t. the swarm coordinate system $\mathbb{C}$. In order to assess the property of the two problems separately, we use the polar coordinate system $\mathbb{P}$ corresponding to $\mathbb{C}$ as the default coordinate system in this section and omit the superscript $\mathbb{P}$. The agent and source's polar coordinates are $\mathbf{p}_u = \mathrm{vec}\{d_u, \theta_u\}, \forall \mathbb{o}_u \in \mathcal{A}$ and $\mathbf{p}_v = \mathrm{vec}\{d_v, \theta_v\}$, respectively. The source $\mathbb{o}_v$ emits a signal $s_v(t)$ which is received by all agents. We generally assume some nuisance parameters $\mathbf{a}_v$ which need to be jointly estimated with the source's position. The joint parameter vector to be estimated is thus $\mathbf{x}_v = \mathrm{vec}\{\mathbf{p}_v, \mathbf{a}_v\}$. Analogous to (3.5) and (3.6) the EFIM of $\mathbf{p}_v$, denoted as $\tilde{\mathbf{I}}_{\mathbf{p}_v}$ can be derived using the Schur

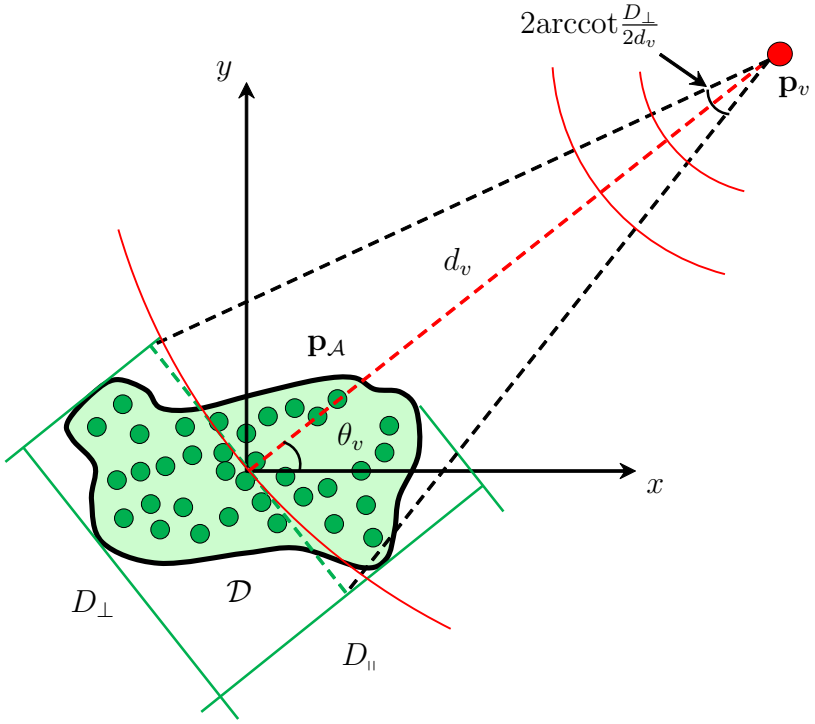

Figure 3.4. *Graph representation of swarm source localization: Red and green dot(s) indicate a source and agents, respectively. Agents' positions in $\mathbb{C}$ are assumed known. Definitions of different apertures introduced in Section 3.4.1 are illustrated.*

complement as

$$\tilde{\mathbf{I}}_{\mathbf{p}_v} = \mathbf{I}_{\mathbf{p}_v} - \underbrace{\mathbf{I}_{\mathbf{p}_v,\mathbf{a}_v}\mathbf{I}_{\mathbf{a}_v}^{-1}}_{\mathbf{D}_{\mathbf{a}_v\to\mathbf{p}_v}}\mathbf{I}_{\mathbf{p}_v,\mathbf{a}_v}^T, \tag{3.67}$$

where $\mathbf{I}_{\mathbf{p}_v}$ is the information about $\mathbf{p}_v$ given the nuisance parameters $\mathbf{a}_v$. The term $\mathbf{D}_{\mathbf{a}_v\to\mathbf{p}_v}$ shows the degradation of the information about $\mathbf{p}_v$ when $\mathbf{a}_v$ is unknown. The components of (3.67) are defined as

$$\begin{aligned}
\mathbf{I}_{\mathbf{p}_v} &= \sum_{\mathfrak{a}_u\in\mathcal{A}} \iota_{g_{uv}} \left(\frac{\partial g_{uv}}{\partial d_{uv}}\right)^2 \nabla_{\mathbf{p}_v} d_{uv} \nabla_{\mathbf{p}_v^T} d_{uv}, \\
\mathbf{I}_{\mathbf{p}_v,\mathbf{a}_v} &= \sum_{\mathfrak{a}_u\in\mathcal{A}} \iota_{g_{uv}} \frac{\partial g_{uv}}{\partial d_{uv}} \nabla_{\mathbf{p}_v} d_{uv} \nabla_{\mathbf{a}_v^T} g_{uv}, \\
\mathbf{I}_{\mathbf{a}_v} &= \sum_{\mathfrak{a}_u\in\mathcal{A}} \iota_{g_{uv}} \nabla_{\mathbf{a}_v} g_{uv} \nabla_{\mathbf{a}_v^T} g_{uv}.
\end{aligned} \tag{3.68}$$

For a large-scale swarm, the observability of certain parameters, e.g. source position, is decisively determined by the swarm collective aperture $\mathcal{D}$ and the observation models, instead of the number of agents for observation. From a macroscopic perspective, a swarm with a massive number of agents in 2D, i.e. $|\mathcal{A}|\to\infty$, and a finite aperture

size $D = 2R$, can be considered as a surface which captures signals in a spatially continuous manner. The agent positions can be treated as known independent and identically distributed (i.i.d.) random variables with a pdf of $p(d_u, \theta_u)$. Hence the summation of a certain function $f(d, \theta)$ sampled at every agent $f(d_u, \theta_u),\ \forall \mathbb{a}_u \in \mathcal{A}$, can be asymptotically approximated by the expectation over the agent's spatial distribution, i.e.

$$\lim_{|\mathcal{A}|\to\infty} \sum_{\mathbb{a}_u \in \mathcal{A}} f(d_u, \theta_u) = |\mathcal{A}|\ \mathbb{E}_{\mathbf{p}_u}\left[f(d_u, \theta_u)\right]. \tag{3.69}$$

With this approximation we can rewrite (3.68) with expectations and focus on the collective aperture covered by the swarm instead of particular swarm formation, which provides more insights on the geometrical interpretation of source localization. A 2D aperture $\mathcal{D}$ can be projected on the direction perpendicular to the source's AoA, referred to as the tangential aperture $\mathcal{D}_\perp$, and on the direction of the source's AoA, referred to as the radial aperture $\mathcal{D}_{\shortparallel}$. In addition, the angular aperture is defined as ${}^{D_\perp}/_{d_v}$, which measures the relative geometrical relationship of the swarm-source system. The definitions of different apertures are illustrated in Figure 3.4. We will investigate the impacts of the aperture on individual direction on source localization.

3.4.2 Impacts of Nuisance Parameters

From the models in Section 2.4 we observe that the position information of an isotropic point source, i.e. distance d_v and AoA θ_v from the swarm perspective, is inferred essentially from the distances d_{uv} between the source $\mathbb{a}_v$ and agents $\forall \mathbb{a}_u \in \mathcal{A}$.

The AoA, θ_v, can be estimated utilizing the fact that signal emitted from an isotropic point propagates radially. The tangent plane (in 3D), or tangent line (in 2D), of the signal front is always perpendicular to the source's direction. Especially when the source is distant from the swarm, the signal front is approximately planar. Agents along a line perpendicular to the direction of the source will observe nearly identical signal values. Intuitively, the AoA of the source can be fully determined from the directions of these lines, independently from the knowledge of the nuisance parameters. Hence the AoA information of a distant source can be captured only by the tangential aperture of the swarm. Contrarily, the distance information of a distant source is solely contained in the observation from the radial aperture, since the signal feature $g_{uv} = g(d_{uv}, \mathbf{a}_v)$ only obtains distinguishable values in the radial direction. Without nuisance parameters, distance between source and agent d_{uv} can be directly derived from a signal feature $g_{uv} = g(d_{uv})$. The source to swarm distance d_v can be estimated by averaging over the range measurements from all agents. The rest of this

subsection is dedicated to the case in presence of a nuisance parameter. We consider a generic signal feature $g_{uv} = g(d_{uv}, a_v)$ as an arbitrary function of the source to agent distance d_{uv} and a single nuisance parameter a_v. We prove that there is only one class of signal feature model, where a nuisance parameter can not be separated from the source distance by the radial aperture. Hence, the source distance is not observable by the radial aperture $\mathcal{D}_{\shortparallel}$. However, it can be estimated from the tangential aperture $\mathcal{D}_{\perp}$, which will be discussed in Section 3.4.3.

Let us consider a linear swarm, i.e. a swarm composed of agents on a line, along the $x-$axis with known positions in polar coordinate system $\mathbf{p}_{\mathcal{A}} = \text{vec}\{[d_u, \theta_u]^T : d_u < R, \theta_u \in (0, \pi], \mathbb{a}_u \in \mathcal{A}\}$. A source is located on the positive $x-$axis at distance d_v to the swarm, i.e. $\theta_v = 0$ and known. Let us further assume the signal feature at agent $\mathbb{a}_u$ is $g_{uv} = g(d_v - x_u, a_v)$. The FIM of $\mathbf{x}_v = \text{vec}\{d_v, a_v\}$ is then approximated with expectation as

$$\mathbf{I}_{\mathbf{x}_v} \approx |\mathcal{A}| \, \mathbb{E}_{\mathbf{p}_u} \left[\iota_{g_{uv}} \begin{pmatrix} \left(\frac{\partial g_{uv}}{\partial d_v}\right)^2 & \frac{\partial g_{uv}}{\partial d_v}\frac{\partial g_{uv}}{\partial a_v} \\ \frac{\partial g_{uv}}{\partial d_v}\frac{\partial g_{uv}}{\partial a_v} & \left(\frac{\partial g_{uv}}{\partial a_v}\right)^2 \end{pmatrix} \right]. \tag{3.70}$$

The source distance is not observable i.f.f.

$$\det\left[\mathbf{I}_{\mathbf{x}_v}\right] = 0, \tag{3.71}$$

which leads to the following lemma.

Lemma 3.4.1 (Condition for Source Localizability)**.** *A linear swarm cannot observe its distance to a collinear source d_{uv} and the nuisance parameter a_v i.f.f. the following PDE holds*

$$K\frac{\partial g(d_{uv}, a_v)}{\partial d_{uv}} = \frac{\partial g(d_{uv}, a_v)}{\partial a_v}, \tag{3.72}$$

where K is an arbitrary constant coefficient.

Proof. See Appendix C.2. □

The PDE in (3.72) belongs to the class of first-order PDE with a constant coefficient. Discarding the trivial solution of $g(d_{uv}, a_v) = C$, the general solution of this type of PDE is expressed in [92, p. 359] as

$$g(d_{uv}, a_v) = F(d_{uv} + Ka_v), \tag{3.73}$$

where $F(\xi)$ is any differentiable function of a single variable ξ. With this observation, the following proposition can be readily stated.

Proposition 3.4.1 (Source Localizability by a Collinear Swarm)**.** *A linear swarm is able to observe the distance to a collinear source d_{uv} and the nuisance parameter a_v i.f.f. the signal feature function $g(d_{uv}, a_v)$ possess a form other than* (3.73)*.*

This proposition can be interpreted such that a nuisance parameter which brings a arbitrary bias to distance observations, e.g. a clock offset for ToA, or a carrier phase offset for PoA, will fully neutralize the source distance information in the observations of the radial aperture. Contrarily, for arbitrary types of signal feature $g(d_{uv}, a_v)$ other than the class defined by (3.73), the distance to a collinear source can still be estimated by the linear swarm with a reduced accuracy, compared to the case of known nuisance parameter. One example is the gas concentration with scaling and exponent factors as nuisance parameters, introduced in (2.29).

Even in the worst case, where the source's distance is not distinguishable from a nuisance parameter by the radial aperture, it can be estimated by with the observations from the tangential aperture through observing the curvature of the signal, as we discussed in [67]. In the next section we provide a geometrical interpretation of the extractable source position information from the signal's curvature.

3.4.3 Source Distance Information in Signal's Curvature

The concept of CoA based source distance estimation is intuitively illustrated by an example in Figure 3.5. A source located at $\mathbf{p}_v$ transmits a sine wave which propagates to the swarm aperture $\mathcal{D}$ as illustrated by the black curve. From the view of the 1D collinear swarm aperture (Figure 3.5a), the received signal would be identical to the one (red curve) transmitted at an offseted position $\tilde{p}_v$ with a corresponding delay offset δ. From the view of a 2D swarm aperture (Figure 3.5b), a distance offset leads to a different arriving curvature of the signal, which makes these two curves distinguishable. Hence the source distance can uniquely be determined. Now we quantify the extractable distance information from the CoA. We assume a single nuisance parameter a_v and a signal feature $g(d_{uv}, a_v) = g(d_{uv} + Ka_v)$ fulfilling (3.73). Additionally, we assume the source distance is much larger than the size of the swarm's aperture, i.e. $d_v \gg \max\{d_u : \forall \mathbb{a}_u \in \mathcal{A}\}$, so that $\iota_{g_{uv}}$ and $\partial g(d_{uv}, a_v)/\partial d_v$ can be approximated by their value at $d_{uv} = d_v$. The EFIM $\tilde{\mathbf{I}}_{\mathbf{p}_v}$ can then be approximated as

$$\tilde{\mathbf{I}}_{\mathbf{p}_v} \approx \iota_{d_v} |\mathcal{A}| \, \mathbb{E}_{\mathbf{p}_u} \left[\nabla_{\mathbf{p}_v} d_{uv} \nabla_{(\mathbf{p}_v)^T} d_{uv} \right] - \iota_{d_v} |\mathcal{A}| \, \mathbb{E}_{\mathbf{p}_u} \left[\nabla_{\mathbf{p}_v} d_{uv} \right] \mathbb{E}_{\mathbf{p}_u} \left[\nabla_{(\mathbf{p}_v)^T} d_{uv} \right], \quad (3.74)$$

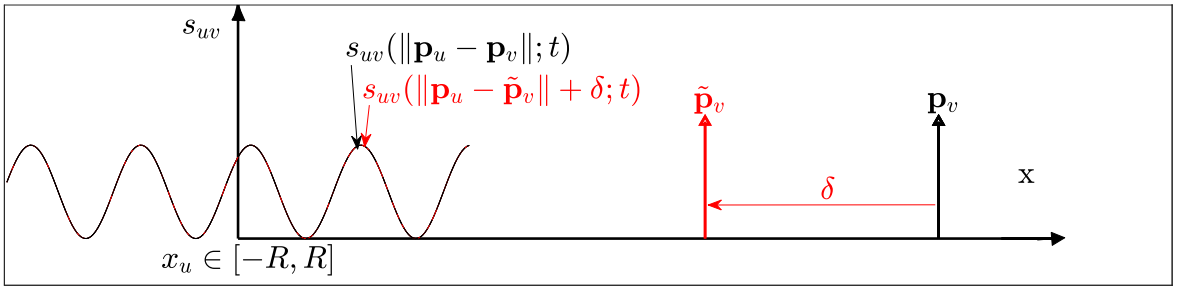

(a) *1D aperture: The source at the true position* $\mathbf{p}_v$ *(black) and the offsetted hypothesis* $\tilde{\mathbf{p}}_v$ *(red) generate non-distinguishable signals (black and red) in the one-dimensional (1D) colinear aperture.*

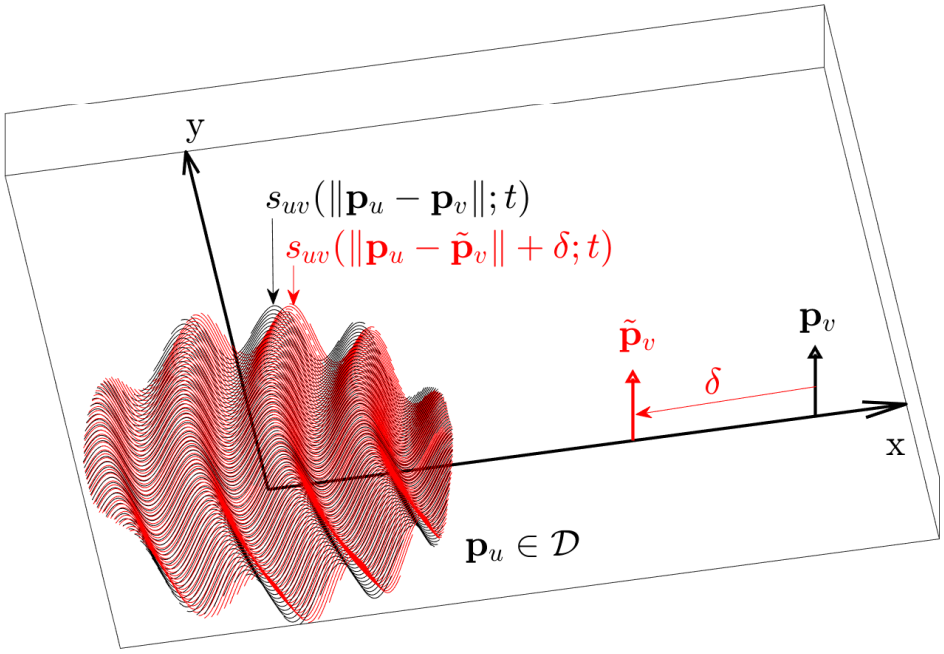

(b) *2D aperture: The source at the true position* $\mathbf{p}_v$ *(black) and the offsetted hypothesis* $\tilde{\mathbf{p}}_v$ *(red) generate distinguishable signals (black and red) in the 2D aperture.*

Figure 3.5. *Observability of source distance* d_v *in the presence of a distance offset* δ *as nuisance parameter: Figure 3.5a shows that* d_v *is not separable from* δ *by a 1-D aperture. Figure 3.5b shows that* d_v *is separable from* δ *through observing the CoA by a 2-D aperture.*

where ι_{d_v} is the RII at the swarm center defined as

$$\iota_{d_v} \triangleq \iota_{g_{uv}} \left(\frac{\partial g_{uv}}{\partial d_{uv}} \right)^2 \Big|_{d_{uv}=d_v}. \tag{3.75}$$

Besides, the S2A distance d_{uv} is approximated by its second-order Taylor expansion $\tilde{d}_{uv}$ around $d_u = 0$ as

$$\tilde{d}_{uv} \approx d_v - d_u \cos(\theta_u - \theta_v) + \frac{d_u^2}{2d_v} \sin^2(\theta_u - \theta_v). \tag{3.76}$$

Additionally, we consider a large-scale swarm, whose agents are randomly deployed on a dish $\mathcal{D}$, centered at the origin with a radius of R. The positions of agents are statistically i.i.d. with a uniform distribution in Cartesian coordinate system $\mathbb{C}$ within the dish $\mathcal{D}$, as shown in Figure 3.15. The EFIM of the source's position $\mathbf{p}_v = \text{vec}\{d_v, \theta_v\}$ in (3.74) is further approximated as

$$\tilde{\mathbf{I}}_{\mathbf{p}_v} \approx \underbrace{\iota_{d_v}|\mathcal{A}| \begin{pmatrix} \frac{32d_v^4 - 8d_v^2R^2 + R^4}{32d_v^4} & 0 \\ 0 & \frac{6d_v^2R^2 + R^4}{24d_v^2} \end{pmatrix}}_{\approx \mathbf{I}_{\mathbf{p}_v}} - \underbrace{\iota_{d_v}|\mathcal{A}| \begin{pmatrix} \frac{64d_v^4 - 16d_v^2R^2 + R^4}{64d_v^4} & 0 \\ 0 & 0 \end{pmatrix}}_{\approx \mathbf{D}_{\mathbf{a}_v \to \mathbf{p}_v}}, \tag{3.77}$$

where $\mathbf{I}_{\mathbf{p}_v}$ is the EFIM assuming known nuisance parameter. Applying the assumption of $d_v \gg D$, where $D \triangleq 2R$ denotes the aperture size of the swarm, leads to the approximated CRBs as follows.

Theorem 3.4.1 (Nuisance Parameter Impact on Source Localization CRBs)**.** *With known nuisance parameter, the CRB of* $\mathbf{p}_v$ *is approximated by*

$$\text{CRB}[\mathbf{p}_v|\mathbf{a}_v] \approx \frac{1}{\iota_{d_v}|\mathcal{A}|} \begin{pmatrix} 1 & 0 \\ 0 & \frac{4}{R^2} \end{pmatrix}. \tag{3.78}$$

With unknown nuisance parameter, the CRB of $\mathbf{p}_v$ *is approximated by*

$$\text{CRB}[\mathbf{p}_v] \approx \frac{1}{\iota_{d_v}|\mathcal{A}|} \begin{pmatrix} 64\left(\frac{d_v}{R}\right)^4 & 0 \\ 0 & \frac{4}{R^2} \end{pmatrix}. \tag{3.79}$$

The first diagonal entries of $\text{CRB}[\mathbf{p}_v|\mathbf{a}_v]$ and $\text{CRB}[\mathbf{p}_v]$ are the source distance estimation lower bounds with known and unknown nuisance parameters, respectively. The second diagonal entries are the corresponding source AoA estimation lower bounds. The AoA estimation variance is inverse quadratically proportional to the aperture size D and independent of the nuisance parameters. Contrarily, the nuisance parameters severely degrade distance estimation, as the distance estimation variance in that case

is inverse quartically proportional to the size of the angular aperture defined as D/d_v.

In the next section we investigate a particular application, where the RF carrier phases of S2A signals are exploited for source localization.

3.4.4 Curvature of Arrival(CoA) based RF Source Localization

3.4.4.1 Theoretical Analysis

For a RF source $\mathbb{o}_v \in \mathcal{S}_{\mathrm{RF}}$, which radiates a single-carrier signal at carrier frequency f_s with transmit power of A_v^2, the source position information can be extracted collectively by the agents from the received signal phases with a unit of meters $\Phi_{uv} = d_{uv} + \phi_v$, $\forall \mathbb{o}_u \in \mathcal{A}$ as defined in (2.21) and (2.26). In this case the nuisance parameter is the unknown phase offset of the source ϕ_v, which is additive to the distance d_{uv}. The swarm $\mathcal{A}$ is collectively considered as a large-scale phased array. Traditionally, the signal phases observed by a phased array are utilized only for AoA estimation with the plane wave model, since the source is normally located in the far field of the array, i.e. $d_v \gg d_{\mathrm{F}} = \frac{2D_\perp^2}{\lambda_s}$, where d_{F} is called the Fraunhofer distance [93], λ_s is the wavelength, and $D_\perp$ is the tangential aperture length. In our case, the aperture composed by the swarm is significantly larger than the one from traditionally considered phased arrays. Therefore, the spherical wave model has to be applied, which enables CoA-based source localization. In Figure 3.6, the concepts of far-field and near-field source localization with carrier phase is illustrated, where the swarm forms a uniform rectangular array (URA) as an example.

The generic notation of $\mathbb{A}^{(x_1,x_2)}$ indicates a 2D coordinate system with x_1 as the first axis and x_2 as the second axis. The Cartesian coordinate system $\mathbb{C}^{(\xi\varphi)}$ in Figure 3.6b is the swarm coordinate system $\mathbb{C}$ rotated by θ_v, whose $\xi-$axis is aligned with the AoA. The signal CoA at the center of swarm P_o can be defined as follows.

Definition 1 (RF Signal CoA)**.** *The signal CoA κ_v is defined as the extrinsic curvature of $-\Phi_v c/\omega_s$ along the φ-axis of $\mathbb{C}^{(\xi\varphi)}$. With the spherical wave model, CoA is proportional to the absolute value of the phase's second-order derivative and equals to the reciprocal of d_v, i.e.*

$$\kappa_v \triangleq -\frac{c}{\omega_s}\frac{\partial^2 \Phi_v}{\partial \varphi^2} \Big|_{P_o} = \frac{1}{d_v}, \tag{3.80}$$

where $\Phi_v = d_v + \phi_v$ is the virtual phase observation at P_o, since there is generally no agent at point P_o.

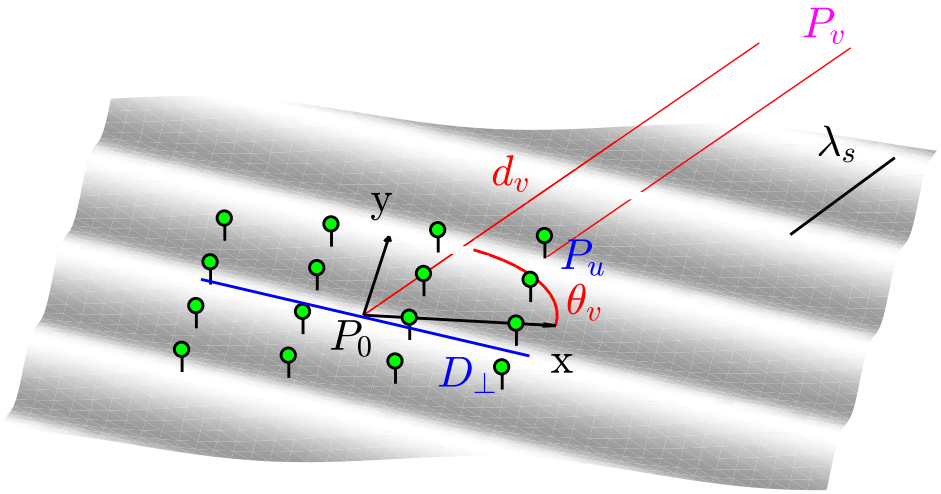

(a) *Far-field AoA estimation*

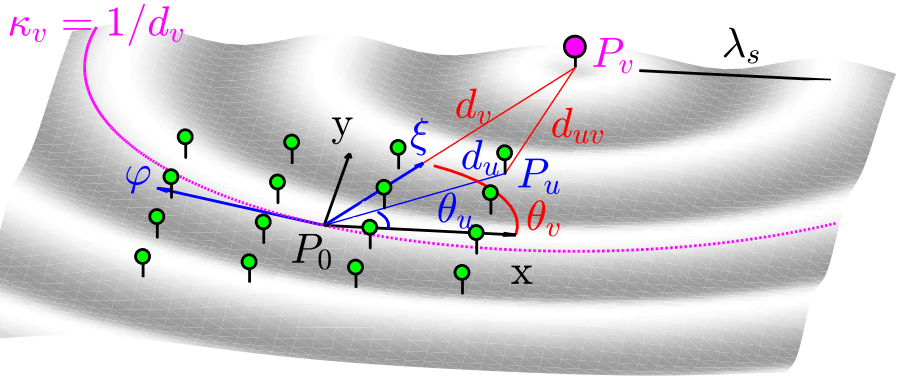

(b) *Near-field AoA/distance estimation*

Figure 3.6. *Far-field vs. near-field source localization.*

The definition of the signal CoA will be used in Section 3.4.4.3 to derive a low complexity CoA-based source localization algorithm. The total FIM of $\mathbf{x}_v$ can be calculated similarly as in [94]. The source position CRB denoted as $\mathrm{CRB}[\mathbf{p}_v]$ can be obtained by applying the Schur complement to the position corresponded sub-matrix of the FIM defined in (3.67). We assume free-space pathloss, and the array aperture size to be small compared to the source distance d_v, but still large enough to capture the signal's CoA. Therefore, the distance-related attenuation differences among elements are negligible. Hence given $A_{uv} = {}^{A_v c}/_{2\omega_s d_v}$, the positioning CRB states

$$\mathrm{cov}[\hat{\mathbf{p}}_v] \succcurlyeq \mathrm{CRB}[\mathbf{p}_v] = \frac{2N_0 d_v^2}{A_v^2}\Big(\Big(\sum_{\mathbb{o}_u\in\mathcal{A}} \nabla_{\mathbf{p}_v} d_{vu} \nabla_{\mathbf{p}_v^T} d_{vu}\Big) - \frac{1}{|\mathcal{A}|}\sum_{\mathbb{o}_u\in\mathcal{A}} \nabla_{\mathbf{p}_v} d_{vu} \sum_{\mathbb{o}_w\in\mathcal{A}} \nabla_{\mathbf{p}_v^T} d_{vw}\Big)^{-1}, \tag{3.81}$$

where the factor in front ${}^{2N_0 d_v^2}/_{A_v^2}$ indicates the effect of SNR. To infer the geometry impacts on CoA-based source localization, we first investigate a linear swarm forming a symmetric linear array (SLA) along the x-axis, with an aperture length D. We define the k^{th} empirical moment of the normalized agents' spatial distribution $M_k = \sum_{\mathbb{o}_u\in\mathcal{A}}(d_u/D)^k/|\mathcal{A}|$, and the tangential aperture length $D_\perp = D\sin\theta_v$, to characterize the array geometry.

Theorem 3.4.2 (Source Position CRB for SLA)**.** *For the SLA, assuming* $|\mathcal{A}| \gg 1$ *and* $d_v \gg D$*, the CRB of AoA estimate can be approximated by*

$$\mathrm{CRB}[\theta_v] \approx \frac{2N_0 d_v^2}{A_v^2 |\mathcal{A}| D_\perp^2 M_2}, \tag{3.82}$$

whereas the distance CRB is approximated by

$$\mathrm{CRB}[d_v] \approx \frac{2N_0 d_v^2}{A_v^2}\frac{4d_v^4}{|\mathcal{A}| D_\perp^4 (M_4 - M_2^2)}. \tag{3.83}$$

Proof. See Appendix C.3. □

Both CRBs in (3.82) and (3.83) linearly decrease with the number of agents $|\mathcal{A}|$. The CRB for AoA decreases quadratically with $D_\perp$. The distance CRB experiences a quartic growth with the angular aperture $d_v/D_\perp$, indicating a strong impact from the relative geometry. These two conclusions coincide with the continuous dish aperture asymptotics analysis of a random swarm in Theorem 3.4.1.

In addition, the CRB for AoA decreases linearly with the antennas' spatial spread M_2, whereas the distance CRB decreases with $M_4 - M_2^2$, which describes the shape of the antennas' spatial distribution. These two discoveries may be further exploited

for swarm formation optimization according to a preference of estimating the source's direction or distance.

More importantly, when $\theta_v = 0\,^\circ$, both CRBs approach infinity. Hence, the signal captured by the swarm's radial aperture expanded in $\xi-$direction contains no information of the source's position. With the last observation, we extend Theorem 3.4.2 to arbitrary 2D centro-symmetric arrays (CSAs). Many typical arrays are centro-symmetric, e.g. uniform circular/linear arrays, the ones in [94], as well as the URA illustrated in Figure 3.6.

Corollary 3.4.1 (Linear Projection of a CSA)**.** *A CSA centered at P_0 can be projected on the $\varphi-$axis, forming a virtual SLA.*

Proof. By the definition of centro-symmetry, for any non-centered element u with position $\mathbf{p}_u = \mathrm{vec}\{d_u, \theta_u\}$, there exists an element w with position $\mathbf{p}_w = \mathrm{vec}\{d_u, \theta_u + \pi\}$. Elements u and w are projected on the $v-$axis at $\pm d_u \sin(\theta_u - \theta_v)$ respectively and are symmetric w.r.t. P_0. Hence the projected array is an SLA. □

Since the aperture expanded in $\xi-$direction does not contain position information, the projected virtual linear array along the $\varphi-$axis is almost equivalent to the original CSA in the sense of CoA source localization. Hence, the positioning CRB with a URA can be approximated by applying Theorem 3.4.2 to the projected virtual SLA.

Figure 3.7 illustrates the optimized swarm formations for source AoA (Figure 3.7a) and distance (Figure 3.7b) estimation, according to Theorem 3.4.2 and Corollary 3.4.1, s.t. a fixed tangential aperture length $D_\perp$ and formation rigidity. For source AoA estimation, agents are in favor of spreading to the tips of the tangential aperture, since it maximizes M_2. For source distance estimation, half of the agents are deployed to the tips of the tangential aperture, whereas the other half are at the middle. In this way the value of $M_4 - M_2^2$ is maximized. For a swarm with unconstrained tangential aperture length, agents are spreading as far as possible in the tangential direction for source AoA estimation. For source distance estimation, new agents are deployed to extend the tangential aperture i.f.f. the new tangential aperture length fulfills $D_\perp > 2\sqrt{2M_2}$. Otherwise, the new agents should be added at the center of the tangential aperture.

3.4.4.2 Survey on Spherical Wave Source Localization Algorithm

As discussed in Section 3.4.4, the swarm $\mathcal{A}$ can be collectively considered as a phased array towards a RF source $\mathbb{o}_v \in \mathcal{S}_{\mathrm{RF}}$. In classical phased array processing, the sources are assumed to be located in the far-field of the phased array. AoA is estimated from the carrier phase differences between antennas [95, 96, 97]. In order to localize the sources multiple arrays are required. Alternatively, distance of the source needs to be estimated

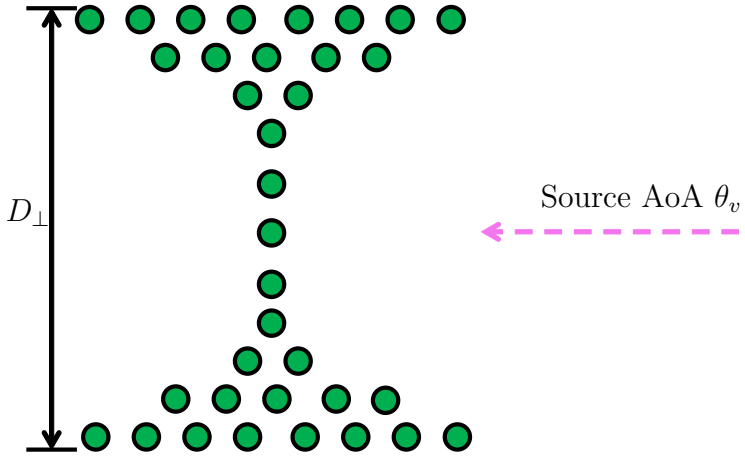

(a) *Optimized formation for source AoA estimation.*

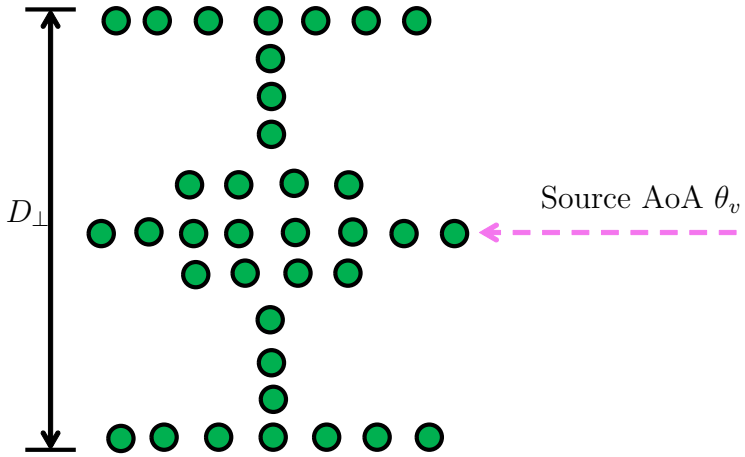

(b) *Optimized formation for source distance estimation.*

Figure 3.7. *Optimized swarm formations for source AoA (Figure 3.7a) and distance (Figure 3.7b) estimation, s.t. a fixed tangential aperture length $D_\perp$ and formation rigidity, green dots indicate agents, magenta arrow illustrates the source AoA.*

with e.g. ToA and multi-way ranging, subject to synchronization or bi-directional communications between array and the source [29]. Unlike traditional phased arrays, the swarm array has a significantly larger collective aperture $\mathcal{D}$, which leads to a large Fraunhofer distance. For example, for a swarm spreading a tangential aperture of length $D_\perp = 100\,\mathrm{m}$, its Fraunhofer distance to a RF source with a carrier frequency of $f_s = 20\,\mathrm{MHz}$ is 3000 m. The signal wavefront received by the swarm is modeled as spherical wave. The spherical wave model has been exploited for antenna phase center determination in [98], for LOS-multiple-input and multiple-output (MIMO) communications in [99], as well as for source localization in [100, 101, 102, 103]. We are interested in the applications of source localization. Under this model, not only AoA but also distance information of the source is contained in the carrier phase, which enables localization of the source [67]. Source localization approaches exploiting the spherical wave model are commonly referred to as near field source localization in the literature [101]. However, it is also applicable for a source located at the beginning of the Fraunhofer far field region. Therefore, to be precise, we use the term spherical wave source localization instead of near-field source localization. Most previous spherical wave source localization algorithms apply the Fresnel approximation to arrays with special geometries, e.g. uniform linear arrays (ULAs) [101, 102, 103], and introduce a model mismatch. This mismatch has recently been noticed to jeopardize the achievable positioning precision [104]. In [105] a lookup table is used for ULA model correction. The ML algorithm in [100] exploits the exact model, but includes a computationally expansive recursion.

3.4.4.3 CoA based Source Localization Algorithm

In the section, we propose a low complexity CoA-based source localization algorithm, directly utilizing the signal CoA defined in Definition 1. The proposed algorithm avoids recursions and reduces the model error from the Fresnel approximation. More importantly, it can be operated in a decentralized fashion, which is particularly preferable for swarm localization. The proposed algorithm can be applied either directly as a realtime positioning variant or to initialize a recursive algorithm like an ML estimator [100]. The objective of the CoA-based source localization algorithm is to estimate the position of the source $\mathbf{p}_v^{\mathbb{C}}$ in the swarm Cartesian coordinate system $\mathbb{C}$. We define groups of swarm $\mathcal{P}_i$ composed of at least three adjacent agents and centered at points P_i. The estimated local AoA $\hat{\theta}_{vi}$ can be calculated by traditional far-field AoA estimation methods [97], applying the plane wave model on all applicable agent pairs

$\mathbb{o}_l, \mathbb{o}_m \in \mathcal{P}_i$

$$\phi_{lm} \approx -\mathbf{e}_{vi}^T \mathbf{p}_{lm} \omega_s / c, \quad \forall d_{lm} \omega_s / c < \pi/2, \tag{3.84}$$

where $\mathbf{p}_{lm} = \mathbf{p}_l^{\mathbb{C}} - \mathbf{p}_m^{\mathbb{C}}$, $\phi_{lm} = \phi_l - \phi_m$ and $\mathbf{e}_{vi} = \text{vec}\{\cos\theta_{vi}, \sin\theta_{vi}\}$. To estimate the group's curvature κ_i, a coordinate system $\mathbb{C}^{(\xi_i \varphi_i)}$ centered at $\mathcal{P}_i$ is defined, whose $\xi-$axis is aligned to the AoA of the source, similarly as in Figure 3.6. The second order derivative of phase local to $\mathcal{P}_i$ can be approximated by a double difference with three adjacent agents $\mathbb{o}_l, \mathbb{o}_m, \mathbb{o}_n \in \mathcal{P}_i$, which leads to a curvature estimate as

$$\tilde{\kappa}_{lmn} = 2\frac{\triangle_{lm} - \triangle_{mn}}{\varphi_{lm} + \varphi_{mn}}, \text{ where } \triangle_{gh} = \frac{\phi_{gh} c/\omega_s + \xi_{gh}}{\varphi_{gh}},$$
$$\begin{bmatrix} \xi_{gh} \\ \varphi_{gh} \end{bmatrix} = \begin{bmatrix} \hat{\mathbf{e}}_{vi}^T \\ \hat{\mathbf{e}}_{vi,\perp}^T \end{bmatrix} \mathbf{p}_{gh} \quad \text{and} \quad \hat{\mathbf{e}}_{vi,\perp} = \begin{bmatrix} \sin\hat{\theta}_{vi} \\ -\cos\hat{\theta}_{vi} \end{bmatrix}.$$

The coarse estimate of the group's curvature $\tilde{\kappa}_i$ is obtained by averaging $\tilde{\kappa}_{lmn}$ over all the effective combinations of $\mathbb{o}_l, \mathbb{o}_m$ and $\mathbb{o}_n$, i.e. $\forall\, l, m, n,$ where $\|\varphi_{lm}\|, \|\varphi_{mn}\|$ and $\|\varphi_{lm} + \varphi_{mn}\| \gg 0$. The curvature estimated from a single group is heavily distorted by noise. To get a stable estimate, an extra smoothing step is applied, exploiting the geometry equality

$$\mathbf{p}_v^{\mathbb{C}} = \kappa_i^{-1} \mathbf{e}_{vi} + \mathbf{p}_i^{\mathbb{C}} = \frac{\sum_{\forall \mathcal{P}_i} \mathbf{e}_{vi} + \kappa_i \mathbf{p}_i^{\mathbb{C}}}{\sum_{\forall \mathcal{P}_i} \kappa_i}. \tag{3.85}$$

The group's curvature estimate can be refined as

$$\hat{\kappa}_i = \Big\| \Big(\sum_{\forall \mathcal{P}_j} \tilde{\kappa}_j \Big)^{-1} \Big(\sum_{\forall \mathcal{P}_j} \hat{\mathbf{e}}_{vj} + \tilde{\kappa}_j \mathbf{p}_j^{\mathbb{C}} \Big) - \mathbf{p}_i^{\mathbb{C}} \Big\|^{-1}. \tag{3.86}$$

Finally, the transmitter's position can be estimated by replacing θ_{vi} and κ_i in (3.85) with their estimates $\hat{\theta}_{vi}$ and $\hat{\kappa}_i$. We can observe that only summations across the groups are involved in the proposed algorithm, which can be implemented in a decentralized fashion with average consensus algorithms.

3.5 Swarm Joint Self- and Source Localization

As the final investigation on the theoretical aspects of swarm localization, we look into the joint swarm self- and source localization, i.e. $\mathcal{X} = \mathcal{A} \cup \mathcal{S}$, for the extended swarm system introduced in Section 2.1, with all the potential observations described in Section 2.4. Graph representations of the two examples of joint self- and source

localization are illustrated in Figure 3.8. Figure 3.8a, which is a sub-graph of the Mars swarm exploration system in Figure 2.1, shows a scenario where only the swarm $\mathcal{A}$ and RF sources $\mathcal{S}_{\text{RF}}$ are included for joint localization, i.e. $\mathcal{V} = \mathcal{A} \cup \mathcal{S}_{\text{gas}}$. Figure 3.8b, which is the same graph as in Figure 2.1, shows the joint localization of the whole extended swarm network, i.e. $\mathcal{V} = \mathcal{A} \cup \mathcal{S}_{\text{gas}} \cup \mathcal{S}_{\text{RF}} \cup \mathcal{B}$. Agents, a gas source, RF sources and beacons, are illustrated as green, red, magenta and blue dot(s), respectively. Different links are shown with lines and arrows, same as in Figure 2.1. The first case is an anchor-free scenario, where swarm and multiple RF sources are jointly localized w.r.t. the swarm coordinate system. The symbol delay of both A2A and S2A signals as well as the carrier phase of the S2A signals are exploited for localization. Both clock offsets and carrier phase offsets of all nodes are considered as the unknown nuisance parameters. The swarm Cartesian system $\mathbb{C}$ is applied for agents since the self- localization performance evaluated in position domain is eventually of interest for agents. The sources localization is performed in the swarm polar coordinate system $\mathbb{P}$ so that the distance and AoA performance can be assessed individually. The second case is illustrated in Figure 1.2 as an extension of the first one. One gas source and three beacons are additionally included. All the states of beacons are known. The position $\mathbf{p}_v$ and nuisance parameters a_{g} and b_{g} of the gas source $\text{q}_v \in \mathcal{S}_{\text{gas}}$ are unknown. In Section 3.5.1, the assembling of FIM for joint self- and source localization is discussed. In Section 3.5.2, we derive the joint localization CRB with the swarm reference system. Numerical analysis of both cases are demonstrated in Section 3.6.3.

3.5.1 FI of Joint Self- and Source Localization

Signals from different links $\text{e}_{uv} \in \mathcal{E}_0$ are considered independent to each other. If multiple signal features $\mathbf{g}_{uv}$ are extracted from a link e_{uv}, e.g. amplitude A_{uv}, phase Φ_{uv} and symbol delay τ_{uv} from a RF link, the signal features are also considered as independent, which is justified by (3.23). The signal features applied for localization are indicated with an index set $\mathcal{I}_{uv}$. Fundamentally, the total state FIM can be expressed as in (3.14), which does not provide intuitive insights of the impacts of each building components, e.g. different types of links, nodes, signal features and nuisance parameters, on localization. As we discussed in both swarm self-localization in Section 3.3 and source localization in Section 3.4, the swarm localization problem can be essentially interpreted as extracting geometrical relationship among nodes from distances or distance differences between transceivers. In order to unveil the insights, we expand the total FIM with a chain of transformations $r_{uv}(t) \rightarrow \mathbf{g}_{uv} \rightarrow d_{uv} \rightarrow \mathbf{x}$, $\forall \text{e}_{uv} \in \mathcal{E}_0$. Hence we start from the received signal $r_{uv}(t)$ to formulate the FI in the signal features $\mathbf{g}_{uv}$, denoted as $\mathbf{I}_{\mathbf{g}_{uv}}$, as in (3.16). Then the signal features are transformed to distance

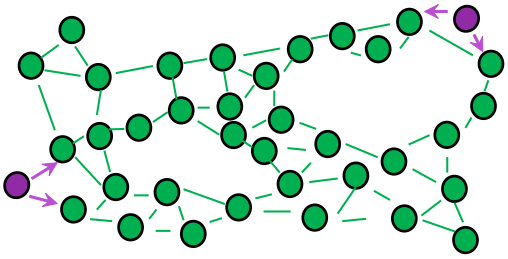

(a) *Anchor-free RF network.*

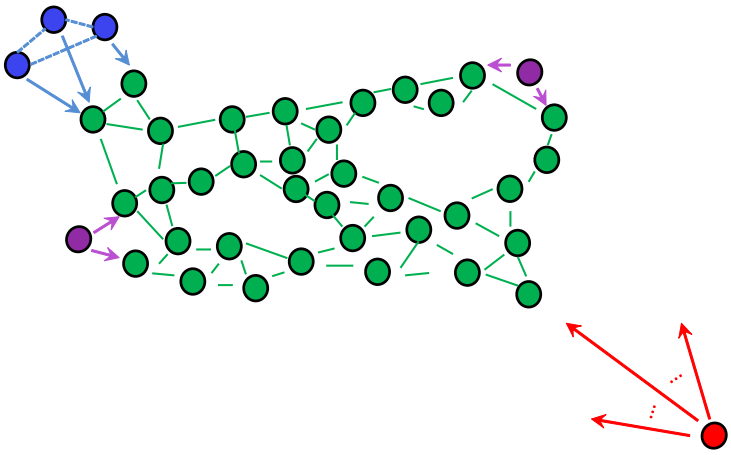

(b) *Extended swarm network in Figure 2.1.*

Figure 3.8. *Graph representations of two joint swarm self- and source localization examples: Agents, a gas source, RF sources and beacons, are illustrated as green, red, magenta and blue dot(s), respectively. Different links are shown with lines and arrows.*

domain to get the RII denoted as $\iota_{d_{uv}}$, similar to (3.24). Finally, we apply the distance-to-state transformation to obtain the FIM of the total states $\mathbf{I}_{\mathbf{x}}$, similar to (3.33). The FIM expansion is summarized as follows. The FI of the l^{th} signal feature $[\mathbf{g}_{uv}]_l, l \in \mathcal{I}_{uv}$ on a link $\mathbb{e}_{uv} \in \mathcal{E}_0$ is written as

$$\iota_{[\mathbf{g}_{uv}]_l} = \frac{2}{N_0} \Re \left\{ \int_0^{T_o} \left\| \frac{\partial s_{uv}(t)}{\partial [\mathbf{g}_{uv}]_l} \right\|^2 \mathrm{d}t \right\}. \tag{3.87}$$

The FI contained in $[\mathbf{g}_{uv}]_l$ about the link distance d_{uv}, i.e. the RII in $[\mathbf{g}_{uv}]_l$ is expressed as

$$\iota_{d_{uv}}^{[\mathbf{g}_{uv}]_l} = \iota_{[\mathbf{g}_{uv}]_l} \left\| \frac{\partial [\mathbf{g}_{uv}]_l}{\partial d_{uv}} \right\|^2. \tag{3.88}$$

The total RII of the link $\mathbb{e}_{uv}$ is obtained by the RIIs summation for all the considered signal features, i.e.

$$\iota_{d_{uv}} = \sum_{l \in \mathcal{I}_{uv}} \iota_{d_{uv}}^{[\mathbf{g}_{uv}]_l}. \tag{3.89}$$

The FI contained in a single link $\mathbb{e}_{uv}$ about the total states $\mathbf{x}$ is expressed as

$$\mathbf{I}_{\mathbf{x}}^{\mathbb{e}_{uv}} = \iota_{d_{uv}} \nabla_{\mathbf{x}} d_{uv} \nabla_{\mathbf{x}^T} d_{uv}. \tag{3.90}$$

The FIM of $\mathbf{x}$ in one type of links in set $\mathcal{E}_{\mathcal{P}} \in \{\mathcal{E}_{\mathcal{A}}, \mathcal{E}_{\mathcal{B}}, \mathcal{E}_{\mathcal{S}}\}$, i.e. all the A2A, $B2A$, or $S2A$ links, is expressed as

$$\mathbf{I}_{\mathbf{x}}^{\mathcal{E}_{\mathcal{P}}} = \sum_{\mathbb{e}_{uv} \in \mathcal{E}_{\mathcal{P}}} \mathbf{I}_{\mathbf{x}}^{\mathbb{e}_{uv}}. \tag{3.91}$$

At the end, the total FIM of the extended swarm network can be written as

$$\mathbf{I}_{\mathbf{x}} = \sum_{\mathcal{E}_{\mathcal{P}} \in \{\mathcal{E}_{\mathcal{A}}, \mathcal{E}_{\mathcal{B}}, \mathcal{E}_{\mathcal{S}}\}} \mathbf{I}_{\mathbf{x}}^{\mathcal{E}_{\mathcal{P}}}. \tag{3.92}$$

The chain of information flow is visualized in Figure 3.9. It can be observed that the contributions of every components to the total state FIM are individually addable. This observation allows us to flexibly compare different scenarios of swarm joint self- and source localization.

1) Impacts of particular signal features

The performance of swarm localization decisively depends on the exploited signal

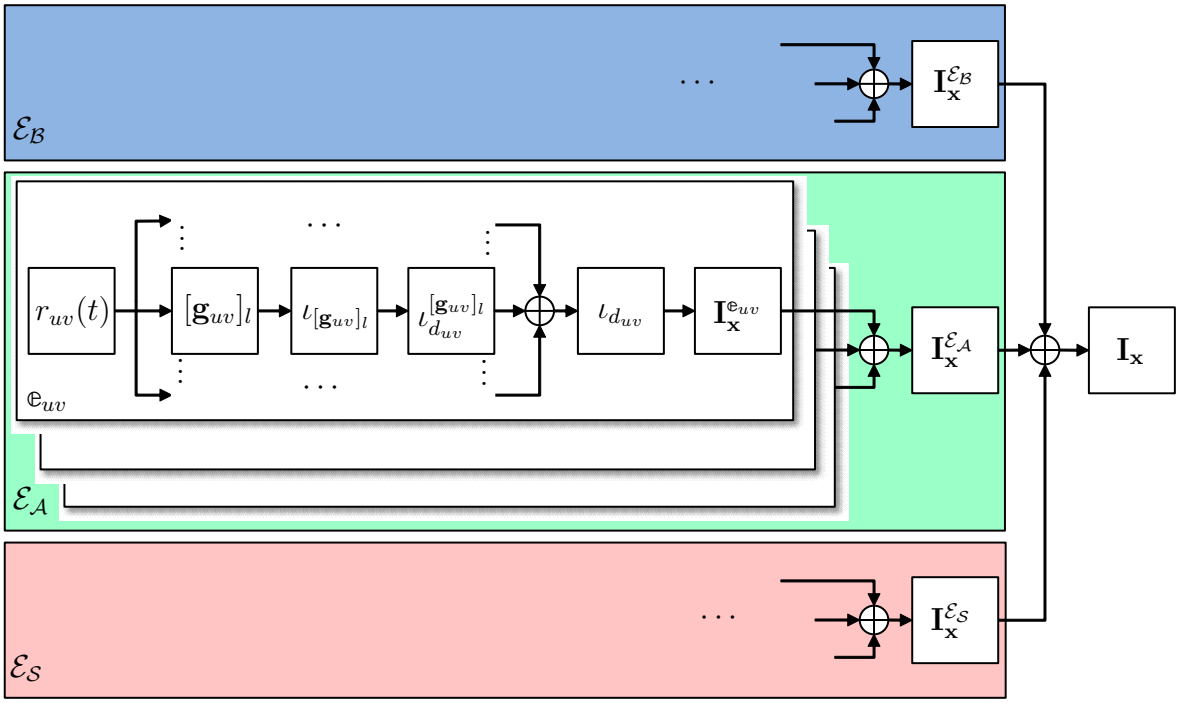

Figure 3.9. *The chain of information flow from the continuous observations to the total states FIM.*

features. In order to assess their impacts on swarm localization, we can add or remove a particular signal feature's index l into the considered signal feature set $\mathcal{I}_{uv}$.

2) Impacts of particular links

The impacts of particular links or link sets can be evaluated by adding or removing $\mathbb{e}_{uv}$ or $\mathcal{E}_{\mathcal{B}}/\mathcal{E}_{\mathcal{A}}/\mathcal{E}_{\mathcal{S}}$ blocks depicted in Figure 3.9. With this manipulation to the FIM, we can analyze the gain for swarm self- and source localization through agent collaborations.

3) Impacts of the knowledge of particular states

If particular states are assumed to be known, we can remove them from the state vector $\mathbf{x}$, meantime keeping all the observations related to the corresponding nodes. This approach can be utilized to analyze different scenarios. If the removed states are coordinates of the nodes, the truncated FIM represents a scenario where the corresponding nodes are considered as beacons. If the removed states are nuisance parameters, with the truncation of the FIM, we are able to compare the absolute observations for example RSS, PoA, ToA, with their differential counterparts, DRSS, PDoA, TDoA.

4) Impacts of particular nodes

If we would like to exam the impacts of particular nodes on the swarm localization, the nodes should be excluded or included together with the measurements associated with them. One application is to investigate the gain of swarm self-localization by collectively estimating positions of some sources.

3.5.2 Swarm Reference System Constraints

In some scenarios the reference system is not defined, e.g. in Figure 3.8a, the coordinate system and reference system for the nuisance parameters, such as a common clock and phase base, are not defined. As a consequence, the FIM is singular, similarly to anchor-free self-localization. In this case, the swarm aims to localize itself and the source in a swarm reference system. Hence only a partition (the swarm) of the considered network can be used to define the reference system. The sources have to be excluded for determining the reference system. Constraints unifying a reference system needs to be considered in order to convert the total FIM into CRB. A baseline in the swarm can be selected as the constraints like in Section 3.3.2.1. This is not optimal, since an additional coordinate system uncertainty is introduced. Optimal swarm constraints can be expressed similarly as in Section 3.3.2.2. For the coordinate system, the group motions of the agents as introduced in (3.38) and (3.39) can be selected as the constraints. As explained in [106], since the group motion constraints are only applied on $\mathcal{A}$, which is a subset of the extended node set $\mathcal{V}$, the alternative Moore-Penrose pseudoinverse expression in (3.42) cannot be employed, since it implies that both swarm and the sources are utilized to define the reference system. For the nuisance parameters, like common clock and phase bases, a centroid constraints analogous to the translation constraints of the coordinate system can be applied. We derive the joint self- and source localization CRB for the scenario illustrated in Figure 3.8a to demonstrate the reference system defined by a subset of nodes, for example the swarm $\mathcal{A}$. The unknowns of agent $\mathbb{a}_u \in \mathcal{A}$ are its position and clock offset, i.e. $\mathbf{x}_u = \text{vec}\{\mathbf{p}_u, \delta_u\}$, whereas the unknowns of source $\mathbb{a}_v \in \mathcal{S}_{\text{RF}}$ are its position, clock offset and carrier phase offset, i.e. $\mathbf{x}_v = \text{vec}\{\mathbf{p}_v, \delta_v, \phi_v\}$. The total agents' unknowns are $\mathbf{x}_\mathcal{A} = \text{vec}\{\mathbf{x}_u : \mathbb{a}_u \in \mathcal{A}\}$. The total sources' unknowns are $\mathbf{x}_\mathcal{S} = \text{vec}\{\mathbf{x}_v : \mathbb{a}_v \in \mathcal{S}_{\text{RF}}\}$. The total unknowns of the system are $\mathbf{x} = \text{vec}\{\mathbf{x}_\mathcal{A}, \mathbf{x}_\mathcal{S}\}$. The total FIM can be written as

$$\mathbf{I}_\mathbf{x} = \underbrace{\begin{pmatrix} \mathbf{I}^{\mathcal{E}_\mathcal{A}}_{\mathbf{x}_\mathcal{A}} & \mathbf{0} \\ \mathbf{0} & \mathbf{0} \end{pmatrix}}_{\substack{\mathbf{I}^{\mathcal{E}_\mathcal{A}}_\mathbf{x} \\ \text{(information in A2A links)}}} + \underbrace{\begin{pmatrix} \mathbf{I}^{\mathcal{E}_\mathcal{S}}_{\mathbf{x}_\mathcal{A}} & \mathbf{I}^{\mathcal{E}_\mathcal{S}}_{\mathbf{x}_\mathcal{A},\mathbf{x}_\mathcal{S}} \\ \mathbf{I}^{\mathcal{E}_\mathcal{S}}_{\mathbf{x}_\mathcal{S},\mathbf{x}_\mathcal{A}} & \mathbf{I}^{\mathcal{E}_\mathcal{S}}_{\mathbf{x}_\mathcal{S}} \end{pmatrix}}_{\substack{\mathbf{I}^{\mathcal{E}_\mathcal{S}}_\mathbf{x} \\ \text{(information in S2A links)}}}, \tag{3.93}$$

where the first term $\mathbf{I}_{\mathbf{x}}^{\mathcal{E}_{\mathcal{A}}}$ and the second term $\mathbf{I}_{\mathbf{x}}^{\mathcal{E}_{\mathcal{S}}}$ indicate the information about the total states $\mathbf{x}$, in all A2A links and all S2A links, respectively. For the joint self- and source localization and synchronization problem, the FIM is rank-four deficient, since the positions are subject to arbitrary group rotation (one degree of freedom) and translation (two degrees of freedom), and the clock offset estimates are subject to arbitrary group offset (one degree of freedom). In the scenario under investigation, we are interested in the accuracy of the joint self- and source localization w.r.t. the swarm. Therefore, an optimal Cartesian coordinate system $\mathbb{C}$ is defined by constraining the group rotations and translations of the swarm [106]. An optimal clock reference system of the formation is defined by setting the mean clock offset to a constant, similarly to the position group translation. The constrains of the reference system are represented by the subspace of the swarm $\bar{\mathbf{U}}_{\perp} = (\mathbf{u}_x, \mathbf{u}_y, \mathbf{u}_\delta, \mathbf{u}_r)$, with orthonormal bases of translations in x and y directions $\mathbf{u}_x$ and $\mathbf{u}_y$, clock offset $\mathbf{u}_\delta$ and rotation $\mathbf{u}_r$ defined as

$$(\mathbf{u}_x, \mathbf{u}_y, \mathbf{u}_\delta) = \frac{1}{\sqrt{|\mathcal{A}|}} \mathbf{1}_{1\times|\mathcal{A}|} \otimes \mathbf{I}_{3\times 3}, \tag{3.94}$$

$$\mathbf{u}_r = \frac{1}{\|\mathbf{p}_{\mathcal{A}}\|} \mathrm{vec}\{y_u, -x_u, 0 : \mathbb{o}_u \in \mathcal{A}\}. \tag{3.95}$$

The bases $\mathbf{U}_{\perp}$ spans the left nullspace of the swarm's state space, i.e. the reference constraints. Since the sources' unknowns are not involved in the constraints determination, the left nullspace of the total state space $\bar{\mathbf{U}}_{\perp}$ can be acquired by padding zeros to $\mathbf{U}_{\perp}$, i.e.

$$\bar{\mathbf{U}}_{\perp} = \left(\mathbf{U}_{\perp}^T, \mathbf{0}_{4|\mathcal{S}_{\mathrm{RF}}|\times 4}\right)^T. \tag{3.96}$$

The orthonormal bases of column space $\mathbf{U}_{\shortparallel}$ can be determined by the eigenvalue decomposition as

$$\mathbf{I} - \bar{\mathbf{U}}_{\perp}\bar{\mathbf{U}}_{\perp}^T = \begin{pmatrix} \mathbf{I} - \mathbf{U}_{\perp}\mathbf{U}_{\perp}^T & \mathbf{0} \\ \mathbf{0} & \mathbf{I} \end{pmatrix} = \begin{pmatrix} (\mathbf{U}_{\shortparallel}, \tilde{\mathbf{U}}_{\perp}) \begin{pmatrix} \mathbf{\Lambda} & \mathbf{0} \\ \mathbf{0} & \mathbf{0} \end{pmatrix} \begin{pmatrix} \mathbf{U}_{\shortparallel}^T \\ \tilde{\mathbf{U}}_{\perp}^T \end{pmatrix} & \mathbf{0} \\ \mathbf{0} & \mathbf{I} \end{pmatrix} \tag{3.97}$$

$$= \begin{pmatrix} \mathbf{U}_{\shortparallel}\mathbf{\Lambda}\mathbf{U}_{\shortparallel}^T & \mathbf{0} \\ \mathbf{0} & \mathbf{I} \end{pmatrix} = \begin{pmatrix} \mathbf{U}_{\shortparallel} & \mathbf{0} \\ \mathbf{0} & \mathbf{I} \end{pmatrix} \begin{pmatrix} \mathbf{\Lambda} & \mathbf{0} \\ \mathbf{0} & \mathbf{I} \end{pmatrix} \begin{pmatrix} \mathbf{U}_{\shortparallel}^T & \mathbf{0} \\ \mathbf{0} & \mathbf{I} \end{pmatrix} \triangleq \tilde{\mathbf{U}}_{\shortparallel}\tilde{\mathbf{\Lambda}}\tilde{\mathbf{U}}_{\shortparallel}^T. \tag{3.98}$$

It can be observed that the eigenvectors representing the column space of the total state space $\tilde{\mathbf{U}}_{\shortparallel}$ are the ones for the swarm $\mathbf{U}_{\shortparallel}$ extended by an identity matrix. The total

FIM can be projected onto the column space, expressed as $\tilde{\mathbf{U}}_{\shortparallel}^T \mathbf{I}_{\mathbf{x}} \tilde{\mathbf{U}}_{\shortparallel}$, which is full-rank. Finally, the CRB of $\mathbf{x}$ is calculated by inverting the projected FIM and transforming back to the parameter space as

$$\mathrm{CRB}[\mathbf{x}] = \tilde{\mathbf{U}}_{\shortparallel} \left(\tilde{\mathbf{U}}_{\shortparallel}^T \mathbf{I}_{\mathbf{x}} \tilde{\mathbf{U}}_{\shortparallel} \right)^{-1} \tilde{\mathbf{U}}_{\shortparallel}^T \tag{3.99}$$

$$= \begin{pmatrix} \mathbf{U}_{\shortparallel} & \mathbf{0} \\ \mathbf{0} & \mathbf{I} \end{pmatrix} \begin{pmatrix} \mathbf{U}_{\shortparallel}^T \left(\mathbf{I}_{\mathbf{x}_{\mathcal{A}}}^{\mathcal{E}_{\mathcal{A}}} + \mathbf{I}_{\mathbf{x}_{\mathcal{A}}}^{\mathcal{E}_{\mathcal{S}}} \right) \mathbf{U}_{\shortparallel} & \mathbf{U}_{\shortparallel}^T \mathbf{I}_{\mathbf{x}_{\mathcal{A}}, \mathbf{x}_{\mathcal{S}}}^{\mathcal{E}_{\mathcal{S}}} \\ \mathbf{I}_{\mathbf{x}_{\mathcal{S}}, \mathbf{x}_{\mathcal{A}}}^{\mathcal{E}_{\mathcal{S}}} \mathbf{U}_{\shortparallel} & \mathbf{I}_{\mathbf{x}_{\mathcal{S}}}^{\mathcal{E}_{\mathcal{S}}} \end{pmatrix}^{-1} \begin{pmatrix} \mathbf{U}_{\shortparallel}^T & \mathbf{0} \\ \mathbf{0} & \mathbf{I} \end{pmatrix}. \tag{3.100}$$

3.6 Numerical Analysis

Numerical analysis is provided to verify the theoretical aspects of swarm localization. The numerical analysis can be further divided into three parts, namely self-localization in Section 3.6.1, source localization in Section 3.6.2, and joint self- and source localization in Section 3.6.3.

For self-localization, the effects of geometry and resource allocation on ZCRB are illustrated in Section 3.6.1.1-3.6.1.3. Experimental data and both non-Bayesian and Bayesian estimators, are employed for further verification, which is presented in Section 3.6.1.4.

For source localization, we first illustrate in Section 3.6.2.1 the effects of different types of nuisance parameters, on the performance of source distance and AoA estimation. Then we compare in Section 3.6.2.2 the exact and approximated CRBs of the source distance and AoA. With this comparison, the approximations of the CRBs are validated. The performances of different source localization algorithms are evaluated as well, including the proposed CoA based algorithm, an ML algorithm and a state of the art algorithm based on Fresnel approximation.

For joint self- and source localization, in Section 3.6.3.1 mutual improvement of self- and RF source localization is demonstrated. In Section 3.6.3.2 the joint localization CRBs, of the swarm, the RF source and the gas source, are evaluated for the Mars swarm exploration mission introduced in Figure 1.2.

3.6.1 Swarm Self-Localization

3.6.1.1 Geometry Effects

In this section, we demonstrate the geometry effects on swarm self-localization. When a swarm in open space is controlled with a homogeneous strategy, i.e. agents are manipulated by the same control rules, a formation with regular patterns often emerge. For example, a swarm controlled by the flocking algorithm proposed in [41] is stabilized

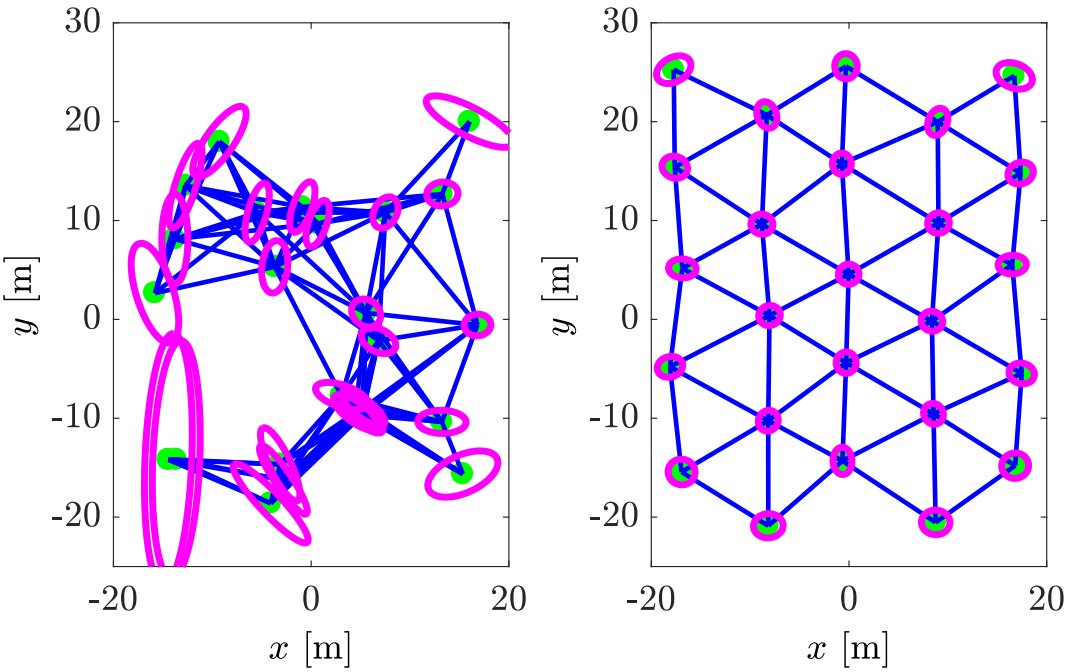

(a) *Random formation* **(b)** *Quasi-lattice formation*

Figure 3.10. *Comparison of the CRB ellipses for a random (Figure 3.10a) and a quasi-lattice (Figure 3.10b) formation. The agents are illustrated with green dots. The blue lines show the connectivity of the swarm network, with a ranging standard deviation of 1 m. The CRB of each agent is illustrated by magenta error ellipse.*

in a quasi-lattice formation. Agents in a quasi-lattice formation, compared to the ones in a random formation, are more likely to have neighbors in all directions, which is preferable for their self-localization.

Figure 3.10 shows a comparison of the CRB ellipses of self-localization for a random (Figure 3.10a) and a quasi-lattice (Figure 3.10b) formation. The CRB ellipse of each agent is illustrated in magenta color, which is the lower bound of the RMSE of self-localization under group motion constraints. A ranging standard deviation of 1 m is assumed. It can be observed that for this setup, the CRB ellipses of the lattice formation are, on average, an order of magnitude smaller than the ones of a random formation, due to the regular geometry.

3.6.1.2 Multi-link Ranging

In this section, the effects of resource limitation on multi-link ranging are evaluated. We consider OFDM modulated signals for ranging, with a carrier frequency of $f_c = 5.5\,\text{GHz}$, a bandwidth of $B_c = 36.6\,\text{MHz}$, 2499 subcarriers with a spacing of $f_{sc} = 14.65\,\text{KHz}$. The received ranging signals are distorted with AWGN. Agents are assumed to be synchronized to conduct ToA based ranging measurements. A prede-

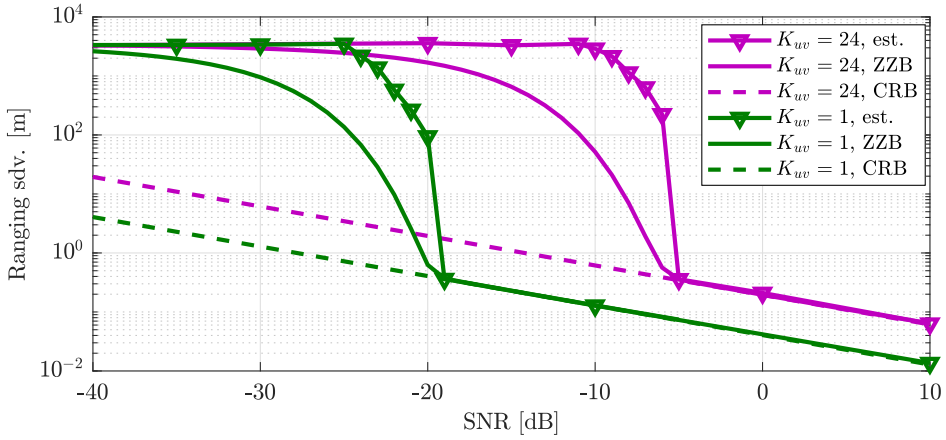

Figure 3.11. *Comparison of CRB, ZZB and an MMSE estimator for ranging with a single link ($K_{uv} = 1$) and 24 simultaneous random OFDMA links ($K_{uv} = 24$).*

fined orthogonal subcarrier allocation on K_{uv} ranging links is assumed, where each subcarrier is selected for ranging with a probability of $1/K_{uv}$. An *a-priori* window of T_o $c = 10\,\text{km}$ is considered, where the true distance is uniformly distributed inside the window. The ranging CRBs and ZZBs as well as the RMSE of a correlation-based MMSE range estimator, for single link ($K_{uv} = 1$) and 24 simultaneous links ($K_{uv} = 24$) are shown in Figure 3.11. As we discussed in Section 3.3.3.1, for a low SNR, the ZZB converges to $\sqrt{c^2 T_o^2/12}$ as the MMSE solution using only the *a-priori* information. For a high SNR, the ZZB converges to the CRB. For a SNR value in between (threshold region), the ZZB starts diverging from the CRB. The MMSE estimator performs with the same tendency of ZZB. From single link to multi-link, all the performance curves shift to a higher SNR by roughly 13.8 dB, i.e. with K_{uv} times higher SNR, which coincides with the conclusion of Lemma 3.3.1.

3.6.1.3 Connectivity-Ranging Trade-off

By jointly considering the geometry and multi-link resource allocation effects, we can evaluate the connectivity-ranging accuracy trade-off for swarm self-localization. The averaged self-localization ZCRB, introduced in Section 3.3.3.3, of the random and quasi-lattice formations are plotted against the measurement coverage in Figure 3.12. An SNR of -5 dB under the usage of all subcarriers (single link) is assumed for all links. The resource sharing factor K_{uv} increases together with the measurement coverage, while the number of subcarriers used per link is reduced. As a consequence, the SNR of each link is reduced accordingly. The *a-priori* map size is constrained to 60 m. For each set of simulation parameters, 1000 simulation runs are employed. The impact of connectivity-ranging accuracy trade-off on self-localization can be seen. When the measurement coverage is too small the expected self-localization performance is

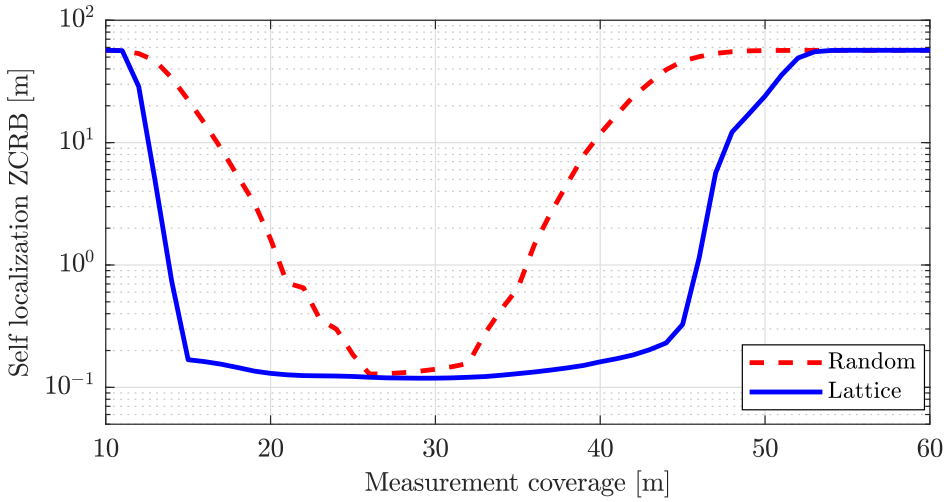

Figure 3.12. *Average ZCRB of random and quasi-lattice formation with -5 dB SNR under the usage of all subcarriers (single link).*

poor due to the lack of connectivity, i.e. the network is no longer rigid. When the measurement coverage is too large, the expected performance is also poor, due to the insufficient subcarriers allocated on each link. According to ZCRB, the quasi-lattice formation has a larger preferable coverage range due to the regularity of the formation. For quasi-lattice formations, self-localization may additionally suffer from the folding ambiguity. Hence, the position estimates of a sub-group of agents are folded along a quasi-line due to the formation's regularity. The folding ambiguity is not considered in the CRB type of evaluation. In practice, the folding ambiguity can be resolved by Bayesian tracking with *a-priori* information, which will be shown in the next section.

3.6.1.4 Experimental Validation

In order to validate the connectivity-ranging accuracy trade-off investigated in the previous sections, we conduct an experiment with the data collected from a measurement campaign with our ranging test-bed in 2013. At that time, we have only a single link ranging test bed, which is implemented by my colleague Dr. Emanuel Staudinger, with details introduced in [88]. This test-bed consists of a master node and a mirror node. The master node can apply two-way ranging by transmitting an OFDM signal, and receiving the amplified and forwarded signal from the mirror node. The OFDM signals applied for two-way ranging have the same bandwidth and subcarrier spacing as the simulation setup. Carrier frequencies for the forward link from the master node to the mirror node are 5.5 GHz, and 5.7 GHz for the return link with a transmit power of 20 dBm. We conducted outdoor measurements to collect ranging data at different distance on a parking lot at the DLR, see Figure 3.13. Both nodes are mounted on

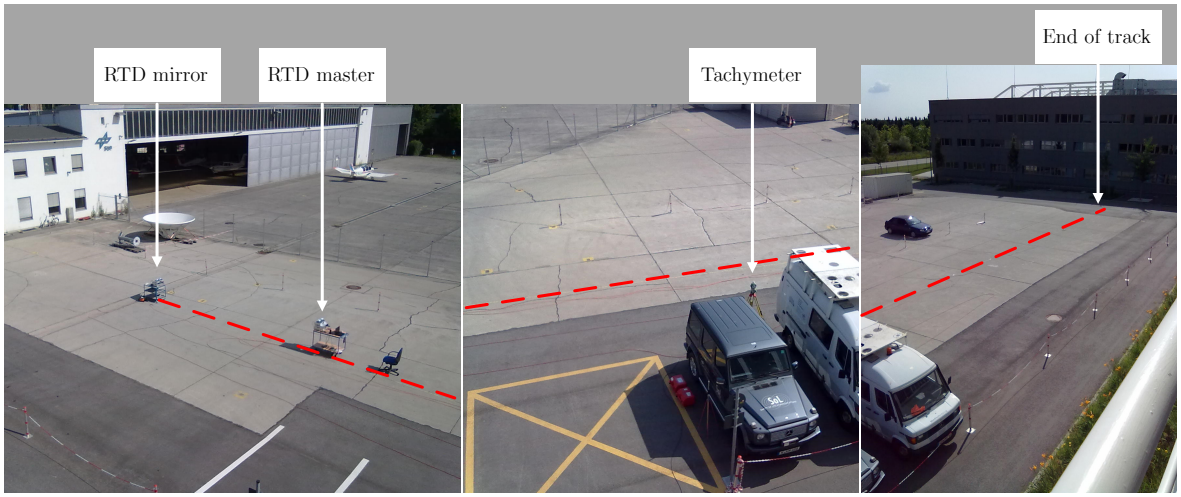

Figure 3.13. *Images of the parking lot with placed ranging nodes [88]. The red dashed line shows the measurement track from* 1 *m to* 60 *m.*

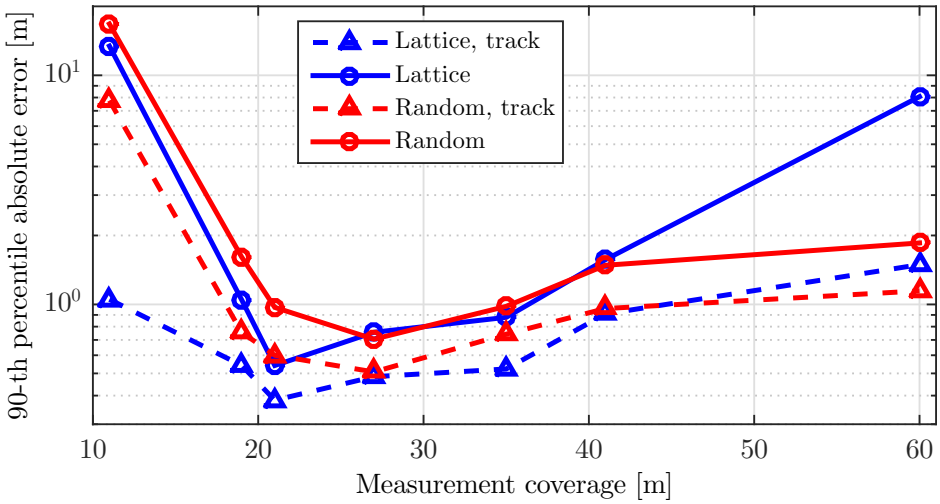

Figure 3.14. *90^{th} percentile of the absolute framework distance error ε_{uv} of random and lattice formations in non-tracking and tracking scenarios.*

trolleys with the same heights. The mirror node is placed on a fixed position. The master node is placed on specific points with approximately 1 m separation along a 60 m long track. The ground truth positions of the nodes are measured with a *Leica* tachymeter. At each point we acquired 1000 ranging snapshots for post-processing.

We use the measurement data, apply random subcarrier allocation for a specific number of multiple links K_{uv}, and regenerate the synthetic ranging measurements at different distance with a correlation-based first-peak detector [107]. Self-localization simulation is conducted with random and quasi-lattice formations, with randomly picked ranging values from the synthetic ranging measurements, given the link distance d_{uv} and the resource sharing factor K_{uv}. A distributed particle filtering (DPF) as in [51] is implemented at each agent to estimate its position. Details on the design of

the distributed self-localization algorithm will be described in Chapter 4. Two scenarios, namely non-tracking and tracking, are considered. In the non-tracking scenario, uniform distribution of the agents within the map is assumed as the initial *a-priori* position distribution. In the tracking scenario, the initial *a-priori* position distribution is assumed to be a Gaussian distribution with a mean at the true position and a standard deviation of 1 m in each dimension. The absolute framework distance error $\varepsilon_{uv} = \|\hat{d}_{uv} - d_{uv}\|$ as introduced in Section 2.2 is used as the metrics for performance evaluation, so that the coordinate system uncertainty is inherently eliminated. The 90^{th} percentile error curves are shown in Figure 3.14. For a small coverage, the performances are poor for almost all the scenarios, except for lattice formation tracking. This observation indicates that in that coverage range, the random formations are non-rigid with a high probability, whereas the lattice formations are rigid but not globally rigid. For the lattice formation tracking case, the folding ambiguity caused by non globally rigid formations is resolved by *a-priori* information. For a large coverage, the network connectivity is high, but the ranging measurements are distorted with larger noise. In this case, the non-tracking self-localization with a random formation outperforms the lattice case. That is because of the regularity of the lattice formations, which leads to a severe local minima problem to DPF. Again, the local minima problem can be resolved by tracking. The overall tendency of the experimental performance coincides with the one of ZCRB in Figure 3.12.

3.6.2 Swarm Source Localization

3.6.2.1 Impacts of Nuisance Parameters

In this section, the impacts of nuisance parameters on source localization are demonstrated, with two generic source observation models.

In the first model, the nuisance parameter δ acts on the source to agent distance d_{uv} as an offset, i.e. $g(d_{uv}, \delta) = F(d_{uv} + \delta)$. The type of observation model is widely applied for the signal propagation time based observation such as symbol delay based observations with unknown clock offsets, or carrier phase based observations with unknown phase offsets.

In the second model, two nuisance parameters, namely a scaling factor a_1 and an exponent factor a_2, are considered, i.e. $g(d_{uv}, a_1, a_2) = F(a_1 d_{uv}^{a_2})$. This model is closely related to energy intensity based observations, such as RSS and the gas concentration.

A swarm of 50 agents are randomly deployed in a dish area with a radius of $R = 50\,\text{m}$, whereas a single source is located $d_v = 240\,\text{m}$ away from the center of the swarm. The agents' position are assumed to be known, in order to concentrated on the impacts

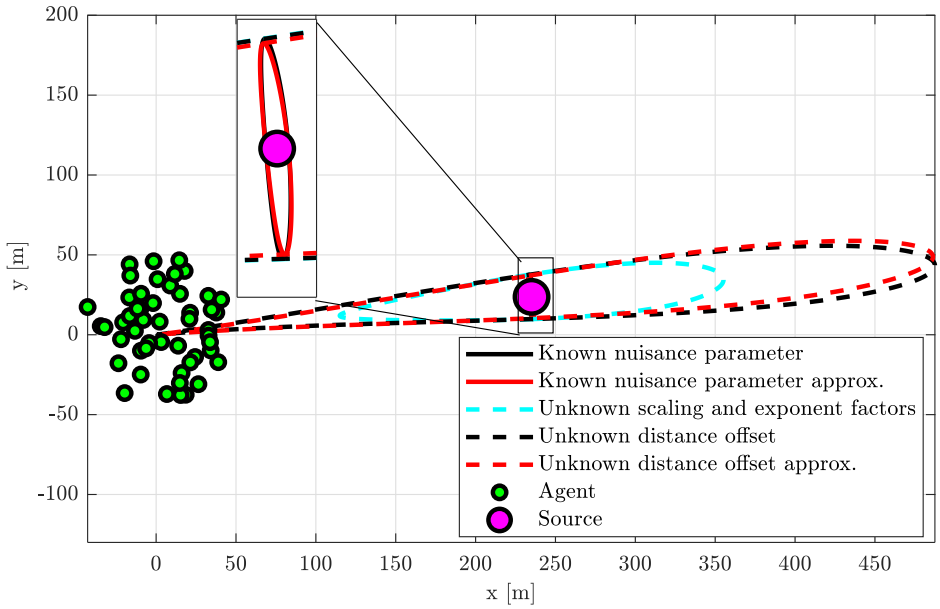

Figure 3.15. *Comparison of 10 σ CRB of source's polar coordinates, with/out nuisance parameters of scaling and exponent factors and distance offset.*

of nuisance parameters on source localization. Numerical analysis of joint self- and source localization will be discussed in Section 3.6.3. The CRB with the offset model is independent to the value of the offset δ. For the second model, we set $a_1 = 1$ and $a_2 = -1$ for generating the source localization CRB. With each model, source localization CRBs are calculated for the both cases of known and unknown nuisance parameters. The signal feature functions $g(d_{uv}, a)$ and $g(d_{uv}, a_1, a_2)$ are set in a way, so that CRBs of the known nuisance parameters cases with both models are equal. In this manner, the geometrical impacts of the nuisance parameters can be better illustrated. Figure 3.15 shows the source localization CRBs of both types of nuisance parameters. Similar to the ellipse interpretation in a Cartesian coordinate system, we obtain the 10 σ of the source position CRBs in the swarm polar coordinate system $\mathbb{P}$ and visualize them in the corresponding Cartesian coordinate system $\mathbb{C}$. After the polar to Cartesian coordinate transformation, the shapes of position CRBs are no longer ellipses. The distance offset case is shown in black. The scaling and exponent factors case is shown with cyan curves. The cases of known nuisance parameters are shown by the solid lines, whereas the cases of unknown nuisance parameters are shown by dashed lines. In addition, the approximated CRBs of the distance offset case, expressed in (3.78) and (3.79), are plotted in red. As expected, the AoA accuracy is not affected by the knowledge of the nuisance parameters. With known nuisance parameters, the approximated and true CRBs overlap. The AoA uncertainty dominates the position estimation error. With an unknown distance offset, the distance CRB approximation matches the exact one well.

In addition, the distance uncertainty dominates the source's position uncertainty. In the case of unknown scaling and exponent factors as nuisance parameters, the distance CRB is larger than the known parameter case and smaller than the distance offset case, since the source distance can be also estimated by the parallel aperture concluded in Section 3.4.2. An intuitive explanation is that the unknown scaling parameter can be determined by the slope of observation values along the direction of the source.

3.6.2.2 CoA based RF Source Localization

In this section, we evaluate CoA based RF source localization by comparing the approximated CRBs derived in Section 3.4.4 with the exact CRBs and three different source localization algorithms. The algorithms under investigation are the proposed low complexity CoA based algorithm, an ML algorithm initiated with the proposed algorithm, and a state of the art near field source localization algorithm based on Fresnel approximation. For the proposed algorithm, the groups in Section 3.4.4.3 are constructed by 3×3 elements for the URA and 1×3 for the ULAs. Three swarm formations with different apertures orientated along the x-axis are considered in the investigation. The first formation is uniform rectangular along the $x-$ and $y-$axis, with aperture length in each dimension $D_x = 75\,\mathrm{m}$, $D_y = 15\,\mathrm{m}$. The rest two formations are uniform linear, with aperture lengths 15 m and 75 m. All three formations operate as phased arrays, i.e. one URA and two ULAs, for a carrier frequency of $f_s = 20\,\mathrm{MHz}$, with element spacing of $\lambda_s/4$. A single antenna transmitter is deployed at distances from 10 m to 10000 m and with AoAs from $0\,^\circ$ to $90\,^\circ$, to the center of the arrays, transmitting a single-carrier signal with 0 dBm transmit power at 20 MHz carrier frequency. Free-space pathloss with an additional noise figure of 15 dB is assumed.

First, the performance of the URA is investigated. The approximated and the exact CRBs, as well as the RMSEs of the proposed CoA based algorithm an the ML algorithm, are compared in Figure 3.16. For each parameter set 100 Monte Carlo runs have been conducted. The RMSE of the ML estimator always overlaps with the exact CRB for both source distance and AoA estimation, which validates the tightness of the CRBs in the considered setup. For small d_v, a slight mismatch between the approximated and the exact CRBs are observed, which come from the Taylor expansion applied to approximate the CRBs. At most of the evaluation points where $d_v > 100\,\mathrm{m}$, the approximated and exact CRBs coincide, which verifies the CRB approximations for CSAs in Section 3.4.4. With increasing d_v, the RMSEs of the proposed CoA based algorithm firstly decrease due to a decreasing model error, and then increase because of the reducing SNR and worsen geometry. For small d_v, the model error varies with θ_v, but only leads to small estimation errors.

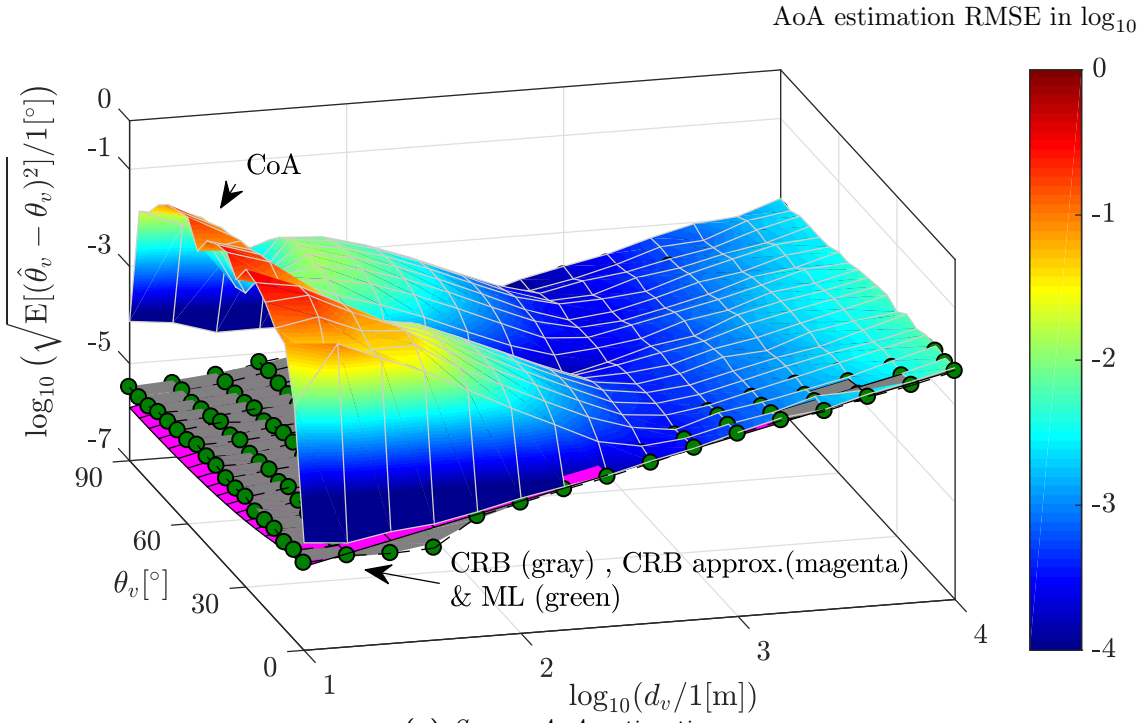

(a) *Source AoA estimation*

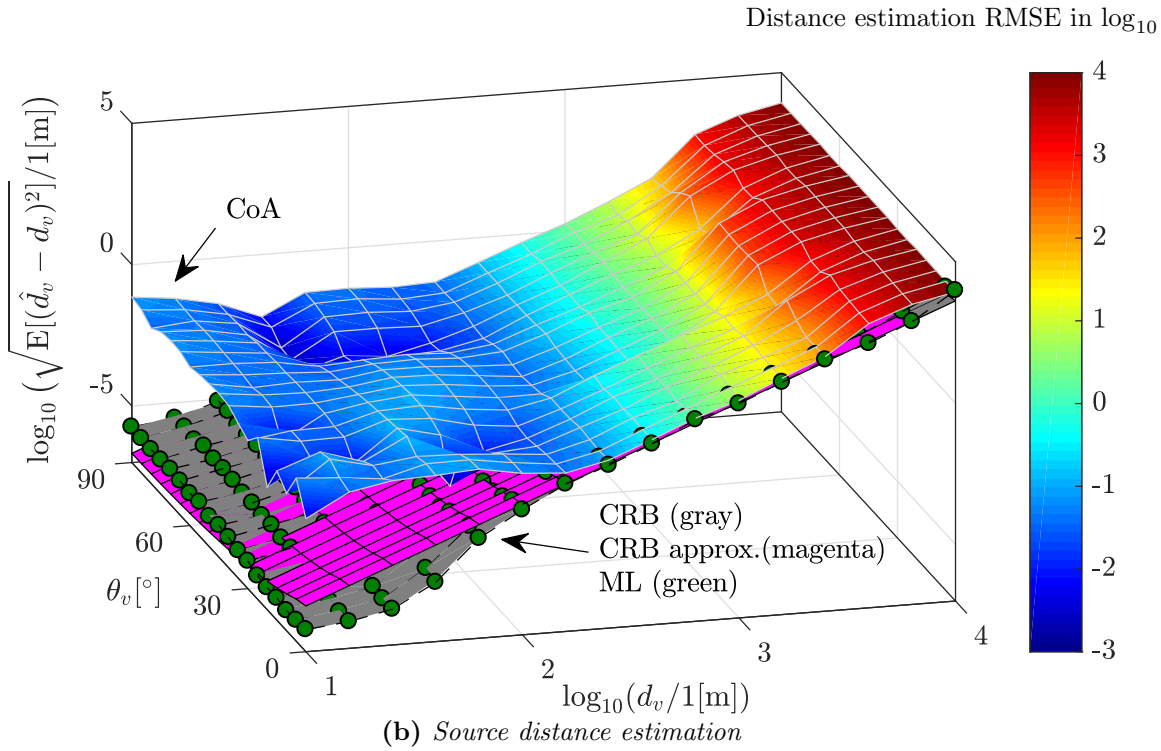

(b) *Source distance estimation*

Figure 3.16. *Source localization performance of a URA aligned with x- and y-axis with aperture lengths in x-direction* $D_x = 75\,\mathrm{m}$ *and in y-direction* $D_y = 15\,\mathrm{m}$, $f_s = 20\,\mathrm{MHz}$ *and element spacing of* $\lambda_s/4$.

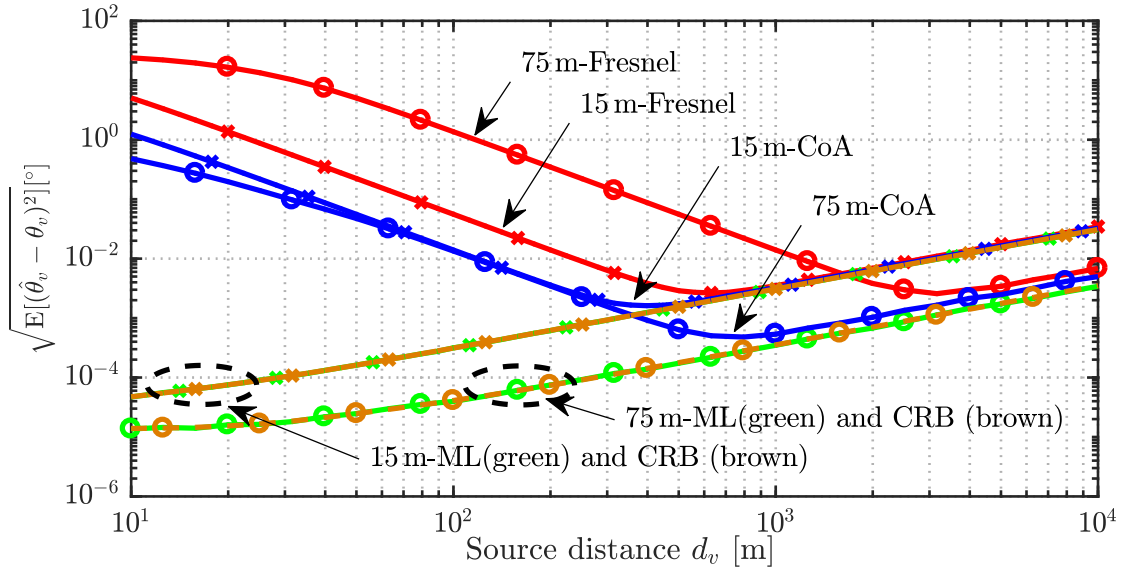

(a) *AoA estimation error versus source distance*

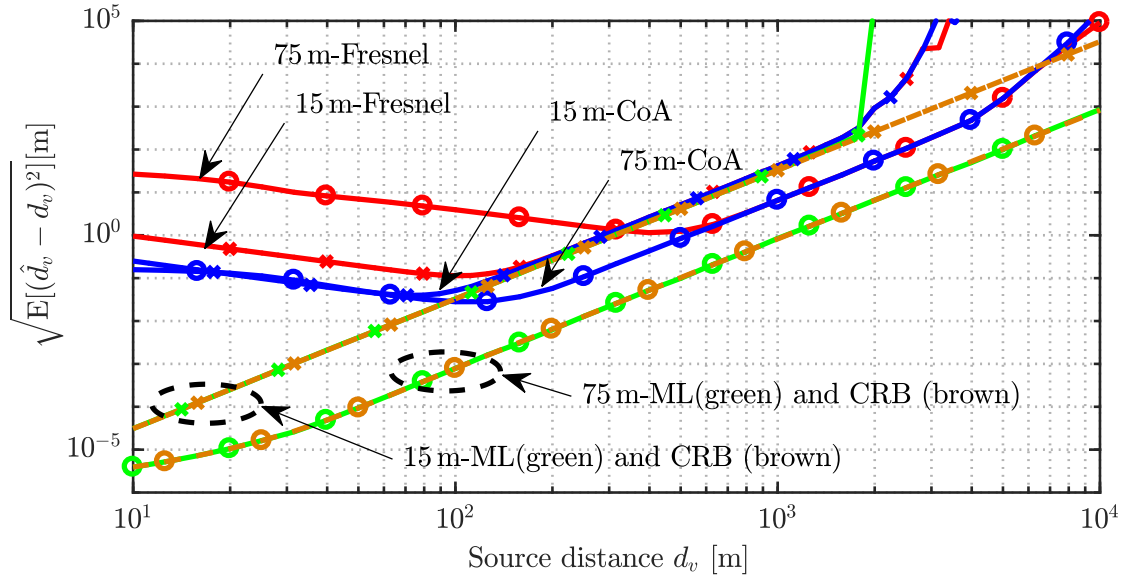

(b) *Distance estimation error versus source distance*

Figure 3.17. *Source localization performance against source distance, of two ULAs along x-axis with aperture lengths $D = 15\,\mathrm{m}$ and $75\,\mathrm{m}$, $f_s = 20\,\mathrm{MHz}$ and an element spacing of $\lambda/4$.*

Next we compare the proposed low complexity CoA based source localization algorithm to a state of the art near field source localization algorithm with the ULAs, since most low complexity near field source localization algorithms apply the Fresnel approximation on ULAs, [101], [103]. To remove the outliers occurring at small θ_v, the RMSEs are calculated only for AoAs range between $30\,^\circ$ and $90\,^\circ$. Figure 3.17 shows the performance of the proposed CoA based algorithm, the Fresnel based approach in [103], the CoA initialized ML algorithm and the CRBs for different d_s. The Fresnel based approach has a larger model error for larger arrays. In contrast, the CoA source localization only experiences model mismatch within individual groups, independently of the total aperture. Therefore, the proposed CoA based algorithm outperforms the Fresnel based approach for shorter distances and larger arrays. At larger distances, the model error is no longer decisive, and all algorithms perform similarly along the CRBs. For the 15 m ULA at small θ_v and $d_v > 2000\,\mathrm{m}$, the ratio $d_v/D_\perp$ is so small, that none of the three algorithms is able to effectively estimate the distance. As a final result, for the 75 m sized ULA, the distance estimate can be achieved with a sub-meter RMSE by the proposed CoA based algorithm up to 600 m. The ML algorithm initialized with the proposed CoA based algorithm extends the applicable distance to 1000 m for the 75 m sized ULA.

3.6.3 Joint Self- and Source Localization

3.6.3.1 Mutual Improvement of Self- and Source Localization

In this section, we show that the swarm self- and source localization are mutually improved by joint estimation. Similar as the setup in Section 3.6.2.1, a swarm of 50 agents are randomly deployed in a dish area with a radius of $R = 100\,\mathrm{m}$. Different number of RF sources from 0 to 27 are uniformly located on rings around the center of the swarm with distances d_v from 10 m to 1000 m. The swarm coordinate system constrained on group motions $\mathbb{C}$ is used for describing the positions of agents and used as the default coordinate system. The corresponding polar coordinate system $\mathbb{P}$ is applied to describe the source distance and AoA separately. The RF signals propagating on A2A links use a carrier frequency of $f_c = 5.2\,\mathrm{GHz}$ and a bandwidth of $B_c = 37\,\mathrm{MHz}$, whereas the ones on S2A links use a carrier frequency of $f_s = 20\,\mathrm{MHz}$ and a bandwidth of $B_s = 1\,\mathrm{KHz}$. For both RF types, a transmit power of 0 dBm, a free-space pathloss model and an additional noise figure of 15 dB are assumed. All the agents and sources are neither carrier nor symbol synchronized. The symbol delays of the A2A and S2A links and the carrier phases of the S2A links are exploited for joint swarm self- and source localization. We also consider one case where agents' locations

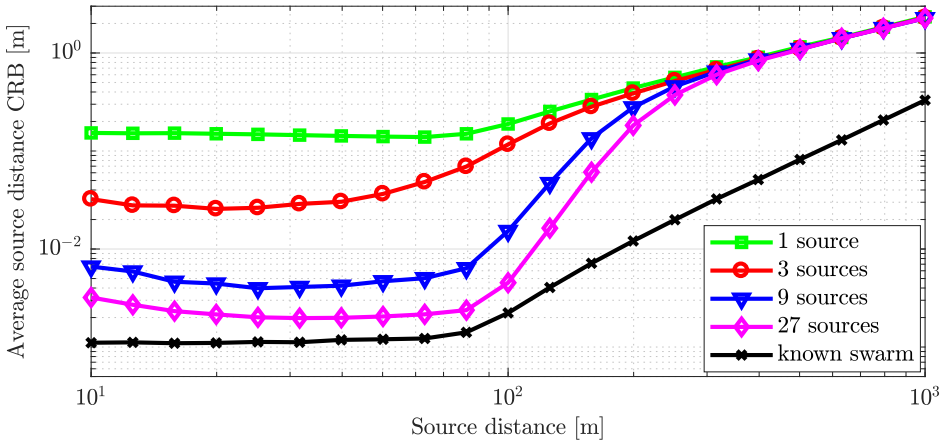

(a) *Source distance estimation CRBs.*

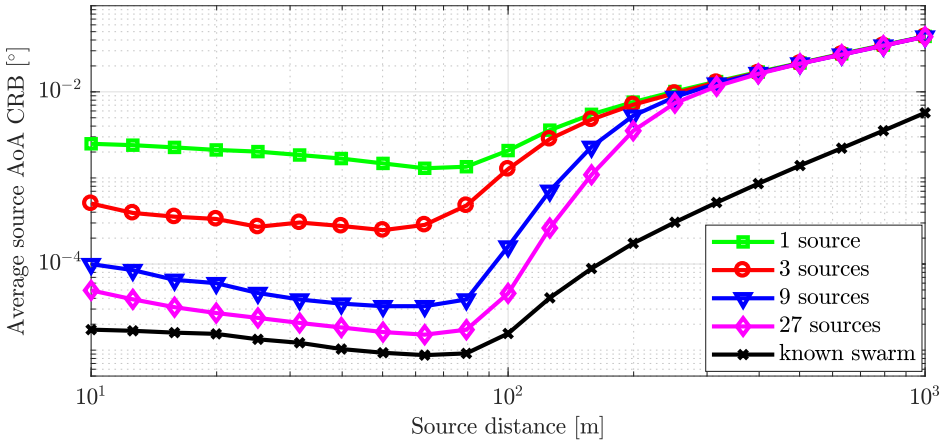

(b) *Source AoA estimation CRBs.*

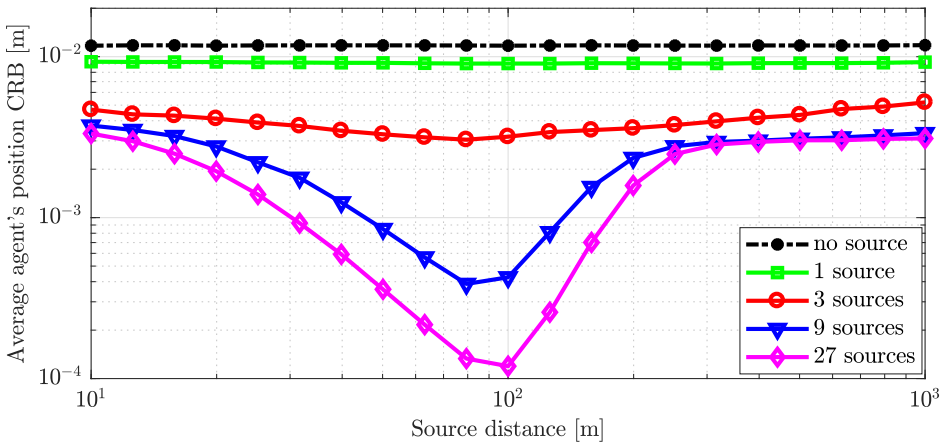

(c) *Swarm self-localization CRBs.*

Figure 3.18. *CRBs of the joint swarm self- and source localization with A2A links:* $f_c = 5.2\,\mathrm{GHz}$, $B_c = 37\,\mathrm{MHz}$, *and S2A links:* $f_s = 20\,\mathrm{MHz}$, $B_s = 1\,\mathrm{KHz}$.

and clock offsets are perfectly known as benchmarks. The perfect agents' knowledge assumption is valid when the number of targets approaches infinity, or the swarm is precisely localized with other measurements, e.g. from radar, optical sensors or the phased array for A2A signal.

The partial derivatives required for the CRB calculation with a mixture of swarm Cartesian coordinate system $\mathbb{C}$ and the swarm polar coordinate system $\mathbb{P}$ are listed in Appendix Section C.4. The square root of CRBs of the source's distance and AoA estimation are plotted in Figure 3.18a and Figure 3.18b, respectively. The root mean CRBs of the swarm self-localization, i.e. the position error bound averaged over all agents, are illustrated in Figure 3.18c. 1000 Monte Carlo runs have been conducted for each set of parameters.

First of all, both self- and source localization performances significantly improved by adding more sources. Especially when the sources are close to the swarm, the improvements approach to the benchmark for a larger number of sources.

Second, the CRBs of sources' distance estimates are stable inside the swarm, and increasing while sources are moving to the outside of the the swarm.

Third, the CRBs of sources' AoA estimates are decreasing inside the swarm, due to the higher angular sensitivity around the coordinate system's origin, and increasing while sources are moving to the outside of the the swarm.

Last but not least, the sources improve the swarm self-localization CRBs more significantly when moving towards the border of swarm from inside, which is due to a desirable sources' geometry. The improvements decreases when the sources move away from the swarm, which is due to the increasing uncertainty in source localization.

3.6.3.2 Localization in Mars Swarm Exploration Mission

As the last numerical analysis of this chapter, we demonstrate the swarm joint self- and source localization with the case study of the Mars swarm mission illustrated in Figure 1.2.

Three beacons are deployed near the mission base, with known positions in the global coordinate system $\mathbb{G}$ and clock offsets. A gas source and two RF sources are located remotely from the mission base. All sources' positions and nuisance parameters are considered unknown. The unknown clock and carrier phase offsets of RF sources are set to zero. Both types of RF signals employ the same system parameters as in Section 3.6.3.1. In addition, measurement coverage is considered for the A2A symbol delay observations and the S2A and B2A carrier phase observations, similarly as in [85] in order to reflect issues like low SNR or distortions from propagation in practice. The observation uncertainty increases rapidly and smoothly when the link distance

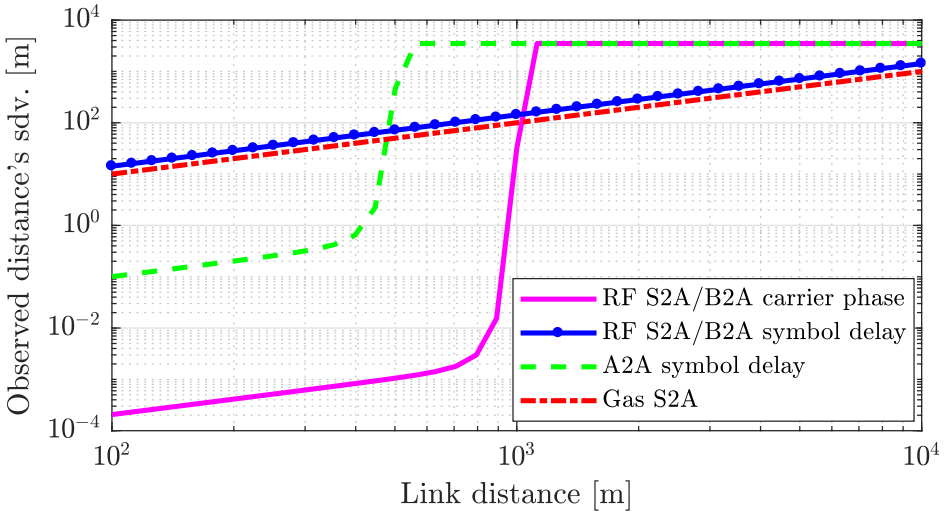

Figure 3.19. *The standard deviations of the observed distance according to the signal models under investigation.*

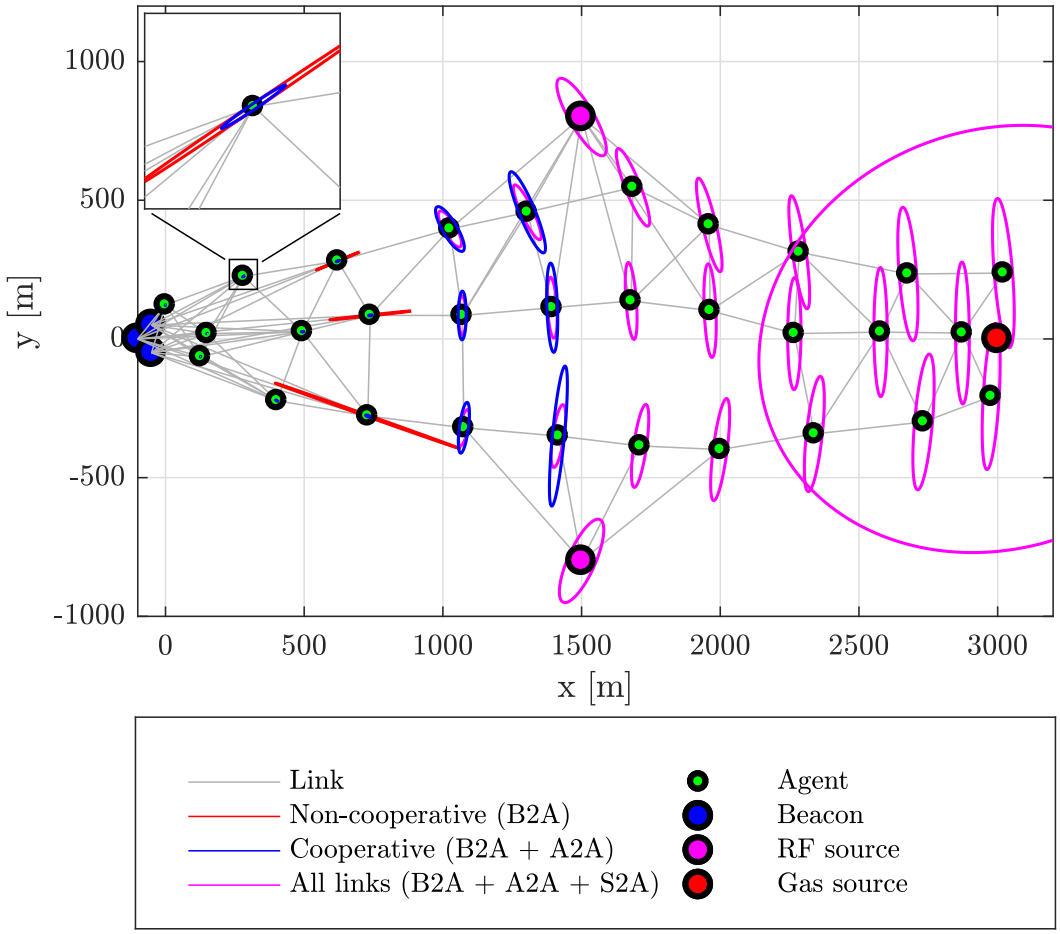

Figure 3.20. *Swarm exploration scenario with two RF sources and one gas source and 30 agents. Links are indicated in light grey. Colored ellipses represent the* 50σ *snapshot position CRB for agents (very large ellipses are omitted) and sources, respectively. The cases of non-cooperative (only B2A links), cooperative (B2A + A2A links) and all links are shown.*

exceeds the measurement coverage, which can be modeled with either ZZB introduced in Section 3.3.3.3 or empirical data as in Section 3.6.1.4. Agents can also measure the gas concentration level at their positions. The scaling and exponent parameters introduced in (2.29) of the gas source are set to $a_{\mathrm{g}} = 1$ and $b_{\mathrm{g}} = 9.2103$, respectively. The standard deviations of the observed distance from the signal models are plotted in (2.29). From these models, modified RII can be calculated to derive the modified joint localization CRB, accounting for low SNR of A2A links, and propagation effects on carrier phase of B2A and S2A links. A swarm of 50 agents assembles in a predefined formation connecting the beacons and the gas source. The modified position CRBs of agents and sources considering different observations are shown in Figure 3.20. The beacons, agents, RF sources and a gas source are illustrated by the blue, green, magenta and red dot(s), respectively. The effective RF measurement links, i.e. the links where the observed distance standard deviations are smaller than 10 m, are indicated with gray lines. The ellipses in red, blue and magenta are the 50 σ CRB ellipses for non-cooperative (exploiting B2A links only), cooperative (exploiting B2A + A2A links) and whole extended network localization. The very large ellipses are omitted for better visualization.

Firstly, for non-cooperative localization, the red CRB ellipses at the left part of the figure quickly expand in the B2A link direction when an agent is further away from the beacons. This is due to the clock offset between beacons and agents, and coincides with the discovery in (3.79). Hence, the distance uncertainty dominates the position error when an offset type nuisance parameter is unknown.

Secondly, by A2A cooperative links, the agent position accuracy improves significantly, which is illustrated by the blue ellipses in the middle of the figure. The uncertainty in this case is mainly on the perpendicular direction of the A2A link. That is because the A2A links are symmetric dual links, where the clock offsets are compensated out. Hence, an A2A link $\mathbb{l}_{uv}$ is equivalent to a synchronized ToA link.

Last but not least, a further improvement can be obtained by jointly estimating source positions with the whole extended network, which is visible at the right part of the figure.

Chapter 4

Decentralized Swarm Localization Algorithms

After investigating theoretical aspects of swarm localization, in this chapter we focus on practical aspects. More precisely, based on the theoretical analysis from Chapter 3, we look at the design of decentralized localization algorithms suitable for swarms.

We propose a decentralized swarm self-localization algorithm dubbed DiPNet. A node's position is directly inferred from the received signals, incorporating position uncertainty of neighboring nodes. The propagation effects, namely multipath and NLOS propagation, on DiPNet become insignificant for dense networks, due to the multi-link collective PHY layer signal processing. DiPNet achieves a near-optimal performance with low complexity, which is particularly attractive for realtime dense-network localization. In this chapter, we only focus on swarm self-localization, i.e. $\mathcal{V} = \mathcal{X} = \mathcal{A}$. The direct localization concept can be straightforwardly extended to source localization as well.

A brief survey on network localization is provided in Section 4.1, which can be generalized to a wide range of specific applications including swarm self-localization. As in particular to swarm localization introduced in Section 1.2.1, we are interested in decentralized localization algorithms suitable for large-scale dense networks, with high reliability and low complexity. The DiPNet proposed in Section 4.3 is designed to explicitly meet these requirements. The DiPNet adapts the decentralized Bayesian network localization introduced in Section 4.2, and directly considers the received signals as measurements, instead of taking the range measurements as in traditional two step localization algorithms. DiPNet is proved in Section 4.4 to be more robust against erroneous distance information from unpredictable propagation effects such as multipath and NLOS condition. In Section 4.5, the performances of DiPNet are evaluated with both simulations and experiments.

4.1 Survey on Network Localization

Intensive research has been conducted to network localization. A comprehensive overview of network localization algorithms is provided in [32], and further completed by [33]. We briefly review the algorithm classifications according to different perspectives.

1) Place of Position Estimation

   An algorithm is considered as centralized if the positions of all agents are calculated at a fusion center [108]. Whereas if each agent calculates its own position based on local observations, the algorithm is referred to as decentralized [109, 32].

2) Model of Measurements

   Algorithms can be classified by the extractable position-related signal features, for example, signal power, carrier phase and symbol delay [110, 111]. They can also be classified according to the measurement abstraction level, whether to utilize the received waveform directly as measurement, for example in direct position estimation (DPE) [112], or an abstracted single value measurement with an associated likelihood function. For the latter case, algorithms can be further classified by the measurements extracted from the position-related signal features, such as range, range difference, or AoA [111, 29].

3) Model of Unknowns

   Non-Bayesian algorithms treat unknowns as deterministic variables. An ML approach can be implemented by the least-square (LS) Gauss-Newton algorithm [111], which may suffer from local minima. Alternatively, a convex-relaxation based approach such as semi-definite programming (SDP) [113] and alternating direction method of multipliers (ADMM) [108] can be applied to reduce the effect of local minima. Bayesian algorithms treat unknowns as random variables. The main task of the algorithm is to infer the posterior pdf of the random variables [114]. In general, calculating the exact posterior pdf demands high dimensional marginalization, which makes it impracticable for dense networks. KF-based approaches approximate the system with linear transition and measurement models distorted by Gaussian noise, and solve it with relatively low complexity. Message passing (MP) is a popular category of Bayesian algorithms, where agents infer their posterior pdfs by only marginalizing over the inferences of their neighbors, in a recursive fashion. MP is adaptable to different system models with moderate complexity [110, 32].

4) Multi-Link Fusion

Low complexity algorithms such as LS treat all links identically. Measurement quality can be quantified through some characteristics of the signal, such as SNR, channel impulse response (CIR), propagation condition, etc., and used in for example WLS [111]. For decentralized algorithms, neighbor's position uncertainty can be taken into account in a heuristic way [115], or systematically by the marginalization in MP. The marginalization can be realized by expectation maximization (EM), numerical integrals such as Gaussian quadrature integrals, also known as sigma points [116], or Monte Carlo (MC) integration such as used in DPF [117]. In [28] the impact of neighbor's position uncertainty on agent localization is quantified by the equivalent ranging information intensity (ERII). The ERII can be exploited for example by projecting the neighbor's position uncertainty onto the distance measurement [51]. This projection is also a systematic approach, which has lower complexity compared to MP.

A more exhaustive literature survey on network localization can be found in [32, 33]. In this work, we address decentralized network localization using a Bayesian framework, where position information is extracted from the symbol delays. More precisely, we focus on utilizing the received waveform directly as measurement for localization, with a low complexity systematic multi-link fusion scheme. Synchronization among agents are assumed as in Section 3.3, i.e. only the positions of agents $\mathbf{p}_{\mathcal{A}}$ are included in the states. The concept of decentralized direct localization can be extended to other scenarios with little modifications.

4.2 Decentralized Bayesian Self-Localization

In Bayesian framework, the states, in this chapter the positions of agents $\mathbf{p}_{\mathcal{A}}$, are modeled as random variables. We use a subscript 0 to distinguish the physical quantity of true positions, e.g. $\mathbf{p}_{\mathcal{A},0}$ and $\mathbf{p}_{u,0}$ with $\mathbb{o}_u \in \mathcal{A}$, and the corresponding mathematically modeled positions, e.g. $\mathbf{p}_{\mathcal{A}}$ and $\mathbf{p}_u$, as random variables.

Bayesian tracking formulated in (2.8) is a common approach to incorporate *a priori* density $p(\mathbf{p}_{\mathcal{A}}^{(+)}|\mathbf{z}_{\mathcal{A}}^{(1:-)})$ and likelihood of the measurements $p(\mathbf{z}_{\mathcal{A}}^{(+)}|\mathbf{p}_{\mathcal{A}}^{(+)})$. The *a priori* density $p(\mathbf{p}_{\mathcal{A}}^{(+)}|\mathbf{z}_{\mathcal{A}}^{(1:-)})$ can be inferred from marginalizing the product of the previous *a posteriori* filtered density $p(\mathbf{p}_{\mathcal{A}}^{(-)}|\mathbf{z}_{\mathcal{A}}^{(1:-)})$ and the state transition $p(\mathbf{p}_{\mathcal{A}}^{(+)}|\mathbf{p}_{\mathcal{A}}^{(-)})$ over $\mathbf{p}_{\mathcal{A}}^{(-)}$. In this section, we focus on obtaining the *a posteriori* filtered density from the measurement likelihood and an already inferred *a priori* density. Thus, we use the compact expression of the Bayesian framework in (2.7) and omit the superscript (+)

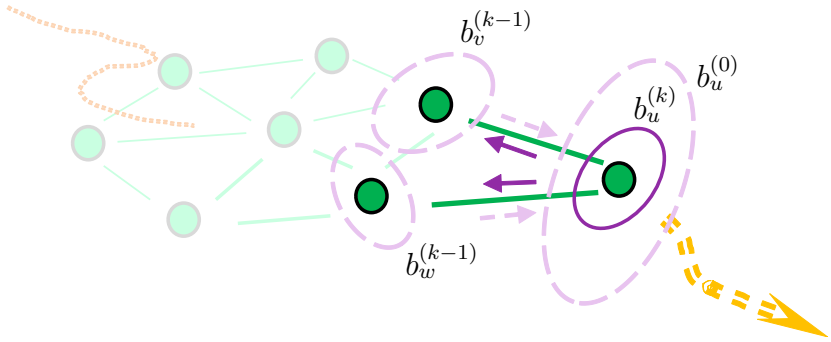

Figure 4.1. *The k^{th} iteration of the belief update of agent $\mathbb{a}_u$: agent $\mathbb{a}_u$ combines its initial belief, the beliefs of neighbors $\mathbb{a}_v$ and $\mathbb{a}_w$ at iteration $k-1$, all illustrated with light dashed ellipses, with the measurements obtained from the A2A links shown in green, update its belief to $b_u^{(k)}$, and passes it to its neighbors.*

for simplicity, i.e.

$$p(\mathbf{p}_{\mathcal{A}}|\mathbf{z}_{\mathcal{A}}) \propto p(\mathbf{p}_{\mathcal{A}})p(\mathbf{z}_{\mathcal{A}}|\mathbf{p}_{\mathcal{A}}). \tag{4.1}$$

For a dense network, a decentralized localization algorithm is often advantageous, where an agent $\mathbb{a}_u \in \mathcal{A}$ estimates its own position using the marginalized *a posteriori* pdf $p(\mathbf{p}_u|\mathbf{z}_{\mathcal{A}})$

$$p(\mathbf{p}_u|\mathbf{z}_{\mathcal{A}}) \propto p(\mathbf{p}_u) \int p(\mathbf{p}_{\mathcal{A}/\mathbb{a}_u}|\mathbf{p}_u) \prod_{\forall \mathbb{e}_{vw} \in \mathcal{E}_0} p(\mathbf{z}_{vw}|\mathbf{p}_v, \mathbf{p}_w) \, \mathrm{d}\mathbf{p}_{\mathcal{A}/\mathbb{a}_u}. \tag{4.2}$$

Due to cooperation among agents, a $2(|\mathcal{A}|-1)$ dimensional integral is needed for an exact decentralized Bayesian estimator of $\mathbf{p}_u$, which makes it impracticable. A popular approach to reduce the complexity of marginalization is belief propagation (BP), for example the sum-product algorithm over a wireless network (SPAWN) algorithm [32]. In SPAWN, an agent $\mathbb{a}_u$ only considers a local framework $\mathcal{F}_u = (\mathcal{G}_u, \mathbf{p}_{\tilde{\mathcal{A}}_u})$ with an agent set $\tilde{\mathcal{A}}_u = \mathcal{A}_u \cup \{\mathbb{a}_u\}$, including its neighbors and itself, and the underlying star subgraph $\mathcal{G}_u = (\tilde{\mathcal{A}}_u, \mathcal{E}_u)$, for example illustrated in Figure 4.1. The edge set $\mathcal{E}_u$ contains all the links between $\mathbb{a}_u$ and its neighbors. The marginalized *a posteriori* pdf $p(\mathbf{p}_u|\mathbf{z}_{\mathcal{A}})$ is approximated by the *belief* $b_u^{(K)}$ of agent $\mathbb{a}_u$, which is updated by exchanging belief with neighbors for K iterations

$$b_u^{(k)} = b_u^{(0)} \prod_{\forall \mathbb{a}_v \in \mathcal{A}_u} \int b_v^{(k-1)} p(\mathbf{z}_{uv}|\mathbf{p}_u, \mathbf{p}_v) \, \mathrm{d}\mathbf{p}_v \quad k = 1, \cdots, K. \tag{4.3}$$

The k^{th} iteration of the belief update of agent $\mathbb{a}_u$ is shown in Figure 4.1.

The SPAWN reduces the complexity to $|\mathcal{A}_u|$ integrals with four dimensions for each

iteration. The marginalization in (4.3) can be realized by Monte Carlo integration as in non-parametric belief propagation (NBP) [109], by numerical integration for example in cubature belief propagation (CBP) [116, 118], or analytically with parametric belief propagation (PBP) for special distributions [87]. For direct localization, the transformation from received signal waveform measurements to position is highly non-linear, which leads to non-Gaussian beliefs. The commonly used Gaussian PBP is not suitable. We also implemented a CBP method with Gaussian-Laguerre integration, which outperforms a Monte Carlo integration based NBP method with same complexity, in the sense of the Kullback–Leibler divergence (KLD). However, there is no significant evidence of improvement in the sense of localization performance. It is due to the fact that the belief directly taking waveform as measurement is steep and multi-modal, which cannot be efficiently represented by the Gaussian-Laguerre integration. Therefore, we omit the investigation of CBP, and use NBP and PBP methods as state of the art algorithms as benchmarks.

The proposed DiPNet is a variant of BP, where non-parametric belief is updated locally and only the first two moments of the belief $b_u^{(k)}$ are broadcasted to the neighbors.

4.3 DiPNet: A Direct Swarm Self-Localization Algorithm

4.3.1 Equivalent Measurement Likelihood (EL)

To further reduce the complexity, we define an equivalent measurement likelihood (EL) based on FI theory, which will be used later for the proposed DiPNet algorithm. The joint pdf $q(\mathbf{p}_{\tilde{\mathcal{A}}_u}, \mathbf{z}_{\mathcal{E}_u})$ of the simplified graph $\mathcal{G}_u$ can be written as

$$q(\mathbf{p}_{\tilde{\mathcal{A}}_u}, \mathbf{z}_{\mathcal{E}_u}) = b_u^{(0)} \prod_{\mathbb{a}_v \in \mathcal{V}_u} b_v^{(k-1)} p(\mathbf{z}_{uv} \mid \mathbf{p}_u, \mathbf{p}_v). \tag{4.4}$$

The BIM $\mathbf{J}_{\tilde{\mathcal{A}}_u}$ of $\mathbf{p}_{\tilde{\mathcal{A}}_u}$ is expressed as

$$\mathbf{J}_{\tilde{\mathcal{A}}_u} = \tilde{\mathbf{J}}_{\tilde{\mathcal{A}}_u} + \mathbf{E}_{\mathbf{p}_{\tilde{\mathcal{A}}_u}, \mathbf{z}_{\mathcal{E}_u}} \left[\triangle_{\mathbf{p}_{\tilde{\mathcal{A}}_u}}^{\mathbf{p}_{\tilde{\mathcal{A}}_u}} \ln p(\mathbf{z}_{\mathcal{E}_u} | \mathbf{p}_{\tilde{\mathcal{A}}_u}) \right], \tag{4.5}$$

where $\tilde{\mathbf{J}}_{\tilde{\mathcal{A}}_u} = \mathrm{diag}\{\tilde{\mathbf{J}}_u^{(0)}, \tilde{\mathbf{J}}_v^{(k-1)} : \forall \mathbb{a}_v \in \mathcal{A}_u\}$, is the *a priori* position information of $\mathbf{p}_{\tilde{\mathcal{A}}_u}$, with individual *a priori* information $\tilde{\mathbf{J}}_w^{(k)}$ defined as

$$\tilde{\mathbf{J}}_w^{(k)} \triangleq -\mathbb{E}_{\mathbf{p}_w} \left[\triangle_{\mathbf{p}_w}^{\mathbf{p}_w} \ln b_w^{(k)} \right]. \tag{4.6}$$

The equivalent Bayesian information matrix (EBIM) $\mathbf{J}_u$ of $\mathbf{p}_u$, derived from the theory of Schur's complement [31], determines the best achievable variance for the *a posteriori* estimate $\hat{\mathbf{p}}_u$. Assuming the beliefs $b_w^{(k)}$ are concentrated at their *a priori* means $\bar{\mathbf{p}}_w = \mathbb{E}_{\mathbf{p}_w}[\mathbf{p}_w]$, the EBIM is approximated as

$$\mathbf{J}_u = \tilde{\mathbf{J}}_u^{(0)} + \sum_{\mathbb{o}_v \in \mathcal{A}_u} \tilde{\iota}_{d_{uv}} \bar{\mathbf{e}}_{uv} \bar{\mathbf{e}}_{uv}^T, \tag{4.7}$$

where $\tilde{\iota}_{d_{uv}}$ is the ERII defined as

$$\tilde{\iota}_{d_{uv}} = \frac{\bar{\iota}_{d_{uv}}}{1 + \bar{\iota}_{d_{uv}} \sigma^2_{v \mapsto uv}}. \tag{4.8}$$

The projection vector $\bar{\mathbf{e}}_{uv}$ and the projected variance $\sigma^2_{v \mapsto uv}$ are defined as

$$\bar{\mathbf{e}}_{uv} \triangleq \frac{(\bar{\mathbf{p}}_u - \bar{\mathbf{p}}_v)}{\|\bar{\mathbf{p}}_u - \bar{\mathbf{p}}_v\|}, \quad \sigma^2_{v \mapsto uv} \triangleq \bar{\mathbf{e}}_{uv}^T (\tilde{\mathbf{J}}_v^{(k-1)})^{-1} \bar{\mathbf{e}}_{uv}, \tag{4.9}$$

which projects the position uncertainty of $\mathbb{o}_v$ onto the line connecting $\mathbb{o}_u$ and $\mathbb{o}_v$. The marginalized RII $\bar{\iota}_{d_{uv}}$ is defined as

$$\bar{\iota}_{d_{uv}} \triangleq -\mathbb{E}_{\mathbf{p}_u, \mathbf{p}_v} \Big[\underbrace{\mathbb{E}_{\mathbf{z}_{uv} | \mathbf{p}_u, \mathbf{p}_v} \Big[\frac{\mathrm{d}^2 \ln p(\mathbf{z}_{uv} | \mathbf{p}_u - \mathbf{p}_v)}{\mathrm{d} d_{uv}^2} \Big]}_{\triangleq \iota_{d_{uv}}} \Big], \tag{4.10}$$

where $d_{uv} = \|\mathbf{p}_u - \mathbf{p}_v\|$. The derivation of (4.7) is detailed in Appendix C.5. A similar result has been reported in [28]. The EBIM in (4.7) has a similar expression as the position information $\mathbf{J}_{(u,u)}$ assuming the neighbor's position is perfectly known:

$$\mathbf{J}_{(u,u)} = \tilde{\mathbf{J}}_u^{(0)} + \mathbb{E}_{\mathbf{p}_{\tilde{\mathcal{A}}_u}} \left[\sum_{v \in \mathcal{A}_u} \iota_{d_{uv}} \mathbf{e}_{uv} \mathbf{e}_{uv}^T \right], \tag{4.11}$$

where $\mathbf{e}_{uv} \triangleq \nabla_{\mathbf{p}_u} d_{uv}$ is the unit vector pointing from $\mathbb{o}_v$ to $\mathbb{o}_u$. Alternatively, equation (4.8) can be expressed by the equivalent ranging uncertainty

$$\tilde{\iota}_{d_{uv}}^{-1} = \bar{\iota}_{d_{uv}}^{-1} + \sigma^2_{v \mapsto uv}. \tag{4.12}$$

Hence the neighbor's position uncertainty can be additively aggregated to the ranging uncertainty. We utilize these observations to define an EL, which can be applied to further reduce the complexity of network localization.

Definition 2 (Equivalent Measurement Likelihood)**.** *An equivalent measurement like-*

lihood (EL) $\tilde{p}(\mathbf{z}_{uv} \mid \mathbf{p}_u, \mathbf{p}_v)$ *is a pdf of* $\mathbf{z}_{uv}$ *given on* $\mathbf{p}_u$ *and* $\mathbf{p}_v$*, such that*

$$-\mathbb{E}_{\mathbf{z}_{uv}|\mathbf{p}_u,\mathbf{p}_v}\left[\frac{\mathrm{d}^2 \ln \tilde{p}(\mathbf{z}_{uv}|\mathbf{p}_u,\mathbf{p}_v)}{\mathrm{d}d_{uv}^2}\right] = \tilde{\iota}_{d_{uv}}. \tag{4.13}$$

The system can be further simplified to non-cooperative localization, where neighboring agents are considered as virtual beacons. Hence, the virtual measurement likelihood function is modeled with the EL and the neighbor's virtual *a priori* pdf is modeled as a Dirac function at point $\hat{\mathbf{p}}_v^{(k-1)}$. The EBIM of the simplified system equals to the original $\mathbf{J}_u$. Low-complexity distributed network localization algorithms can be designed as follows. Agent $\mathbb{o}_u$ receives the first two moments of its neighbor's non-parametric belief, namely the position estimate $\hat{\mathbf{p}}_v^{(k-1)}$ and the covariance estimate $\mathrm{cov}[\hat{\mathbf{p}}_v^{(k-1)}]$, to approximate ERII in (4.8). Instead of the sum-product algorithm in (4.3), the belief can be updated by the simplified model using the EL

$$b_u^{(k)} \approx b_u^{(0)} \prod_{\forall \mathbb{o}_v \in \mathcal{A}_u} \tilde{p}\Big(\mathbf{z}_{uv}|\mathbf{p}_u, \hat{\mathbf{p}}_v^{(k-1)}\Big). \tag{4.14}$$

The EL-based algorithm further reduces the complexity to one 2-dimensional integral per algorithmic iteration, which enables distributed Bayesian network localization in realtime. The concept of EL can be generally applied to any distance-based measurement models. For example in [51], it is used in two-step network localization with Gaussian ranging models by exploiting the equivalent ranging variances (ERVs). In the next section, we introduce the DiPNet algorithm, where an EL is adapted for direct localization from the OFDM waveform.

4.3.2 Direct Self-Localization with RF Signal

In a realistic scenario, the signal is not only distorted by sensor noise, but also affected by the propagation channel. For LOS scenarios, the signal propagates along the LOS path and some additional paths, referred to as MPCs. Whereas for NLOS scenarios, the signal is solely received via the MPCs. A generic path component l, between $\mathbb{o}_u$ and $\mathbb{o}_v$, is defined by its complex amplitude $\alpha_{uv,l} = A_{uv,l}e^{\jmath\phi_{uv,l}}$, with a magnitude $A_{uv,l}$ and a phase $\phi_{uv,l}$ in radians, and the total propagation delay $\tau_{uv,l} = \tau_{uv,0} + \delta_{uv,l} + b_{uv}$, which includes the LOS delay $\tau_{uv,0} = d_{uv,0}$, the NLOS delay b_{uv} and the path's delay additional to the potential LOS path δ_l, all in meters. The NLOS delay b_{uv} is positive for NLOS scenarios and zero for LOS scenarios. The LOS path is denoted with index 0, i.e. $\delta_{uv,0} = 0$. NLOS scenarios are included by setting $A_{uv,0} = 0$. The continuous received signal can be generally written as the superposition of the potential LOS path and L MPCs distorted by AWGN as introduced in (2.23). The received sampled signal

can be generally written as

$$r_{uv}(iT_{\text{sa}}) = \sum_{l=0}^{L} \alpha_{uv,l} s_{uv,l}(iT_{\text{sa}} - \tau_{uv,l}/c) + \epsilon_{uv}(iT_{\text{sa}}), \tag{4.15}$$

with a sampling period T_{sa} and $\forall i = 1, \cdots, N$. The (delayed) signal samples are represented in vector forms, for example, $\mathbf{r} \triangleq \text{vec}\{r(T_{\text{sa}}), \cdots, r(NT_{\text{sa}})\}$ and $\mathbf{s}(\tau) \triangleq \text{vec}\{s(T_{\text{sa}} - \tau), \cdots, s(NT_{\text{sa}} - \tau)\}$. The clock offsets between nodes may bias the delay-based distance information. However, it can be eliminated with multi-way ranging. For the AWGN case, the two-way ranging with an amplify-and-forward scheme [58] is equivalent to the synchronized one-way ranging [82]. For the multipath scenario, it is analogous to the synchronized one-way ranging, with a channel equivalent to the convolution of the forward and backward channels.

The DiPNet algorithm is derived based on a one-path received signal assumption in LOS condition, i.e. $\|\alpha_{uv,0}\| \neq 0$ and $L = 0$. The assumed received signal is denoted as $\mathbf{r}_{uv,0}$, in order to be distinguishable from the true received signal $\mathbf{r}_{uv}$. The one-path signal model enables low complexity position estimation, at the cost of sub-optimality due to model mismatch. In two step approaches, this mismatch may lead to erroneous position estimates. In Section 4.4 it is discussed that the impacts of the model mismatch on the proposed DiPNet algorithm become insignificant in dense networks, as a result of collective PHY processing. The one-path model can be described by the likelihood function $p(\mathbf{r}_{uv,0}|\mathbf{p}_u, \mathbf{p}_v, \alpha_{uv,0})$. The complex amplitude $\alpha_{uv,0}$ is irrelevant to position estimate and estimated separately as

$$\hat{\alpha}_{uv,0} = \frac{\mathbf{s}_{uv}(\|\mathbf{p}_u - \mathbf{p}_v\|/c)^H \mathbf{r}_{uv,0}}{\|\mathbf{s}_{uv}(\|\mathbf{p}_u - \mathbf{p}_v\|/c)\|^2}, \tag{4.16}$$

with a constant denominator expressed as $\|\mathbf{s}_{uv}\|^2$. According to the theory of separable variables [119], the ranging likelihood function can be expressed by inserting the phase estimate into the original likelihood function as

$$p\left(\mathbf{r}_{uv,0}|\mathbf{p}_u, \mathbf{p}_v\right) \propto \exp\left(\frac{\|f(\|\mathbf{p}_u - \mathbf{p}_v\|)\|^2}{N_0\|\mathbf{s}_{uv}\|^2}\right). \tag{4.17}$$

The cross-correlation function $f(\|\mathbf{p}_u - \mathbf{p}_v\|)$ is written as

$$f(\|\mathbf{p}_u - \mathbf{p}_v\|) = \mathbf{r}_{uv,0}^H \, \mathbf{s}_{uv}(\|\mathbf{p}_u - \mathbf{p}_v\|/c). \tag{4.18}$$

The logarithmic likelihood function is proportional to the squared cross-correlation function (SCF) $\|f(\|\mathbf{p}_u - \mathbf{p}_v\|)\|^2$, which is asymptotically maximized at $\|\mathbf{p}_u - \mathbf{p}_v\| =$

$d_{uv,0}$. We will use these properties in Section 4.4 to evaluate the performance of DiPNet in multipath propagation conditions. The ranging uncertainty $\bar{\iota}_{d_{uv}}^{-1}$ in (4.12), i.e. the ranging CRB denoted by CRB_{uv}, is derived as in [51] with the one-path OFDM signal model as

$$\bar{\iota}_{d_{uv}}^{-1} = \mathrm{CRB}_{uv} = \frac{c^2 N_0}{2\|\hat{\alpha}_{uv,0}\|^2 \omega_{\mathrm{sc}}^2 \sum_{n=-\frac{N-1}{2}}^{\frac{N-1}{2}} \|S_n\|^2 n^2}. \tag{4.19}$$

A choice of EL for DiPNet is to aggregate the neighbor's position uncertainty as noise, i.e.

$$\tilde{p}\left(\mathbf{r}_{uv,0} \mid \mathbf{p}_u, \hat{\mathbf{p}}_v^{(k-1)}\right) \propto \exp\left(\frac{\|f(\|\mathbf{p}_u - \hat{\mathbf{p}}_v^{(k-1)}\|)\|^2}{\tilde{\sigma}_{uv}^2 \|\mathbf{s}_{uv}\|^2}\right), \tag{4.20}$$

where $\tilde{\sigma}_{uv}^2$ is the equivalent noise variance (ENV). The corresponding equivalent ranging uncertainty $\tilde{\iota}_{d_{uv}}^{-1}$ has an expression similar to $\bar{\iota}_{d_{uv}}^{-1}$ in (4.19), by replacing N_0 with $\tilde{\sigma}_{uv}^2$. The ENV is derived by inserting $\bar{\iota}_{d_{uv}}^{-1}$ and $\tilde{\iota}_{d_{uv}}^{-1}$ into (4.12) as

$$\tilde{\sigma}_{uv}^2 = N_0 + \frac{2\omega_{\mathrm{sc}}^2 \sigma_{v\mapsto uv}^2}{c^2} \|\hat{\alpha}_{uv,0}\|^2 \sum_{n=-\frac{N-1}{2}}^{\frac{N-1}{2}} \|S_n\|^2 n^2. \tag{4.21}$$

In the proposed DiPNet, the position belief is updated according to (4.14) and (4.20), by replacing the algorithmic signal model $\tilde{\mathbf{r}}_{uv}$ with the real received signal $\mathbf{r}_{uv}$. A DPF is implemented at each agent for non-parametric belief calculation [117], [51]. Q particles $\mathcal{Q}_u^{(0)} = \{Q_u^{(1,0)}, \cdots, Q_u^{(Q,0)}\}$ are drawn at $\mathbb{o}_u$ according to its *a priori* pdf. Each particle $Q_u^{(q,0)} = (\mathbf{p}_u^{(q,0)}, w_u^{(q,0)})$ is defined with its position $\mathbf{p}_u^{(q,0)}$ and a normalized weight $w_u^{(q,0)}$. The non-parametric belief at k^{th} iteration can be represented as

$$b_u^{(k)} \approx \sum_{q=1}^{Q} w_u^{(q,k)} \delta(\mathbf{p}_u - \mathbf{p}_u^{(q,0)}). \tag{4.22}$$

The weight is updated by (4.14) as

$$w_u^{(q,k)} = \frac{w_u^{(q,0)}}{C_u} \prod_{\mathbb{o}_v \in \mathcal{A}_u} \tilde{p}\left(\mathbf{r}_{uv} \mid \mathbf{p}_u^{(q,0)}, \hat{\mathbf{p}}_v^{(k-1)}\right), \tag{4.23}$$

where C_u is a normalization factor. With all building blocks been introduced, we can finally describe the overall DiPNet algorithm for an agent $\mathbb{o}_u$ in Algorithm 1.

For numerical stability, DiPNet is operated in logarithm domain with the Jacobian algorithm as described in [120].

Algorithm 1: DiPNet algorithm for agent $\mathbb{u}_u$

for *algorithmic iteration* $k = 0$ *to* K **do**
  if $k = 0$ **then**
    draw particles $\mathcal{Q}_u^{(0)}$ from *a priori* $p(\mathbf{p}_u)$
  else
    receive moments of $b_v^{(k-1)}, \forall \mathbb{u}_v \in \mathcal{A}_u$
    calculate ENV $\tilde{\sigma}_{uv}^2$ using (4.21), $\forall \mathbb{u}_v \in \mathcal{A}_u$
    for *particle* $q = 1$ *to* Q ***in parallel*** **do**
      update particle $w_u^{(q,k)}$ using (4.23) and (4.20)
    normalize particles $\mathcal{Q}_u^{(k)}$
  calculate and broadcast moments of $b_u^{(k)}$

Table 4.1. *Comparison of algorithms in the sense of complexity and transmitted messages*

Algorithm			**Complexity**	**Message number**
Position (per agent)	Exact		$Q^{\lvert\mathcal{A}\rvert}$	$Q\lvert\mathcal{A}\rvert$
	Sampled SPAWN		$Q^2\lvert\mathcal{A}_u\rvert K$	$Q\lvert\mathcal{A}_u\rvert K$
	EL		$Q\lvert\mathcal{A}_u\rvert K$	$\lvert\mathcal{A}_u\rvert K$
Signal (per link)	Ranging	Correlation	$K_\tau N$	
		SAGE	$K_s(L+1)K_\tau N$	
	β-interpolated IFFT		$\beta N \log \beta N$	
DiPNet (per agent)			$Q\lvert\mathcal{A}_u\rvert K + \lvert\mathcal{A}_u\rvert \beta N \log \beta N$	$\lvert\mathcal{A}_u\rvert K$

DiPNet only requests evaluating cross-correlation function $f(\|\mathbf{p}_u^{(q,0)} - \hat{\mathbf{p}}_v^{(k-1)}\|)$ at Q discrete points. An efficient interpolation technique, for example the inverse fast Fourier transform (IFFT), can be applied to calculate these values. An advanced method can be utilized to further reduce the computational complexity of interpolation [121]. DiPNet has a complexity comparable to the ranging step in two-step approaches, where the evaluation of cross-correlation function $f(d_{uv})$ is also required.

A complexity and communication overhead comparison of different algorithms is summarized in Table 4.1, where K_τ and K_s are the number of iterations for delay estimation and space-alternating generalized expectation-maximization (SAGE), respectively, and $(L+1)$ is the model order in SAGE. The DiPNet composed of EL and β-interpolated IFFT requires only few messages on the order of $|\mathcal{A}_u|K$ to transmit. The computational complexity is nearly linear to the number of particles Q and the number of samples N.

In comparison to the state-of-the-art network localization algorithms mentioned in the introduction, the DiPNet utilizes a low measurement abstraction level as in

DPE. It adapts the Bayesian framework of MP to enable decentralized calculation. Unlike traditional MP, neighbor's belief is exploited to calculate the EL instead of marginalization, to achieve a flexible belief inference while retaining low complexity. The concept of DiPNet even shares some commonality to the vector tracking algorithm of GNSS receivers, where the positioning solution feeds back into the tracking of signal to reject outliers [122].

Compared with the traditional two-step approach, the direct localization approach applied in DiPNet has also a few unfavorable properties. Firstly, the cross correlation function of each link has to be stored in a lookup table, which requires more memory, or communication overhead for a centralized variant, and has limited resolution. Secondly, in order to apply low complexity MP algorithms, for example by numerical integral [116], the measurement message has to possess certain properties, which is not fulfilled by the direct localization approach. Hence, it is not straightforward to extend direct localization to low complexity MP.

In the next section, we first prove that the DiPNet is more robust in the considered multipath environments, in comparison with traditional algorithms. Then in Section 4.5 we verify with simulation and experimental results that for the considered applications, the drawbacks of DiPNet are insignificant compared to its advantages over the traditional algorithms.

4.4 DiPNet in Multipath/NLOS Environments

The multipath propagation condition violates the one-path signal model assumed in DiPNet, which leads to a sub-optimality for localization. Due to the stochastic realizations of network and channel, it is difficult to analyze the impacts of the model mismatch on the DiPNet performance. Instead, we investigate the collective propagation impacts from all links, utilizing the fact that a generic agent $\mathbb{a}_u$ in a dense network is often connected with a large number of neighbors. We consider an agent $\mathbb{a}_u$ surrounded by $|\mathcal{A}_u|$ neighbors. In the last sections, we proposed DiPNet, which includes neighbor's position uncertainty by finding an alternative non-cooperative localization problem. In this section, we assume the neighbors' positions are perfectly known or have already been compensated with DiPNet, in order to focus on the propagation effects on localization. The agent $\mathbb{a}_u$ has a uniformly distributed *a priori* belief of its position $b_u^{(0)}$ and updates its belief to $b_u^{(1)}$ by the received signals $\mathbf{r}_{uv}$, $\forall \mathbb{a}_v \in \mathcal{A}_u$. As mentioned in Section 4.3.2, the updated logarithmic belief can be expressed with the

summation of the SCFs of all links as

$$\log b_u^{(1)} \propto \sum_{\mathbb{o}_v \in \mathcal{A}_u} \|\mathbf{r}_{uv}^H \mathbf{s}_{uv}(\|\mathbf{p}_u - \mathbf{p}_v\|/c)\|^2. \tag{4.24}$$

For discussion convenience, we define a polar coordinate system that originates at the true position $\mathbf{p}_{u,0}$ of $\mathbb{o}_u$, whose axes are aligned with the ones of the original Cartesian coordinate system. The position of $\mathbb{o}_v$ is reformulated with the LOS distance $d_{uv,0}$ and the angle θ_{uv} to $\mathbb{o}_u$ as

$$\mathbf{p}_v = \mathbf{p}_{u,0} + d_{uv,0}[\cos\theta_{uv}, \sin\theta_{uv}]^T. \tag{4.25}$$

The position of $\mathbb{o}_u$, which is apart from the true position with a distance $\triangle\tau$ and an angle $\tilde{\theta}$, is expressed as

$$\mathbf{p}_u = \mathbf{p}_{u,0} + \triangle\tau[\cos\tilde{\theta}, \sin\tilde{\theta}]^T. \tag{4.26}$$

The distance $\|\mathbf{p}_u - \mathbf{p}_v\|$ is reformulated as

$$\|\mathbf{p}_u - \mathbf{p}_v\| = \sqrt{d_{uv,0}^2 + \triangle\tau^2 - 2d_{uv,0}\triangle\tau\cos(\theta_{uv} - \tilde{\theta})}. \tag{4.27}$$

We have in addition the following statistical assumptions of the link parameters:

1) The angle of the neighbor is uniformly i.i.d. around $\mathbf{p}_{u,0}$, i.e. $\theta_{uv} \sim U[0, 2\pi)$;

2) The LOS distance $d_{uv,0}$ between $\mathbb{o}_u$ and $\mathbb{o}_v$ is i.i.d. and independent from θ_{uv};

3) The link's LOS/NLOS condition $X_{uv} \in\{$ LOS, NLOS$\}$ is i.i.d. given $d_{uv,0}$;

4) The number of MPCs L_{uv} of each link is i.i.d. given X_{uv};

5) The amplitude of each path $\alpha_{uv,l}$ is i.i.d., with a power $P_{uv,l} = A_{uv,l}^2$ depending on X_{uv} and $d_{uv,0}$ and a uniformly distributed phase $\phi_{uv,l} \sim U[0, 2\pi)$.

6) The NLOS delay and additional path delay of MPCs, b_{uv} and $\delta_{uv,l}$, are i.i.d. given X_{uv}.

Since the propagation parameters of all links are i.i.d., in an asymptotic case where $|\mathcal{A}_u| \to \infty$, we have

$$\log b_u^{(1)} \to |\mathcal{A}_u|\ \mathbb{E}_{\mathbf{x}_{uv}}\Big[\|\mathbf{r}_{uv}^H \mathbf{s}_{uv}(\|\mathbf{p}_u - \mathbf{p}_v\|/c)\|^2\Big], \tag{4.28}$$

where $\mathbf{x}_{uv}$ is the random variables of the link $\mathbb{e}_{uv}$, including all parameters mentioned above and the noise $\boldsymbol{\epsilon}_{uv}$. Hereafter, the subscripts u and v are omitted for simplicity when a single link $\mathbb{e}_{uv}$ is under investigation. The joint pdf of the link's random variables can be factorized as

$$\begin{aligned} p(\mathbf{x}) =& p(d_0)\ p(\theta)\ p(\boldsymbol{\epsilon})\ \Pr(X=\chi|d_0)\ p(b;\chi)\ p(P_0|d_0;\chi) \\ &\times p(\phi_0)\Pr(L=\tilde{L};\chi)\prod_{l=1}^{\tilde{L}} p(\delta_l;\chi)\ p(P_l|d_0;\chi)\ p(\phi_l). \end{aligned} \tag{4.29}$$

Expanding the received signal $\mathbf{r}$ according to (4.15), the expectation of SCF over link $\mathbb{e}$ becomes

$$\begin{aligned} &\mathbb{E}_{\mathbf{x}}\Big[\|\mathbf{r}^H\mathbf{s}(\|\mathbf{p}_u-\mathbf{p}_v\|/c)\|^2\Big] \\ =&N_0\|\mathbf{s}\|^2+\mathbb{E}_{d_0}\Big[\bar{P}_0\ \mathbb{E}_\theta[\|\mathbf{s}(\tau_0)^H\mathbf{s}(\|\mathbf{p}_u-\mathbf{p}_v\|/c)\|^2]\Big] \\ &+\mathbb{E}_{d_0}\Big[\bar{L}\bar{P}_l\mathbb{E}_{\delta_l,b|d_0}[\mathbb{E}_\theta[\|\mathbf{s}(\tau_l)^H\mathbf{s}(\|\mathbf{p}_u-\mathbf{p}_v\|/c)\|^2]]\Big], \end{aligned} \tag{4.30}$$

with the expected path power $\bar{P}_l = \mathbb{E}_{P_l|d_0}[P_l]$ and the expected MPC number $\bar{L} = \mathbb{E}_{L|d_0}[L]$, given the LOS distance d_0. The derivation of (4.30) is detailed in Appendix C.6. We use the notation $\tau = \|\mathbf{p}_u - \mathbf{p}_v\|$ in derivations for simplicity, keeping in mind that τ is a function of positions $\mathbf{p}_u$ and $\mathbf{p}_v$. Let us further assume that the symbol on each subcarrier has a constant power, for example phase-shift keying (PSK) modulated, i.e. $\|S_n\|^2 = \|\tilde{S}\|^2, \forall n = -\frac{N-1}{2}, \cdots, \frac{N-1}{2}$. The l^{th} path's cross-correlation can be further written as

$$\begin{aligned} &\mathbf{s}(\tau_l)^H\mathbf{s}(\|\mathbf{p}_u-\mathbf{p}_v\|/c) \\ =&\frac{1}{N}\sum_{i=1}^{N}\sum_{m,n=-\frac{N-1}{2}}^{\frac{N-1}{2}} S_n^* e^{-\jmath n\omega_{\text{sc}}(iT-\tau_l/c)} S_m e^{\jmath m\omega_{\text{sc}}(iT-\tau/c)} \\ =&\frac{1}{N}\sum_{m,n=-\frac{N-1}{2}}^{\frac{N-1}{2}} S_n^* S_m e^{\jmath n\omega_{\text{sc}}\tau_l/c-\jmath m\omega_{\text{sc}}\tau/c}\underbrace{\sum_{i=1}^{N} e^{\jmath(m-n)\omega_{\text{sc}}iT}}_{=N\delta(m-n)} \\ =&\|\tilde{S}\|^2\sum_{n=-\frac{N-1}{2}}^{\frac{N-1}{2}} e^{jn\omega_{\text{sc}}(\tau_l-\tau)/c} = \|\tilde{S}\|^2\frac{\sin\left(\omega_{\text{sc}}N(\tau_l-\tau)/2c\right)}{\sin\left(\omega_{\text{sc}}(\tau_l-\tau)/2c\right)} \\ \triangleq&\|\tilde{S}\|^2 D_l(\|\mathbf{p}_u-\mathbf{p}_v\|), \end{aligned} \tag{4.31}$$

where $D_l(\|\mathbf{p}_u-\mathbf{p}_v\|)$ is a circular symmetric function of $\mathbf{p}_u$ around a given $\mathbf{p}_v$, obtained

by rotating the order $(N-1)$ Dirichlet kernel, also known as the periodic sinc function, around $\mathbf{p}_v$.

4.4.1 Asymptotic Localization Unbiasedness

A condition of the DiPNet being asymptotically unbiased for position estimation is that the true position $\mathbf{p}_{u,0}$ is a local maximum of $\log b_u^{(1)}$ for $|\mathcal{A}_u| \to \infty$. Since $D_l^2(\|\mathbf{p}_u - \mathbf{p}_v\|)$ is a smooth function for arbitrary $\|\mathbf{p}_u - \mathbf{p}_v\| \neq 0$, the asymptotic unbiasedness condition can be proved by the derivative test w.r.t. $\triangle\tau$ for $\triangle\tau \to 0$ as

$$\text{stationarity: } \lim_{\triangle\tau\to 0} \frac{\partial \mathbb{E}_{\mathbf{x}}\left[\|\mathbf{r}^H \mathbf{s}(\|\mathbf{p}_u - \mathbf{p}_v\|/c)\|^2\right]}{\partial\, \triangle\tau} = 0, \tag{4.32}$$

$$\text{concavity: } \lim_{\triangle\tau\to 0} \frac{\partial^2 \mathbb{E}_{\mathbf{x}}\left[\|\mathbf{r}^H \mathbf{s}(\|\mathbf{p}_u - \mathbf{p}_v\|/c)\|^2\right]}{\partial\, \triangle\tau^2} < 0. \tag{4.33}$$

The updated logarithmic belief $\log b_u^{(1)}$ is asymptotically proportional to the superposition of the expected contributions from each path, over d_0, θ, b and δ_l, as indicated in (4.30) and (4.31). Therefore, we evaluate the derivatives of the expected $D_l(\|\mathbf{p}_u - \mathbf{p}_v\|)^2$ of the LOS path ($l = 0$) and the MPCs ($l > 0$), w.r.t. $\triangle\tau$ for $\triangle\tau = 0$. The first derivative of the expectation over θ is written as

$$\begin{aligned}
&\lim_{\triangle\tau\to 0} \frac{\partial \mathbb{E}_\theta[D_l(\|\mathbf{p}_u - \mathbf{p}_v\|)^2]}{\partial\, \triangle\tau} \\
=&\mathbb{E}_\theta\Big[\lim_{\triangle\tau\to 0} \frac{\partial D_l(\|\mathbf{p}_u - \mathbf{p}_v\|)^2}{\partial\, \triangle\tau}\Big] \\
=&\mathbb{E}_\theta\Big[2\cos(\theta - \tilde{\theta}) \sum_{m,n=-\frac{N-1}{2}}^{\frac{N-1}{2}} \jmath m\omega_{\text{sc}}/c e^{\jmath S_{mn}\omega_{\text{sc}}(\delta_l + b)/c}\Big] = 0,
\end{aligned} \tag{4.34}$$

with the notation $S_{mn} = m + n$, and proves the stationarity condition (4.32). The second derivative of the expectation over θ is expressed as

$$\begin{aligned}
&\ddot{D}_l^2(\|\mathbf{p}_{u,0} - \mathbf{p}_v\|) \\
\triangleq&\lim_{\triangle\tau\to 0} \frac{\partial^2 \mathbb{E}_\theta[D_l(\|\mathbf{p}_u - \mathbf{p}_v\|)^2]}{\partial\, \triangle\tau^2} \\
=&\mathbb{E}_\theta\Big[\lim_{\triangle\tau\to 0} \frac{\partial^2 D_l(\|\mathbf{p}_u - \mathbf{p}_v\|)^2}{\partial\, \triangle\tau^2}\Big] \\
=&-\pi \sum_{n,m=-\frac{N-1}{2}}^{\frac{N-1}{2}} \Big(S_{mn}^2\omega_{\text{sc}}^2/c^2 + \frac{S_{mn}}{\tau_0}\jmath\omega_{\text{sc}}/c\Big) e^{\jmath S_{mn}\omega_{\text{sc}}(\delta_l + b)/c}.
\end{aligned} \tag{4.35}$$

It can be observed that the expectation of the second derivative is independent of $\tilde{\theta}$. Hence the expectation of $D_l(\|\mathbf{p}_u - \mathbf{p}_v\|)^2$ is isotropic in the sense of concavity around $\mathbf{p}_{u,0}$. For the LOS path, inserting $\delta_0 = 0$ and $b = 0$ into (4.35), the second order derivative states

$$\ddot{D}_0^2(\tau_0) = -\frac{\pi\omega_{\text{sc}}^2 N^2(N^2-1)}{6c^2}. \tag{4.36}$$

The condition of concavity can be reformulated by combining (4.30), (4.31) and (4.33) as

$$\varsigma \triangleq \mathbb{E}_{d_0}\Big[\underbrace{\frac{6\bar{L}\bar{P}_l\mathbb{E}_{\delta_l,b|d_0}[\ddot{D}_l^2(\|\mathbf{p}_{u,0}-\mathbf{p}_v\|)]}{\pi\omega_{\text{sc}}^2N^2(N^2-1)/c^2} - \bar{P}_0}_{\triangleq\tilde{\varsigma}(d_0)}\Big] < 0, \tag{4.37}$$

where ς is dubbed the concavity indicator and $\tilde{\varsigma}(d_0)$ is the conditional concavity indicator (CCI) with a given d_0. The concavity condition holds, if and only if the concavity indicator ς is negative. Most of the communication-related channel parameters, e.g. power-delay profile, delay spread, shadow fading, LOS probability and K-factor, are intensively investigated. In comparison, the localization-related channel characteristics, for example the distribution of δ_l and b, is not always available from the study of channel model. However, for the l^{th} MPC with arbitrarily distributed δ_l and b, an upper-bound of $\ddot{D}_l^2(\|\mathbf{p}_{u,0} - \mathbf{p}_v\|)$ can be formulated from (4.35) as

$$\begin{aligned}\ddot{D}_l^2(\|\mathbf{p}_{u,0}-\mathbf{p}_v\|) \leq& \pi \sum_{n,m=-\frac{N-1}{2}}^{\frac{N-1}{2}} S_{mn}^2\omega_{\text{sc}}^2/c^2 + \frac{\|S_{mn}\|\omega_{\text{sc}}}{\tau_0 c}\\ =& \frac{\pi\omega_{\text{sc}}^2N^2(N^2-1)}{6c^2} + \frac{\pi\omega_{\text{sc}}N(N^2-1)}{3\tau_0 c}.\end{aligned} \tag{4.38}$$

With (4.36), (4.38) and $\omega_{\text{sc}}N = 2\pi B_c$, the CCI can be upper-bounded, which yields a new sufficient negative condition as

$$\varsigma < \mathbb{E}_{d_0}\Big[\underbrace{(1+\frac{c}{\pi B_c d_0})\bar{L}\bar{P}_l - \bar{P}_0}_{\geq\tilde{\varsigma}(d_0)}\Big] < 0. \tag{4.39}$$

For a given non-zero d_0, if the expected LOS path power is larger than the expected total power of all other paths, there exists a minimal bandwidth, inversely proportional to d_0, to guarantee the concavity condition (4.33) holds for arbitrarily distributed δ_l and b. In a few channel models, both δ_l and b are assumed exponentially distributed [123], i.e. $p(b;X{=}\text{NLOS}){=}\text{Exp}(a_{\mathbb{B}})$, $p(\delta_l;X{=}\text{LOS}){=}\text{Exp}(a_{\mathbb{L}})$ and $p(\delta_l;X{=}\text{NLOS}){=}\text{Exp}(a_{\mathbb{N}})$.

The rate parameters $a_{\mathbb{B}}, a_{\mathbb{L}}$ and $a_{\mathbb{N}}$ can be derived from the mean NLOS delay and delay spreads from channel models. The CCI in (4.37) can be expressed in close form by marginalizing over δ_l and b, as detailed in Appendix C.7. The CCI can be utilized to analytically assess the applicability of DiPNet, given limited system and channel characteristics. The DiPNet is an asymptotically unbiased localization algorithm if $\tilde{\varsigma}(d_0) < 0, \forall d_0 \in (d_{\min}, d_{\max})$, where $d_{\min}$ and $d_{\max}$ are the minimum and maximum operational distances of an application. The CCIs in typical urban and rural areas are demonstrated in Figure 4.2 in Section 4.5.

4.4.2 Resistance to Erroneous Distance Information

It is known that two-step localization approaches with Gaussian ranging model are vulnerable to large distance estimation offsets, for example due to wrongly detected paths or clock offset. In order to evaluate the erroneous distance information resistance of DiPNet, we investigate a specific scenario as follows. An agent $\mathbb{a}_u$ has a position belief generically modeled by a smooth isotropic unimodal pdf $b_u^{(0)}$, with the single mode at the origin. The logarithm belief is defined as $g(\mathbf{p}_u)$, which is a monotonically decreasing function of $d_u = \|\mathbf{p}_u\|$. A neighbor $\mathbb{a}_v$ located on the negative x-axis with coordinates $\mathbf{p}_v = [-d_0, 0]^T$, provides inter-agent distance information with a continuous measurement function $z(\mathbf{p}_u)$, which is a function of d_{uv} and smooth at every point except $\mathbf{p}_v$. The new belief h in logarithm domain is expressed as

$$h(\mathbf{p}_u) \triangleq \log b_u^{(1)}(\mathbf{p}_u) = g(\mathbf{p}_u) + z(\mathbf{p}_u). \tag{4.40}$$

Let us assume $z(\mathbf{p}_u)$ reaches its global maximum with an additional distance offset $\delta > -d_0$. This offset may introduce a local maxima shift to the belief $h(\mathbf{p}_u)$, which is under investigation.

Lemma 4.4.1 (Local Maximum Point)**.** *A point $\mathbf{p}_{ox} = vec\{x_{ox}, y_{ox}\}$ is a local maximum point of $h(\mathbf{p}_u)$, if and only if (a) $y_{ox} = 0$, (b) it is a local maximum point over x-domain and (c) $x_{ox} > -d_0$.*

Proof. See Appendix C.8. □

Lemma 4.4.1 indicates that it is sufficient to investigate the local maxima shift of the belief over x-domain only, i.e., in the direction of link $\mathbb{e}_{uv}$. We can redefine function h, z and g as one dimensional function of x_u by setting $y_u = 0$.

Theorem 4.4.1 (General Belief Shift)**.** *For DiPNet, if the neighbor $\mathbb{a}_v$ is separated from $\mathbb{a}_u$ by at least a fractional of sample in distance ϱ_κ defined in Appendix C.9, a*

path with an offset δ shifts the maximum of $\mathbb{o}_u$'s position belief from the origin to a local maximum point $\mathbf{p}_{ox} = [x_{ox}, 0]^T$. The belief shift $\|x_{ox}\|$ is upper bounded by ϱ_κ which decreases from c/B_c to $c/2B_c$ with increasing $\|\delta\|$.

Proof. See Appendix C.9. □

Theorem 4.4.2 (Shift of Bivariate Belief)**.** *In addition to Theorem 4.4.1, if the original position belief is modeled with isotropic bivariate normal distribution $b_u^{(0)} = \mathcal{N}(\mathbf{0}, \sigma_0^2\mathbf{I})$, the belief shift $\|x_{ox}\|$ is more tightly bounded by*

$$\begin{cases} \dfrac{\|\delta\|}{1+\upsilon}, & \forall \|\delta\| < \frac{c}{B_c} \quad (4.41a) \\ \dfrac{\varrho_\kappa}{1+\frac{\upsilon}{3\rho^2(1+\rho^2)}}, & \forall \|\delta\| \geqslant \frac{c}{B_c} \quad (4.41b) \end{cases}$$

where ρ is inversely proportional to $B_c\|\delta\|$ and ν is the ratio between the the measurement and a priori belief uncertainties. Both ρ and ν are defined in Appendix C.10.

Proof. See Appendix C.10. □

The upper bound expressed in (4.41a) is the belief shift introduced by a two step approach, having a Gaussian ranging model with a mean biased by arbitrary δ and a variance modeled by the ranging CRB, denoted as CRB_l. With Theorem 4.4.2 we can observe that for a small distance offset, the belief shift from DiPNet is upper bounded by the shift from the two step approach, i.e. increasing with the distance offset $\|\delta\|$ and bandwidth B_c. For a large distance offset, the belief shift from DiPNet decreases with increasing $\|\delta\|$ and B_c, which is contrary to the two step approach and makes the DiPNet more resistant to erroneous distance information. The belief shift is demonstrated in Figure 4.3, which is explained in more detail in Section 4.5.

4.5 Simulation and Experimental Results

4.5.1 Simulation Results

We conduct simulations using an OFDM system designed for multi-link ranging [82, 58], with parameters as follows: bandwidth $B_c = 37\,\text{MHz}$, number of subcarriers $N = 2569$, subcarrier spacing $f_{sc} = 14.65\,\text{KHz}$, carrier frequency $f_c = 5.2\,\text{GHz}$, transmit power $P_{Tx} = 1\,\text{mW}$ ($0\,\text{dBm}$), temperature of $300\,\text{K}$ for thermal noise calculation and an additional noise figure of $15\,\text{dB}$.

In Figure 4.2, we illustrate the CCI, $\tilde{\varsigma}(d_0)$ defined in Section 4.4.1, with the channel parameters of urban (C2) and rural area (D1) scenarios from the WINNER-II channel

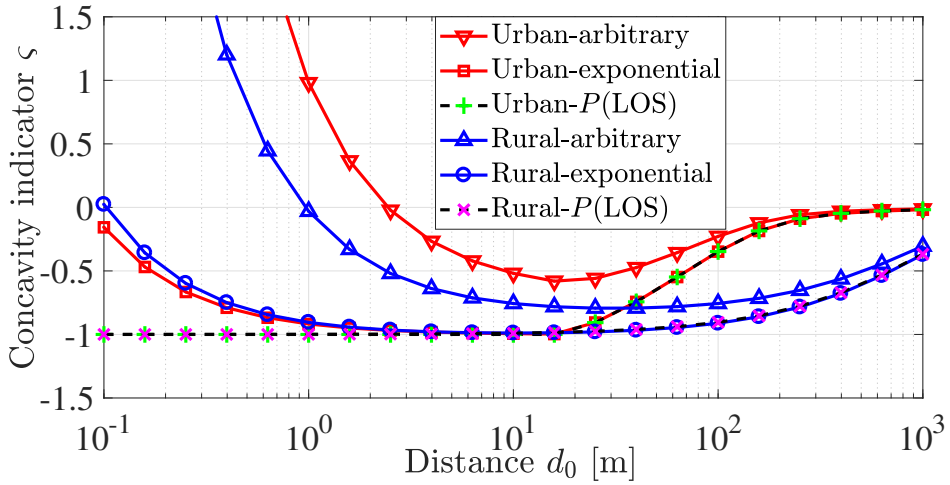

Figure 4.2. *CCIs for urban and rural areas normalized to the LOS path power, benchmarked against the AWGN case, where* $\tilde{\varsigma}(d_0) = -\Pr(X = LOS)$.

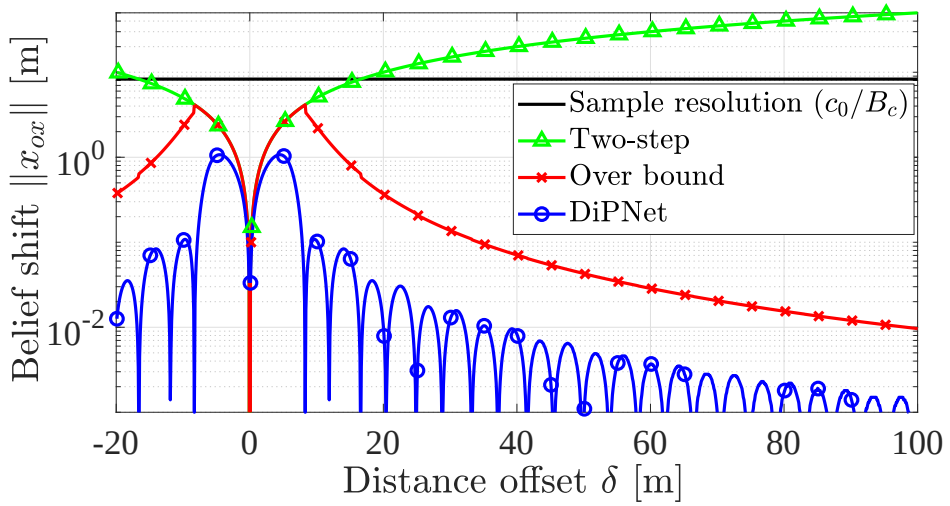

Figure 4.3. *Belief shift of* $\mathbb{u}_u$*'s position.*

model [124]. For arbitrary multipath bias δ_l and NLOS bias b, the upper bound of $\tilde{\varsigma}(d_0)$ defined in (4.39) is calculated with the K-factor, path-loss models and LOS probability $P(\text{LOS})$ listed in the WINNER-II channel model. For exponentially distributed δ_l, delay spreads from the WINNER-II channel model are additionally included to marginalize δ_l. The distribution of NLOS bias b is not included in the WINNER-II model. We assume an exponentially distributed NLOS bias with a mean of 0.3 µs, which is acquired by an urban area raytracing tool developed in project GREAT [125]. AWGN cases are included as benchmarks, where $\tilde{\varsigma}(d_0) = -\Pr(X = \text{LOS})$, representing the unrealistic optimal cases of perfect multipath mitigation and NLOS rejection. For arbitrary δ_l and b, if $d_0 > 2\,\text{m}$ in urban areas or $d_0 > 1\,\text{m}$ in rural areas, $\tilde{\varsigma}(d_0)$ is negative, i.e. DiPNet is an asymptotically unbiased position estimator. For exponentially distributed δ_l and b, DiPNet is asymptotically unbiased for any $d_0 > 0.1\,\text{m}$. All $\tilde{\varsigma}(d_0)$ are converging to the benchmarks with increasing d_0, where LOS probability becomes the decisive factor. The CCI of urban area is significantly larger than the one of rural area for a large d_0, due to a faster decreasing LOS probability. The investigation of the concavity indicator allows us to analytically conclude that DiPNet is asymptotically unbiased in both urban and rural areas. Besides, DiPNet in rural area may outperform the one in urban area due to a higher LOS probability.

In Figure 4.3, we demonstrate Theorem 4.4.2 in Section 4.4.2 with $\nu = 1$. The position belief shift $\|x_{ox}\|$ with DiPNet (in blue), its upper bound (in red), the belief shift with the corresponding Gaussian two-step approach (in green) and a sample expressed in meters (in black) against increasing distance offset δ are plotted. The upper bound derived in Theorem 4.4.2 is always smaller than one sample distance, firstly increases then decreases as the envelope of the DiPNet belief shift and becomes negligible for large $\|\delta\|$. Whereas the belief shift of the Gaussian two-step approach monotonically increases with $\|\delta\|$. This observation verifies the erroneous distance information resistance of DiPNet.

Finally, we conduct simulations of anchor-free network localization in urban and rural area with complete channel models adapted from WINNER-II. Different sizes of fully meshed networks composed of three to thirty agents are simulated. Agents are uniformly deployed in a $100\,\text{m} \times 100\,\text{m}$ area. DiPNet is compared with three two-step algorithms, namely a correlation-based ranging approach [126], a SAGE-based approach for multipath mitigation [127] and a SAGE-based approach with only LOS links as a benchmark for perfect NLOS rejection. All the two-step approaches apply the ERV concept [51] and the Gaussian ranging model, with the one-path ZZB as ranging variance [56, 128]. A DPF with 1000 particles is implemented at each agent for every algorithm with parametric belief exchanges.

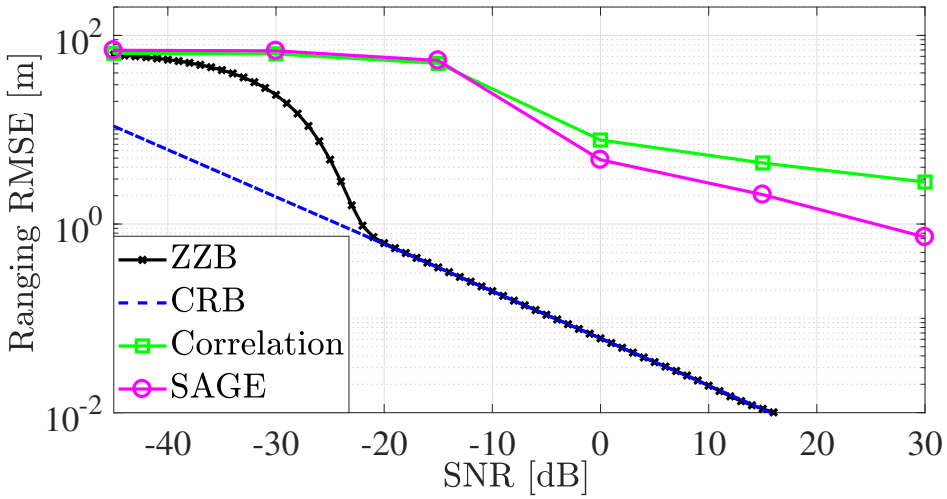

Figure 4.4. *Correlation-based and SAGE-based ranging RMSEs in comparison with CRB and ZZB in both urban and rural areas.*

Figure 4.4 shows the ranging RMSEs from correlation and SAGE, in comparison with the CRB and the ZZB. Ranging samples are collected from all the links in the networks under investigation in both urban and rural areas. SAGE outperforms the correlation-based ranging as expected. However, both ranging RMSEs diverge from the bounds due to the unpredictable multipath and NLOS propagation effects. This divergence directly limits the achievable localization accuracy for two-step approaches with the ranging error modeled by the bounds, as shown next.

In Figure 4.5 and Figure 4.6, the anchor-free network localization performances of the compared algorithms in urban and rural areas are shown. In Figure 4.5a and Figure 4.5b the framework distance RMSEs defined in (2.6) of the compared algorithms with different network sizes are plotted. In Figure 4.6a and Figure 4.6b the CDFs of the absolute framework distance error of different algorithms are compared for networks with three and thirty agents. The RMSEs of all algorithms decrease with an increasing number of agents from three to thirty, which indicates a cooperative gain through mesh networks. Correlation and SAGE-based algorithms result in larger RMSEs than the other two due to the NLOS-bias. The proposed DiPNet performs similarly to the NLOS-rejected SAGE, which verifies that the DiPNet is NLOS-bias resistant as proved in Section 4.4.2. The DiPNet obtains similar sub-meter RMSEs in both urban and rural areas for a number of agents larger than 12. The CDF plots show that in urban area, localization outliers are more often present than in rural area, except the DiPNet and NLOS-rejected SAGE in 30-agent networks. It is due to the fact that the LOS probability in rural area (95.1%) is significantly higher than the one in urban area (65.6%). Both CDF and RMSE plots show a slight outperforming of DiPNet compared to the NLOS-rejected SAGE in dense networks in the sub-meter error range.

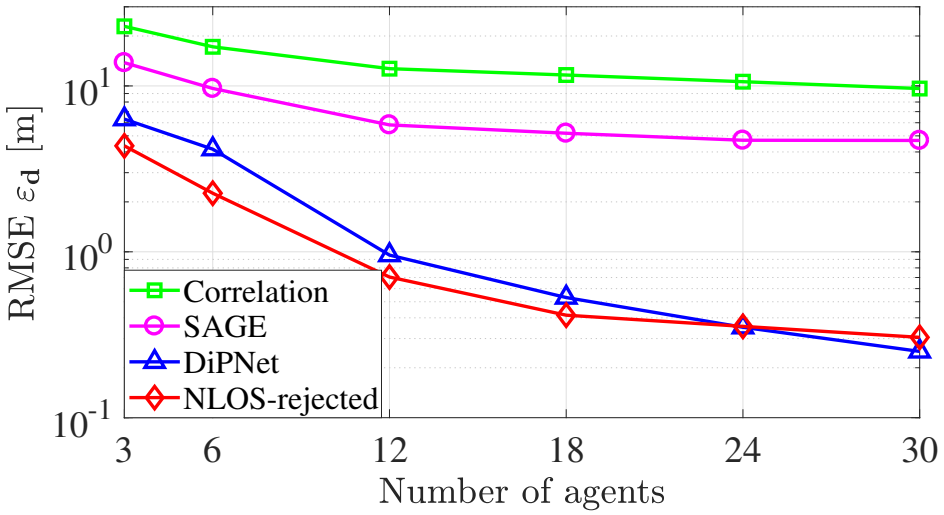

(a) *Urban area RMSE* $\varepsilon_{\mathbf{d}}$

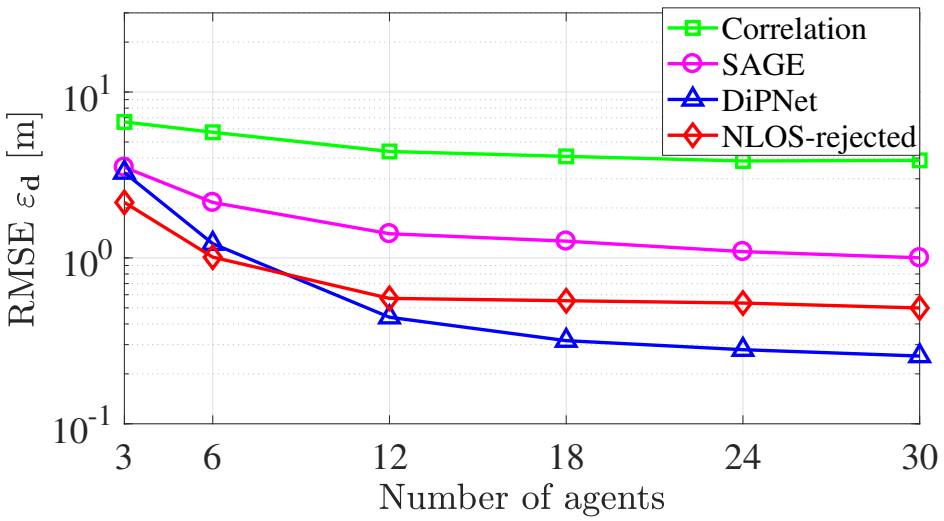

(b) *Rural area RMSE* $\varepsilon_{\mathbf{d}}$

Figure 4.5. *RMSE simulation results in urban and rural areas with DiPNet, correlation-based, SAGE-based and NLOS-rejected SAGE algorithms: (a) and (b) framework distance RMSE for 3 to 30 agents.*

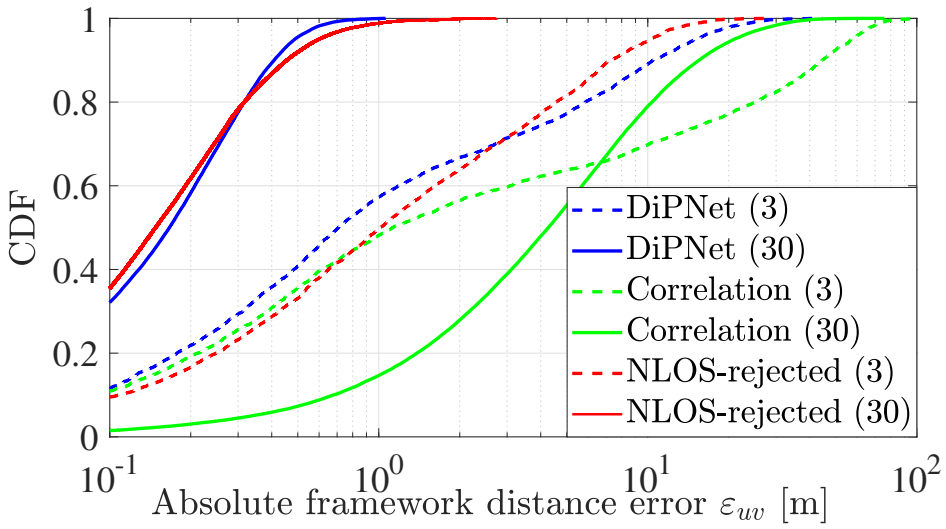

(a) *Urban area CDF of* ε_{uv}

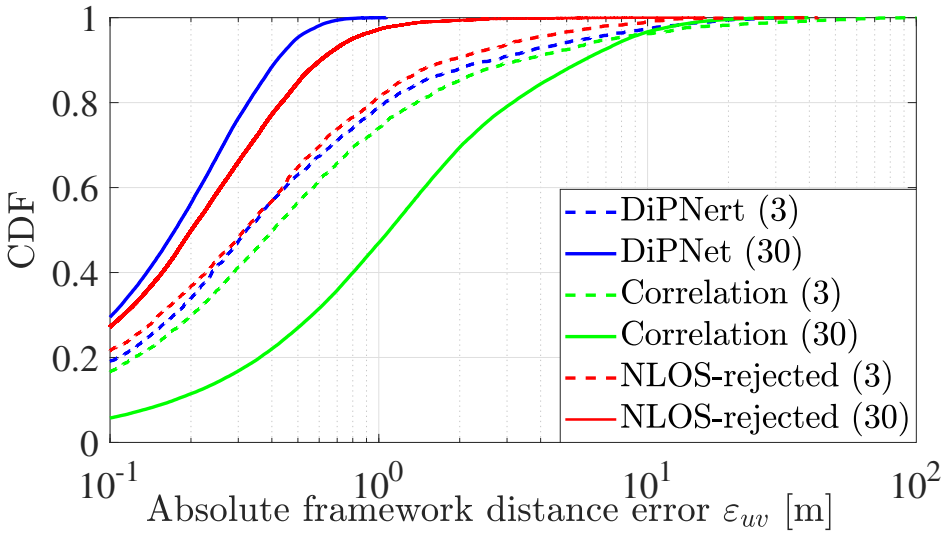

(b) *Rural area CDF of* ε_{uv}

Figure 4.6. *CDF simulation results in urban and rural areas with DiPNet, correlation-based, SAGE-based and NLOS-rejected SAGE algorithms: (a) and (b) absolute framework distance error cumulative distribution function (CDF) for 3 and 30 agents.*

It is caused by the non-resolvable MPCs in SAGE algorithm and approximation error in ZZB.

4.5.2 Experimental Results

We conducted two outdoor experiments with six swarm navigation prototypes developed at our research group [88], on a grass field at the DLR in 2015. At this time, six test-beds has been implemented by Emanuel [88], capable of ranging with an update rate of 100 ms. Two-way ranging between all prototypes is implemented in a sequential fashion, with OFDM signals similarly to simulations, except a transmit power of 100 mW (20 dBm) and a carrier frequency of 5.5 GHz for forward links and 5.7 GHz for backward links are used. A second OFDM symbol with a scattered pilot structure is transmitted additionally for SNR estimation, counteracting non-ideal effects related to hardware. All 30 links are pre-calibrated in our laboratory over cables and RF attenuators to compensate hardware characteristics like the RF front-end delays and the filter frequency responses. Five prototypes are placed in approximately symmetric pentagonal formations, with a dimension of 15 m in experiment 1 and a dimension of 30 m in experiment 2, and remain stationary. The sixth prototype is mounted on a remotely controlled rover, driving around within a 50 m $\times$ 80 m area. An accurate ground truth of agent's position is continuously obtained with a reflecting prism on the rover tracked by a *Leica* tachymeter. The received raw OFDM symbols are collected through Ethernet at a host computer and time-stamped together with the ground truth, so that the experiments can be replayed in laboratory for algorithm comparison. In total 17700 two-way measurements are collected, 260 snapshots for experiment 1 and 330 snapshots for experiment 2. Similar to simulations, we implement a SAGE-based algorithm exchanging parametric beliefs, referred to as parametric SAGE, to compare with DiPNet. In addition, sample-based DPE and SAGE approaches are implemented, where particle represented beliefs are directly exchanged and incorporated in the DPF. To maintain similar complexity for each agent, 7157 particles are used for DiPNet and parametric SAGE, whereas 100 particles are employed for sample-based DPE and sample-based SAGE. The experimental setup is shown in Figure 4.7, including Figure 4.7a images of experiments, where stationary agents are marked in yellow and rover in red, Figure 4.7b agent's true trajectories in experiment 2 and their particle-represented beliefs from DiPNet at snapshot 61, Figure 4.7c and Figure 4.7d agent's true and estimated trajectories in experiment 1 from parametric SAGE and DiPNet. The rover is mostly driving smoothly with a moderate velocity, except from snapshot 250 in experiment 2, where the maximum velocity and rapid turns are experienced by the rover with the trajectory illustrated in Figure 4.7b in red. The moving/stationary condition infor-

mation is not available at agents, i.e. the DPFs at all agents apply the same mobility model. The optimal rigid affine transformation $\mathcal{T}_{\text{opt}}$ is applied to generate Figure 4.7b-Figure 4.7d for visualization convenience [47].

Comparing Figure 4.7c and Figure 4.7d, we can see that DiPNet significantly outperforms parametric SAGE. A more detailed comparison can be found in Figure 4.8 and Figure 4.9, with Figure 4.8a and Figure 4.8b showing the framework distance RMSE for each snapshot and, Figure 4.9a and Figure 4.9b showing the CDF of the absolute framework distance error. In both experiments, the ranging links are distorted with the MPCs from surrounding metallic structures. Additionally, low SNR is observed for some links due to the grass field ground reflection. DiPNet outperforms all three other algorithms in both experiments. Both sample-based DPE and DiPNet perform more robustly than their corresponding two-step counter partners. Sample-based DPE experiences a limited achievable accuracy due to small particle populations, as reported in [87]. A larger network dimension in experiment 2 leads to a higher failure rate for SAGE-based approaches, while only slightly affects the accuracy of DiPNet in sub-meter range. A higher rover dynamics also slightly reduces the DiPNet accuracy in sub-meter level due to a higher uncertainty in the state transition.

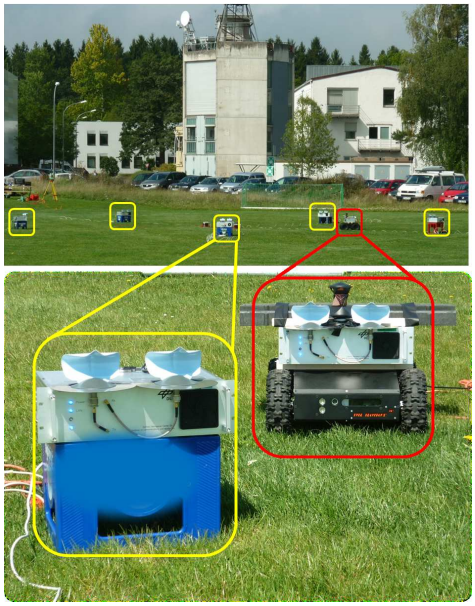

(a) *Experimental setup*

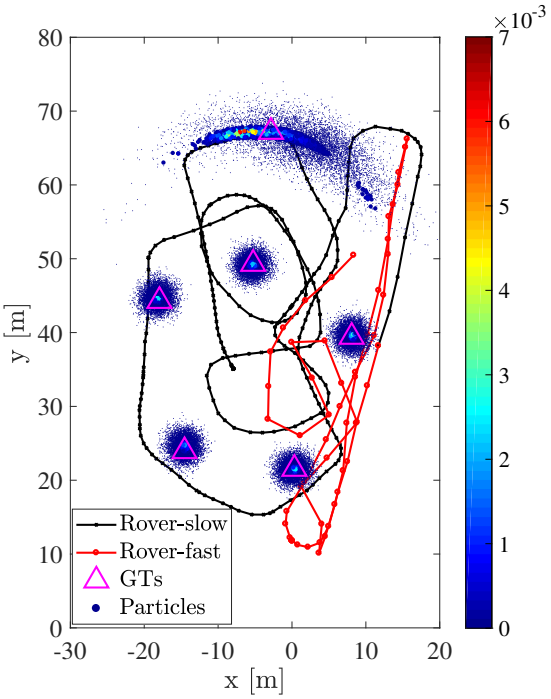

(b) *DiPNet snapshot in experiment 2*

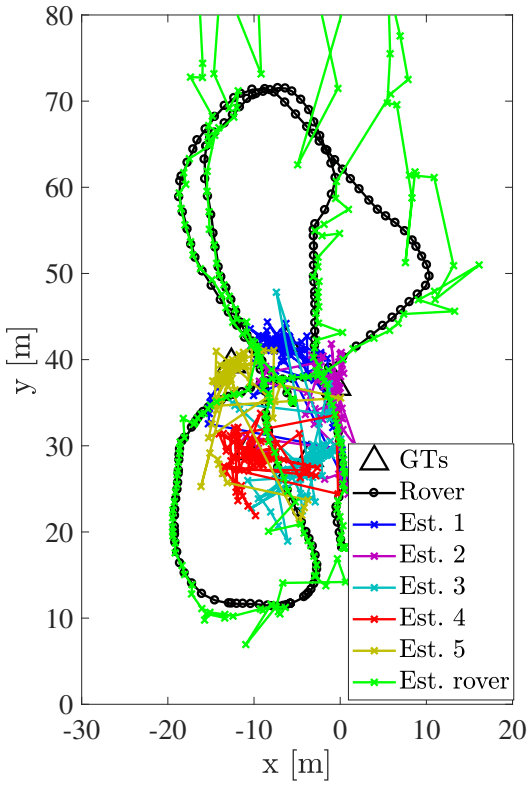

(c) *Parametric SAGE in experiment 1*

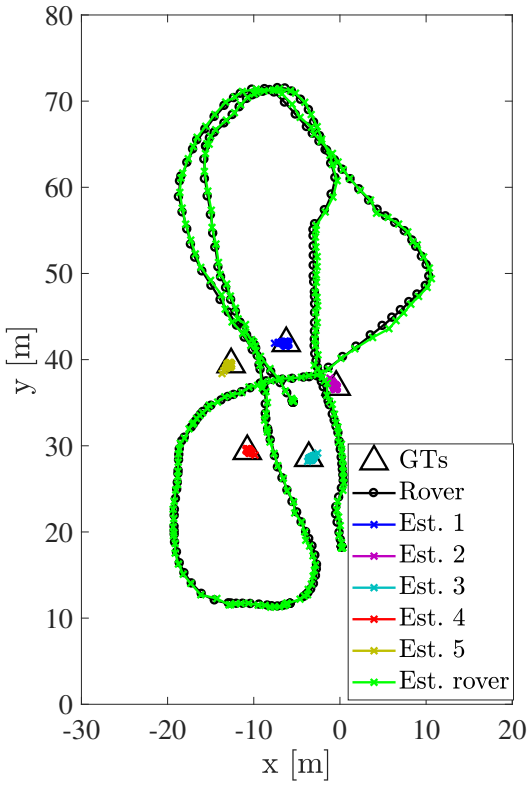

(d) *DiPNet in experiment 1*

Figure 4.7. *Experiments: (a) experimental setup, (b) agent's true trajectories in experiment 2 and particles at snapshot 61, (c) and (d) agent's true and estimated trajectories from parametric SAGE and DiPNet in experiment 1.*

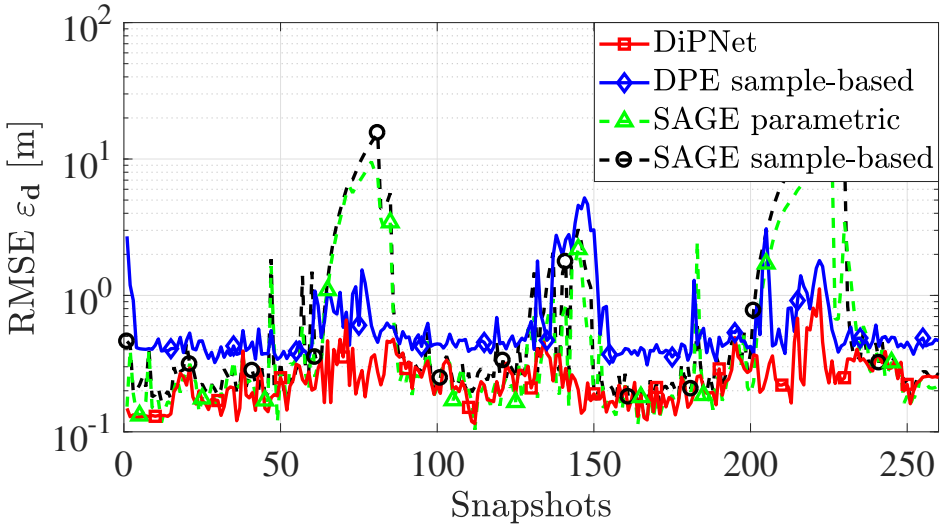

(a) *RMSE $\varepsilon_{\mathbf{d}}$ in experiment 1*

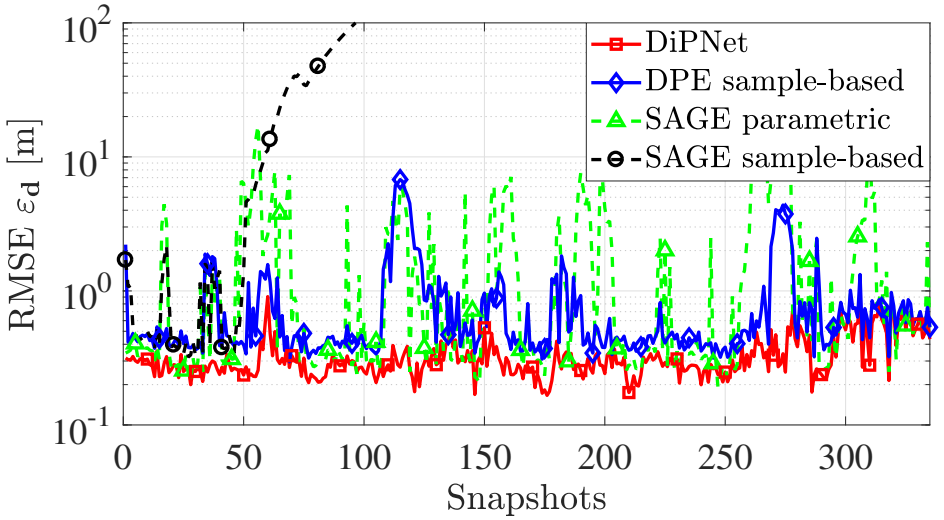

(b) *RMSE $\varepsilon_{\mathbf{d}}$ in experiment 2*

Figure 4.8. *Experimental performance of DiPNet, parametric SAGE, sample-based DPE and sample-based SAGE: (a) and (b) framework distance RMSE at each snapshot.*

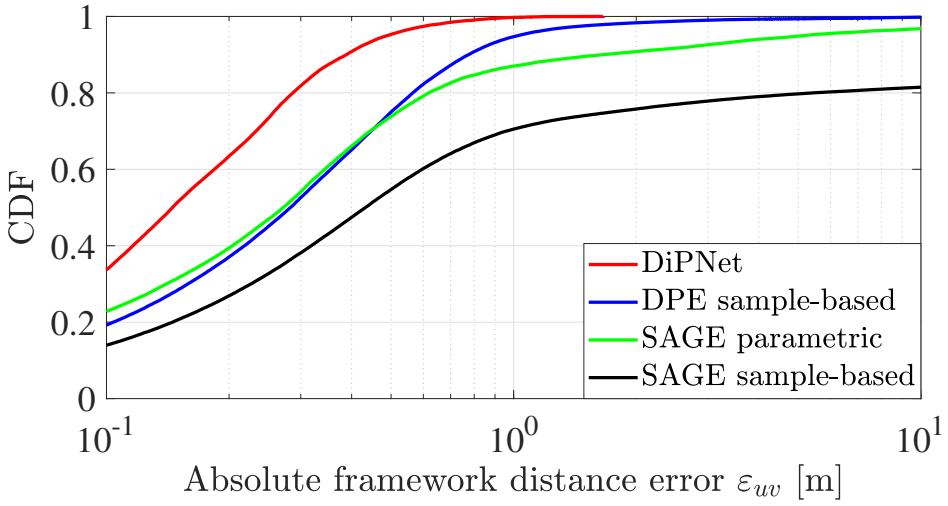

(a) *CDF of ε_{uv} in experiment 1*

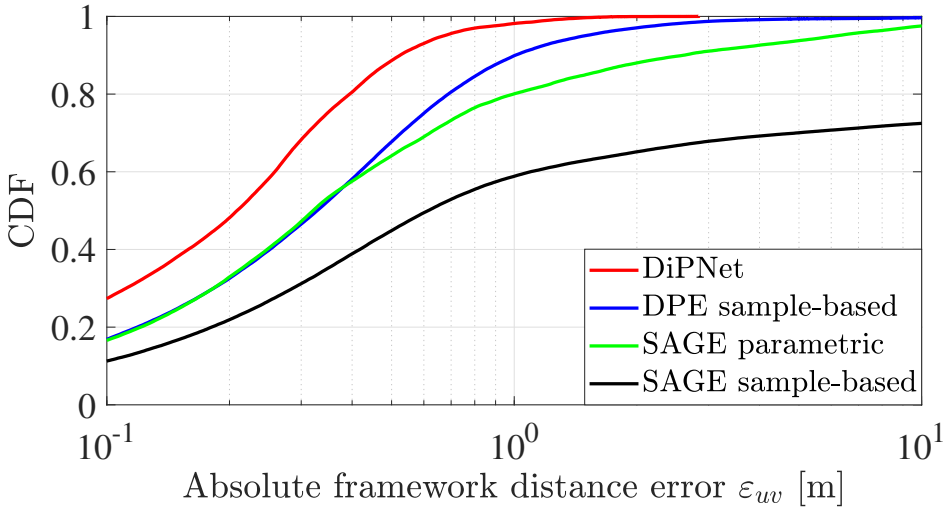

(b) *CDF of ε_{uv} in experiment 2*

Figure 4.9. *Experimental CDF performance of DiPNet, parametric SAGE, sample-based DPE and sample-based SAGE: (a) and (b) absolute framework distance error CDF at each snapshot.*

Chapter 5

Position-Aware Swarm Control

In Chapter 3 we have studied theoretical aspects of swarm navigation, especially the FI and variational CRBs to quantify the expected localization performance. With the help of FI, we are able to reveal the essence of swarm self- and source localization, and to infer the impacts of e.g. geometry, resource allocation, coordinate system, on swarm localization. FI has been also used for designing low complexity swarm localization algorithms in Chapter 4, by defining the equivalent likelihood function. Both Chapter 3 and Chapter 4 aim to answer the first question of autonomous swarm navigation described in Section 1.2, i.e. "Where am I?" In this chapter, we exploit the knowledge of FI/BI and the mobility of the swarm and solve the problem of "Where shall I go?". As an outcome of the proposed position-aware swarm control, swarm formations are assembled, which are preferable for localization. As already been introduced in Chapter 1, the implication of position awareness is threefold.

First, the swarm estimates the positions of itself and the sources, for example, with the swarm localization algorithms introduced in Section 3.4.4 and Chapter 4.

Second, the position estimation uncertainties are inferred with CRBs for non-Bayesian estimators, and with PCRBs for Bayesian estimators as introduced in Chapter 3.

Third, the swarm is aware of the impacts of, e.g. its formation and resource allocation, on position information, e.g. the FI, BI or Shannon information [25]. The swarm actively adapts its formation to maximize the aforementioned information metrics, which is referred to as position information seeking control.

In Figure 5.1, the three levels of position awareness in autonomous swarm navigation systems are illustrated progressively with arrows colored in green, blue and red. The red dashed loop emphasizes the swarm's self-awareness of its navigation process. For traditional navigation systems, the control objectives are externally defined, optionally tolerating the estimation uncertainty. Contrarily, in our autonomous swarm navigation

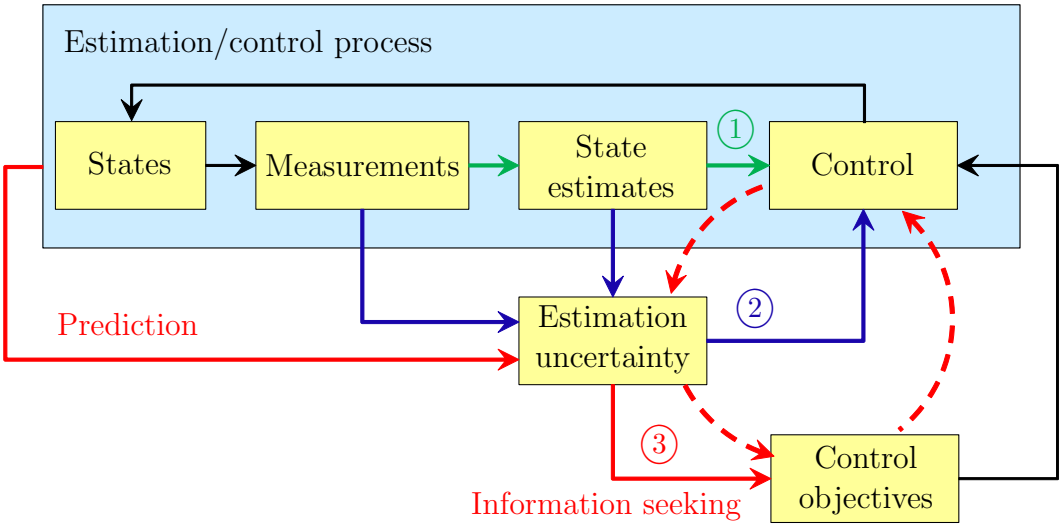

Figure 5.1. *Position awareness in swarm navigation: The three levels of position awareness are illustrated progressively with arrows colored in green, blue and red. The red dashed loop emphasizes the swarm's self-awareness of its navigation process.*

system the estimation uncertainty is a controllable feature. The swarm is aware of not only the state estimation uncertainty but also the causality between its states and the estimation uncertainty. With the later awareness, the swarm can actively adapt its formation minimizing the estimation uncertainty.

We propose a concept of position-aware swarm control based on projected steepest gradient descent (PSGD), maximizing FI or BI, meantime achieving other control objectives, such as goal approaching and collision avoidance. Position CRBs and PCRBs of an arbitrary subset of nodes are utilized as the objective functions and the constraints of the control problem. Thus, the controller can be designed flexibly according to applications. A closed form expression of the gradient based controller is derived to enable low complexity swarm control.

5.1 Survey on Position-Aware Swarm Control

As mentioned in Section 1.2.2, the main focus of swarm control (or multi-agent control) in the literature is on achieving or maintaining a predefined target formation and accomplishing some task with minimized collective efforts. The position uncertainty is often either overlooked, or considered in a tolerance-base, which is only related to the first, i.e. awareness of position estimates, and second, i.e. awareness of position uncertainty, levels of position awareness. There is limited literature on swarm control related to the third level of position awareness, where the swarm is aware of the self- and source localization process, and actively composes formations which is beneficial

for swarm localization. Information seeking controls, e.g. in [46, 25, 129], often exploit information metrics such as Shannon or Fisher information, for designing control objective functions to actively minimize localization uncertainty. In [45], the swarm formation is optimized by minimizing the trace of the rigidity matrix introduced in Section 3.3. This approach can be interpreted as to compose a formation as rigid as possible. The geometry effects on swarm self-localization is considered, whereas the measurement quality effects are overlooked. In [130, 129], the agents' positions are assumed to be known, and the source position FI is utilized to optimize the swarm formation so that the source localization performance is improved. In [46], linear state transition and measurement models are assumed, both distorted by AWGN. With this simplified model, a KF is implemented. The covariance matrix obtained from the KF is used as the cost function to achieve preferable swarm formations for both self- and source localization. In [25], NBP approach is implemented for joint self- and source localization. The swarm formation is optimized by maximizing the negative conditional differential entropy. This approach is suitable for only a few agents due to the high complexity of NBP.

5.2 Gradient based Swarm Control

For the considered large-scale swarm with controllable agents' positions, swarm control formulated in Section 2.3 is a high dimensional non-convex optimization problem. Instead of finding the optimal solution in one step, we adapt the PSGD method [131, Ch. 5] to design a low complexity swarm controller.

5.2.1 Projected Steepest Gradient Descent Control

PSGD is an iterative method to find a local optimal solution of a constrained optimization problem. The general idea of PSGD is to iteratively apply the following four steps:

1) Finding an initial solution pointing against the gradient of the cost function;

2) Checking the potential violation of the constraints;

3) If the constraints are violated, projecting the initial solution on the tangent space of the constraints;

4) checking the potential violation again, and applying necessary corrections to compensate the non-linearity effect of the constraints.

We utilize the general concept of PSGD to generate the control command $\mathbf{b}_\mathcal{A}$ to the swarm from the gradients of the objective functions, including the cost function and the constraints. Instead of iterations applied in PSGD, the cost function and the constraints are evaluated only once at the previous agents' positions. With this modification, a low complexity can be maintained for real-time swarm control, at a risk of possible slight constraint violations. We reformulate the swarm control problem with a generic objective function $f(\mathbf{b}_\mathcal{A})$ to be minimized and L inequality constraints $\mathbf{h}(\mathbf{b}_\mathcal{A}) > \mathbf{0}$, where $\mathbf{h}(\mathbf{b}_\mathcal{A}) = \text{vec}\{h_l(\mathbf{b}_\mathcal{A}) : l = 1, \cdots, L\}$, i.e.

$$\underset{\mathbf{b}_\mathcal{A} \in \mathcal{U}_\mathcal{A}}{\text{minimize}} \quad f(\mathbf{b}_\mathcal{A}), \tag{5.1}$$

$$\text{s.t.} \quad \mathbf{h}(\mathbf{b}_\mathcal{A}) \geq \mathbf{0}. \tag{5.2}$$

The gradient of the objective function is written as

$$\mathbf{c}_\mathcal{A} = \text{vec}\{\mathbf{c}_u : \mathbb{o}_u \in \mathcal{A}\} = \nabla_{\mathbf{b}_\mathcal{A}} f(\mathbf{b}_\mathcal{A}), \tag{5.3}$$

which points to the direction where the value of $f(\mathbf{b}_\mathcal{A})$ ascends fastest. An unconstrained control command $\tilde{\mathbf{b}}_\mathcal{A}$ can be firstly found by the steepest gradient descent method as

$$\tilde{\mathbf{b}}_\mathcal{A} = \text{vec}\{\mathbf{c}_u : \mathbb{o}_u \in \mathcal{A}\} = -\mu \frac{\mathbf{c}_\mathcal{A}}{\|\mathbf{c}_\mathcal{A}\|}, \tag{5.4}$$

where μ is the chosen step size of the gradient descent, such that $\max\{\|\mathbf{c}_u\| : \mathbb{o}_u \in \mathcal{A}\} \leq b_{\max}$. The maximum travel distance in one step is denoted as $b_{\max}$, which is limited by the mechanical capability of the agents. Then we identify the activated constraints $\mathbf{h}_a(\mathbf{b}_\mathcal{A}) = \text{vec}\{h_l(\mathbf{b}_\mathcal{A}) : h_l(\mathbf{0}) \leq 0\}$, i.e. the constraints either have been violated or are at the boundary of violation. The constraints' gradient matrix $\mathbf{N}$ is defined as

$$\mathbf{N} = \nabla_{\mathbf{b}_\mathcal{A}} \mathbf{h}_a(\mathbf{b}_\mathcal{A})^T|_{\mathbf{b}_\mathcal{A}=\mathbf{0}}. \tag{5.5}$$

A projection matrix $\mathbf{P}$ is defined as

$$\mathbf{P} = \mathbf{I} - \mathbf{N}\left(\mathbf{N}^T\mathbf{N}\right)^{-1}\mathbf{N}^T, \tag{5.6}$$

which projects the unconstrained control command $\tilde{\mathbf{b}}_\mathcal{A}$ to the tangent space of the constraints as described in the step (3) of PSGD. The control command $\boldsymbol{\delta}$ after the projection is expressed as

$$\boldsymbol{\delta} = \mathbf{P}\tilde{\mathbf{b}}_\mathcal{A}. \tag{5.7}$$

In addition, the quantity of constraint violations need to be compensated, similar to the step (4) of PSGD, which leads to the final solution of the control command as

$$\mathbf{b}_{\mathcal{A}} = \boldsymbol{\delta} - \mathbf{N}\left(\mathbf{N}^T\mathbf{N}\right)^{-1}\mathbf{h}_a(\mathbf{0}). \tag{5.8}$$

A scaling factor may be applied again if $\mathbf{b}_{\mathcal{A}}$ is not contained in the feasible set of control command $\mathcal{U}_{\mathcal{A}}$ due to the compensation step. From the general step description of PSGD, we can observe that the essence of applying such an algorithm is firstly to design the cost function $f(\mathbf{b}_{\mathcal{A}})$ and the constraints $\mathbf{h}(\mathbf{b}_{\mathcal{A}})$, and secondly to calculate the derivatives of them w.r.t. the controller $\mathbf{b}_{\mathcal{A}}$.

5.2.2 Objective Functions for Swarm Control

Swarm control is often a multi-objective problem. These objectives act as the cost functions or/and the constraints, depending on their priorities defined by the applications. The objectives considered in this thesis are formally expressed as follows.

1) Position information seeking

   Position information seeking control, i.e. controlling the swarm's formation so that the position uncertainties of certain nodes are minimized, is the main control objective considered in this thesis. The trace of the weighted covariance matrix of the total state estimation is utilized as the figure of merit for this objective. Thus, the position information seeking objective, generically denoted as $f_p(\mathbf{b}_{\mathcal{A}})$, is formally expressed as

$$f_p(\mathbf{b}_{\mathcal{A}}) \triangleq \mathrm{Tr}\left[\boldsymbol{\Lambda}^f \mathrm{cov}[\hat{\mathbf{x}}^{(+)}]\right], \tag{5.9}$$

   where the diagonal weighing matrix $\boldsymbol{\Lambda}^f = \mathrm{diag}\{\lambda_i^f : i = 1, \cdots, N_\chi\}$ indicates the objective emphasis on the N_χ dimensional states. The entities λ_i^f of the weighing matrix can be either binary valued from $\{0, 1\}$ to select certain dimensions of the states for optimization, or arbitrary non-negative real valued, which puts different weights at particular dimensions. The weights on non-position states are set to zero.

   If the position information seeking objective function acts as the cost function, the swarm will constantly optimize its formation so that the value of this cost function gradually decreases. The priority of this cost function is lower than the activated constraints.

   If the position information seeking objective function is used as a constraint, it will only affect the swarm controller if it is activated. Hence, only if the value of the

objective function is not smaller a certain maximum tolerated position error $\varepsilon_{\max}$, the swarm controller will act to reduce its value with a higher priority than other objectives served as cost functions. Generally, the weighing matrix of the position information seeking as a cost function can be different from the one as a constraint. The position information seeking objective used as a constraint is denoted as $h_p(\mathbf{b}_{\mathcal{A}})$ with a weighing matrix $\mathbf{\Lambda}^h$, in order to be distinguished from the usage as a cost function, i.e.

$$h_p(\mathbf{b}_{\mathcal{A}}) \triangleq \mathrm{Tr}\left[\mathbf{\Lambda}^h \mathrm{cov}[\hat{\mathbf{x}}^{(+)}]\right]. \tag{5.10}$$

The position information seeking constraint is expressed as

$$\varepsilon_{\max} - h_p(\mathbf{b}_{\mathcal{A}}) \geq 0. \tag{5.11}$$

The covariance matrix is an empirical metrics, which is difficult to be directly exploited as an objective function for two reasons. First, a large number of samples are demanded to evaluate the covariance matrix. Second, even if a covariance matrix has been calculated from samples, it can not be analytically formulated as a function of the control command $\mathbf{b}_{\mathcal{A}}$.

In Section 5.3 and Section 5.4, we use FI and BI as the predicted covariance matrices of non-Bayesian and Bayesian estimators, respectively, to design position information seeking swarm controls.

2) Goal approaching

Goal approaching is a commonly applied objective for a wide variety of swarm control applications. A swarm aims to move from it current position $\mathbf{p}_{\mathcal{A}}^{(-)}$ to a goal point P_g with coordinates $\mathbf{p}_g$.

For an exploration mission, the goal point can be defined as the center of an exploration area of interest, with predefined coordinates in the global coordinate system $\mathbf{p}_g^{\mathbb{G}}$.

In a return-to-mission-base application, the swarm returns to the mission base without the knowledge of the global coordinate system. We consider an even more challenging scenario, where only one beacon is transmitting a low frequency RF signal to guide the swarm back to the mission base. Due to lacking knowledge of the global coordinate system, the beacon is considered as a RF source without position information. In this application, the goal coordinates are defined as the coordinates of the RF source to be estimated, $\mathbf{p}_v^{\mathbb{B}}$ or $\mathbf{p}_v^{\mathbb{C}}, \mathbb{c}_v \in \mathcal{S}_{\mathrm{RF}}$, in a swarm coordinate sys-

tem defined by a baseline $\mathbb{B}$, or defined by the group motions $\mathbb{C}$, as discussed in Section 3.3.

In some applications, like the gas exploration mission illustrated in Figure 1.2, the swarm estimates the position of the gas source w.r.t. the global coordinate system $\mathbb{G}$, while approaching the gas source. In this case, the goal position is the position of the gas source $\mathbf{p}_v^{\mathbb{G}}, \mathbb{o}_v \in \mathcal{S}_{\text{gas}}$.

The objective function of goal approaching $f_g(\mathbf{b}_\mathcal{A})$ is generally formulated as

$$f_g(\mathbf{b}_\mathcal{A}) = -\mathbf{b}_\mathcal{A}^T \cdot \mathbf{e}_g, \tag{5.12}$$

$$\text{where} \quad \mathbf{e}_g = \frac{\mathbf{1}_{|\mathcal{A}|\times 1} \otimes \mathbf{p}_g - \mathbf{p}_\mathcal{A}}{\|\mathbf{1}_{|\mathcal{A}|\times 1} \otimes \mathbf{p}_g - \mathbf{p}_\mathcal{A}\|}. \tag{5.13}$$

The symbol $\otimes$ denotes the Kronecker product, which stacks the goal position into a vector with the same size as $\mathbf{p}_\mathcal{A}$. The gradient of the goal approaching objective function w.r.t. the control command $\mathbf{b}_\mathcal{A}$ can be straightforwardly written as $\mathbf{e}_g$. Hence, the preferable directions of goal approaching points to the goal from individual agents, which is intuitive.

The goal approaching objective is preferably implemented as a cost function since the distance to the goal should gradually decrease through the whole mission. However, it can be also used as a constraint for a mission-duration crucial application, demanding a minimum goal distance reduction $s_{\min}$. The constraint is written as

$$-f_g(\mathbf{b}_\mathcal{A}) - s_{\min} \geq 0. \tag{5.14}$$

3) Collision avoidance

Collision avoidance is another crucial objective for swarm control, which is often considered as a constraint. Due to the imperfection of the controller and the position uncertainty, an agent $\mathbb{o}_u \in \mathcal{A}$ need to keep its distance d_{uv} to another node $\mathbb{o}_v \in \mathcal{V}$ larger than a minimal tolerated distance $d_{\min}$. The objective function can be simply written as

$$d_{uv} - d_{\min} \geq 0, \tag{5.15}$$

where in practice the distance d_{uv} is replaced with its estimate $\|\hat{\mathbf{p}}_u - \hat{\mathbf{p}}_v\|$. However, for collision avoidance which is a safety critical objective, only constraining on the mean distance is often not enough. Therefore, we model d_{uv} as a random variable and further propose to constrain the probability of violation. The collision avoidance

objective function $h_c(\mathbf{b}_\mathcal{A})$ can thus be formulated as

$$h_{c,uv}(\mathbf{b}_\mathcal{A}) \triangleq \beta_{\max} - \Pr\left[d_{uv} \leq d_{\min}\right] \geq 0, \tag{5.16}$$

where $\beta_{\max} \in [0, 1]$ is the maximum acceptable probability of the violation of the minimum tolerated distance $d_{\min}$. In Section 5.5, we will derive this constraint as well as its gradient w.r.t. the control command $\mathbf{b}_\mathcal{A}$ in detail.

By combing the introduced objective functions, the position information seeking swarm control problem can be formulated flexibly according to the application requirement. A typical problem formulation can be expressed as

$$\underset{\mathbf{b}_\mathcal{A} \in \mathcal{U}_\mathcal{A}}{\text{minimize}} \quad \underbrace{w_p f_p(\mathbf{b}_\mathcal{A})}_{\text{(position information seeking)}} + \underbrace{w_g f_g(\mathbf{b}_\mathcal{A})}_{\text{(goal approaching)}} \tag{5.17a}$$

$$\text{s.t.} \quad \varepsilon_{\max} - h_p(\mathbf{b}_\mathcal{A}) \geq 0 \qquad \text{(position information seeking)}, \tag{5.17b}$$

$$- f_g(\mathbf{b}_\mathcal{A}) - s_{\min} \geq 0 \qquad \text{(goal approaching)}, \tag{5.17c}$$

$$h_{c,uv}(\mathbf{b}_\mathcal{A}) \geq 0, \quad \forall \mathbb{l}_{uv} \in \mathcal{L}_{\text{all}} \qquad \text{(collision avoidance)}. \tag{5.17d}$$

The problem formulation can be straightforwardly extended to a heterogeneous swarm control strategy, where the cost functions and the constraints are designed differently for each individual agent.

5.3 Fisher Information Seeking

As discussed in Section 5.2.2, the estimation covariance is an empirical metric and not suitable to be directly used as the objective function. Instead, position information seeking objective functions can be formulated with the predicted FIM, denoted as $\mathbf{I}_{\mathbf{x}^{(+)}}$, given a snapshot of predicted measurements $\tilde{\mathbf{z}}^{(+)}$, i.e. virtual measurements expected to be obtained at the new position. The predicted CRB, denoted as $\text{CRB}[\mathbf{x}^{(+)}]$, is a lower bound of the predicted estimation covariance $\text{cov}_{\tilde{\mathbf{z}}^{(+)};\mathbf{x}^{(+)}}[\hat{\mathbf{x}}^{(+)}]$, i.e.

$$\text{cov}_{\tilde{\mathbf{z}}^{(+)}}[\hat{\mathbf{x}}^{(+)}] \succcurlyeq \text{CRB}[\mathbf{x}^{(+)}]. \tag{5.18}$$

Moreover, as discussed in [29], the CRB is a tight bound in a scenario of preferable node geometry and high SNR, and thus, is used as the approximation of the estimation covariance exploiting only a snapshot of measurements. As discussed in the general description of the PSGD algorithm in Section 5.2, the essential step is to derive the gradient of the trace of the CRB weighted by a generic weighing matrix $\mathbf{\Lambda}$ w.r.t. the

control command $\mathbf{b}_{\mathcal{A}}$, i.e.

$$\mathbf{c}_{\mathcal{A}} = \nabla_{\mathbf{b}_{\mathcal{A}}} \mathrm{Tr}\left[\mathbf{\Lambda} \mathrm{CRB}[\mathbf{x}^{(+)}]\right]. \tag{5.19}$$

In scenarios where the FIM has a full rank, the CRB is expressed as the inverse of the FIM. The scenarios includes the applications with sufficient beacons to define a global coordinate system $\mathbb{G}$, like the extended network illustrated in Figure 3.8b, or anchor-free applications with a swarm coordinate system $\mathbb{B}$, defined by a baseline B. Subsequently, a closed-form expression of the derivative c_l of the trace of the weighted CRB, $\mathrm{Tr}[\mathbf{\Lambda}\mathbf{I}^{-1}_{\mathbf{x}^{(+)}}]$ w.r.t. the l^{th} element of $\mathbf{b}_{\mathcal{A}}$, i.e. $b_l = [\mathbf{b}_{\mathcal{A}}]_l$ is derived. Utilizing the derivative chain rule $\partial \mathbf{A}^{-1} = -\mathbf{A}^{-1}\partial\mathbf{A}\mathbf{A}^{-1}$ and the property of the trace $\mathrm{Tr}[\mathbf{AB}] = \mathrm{Tr}[\mathbf{BA}]$, the derivative can be rewritten in the form

$$\frac{\partial \mathrm{Tr}[\mathbf{\Lambda}\mathbf{I}^{-1}_{\mathbf{x}^{(+)}}]}{\partial c_l} = -\mathrm{Tr}\left[\underbrace{\mathbf{I}^{-1}_{\mathbf{x}^{(+)}}\mathbf{\Lambda}\mathbf{I}^{-1}_{\mathbf{x}^{(+)}}}_{\triangleq \mathbf{A}} \frac{\partial \mathbf{I}_{\mathbf{x}^{(+)}}}{\partial c_l}\right]. \tag{5.20}$$

The expanded closed-form expression of Section 5.3 is lengthy, and therefore is stored in Appendix C.11. The derivative $\mathbf{c}_{\mathcal{A}}$ of $\mathrm{Tr}[\mathbf{\Lambda}\mathbf{I}^{-1}_{\mathbf{x}^{(+)}}]$ w.r.t. $\mathbf{b}_{\mathcal{A}}$ is obtained by stacking all c_l, i.e. $\mathbf{c}_{\mathcal{A}} = \mathrm{vec}\{c_l : l = 1, \cdots, N_\chi\}$, which can be used for controller design based on the PSGD introduced in Section 5.2. In practice, the initiated control can be set to zero, i.e. $\mathbf{b}_{\mathcal{A}} = \mathbf{0}$, and the current agents' positions are replaced by their estimates. Hence, the gradient is evaluated at the current agents' estimated positions.

We also derive the gradient of the weighted CRB for an anchor-free self-localization scenario with the group motion constrained swarm coordinate system $\mathbb{C}$. The FIM is singular, and the Moore-Penrose pseudoinverse has to be applied to express the position CRB, i.e. $\mathrm{CRB}[\mathbf{p}^{(+)}_{\mathcal{A}}] = \mathbf{I}^{\dagger}_{\mathbf{p}^{(+)}_{\mathcal{A}}}$. Utilizing the derivative law of a symmetric matrix's Moore-Penrose pseudoinverse $\mathbf{A}^{\dagger}$ [119]

$$\partial \mathbf{A}^{\dagger} = -\mathbf{A}^{\dagger}\partial\mathbf{A}\mathbf{A}^{\dagger} + \mathbf{A}^{\dagger}\mathbf{A}^{\dagger}\partial\mathbf{A}(\mathbf{I} - \mathbf{A}\mathbf{A}^{\dagger}) + (\mathbf{I} - \mathbf{A}^{\dagger}\mathbf{A})\partial\mathbf{A}\mathbf{A}^{\dagger}\mathbf{A}^{\dagger}, \tag{5.21}$$

the gradient of the weighted anchor-free self-localization CRB can be derived as

$$\frac{\partial \mathrm{Tr}[\mathbf{\Lambda}\mathbf{I}^{\dagger}_{\mathbf{x}^{(+)}}]}{\partial c_l} = -\mathrm{Tr}\Bigg[\underbrace{\left(\mathbf{I}^{\dagger}_{\mathbf{x}^{(+)}} + \mathbf{I}_{\mathbf{x}^{(+)}}\mathbf{I}^{\dagger}_{\mathbf{x}^{(+)}} - \mathbf{I} + \left(\mathbf{I}^{\dagger}_{\mathbf{x}^{(+)}}\right)^2\right)\mathbf{\Lambda}\left(\mathbf{I}^{\dagger}_{\mathbf{x}^{(+)}} + \mathbf{I}^{\dagger}_{\mathbf{x}^{(+)}}\mathbf{I}_{\mathbf{x}^{(+)}} - \mathbf{I} + \left(\mathbf{I}^{\dagger}_{\mathbf{x}^{(+)}}\right)^2\right)}_{\triangleq \bar{\mathbf{A}}} \frac{\partial \mathbf{I}_{\mathbf{x}^{(+)}}}{\partial c_l}\Bigg], \tag{5.22}$$

which can be expressed in closed-form similarly to the previously discussed full-rank case in Section 5.3 and Appendix C.11. Especially, for swarm self-localization with multi-way ranging as discussed in Section 3.3 and Chapter 4, the FI seeking objective function can be formulated by setting the weighting matrix to the identity matrix, i.e. $\mathbf{\Lambda} = \mathbf{I}$. In this case, the swarm formation is optimized by minimizing the RMSE of the swarm self-localization. The gradient of the objective function in (5.22) simplifies to

$$\frac{\partial \mathrm{Tr}[\mathbf{I}^{\dagger}_{\mathbf{x}^{(+)}}]}{\partial c_l} = -\mathrm{Tr}\left[\left(\mathbf{I}^{\dagger}_{\mathbf{x}^{(+)}}\right)^2 \frac{\partial \mathbf{I}_{\mathbf{p}^{(+)}}}{\partial c_l}\right], \tag{5.23}$$

which has almost the same expression as the full-rank case, only replacing the inverse with the Moore-Penrose pseudoinverse. To obtain (5.23), we have utilized the trace property again and the following equalities of a real symmetric matrix $\mathbf{A}$:

$$\mathbf{A}^{\dagger}\mathbf{A}^{\dagger} - \mathbf{A}^{\dagger}\mathbf{A}^{\dagger}\mathbf{A}^{\dagger}\mathbf{A} = \mathbf{A}^{\dagger}\mathbf{A}^{\dagger} - \mathbf{A}^{\dagger}(\mathbf{A}\mathbf{A})^{\dagger}\mathbf{A} = \mathbf{A}^{\dagger}\mathbf{A}^{\dagger} - \mathbf{A}^{\dagger}\mathbf{A}^{\dagger} = \mathbf{0}. \tag{5.24}$$

With the gradient of weighted estimation CRB w.r.t. the control command $\mathbf{b}_{\mathcal{A}}$ being derived, the FI seeking controller can be designed.

5.4 Bayesian Information Seeking

For the BI seeking swarm control, the state $\mathbf{x}^{(+)}$ is considered as a random vector. Not only the predicted snapshot measurements $\tilde{\mathbf{z}}^{(+)}$ but also the historical measurements $\mathbf{z}^{(1:-)}$ are exploited for the state estimation. We focus on full rank cases. Hence, the PCRB, which is a lower bound of the covariance matrix of a Bayesian estimate $\hat{\mathbf{x}}^{(+)}$, is expressed as the inverse of the BIM, denoted as $\mathbf{J}_{\mathbf{x}^{(+)}}$, i.e.

$$\mathrm{cov}_{\mathbf{x}^{(+)}|\mathbf{z}^{(1:-)},\tilde{\mathbf{z}}^{(+)}}[\hat{\mathbf{x}}^{(+)}] \succcurlyeq \mathrm{PCRB}[\mathbf{x}^{(+)}] \triangleq \mathbf{J}^{-1}_{\mathbf{x}^{(+)}}. \tag{5.25}$$

The full rank BIM assumption is valid for swarm navigation in a global coordinate system $\mathbb{G}$ with a sufficient number of beacons, or in the baseline constrained swarm coordinate system $\mathbb{B}$. The information about $\mathbf{x}^{(+)}$ in the predicted measurements $\tilde{\mathbf{z}}^{(+)}$ is denoted as $\mathbf{I}_{\mathbf{x}^{(+)}}$, which has a similar expression as the FI in the non-Bayesian case. With the linear state transition model and the non-linear observation model both distorted by AWGN described in Section 2.3, the BIM simplifies to

$$\mathbf{J}_{\mathbf{x}^{(+)}} = \mathbb{E}_{\mathbf{x}^{(+)}}\left[\mathbf{I}_{\mathbf{x}^{(+)}}\right] + \underbrace{\left(\mathbf{Q}(\mathbf{b}_{\mathcal{A}}) + \mathbf{J}^{-1}_{\mathbf{x}^{(-)}}\right)^{-1}}_{\triangleq \tilde{\mathbf{J}}_{\mathbf{x}^{(+)}}}. \tag{5.26}$$

The term $\tilde{\mathbf{J}}_{\mathbf{x}^{(+)}}$ is the *a-priori* information after the state transition and prior to obtaining the measurements $\tilde{z}^{(+)}$. The term $\mathbf{Q}(\mathbf{b}_{\mathcal{A}})$ is the covariance matrix of the state transition noise introduced in Section 2.3, which depends on the step size of the individual agent $\|\mathbf{b}_u\|$.

A lower bound of the estimation covariance without the predicted measurements $\tilde{\mathbf{z}}^{(+)}$ is obtained by the inverse of $\tilde{\mathbf{J}}_{\mathbf{x}^{(+)}}$, i.e.

$$\mathrm{cov}_{\mathbf{x}^{(+)}|\mathbf{z}^{(1:-)}}[\hat{\mathbf{x}}^{(+)}] \succcurlyeq \left(\tilde{\mathbf{J}}_{\mathbf{x}^{(+)}}\right)^{-1}, \tag{5.27}$$

which will be used for the collision avoidance objective in Section 5.5. Similar to the FI seeking control, the essential step of the BI seeking control, both as a cost function and as a constraint, is to derive the gradient of the trace of the PCRB weighted by a generic diagonal weighing matrix $\mathbf{\Lambda}$ w.r.t. the control command $\mathbf{b}_{\mathcal{A}}$, i.e.

$$\mathbf{c}_{\mathcal{A}} = \nabla_{\mathbf{b}_{\mathcal{A}}} \mathrm{Tr}\left[\mathbf{\Lambda}\mathrm{PCRB}[\mathbf{x}^{(+)}]\right] = \nabla_{\mathbf{b}_{\mathcal{A}}} \mathrm{Tr}\left[\mathbf{\Lambda}\mathbf{J}^{-1}_{\mathbf{x}^{(+)}}\right]. \tag{5.28}$$

The partial derivative $\nabla_{\mathbf{b}_{\mathcal{A}}} \mathrm{Tr}\left[\mathbf{\Lambda}\mathbf{J}^{-1}_{\mathbf{x}^{(+)}}\right]$ can be derived similarly as the one for the FI seeking case in Section 5.3. The derivative w.r.t. the l-th element of $\mathbf{b}_{\mathcal{A}}$, i.e. $b_l = [\mathbf{b}_{\mathcal{A}}]_l$

is expressed as

$$\frac{\partial \mathrm{Tr}\left[\mathbf{\Lambda}\mathbf{J}_{\mathbf{x}^{(+)}}^{-1}\right]}{\partial b_l} = -\mathrm{Tr}\left[\underbrace{\mathbf{J}_{\mathbf{x}^{(+)}}^{-1}\mathbf{\Lambda}\mathbf{J}_{\mathbf{x}^{(+)}}^{-1}}_{\triangleq\tilde{\mathbf{A}}}\frac{\partial \mathbf{J}_{\mathbf{x}^{(+)}}}{\partial b_l}\right] \tag{5.29}$$

$$= -\mathrm{Tr}\left[\tilde{\mathbf{A}}\left(\frac{\partial \mathbb{E}_{\mathbf{x}^{(+)}}\left[\mathbf{I}_{\mathbf{x}^{(+)}}\right]}{\partial b_l} + \frac{\partial \tilde{\mathbf{J}}_{\mathbf{x}^{(+)}}}{\partial b_l}\right)\right] \tag{5.30}$$

$$= -\mathrm{Tr}\left[\tilde{\mathbf{A}}\frac{\partial \mathbb{E}_{\mathbf{x}^{(+)}}\left[\mathbf{I}_{\mathbf{x}^{(+)}}\right]}{\partial b_l}\right] + \mathrm{Tr}\left[\mathbf{B}\frac{\partial \mathbf{Q}(\mathbf{b}_{\mathcal{A}})}{\partial b_l}\right]$$

$$= -\mathrm{Tr}\left[\tilde{\mathbf{A}}\frac{\partial \mathbb{E}_{\mathbf{x}^{(+)}}\left[\mathbf{I}_{\mathbf{x}^{(+)}}\right]}{\partial b_l}\right] + \frac{\sigma^2 b_l}{\|\mathbf{b}_u\|}\mathrm{Tr}[\mathbf{B}_{<\mathbf{p}_u,\mathbf{p}_u>}], \tag{5.31}$$

where

$$\mathbf{B} \triangleq \tilde{\mathbf{J}}_{\mathbf{x}^{(+)}}\tilde{\mathbf{A}}\tilde{\mathbf{J}}_{\mathbf{x}^{(+)}}, \tag{5.32}$$

and $\mathbf{A}_{<\mathbf{x}_1,\mathbf{x}_2>}$ denotes a submatrix of a generic matrix $\mathbf{A}$, truncated at the rows and columns corresponding to the state $\mathbf{x}_1$ and $\mathbf{x}_2$, respectively. The term $\mathbf{B}_{<\mathbf{p}_u,\mathbf{p}_u>}$ is the 2×2 matrix, truncated from $\mathbf{B}$ at the two rows and two columns with the indices of $\mathbf{p}_u$ from the total state $\mathbf{x}$. In order to evaluate the expectation over $\mathbf{x}^{(+)}$, the *a posteriori* pdf of $\mathbf{x}^{(+)}$ needs to be estimated, which makes the Bayesian controller unattractive for a large-scale swarm [25]. Intensive research has been conducted on the *a posteriori* pdf inference with reduced complexity [116, 32]. This work focuses on the concept of exploiting the position information awareness for swarm formation optimization. Therefore we use the value calculated from the estimated position $\hat{\mathbf{x}}^{(+)}$ to replace the expectation without further investigation of Bayesian inference techniques to maintain the low complexity of the swarm controller. The derivative $\mathbf{c}_{\mathcal{A}}$ of $\mathrm{Tr}\left[\mathbf{\Lambda}\mathbf{J}_{\mathbf{x}^{(+)}}^{-1}\right]$ w.r.t. $\mathbf{b}_{\mathcal{A}}$ can be expressed as $\mathbf{c}_{\mathcal{A}} = \mathrm{vec}\{c_i : i = 1,\cdots,N_\chi\}$ and used for a gradient-based controller similar to the one in Section 5.3.

We can observe that the second term in (5.31) depends only on the direction of the control vector instead of the step size. Additionally, it is proportional to the directional vector of the control command. Hence, it does not change the direction of the control commands for each agent, but only reduces their step size. This reduction is due to the step size dependent transition uncertainty defined in (2.13). The amount of step size reduction differs from agent to agent. With these observations we can set the initiated control to zero, i.e. $\mathbf{b}_{\mathcal{A}} = \mathbf{0}$, to calculate the direction of the gradient from the first

term in (5.31). Then we assume the control vector points into the opposite direction to the gradient to calculate the step size reduction by the second term.

5.5 Collision Avoidance

We employ the probability formulation of the collision avoidance objective in (5.16), because it is a safety crucial objective. The PCRB provides an approximation of the covariance of a Bayesian estimation. However, it does not provide any information of the distribution of the state, which is needed to evaluate the probability in (5.16). We propose a conservative criterion to guarantee collision avoidance probability based on a multi-variant generalization of the Chebyshev inequality with arbitrary distribution introduced in [132]. We define a vector $\mathbf{p}_{uv} = \mathbf{p}_u - \mathbf{p}_v$, which is a random variable with an *a-priori* mean $\bar{\mathbf{p}}_{uv} = \mathbb{E}_{\mathbf{p}|\mathbf{z}^{(1:-)}}[\mathbf{p}_{uv}]$, and an *a-priori* covariance matrix $\mathbf{C}_{uv} = \mathrm{cov}_{\mathbf{p}|\mathbf{z}^{(1:-)}}[\mathbf{p}_{uv}]$. Only the case of $\|\bar{\mathbf{p}}_{uv}\| > d_{\min}$ is considered. If the mean distance is smaller than the minimum tolerated distance, the trivial objective function in (5.15) can be firstly employed. According to the Chebyshev inequality, we have

$$\Pr_{\mathbf{p}|\mathbf{z}^{(1:-)}}\left[(\mathbf{p}_{uv} - \bar{\mathbf{p}}_{uv})^T \mathbf{C}_{uv}^{-1} (\mathbf{p}_{uv} - \bar{\mathbf{p}}_{uv}) < \varepsilon\right] \geqslant 1 - \frac{2}{\varepsilon} = 1 - \beta_{\max}. \tag{5.33}$$

The mean $\bar{\mathbf{p}}_{uv} = \mathbb{E}_{\mathbf{p}|\mathbf{z}^{(1:-)}}[\mathbf{p}_{uv}]$ is expressed as

$$\bar{\mathbf{p}}_{uv} = \bar{\mathbf{p}}_u^{(+)} - \bar{\mathbf{p}}_v^{(+)} = \bar{\mathbf{p}}_u^{(-)} - \bar{\mathbf{p}}_v^{(-)} + \mathbf{b}_u - \mathbf{b}_v. \tag{5.34}$$

The covariance matrix $\mathbf{C}_{uv}$ is calculated from the corresponding elements in $\tilde{\mathbf{J}}^{-1}_{\mathbf{x}^{(+)}}$ as

$$\mathbf{C}_{uv} = \mathbf{Q}_u + \mathbf{Q}_v + \mathbf{B}_{uv}, \tag{5.35}$$

where

$$\mathbf{B}_{uv} \triangleq (\mathbf{J}^{-1}_{\mathbf{x}^-})_{<\mathbf{p}_u,\mathbf{p}_u>} + (\mathbf{J}^{-1}_{\mathbf{x}^-})_{<\mathbf{p}_v,\mathbf{p}_v>} - (\mathbf{J}^{-1}_{\mathbf{x}^-})_{<\mathbf{p}_u,\mathbf{p}_v>} - (\mathbf{J}^{-1}_{\mathbf{x}^-})_{<\mathbf{p}_v,\mathbf{p}_u>}, \tag{5.36}$$

which is independent from $\mathbf{b}_{\mathcal{A}}$.

The geometric interpretation of (5.33) is that the random vector $\mathbf{p}_{uv}$ gets its value inside an ellipse $\mathcal{E}(\bar{\mathbf{p}}_{uv}, \varepsilon\mathbf{C}_{uv})$ with at least probability $1 - \frac{2}{\varepsilon}$. The notation $\mathcal{E}(\mathbf{x}, \mathbf{C})$ denotes an ellipse centered at $\mathbf{x}$. The shape of the ellipse is defined with the eigenvalue decomposition of $\mathbf{C}$

$$\mathbf{C} = \mathbf{U}(\theta)\mathrm{diag}[\lambda_1^2, \lambda_2^2]\mathbf{U}(\theta)^T \tag{5.37}$$

where $\lambda_1 \geqslant \lambda_2 > 0$ are the major and minor axes, respectively, and $\mathbf{U}(\theta)$ is the rotation matrix applying an angle θ rotation to the ellipse.

We define a critical circle $\mathcal{E}(\mathbf{0}, d_{\min}\mathbf{I})$, whose boarder is expressed as

$$\mathbf{p}_{uv}^T \mathbf{p}_{uv} = d_{\min}^2. \tag{5.38}$$

A realization of $\mathbf{p}_{uv}$ violates the minimum tolerated distance, i.f.f. it lies inside the critical circle. The collision avoidance probability can be guaranteed if the area of the defined ellipse and the critical circle are mutually exclusive. We have the following lemma, equivalent to (5.33).

Lemma 5.5.1 (Collision Avoidance)**.** *The collision avoidance probability can be guaranteed if there exists a scaling factor $a > 1$, so that the scaled ellipse $\mathcal{E}(\bar{\mathbf{p}}_{uv}, a\varepsilon\mathbf{C}_{uv})$ is externally tangent to the critical circle.*

The tangent point $\check{\mathbf{p}}_{uv}$ fulfills

$$\check{\mathbf{p}}_{uv} = d_{\min} \frac{\mathbf{C}_{uv}^{-1}(\bar{\mathbf{p}}_{uv} - \check{\mathbf{p}}_{uv})}{\|\mathbf{C}_{uv}^{-1}((\bar{\mathbf{p}}_{uv} - \check{\mathbf{p}}_{uv})\|}. \tag{5.39}$$

The collision avoidance constraint can be reformulated as

$$(\check{\mathbf{p}}_{uv} - \bar{\mathbf{p}}_{uv})^T \mathbf{C}_{uv}^{-1}(\check{\mathbf{p}}_{uv} - \bar{\mathbf{p}}_{uv}) = a\varepsilon > \varepsilon. \tag{5.40}$$

Equation (5.40) can be expanded as

$$a(d_{\min}^2) + b(d_{\min}) + \bar{\mathbf{p}}_{uv}^T \mathbf{C}_{uv}^{-1} \bar{\mathbf{p}}_{uv} > \varepsilon. \tag{5.41}$$

The first term in (5.41) is defined as

$$a(d_{\min}^2) = \frac{d_{\min}^2 (\bar{\mathbf{p}}_{uv} - \check{\mathbf{p}}_{uv})^T \mathbf{C}_{uv}^{-3} (\bar{\mathbf{p}}_{uv} - \check{\mathbf{p}}_{uv})}{(\bar{\mathbf{p}}_{uv} - \check{\mathbf{p}}_{uv})^T \mathbf{C}_{uv}^{-2} (\bar{\mathbf{p}}_{uv} - \check{\mathbf{p}}_{uv})} > 0, \tag{5.42}$$

which is positive because $\mathbf{C}_{uv}$ is positive definite. The second term in (5.41) is lower bounded by Cauchy–Schwarz inequality

$$b(d_{\min}) = -2d_{\min} \frac{(\bar{\mathbf{p}}_{uv} - \check{\mathbf{p}}_{uv})^T \mathbf{C}_{uv}^{-2} \bar{\mathbf{p}}_{uv}}{\|\mathbf{C}_{uv}^{-1}(\bar{\mathbf{p}}_{uv} - \check{\mathbf{p}}_{uv})\|} \tag{5.43}$$

$$\geqslant -2d_{\min} \frac{\|\mathbf{C}_{uv}^{-1}(\bar{\mathbf{p}}_{uv} - \check{\mathbf{p}}_{uv})\| \cdot \|\mathbf{C}_{uv}^{-1} \bar{\mathbf{p}}_{uv}\|}{\|\mathbf{C}_{uv}^{-1}(\bar{\mathbf{p}}_{uv} - \check{\mathbf{p}}_{uv})\|} \tag{5.44}$$

$$= -2d_{\min} \|\mathbf{C}_{uv}^{-1} \bar{\mathbf{p}}_{uv}\|. \tag{5.45}$$

Finally we can state a constraint for collision avoidance more conservative than

Lemma 5.5.1 as

$$h_{c,uv}(\mathbf{b}_{\mathcal{A}}) = -2d_{\min}\|\mathbf{C}_{uv}^{-1}\bar{\mathbf{p}}_{uv}\|+\bar{\mathbf{p}}_{uv}^{T}\mathbf{C}_{uv}^{-1}\bar{\mathbf{p}}_{uv} - \varepsilon > 0. \tag{5.46}$$

It is worth to notice when $d_{\min} = 0$, the constraint reduces to $\bar{\mathbf{p}}_{uv}^{T}\mathbf{C}_{uv}^{-1}\bar{\mathbf{p}}_{uv} > \varepsilon$, indicating the origin is outside the ellipse $\mathcal{E}(\bar{\mathbf{p}}_{uv}, \varepsilon\mathbf{C}_{uv})$. The derivative of $h_{c,uv}(\mathbf{b}_{\mathcal{A}})$ w.r.t. $\mathbf{b}_u$ is expressed as

$$\frac{\partial h_{c,uv}(\mathbf{b}_{\mathcal{A}})}{\partial \mathbf{b}_u} = 2\mathbf{C}_{uv}^{-1}\bar{\mathbf{p}}_{uv} - \frac{2d_{\min}\mathbf{C}_{uv}^{-2}\bar{\mathbf{p}}_{uv}}{\|\mathbf{C}_{uv}^{-1}\bar{\mathbf{p}}_{uv}\|} + \frac{\sigma^2\mathbf{b}_u}{\|\mathbf{b}_u\|}\left(\bar{\mathbf{p}}_{uv}^{T}\mathbf{C}_{uv}^{-2} - \frac{2d_{\min}\bar{\mathbf{p}}_{uv}^{T}\mathbf{C}_{uv}^{-3}}{\|\mathbf{C}_{uv}^{-1}\bar{\mathbf{p}}_{uv}\|}\right)\bar{\mathbf{p}}_{uv}. \tag{5.47}$$

The derivation details of (5.47) can be found in Appendix C.12.

In practice, the mean $\bar{\mathbf{p}}_{uv}$ can be replaced with the estimates $\hat{\mathbf{p}}_{uv} = \hat{\mathbf{p}}_u - \hat{\mathbf{p}}_v$. The collision avoidance introduced in this section assumes a Bayesian model of the state. However, it can be analogically extended to the non-Bayesian case, with the mean $\bar{\mathbf{p}}_{uv}$ as the true value and the covariance matrix approximated with the CRB calculated from the snapshot of measurements.

5.6 Simulation Results

Simulations with a variety of scenarios are conducted. The simulation results are not only to validate the proposed position-aware swarm control, but also consolidate the theoretic findings from Chapter 3.

Four scenarios are investigated, namely formation optimization for swarm self-localization, swarm returning to mission base guided by a single RF source, swarm navigation beyond the beacons' coverage and the case study of the Mars swarm exploration mission. None of the control objectives in these four applications could be accomplished by a single agent. However, the objectives can be achieved collectively by a swarm.

In Section 5.6.1, the swarm's formation is optimized for better self-localization performance by FI seeking. The impact of the choice of a swarm coordinate system, i.e. the baseline constrained swarm coordinate system $\mathbb{B}$ and the group motion constrained swarm coordinate system $\mathbb{C}$, is evaluated. The results verify the theoretical analysis in Section 3.3.

In Section 5.6.2, a returning to mission base application is considered. A single RF source is located at the mission base remotely from the swarm. The swarm optimizes its formation to minimize the position CRBs of itself and the RF source w.r.t. $\mathbb{B}$ in order

to return to the mission base. The emerging formation coincides with the preferable aperture analysis of the source localization in Section 3.4.

In Section 5.6.3, the swarm aims to navigation outside the beacons' measurement coverage, maintaining its self-localization ability. Two control strategies are compared, namely the homogeneous one, where all agents obey the same control rules, and the heterogeneous one, where one agent set the priorities of the objectives differently than the other agents. Both FI and BI seeking controls are evaluated. We also assess the benefit of having additional RF sources for swarm joint self- and source localization. These investigations are closely related to Section 3.3 - 3.5.

As the final scenario, the control aspect of the Mars swarm exploration mission introduced in Figure 1.2 is investigated in Section 5.6.4. A swarm intents to localize, and optionally to approach a gas source, while remaining a high accuracy of its self-localization. The scenarios of different nuisance parameters assumptions, number of RF sources, control strategies, objectives' combinations and information criteria, are evaluated. The final scenario demonstrates the adaptivity of the proposed position-aware swarm control. More importantly, it verifies the complete concept of the autonomous swarm navigation system proposed in this thesis.

The parameter set used in this section is summarized as follows. The same observation models as applied in Section 3.6.3.2 are used. The observed distance's standard deviations have been plotted in Figure 3.19 and will not be repeated here. Nuisance parameters include the clock offsets of the agents and RF sources, the carrier phase offsets of the RF sources, the scaling a_g and exponent factors b_g of the gas source. Agents move according to the mobility model described in (2.11)-(2.13), with $\sigma^2 = 0.1\,\mathrm{m}$ determining the agent's mobility uncertainty. Hence when an agent aims to move by 1000 m, it will suffer from a position noise with variance $100\,\mathrm{m}^2$. The maximum agent's step size is set to 0.2 m. The collision avoidance constraint is applied in all scenarios, with a minimum tolerated A2A distance of $d_{\min} = 50\,\mathrm{m}$ and a maximum acceptable violation probability of $\beta_{\min} = 5\%$. When the position information seeking objective is applied as a constraint, a maximum tolerated position error is set to $\varepsilon_{\max} = 1\,\mathrm{m}^2$. When the position information seeking objective and the goal approaching objective are jointly exploited as the cost function, the unconstrained preferable direction is generated by combing the gradient of the position information seeking objective $\mathbf{c}_{\mathcal{A}}^{p}$ and the gradient of the goal approaching objective $\mathbf{c}_{\mathcal{A}}^{g}$ as

$$\tilde{\mathbf{b}}_{\mathcal{A}} \propto -0.4\frac{\mathbf{c}_{\mathcal{A}}^{p}}{\|\mathbf{c}_{\mathcal{A}}^{p}\|} - 0.6\frac{\mathbf{c}_{\mathcal{A}}^{g}}{\|\mathbf{c}_{\mathcal{A}}^{g}\|}. \tag{5.48}$$

When both the heterogeneous control strategy and the goal approaching objective are

applied, the first agent $\mathbb{o}_1$ is assigned as the leader, whose unconstrained preferable direction is set to

$$\tilde{\mathbf{b}}_u \propto -0.001\frac{\mathbf{c}_u^p}{\|\mathbf{c}_{\mathcal{A}}^p\|} - 0.999\frac{\mathbf{c}_u^g}{\|\mathbf{c}_{\mathcal{A}}^g\|}, \tag{5.49}$$

where $\mathbf{c}_u^p$ and $\mathbf{c}_u^g$ are the components in $\mathbf{c}_{\mathcal{A}}^p$ and $\mathbf{c}_{\mathcal{A}}^g$, corresponding to $\mathbf{b}_u$. Agent $\mathbb{o}_1$ is referred to as a leader since when the position information seeking and the goal approaching objectives generate contradictory preferable directions, the agent $\mathbb{o}_1$ will have a higher priority to follow the goal approaching objective. We aim to verify the the proposed position-aware swarm control concept in general, rather than design a particular controller for certain applications. With the proposed concept, different swarm controller can be designed, given the criteria of the applications. In order to focus on the control aspect, a centralized EKF is implemented to track the state $\mathbf{x}_{\mathcal{X}}$ over time steps. EKF is a widely used Bayesian tracking algorithm with low complexity, which performs well with small state transition and measurement noise. In a real swarm application, a sophisticated and potentially decentralized tracking algorithm, for example the ones in [32, 33], or the proposed DiPNet and the CoA based source localization algorithm, could be preferable.

Different simulation scenarios are summarized in Table 5.1, with section index (**Sec.**), figure index (**Fig.**), number of agents ($|\mathcal{A}|$), RF sources ($|\mathcal{S}_{\text{RF}}|$), gas sources ($|\mathcal{S}_{\text{gas}}|$) and beacons ($|\mathcal{B}|$), coordinate system (**Coo.**), information criterion (**Info.**), cost functions (**Cost**), and the existence of unknown nuisance parameters (**Nui. par.**), position error constraint (**Pos. const.**) and leader (**Leader**). [1]

5.6.1 Formation Optimization for Self-Localization

The first scenario under investigation is the swarm formation optimization for self-localization. The swarm formation is optimized according to FI seeking control, so that the self-localization CRB is minimized. We are particularly interested in the impact of the choice of the swarm coordinate system on the emerging formations. The resulting formations considering the baseline constrained swarm coordinate system $\mathbb{B}$ and the group motion constrained swarm coordinate system $\mathbb{C}$ are compared. 30 agents are considered in the network, i.e. $\mathcal{V} = \mathcal{X} = \mathcal{A}$. Ranging measurements between agents are assumed, without the impact of clock offset. Hence only agents' positions are in the state vector, i.e. $\mathbf{x} = \mathbf{p}^{\mathbb{A}} = \mathbf{p}_{\mathcal{A}}^{\mathbb{A}}$, $\mathbb{A} \in \{\mathbb{B}, \mathbb{C}\}$. Position CRBs of agents are exploited as the cost function with equal weights, i.e. $f_p(\mathbf{b}_{\mathcal{A}}) = \text{Tr}[\text{CRB}[\mathbf{p}^{\mathbb{A}}]]$.

[1] Video clips of the position-aware swarm control performance in all considered scenarios can be found at https://ieeexplore.ieee.org/abstract/document/9089222.

Table 5.1. *Position-aware swarm control setup.*

Sec.	**Fig.**	$\lvert\mathcal{A}\rvert$	$\lvert\mathcal{S}_{\text{RF}}\rvert$	$\lvert\mathcal{S}_{\text{gas}}\rvert$	$\lvert\mathcal{B}\rvert$	**Coo.**	**Info.**	**Cost**	**Nui. par.**	**Pos. const.**	**Leader**
5.6.1	5.2	34	0	0	0	$\mathbb{B}$	FI	$\mathbf{\Lambda}_{\mathbf{p}_\mathcal{A}}$			
5.6.1	5.3	34	0	0	0	$\mathbb{C}$	FI	$\mathbf{\Lambda}_{\mathbf{p}_\mathcal{A}}$			
5.6.2	5.4	30	1	0	0	$\mathbb{B}$	FI	$\mathbf{\Lambda}_{\mathbf{p}_\mathcal{X}}$ goal			
5.6.3	5.5	50	0	0	6	$\mathbb{G}$	FI	$\mathbf{\Lambda}_{\mathbf{p}_\mathcal{A}}$ goal	✓	✓	
5.6.3	5.6	50	0	0	6	$\mathbb{G}$	FI	$\mathbf{\Lambda}_{\mathbf{p}_\mathcal{A}}$ goal	✓	✓	$\mathbb{c}_1$
5.6.3	5.7a	50	0	0	6	$\mathbb{G}$	BI	$\mathbf{\Lambda}_{\mathbf{p}_\mathcal{A}}$ goal	✓	✓	$\mathbb{c}_1$
5.6.3	5.7b	50	2	0	6	$\mathbb{G}$	BI	$\mathbf{\Lambda}_{\mathbf{p}_\mathcal{A}}$ goal	✓	✓	$\mathbb{c}_1$
5.6.4	5.8a	50	0	1	3	$\mathbb{G}$	FI	$\mathbf{\Lambda}_{\mathbf{p}_{\mathcal{S}_{\text{gas}}}}$		✓	
5.6.4	5.8b	50	2	1	3	$\mathbb{G}$	FI	$\mathbf{\Lambda}_{\mathbf{p}_{\mathcal{S}_{\text{gas}}}}$		✓	
5.6.4	5.9a	50	0	1	3	$\mathbb{G}$	FI	$\mathbf{\Lambda}_{\mathbf{p}_{\mathcal{S}_{\text{gas}}}}$	✓	✓	
5.6.4	5.9b	50	2	1	3	$\mathbb{G}$	FI	$\mathbf{\Lambda}_{\mathbf{p}_{\mathcal{S}_{\text{gas}}}}$	✓	✓	
5.6.4	5.10	50	0	1	3	$\mathbb{G}$	BI	$0.9\mathbf{\Lambda}_{\mathbf{p}_{\mathcal{S}_{\text{gas}}}}$ $0.1\mathbf{\Lambda}_{\mathbf{p}_\mathcal{A}}$ goal	✓	✓	$\mathbb{c}_1$
5.6.4	5.11	50	2	1	3	$\mathbb{G}$	BI	$0.9\mathbf{\Lambda}_{\mathbf{p}_{\mathcal{S}_{\text{gas}}}}$ $0.1\mathbf{\Lambda}_{\mathbf{p}_\mathcal{A}}$ goal	✓	✓	$\mathbb{c}_1$

Four snapshots of each coordinate system, $\mathbb{B}$ and $\mathbb{C}$, are shown in Figure 5.2 and Figure 5.3, respectively. Agents are illustrated as green dots, except the two defining the swarm coordinate system $\mathbb{B}$ in Figure 5.2, which are shown as the blue dots. Magenta ellipses indicate the 1 σ position CRBs of agents, which are only visible for the first two snapshots in the $\mathbb{B}$ case. An unfavorable short baseline is chosen for $\mathbb{B}$ as initiation. As a consequence, the agents far from the baseline experience large position CRBs, due to the undesirable geometry as discussed with Figure 3.2a. The collision avoidance constraint pushes the agents with large position CRBs away from each other, which can be seen in Figure 5.2b. The information seeking objective inherently optimizes the coordinate system by increasing the length of the baseline, as shown in Figure 5.2c. At the end, the swarm condenses to a regular lattice formation with agent spacing according to the minimal tolerated distance, as shown in Figure 5.2d. The condensed lattice formation is known to be a favorable formation for swarm self-localization, as been discussed with Figure 3.10. The information seeking control considering $\mathbb{C}$ does not need to optimize the coordinate system. Therefore, the swarm directly condenses into the favorable lattice formation faster than the $\mathbb{B}$ case, as shown in Figure 5.3.

5.6.2 Returning to Mission Base

The second considered scenario is a swarm returning to mission base. After exploring an area of interest 10 km away from the mission base, the swarm intends to return. We consider a more challenge case, where only a single RF source is located at the mission base.

The swarm optimizes its formation to improve the localization performances of itself and the RF source w.r.t. $\mathbb{B}$, in order to navigate itself returning to the mission base. 34 agents and one RF source are considered in the network, i.e. $\mathcal{V} = \mathcal{X} = \mathcal{A} \cup \mathcal{S}_{\text{RF}}$. Ranging measurements on A2A and S2A links are assumed, without the impact of clock offset. Hence only nodes' positions are in the state vector, i.e. $\mathbf{x} = \mathbf{p}^{\mathbb{B}} = \text{vec}\{\mathbf{p}^{\mathbb{B}}_{\mathcal{A}}, \mathbf{p}^{\mathbb{B}}_{\mathcal{S}_{\text{RF}}}\}$. Position CRBs of both agents and RF source are exploited as the cost function with equal weights, i.e. $f_p(\mathbf{b}_{\mathcal{A}}) = \text{Tr}[\text{CRB}[\mathbf{p}^{\mathbb{B}}]]$. Meantime goal approaching is desired, where the goal position is set to the RF source position in $\mathbb{B}$, i.e. $\mathbf{p}_g = \mathbf{p}^{\mathbb{B}}_{\mathcal{S}_{\text{RF}}}$.

Four snapshots are shown in Figure 5.4. The direction of the RF source is illustrated with the magenta dashed line. Agents are represented as green dots, except the two defining the swarm coordinate system $\mathbb{B}$, which are shown as the blue dots. Magenta ellipses indicate the position CRBs of agents. The swarm automatically spreads out vertically to direction of the RF source, which significantly increases the tangential aperture for source localization, which coincides with the theoretical analysis in Section 3.4. Meantime, agents remain connected with a regular lattice formation, to

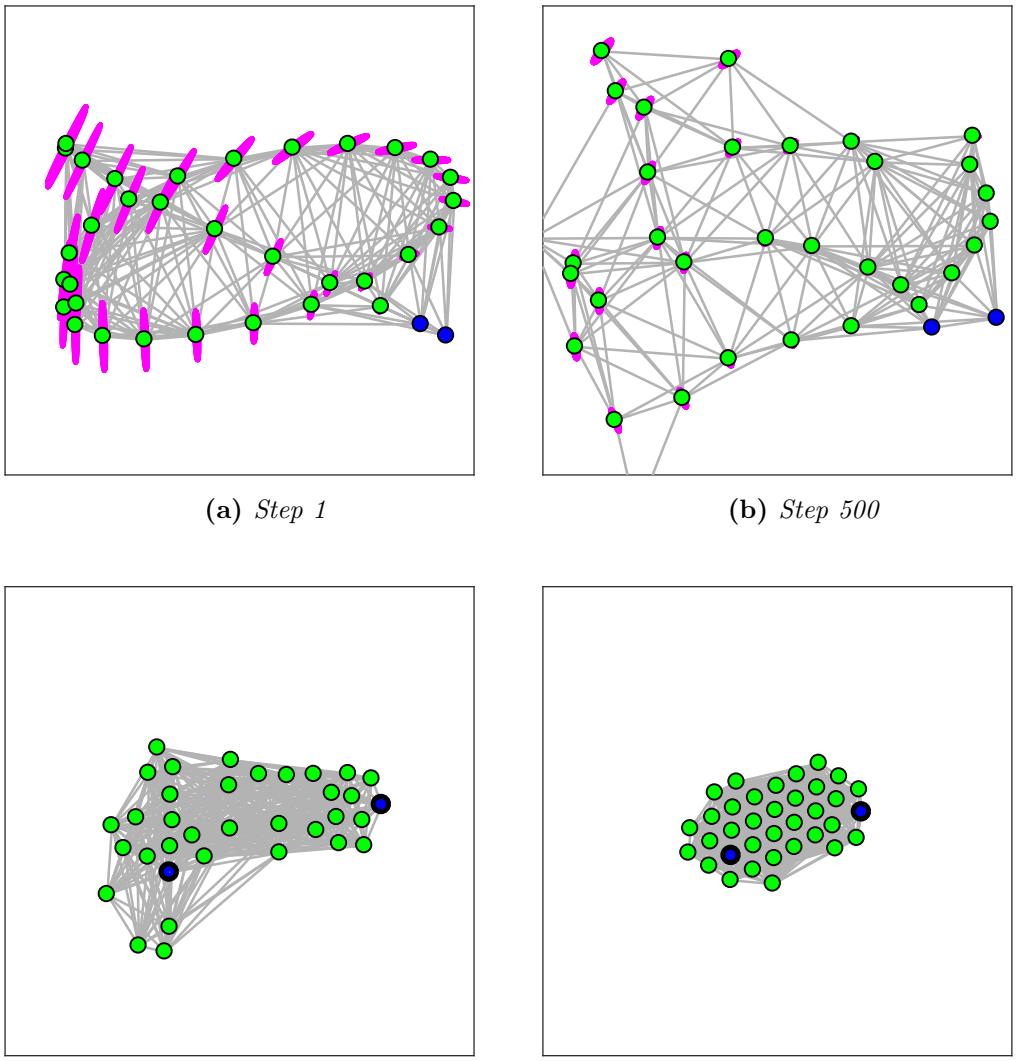

(a) *Step 1*

(b) *Step 500*

(c) *Step 1000*

(d) *Step 2000*

Figure 5.2. *FI seeking for swarm self-localization w.r.t.* $\mathbb{B}$*: Agents are illustrated as green dots, except the two used for defining the swarm coordinate system* $\mathbb{B}$*, which are shown as the blue dots. Magenta ellipses indicate the position CRBs of the agents.*

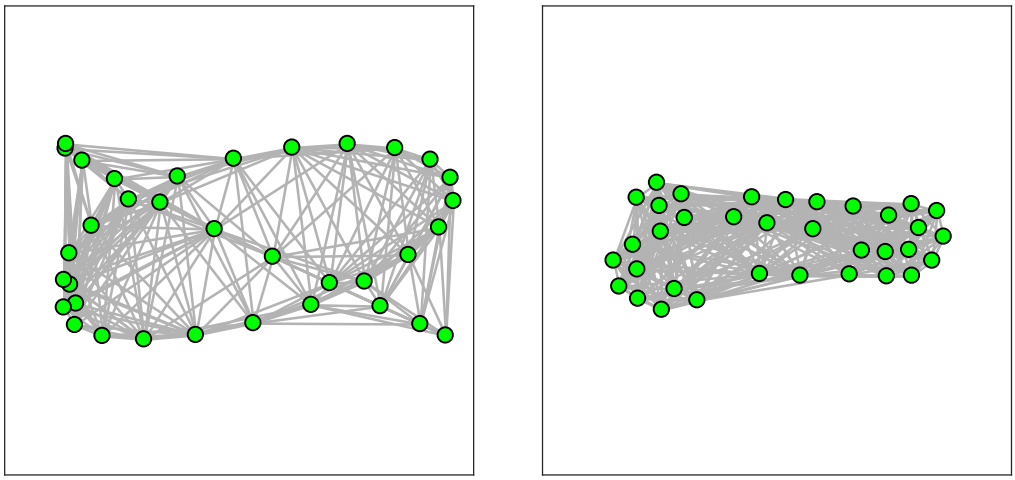

(a) *Step 1*

(b) *Step 100*

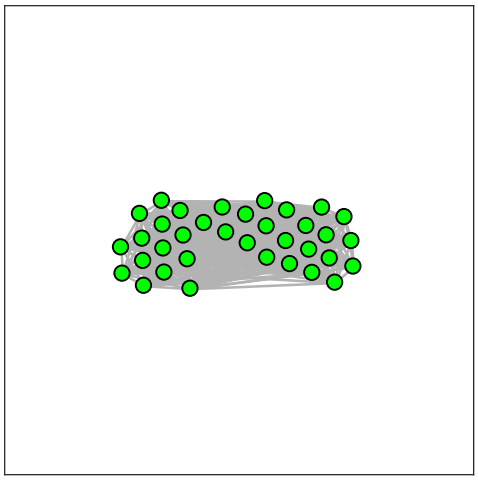

(c) *Step 300*

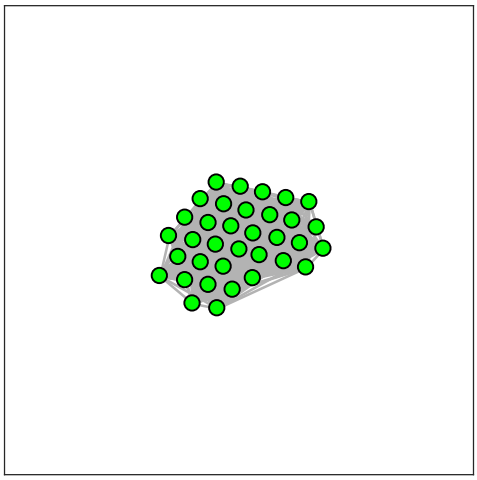

(d) *Step 2000*

Figure 5.3. *FI seeking for swarm self-localization w.r.t.* $\mathbb{C}$*: Similar scenario setup as in Figure 5.2, expect the group motion constrained swarm coordinate system* $\mathbb{C}$ *is applied. The magenta ellipses indicating the position CRBs of the agents are too small to be seen.*

perform self-localization. Similar to the swarm control for self-localization with $\mathbb{B}$ in Figure 5.2, the baseline is stretched, in order to optimized the coordinate system.

5.6.3 Bridging the Coverage Gap

The third scenario is swarm navigation outside the beacons' measurement coverage. Two groups of beacons are located 5 km apart, with the measurement coverage below 1 km. The swarm aims to travel from the left beacon group to the right beacon group, while performing self-localization in the global coordinate system $\mathbb{G}$ spanned by beacons. The goal is set to the center of the beacons on the right, i.e. $\mathbf{p}_g = \text{vec}\{5000, 0\}$. In order to reach the goal, the swarm has to cross an area over 3 km in length outside the carrier phase measurement coverage of the beacons. Nuisance parameters are assumed to be unknown. Four scenarios are considered, which evaluate the homogeneous and heterogeneous control strategies, the FI and BI seeking objectives, and the benefit of having additional RF sources to support swarm self-localization.

In the first scenario shown in Figure 5.5, the nodes with unknown states are only the agents, i.e. $\mathcal{X} = \mathcal{A}$, and total node set includes in addition the beacons, i.e. $\mathcal{V} = \mathcal{X} \cup \mathcal{B}$. The unweighted position CRBs of the agents are used as the FI seeking cost function, together with a goal approaching cost function. The maximum tolerated position error constraint and the homogeneous control strategy are applied. Three snapshots are shown in Figure 5.5. Beacons are shown as the blue dots. Agents are shown as dots with green edges. The gray scale colors on the agent dots illustrate the logarithmic value of the agents' position CRBs. It can be observed that the agents in front move in a cluster, until reaching 2,500 m, where the agents' position CRBs approach the maximum tolerated position error of $\varepsilon_{\max}$.

In the second scenario shown in Figure 5.6, the scenario setup is similar to the one in Figure 5.5, except a heterogeneous control strategy is applied. The agent acts as a leader is marked in orange. The leader moves faster towards the goal, and therefore, pulls its neighbors. The cluster effect is avoided. As a result, the agents in front are stabilized at 3,000 m, which is 500 m closer to the goal compared with the homogeneous control strategy.

The third scenario shown in Figure 5.7a has a similar setup as the second one shown in Figure 5.6, except the position PCRBs are exploited as cost function instead of the CRB. The gray scale colors on agent dots show the logarithmic values of the position PCRBs. With Bayesian tracking, the swarm is able to form a bridge connecting the two areas with beacons. Hence, the swarm can travel from the left area to the right one, fulfilling the position error constraint.

The last scenario further extends the setup of the third one in Figure 5.7a with two

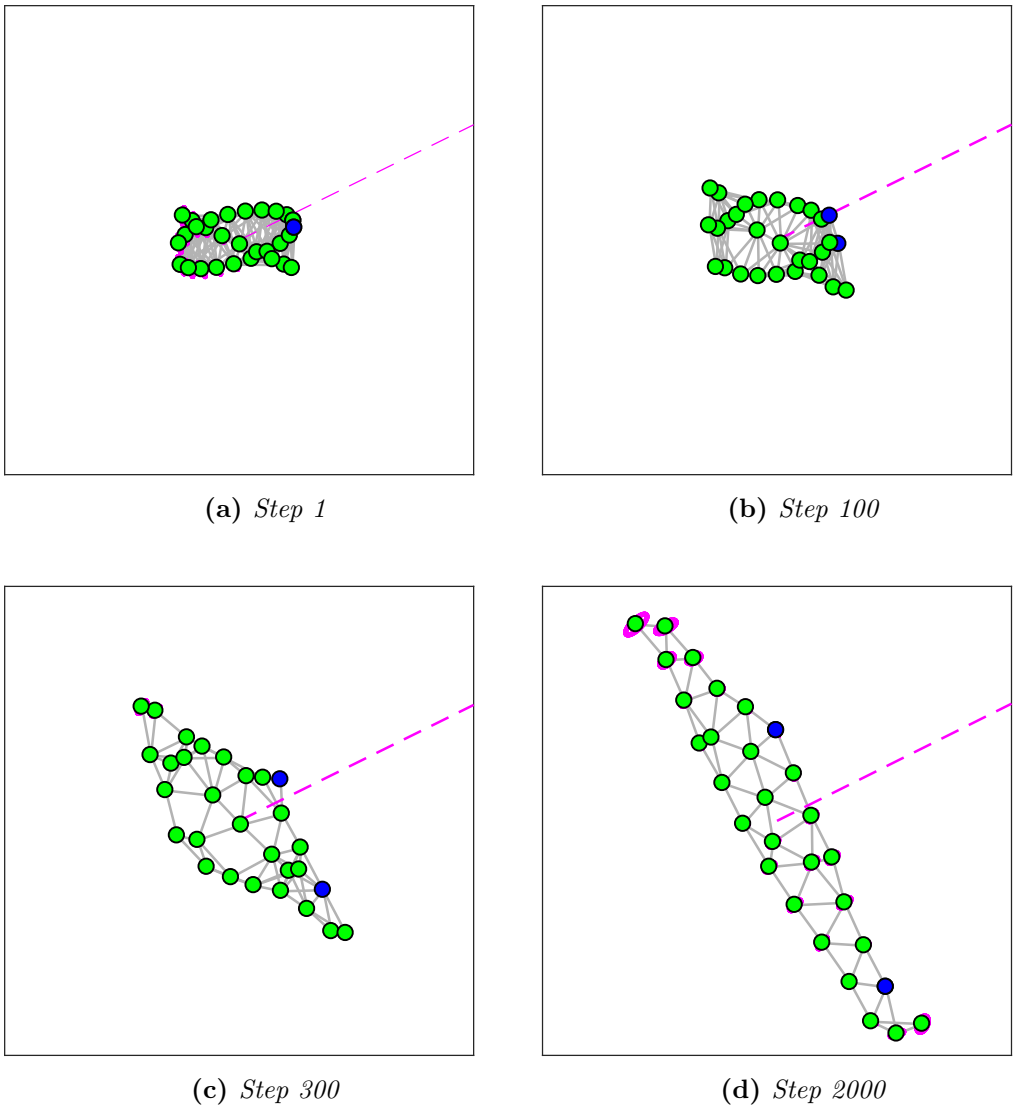

(a) *Step 1* **(b)** *Step 100*

(c) *Step 300* **(d)** *Step 2000*

Figure 5.4. *FI seeking swarm control for swarm self- and RF source localization w.r.t.* $\mathbb{B}$*: A RF source is located at the mission base 10 km from the swarm, whose direction is illustrated with the magenta dashed line. The swarm aims to minimize the position CRBs of itself and the RF source w.r.t.* $\mathbb{B}$ *in order to return to the mission base. Agents are shown as green dots, expect the two used for defining the swarm coordinate system* $\mathbb{B}$*, which are shown as the blue dots. Magenta ellipses indicate the position CRBs of the agents.*

additional RF sources, which is shown in Figure 5.7b. The position of the RF sources are jointly estimated with the swarm position. The RF sources' position PCRBs are not used as the control objectives. It can be observed that with the support of the RF sources, the swarm only needs to build a bridge between the RF sources and the goal. The swarm formation is less stretched with better self-localization performances, in comparison with the third scenario in Figure 5.7a.

5.6.4 Position-Aware Control in Mars Swarm Exploration Mission

In the last scenario we conduct a case study of the proposed position-aware swarm control in the Mars swarm exploration mission introduced in Figure 1.2. A swarm is initially deployed close to the mission base and aim to localize a gas source 4 km away.

We start with the FI seeking control illustrated in Figure 5.8a-Figure 5.9b. Only the position CRB of the gas is considered as the cost function, which is explicitly minimized, i.e. $\mathbf{\Lambda}_p = \mathbf{\Lambda}_{\mathbf{p}_{\text{gas}}}$. Maximum agents' position CRBs constraint and the homogeneous control strategy are applied.

In the first (Figure 5.8a) and second (Figure 5.8b) cases, the nuisance parameters are assumed to be known. In the other two cases illustrated in Figure 5.9a and Figure 5.9b, unknown nuisance parameters are assumed. In Figure 5.8a and Figure 5.9a, there are no RF sources, while in Figure 5.8b and Figure 5.9b, two RF sources are placed in the middle of the field with unknown positions. The gray scale colors on the agent dots represent their position CRBs valued in logarithm.

The formations without nuisance parameters spread out mainly in the direction perpendicular to the gas source's direction, aiming to maximize the tangential swarm aperture towards the gas source, hence improving the source AoA performance. Meantime, the swarm tries to be closer to the source, to improve the measurement quality, s.t. fulfilling the maximum agents' position CRBs constraint.

With nuisance parameters, both source AoA and distance estimation prefer a large swarm tangential aperture. The nuisance parameters a_g and b_g act on the gas concentration as scaling and exponent factor, which are not additive to the link distance d_{uv} as in (3.73). Therefore, according to Section 3.4.2, the source distance information can not only inferred from the observation with the tangential swarm aperture, but also the with the radial aperture. As a result, the swarm intends to also expand in the horizontal direction. Some agents even move in the opposite direction of the source, so that the swarm's radial aperture is maximized s.t. fulfilling the maximum tolerated agents' position CRBs constraint. The additional RF sources support the swarm, in

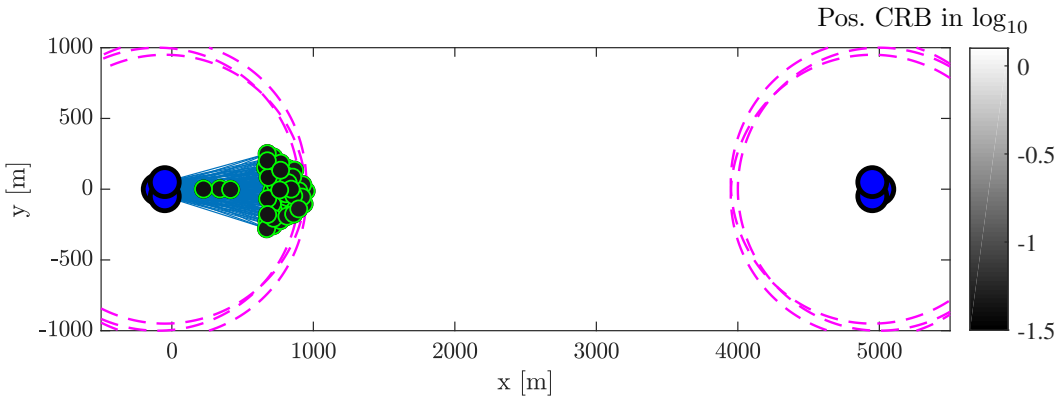

(a) *Step 15,200*

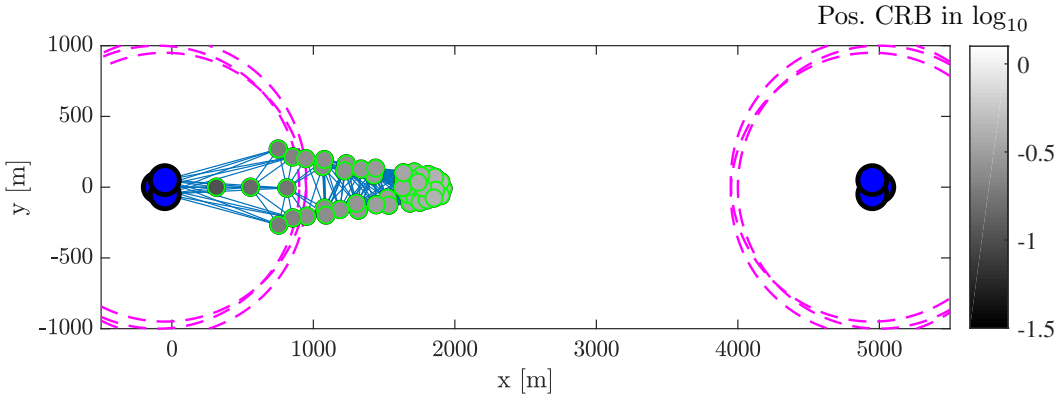

(b) *Step 26,800*

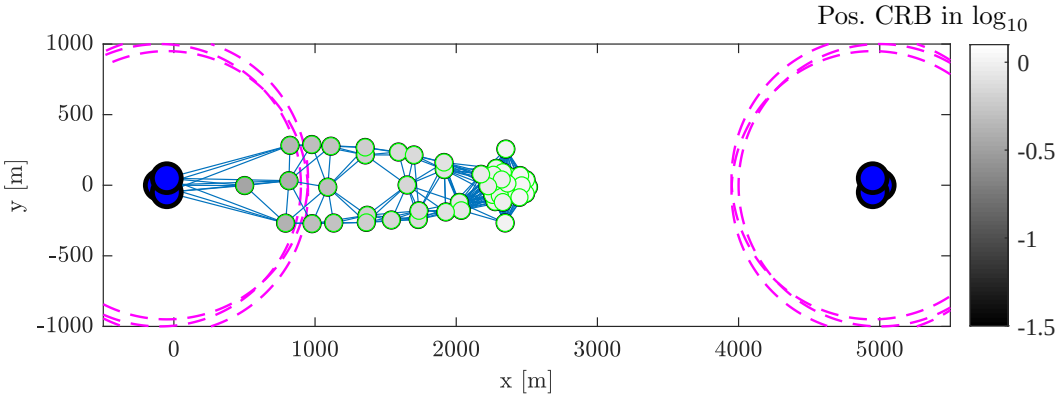

(c) *Step 38,800*

Figure 5.5. *FI seeking swarm control for swarm self-localization w.r.t.* $\mathbb{G}$*: Two groups of beacons are located 5 km apart, with the measurement coverage illustrated as the magenta circles. The swarm aims to travel from the left beacon group to the right beacon group, meantime minimizing its position CRB. The maximum tolerated position error and the homogeneous control strategy are applied. Nuisance parameters are assumed to be unknown. Beacons are shown as the blue dots. Agents are shown as dots with green edges. The colors of the agent dots indicate the value of their position CRBs in logarithm.*

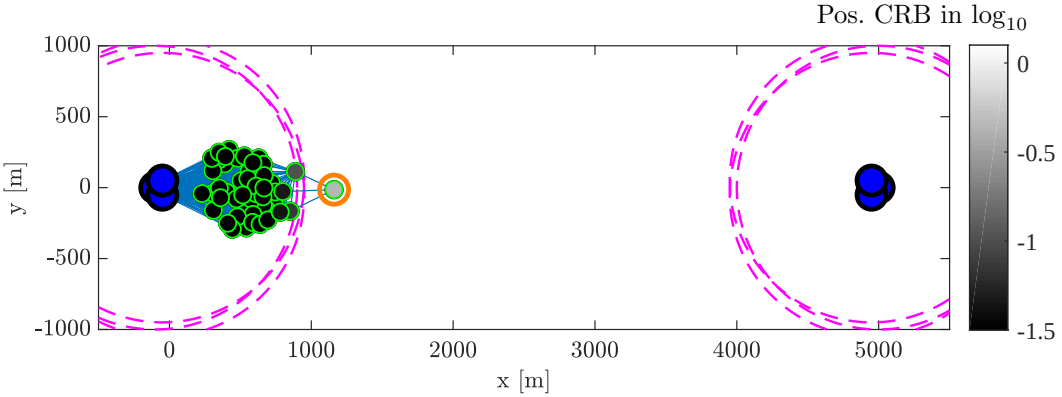

(a) *Step 2,000*

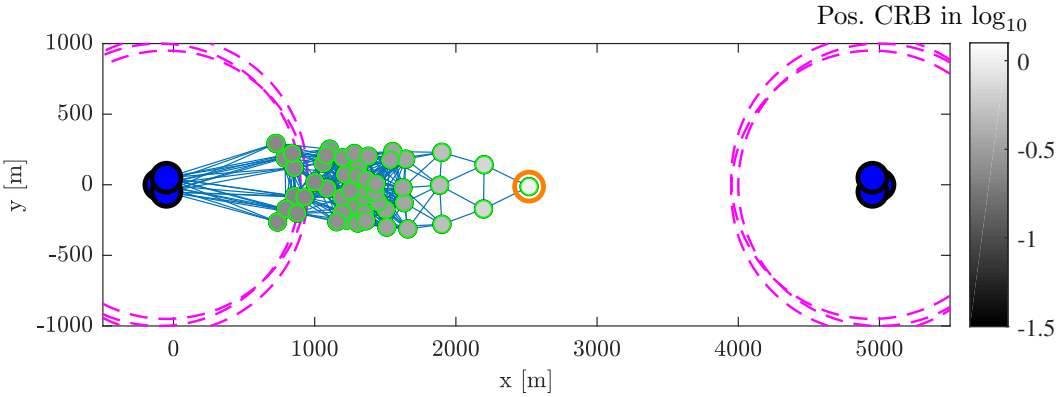

(b) *Step 10,000*

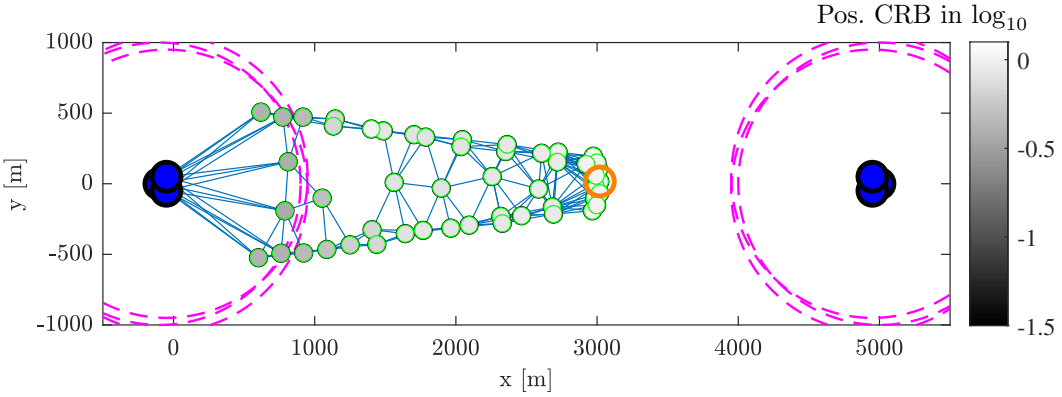

(c) *Step 40,000*

Figure 5.6. *FI seeking swarm control for swarm self-localization w.r.t.* $\mathbb{G}$*: Similar scenario setup as in Figure 5.5, except a heterogeneous control strategy is applied with the leader agent marked with an orange circle.*

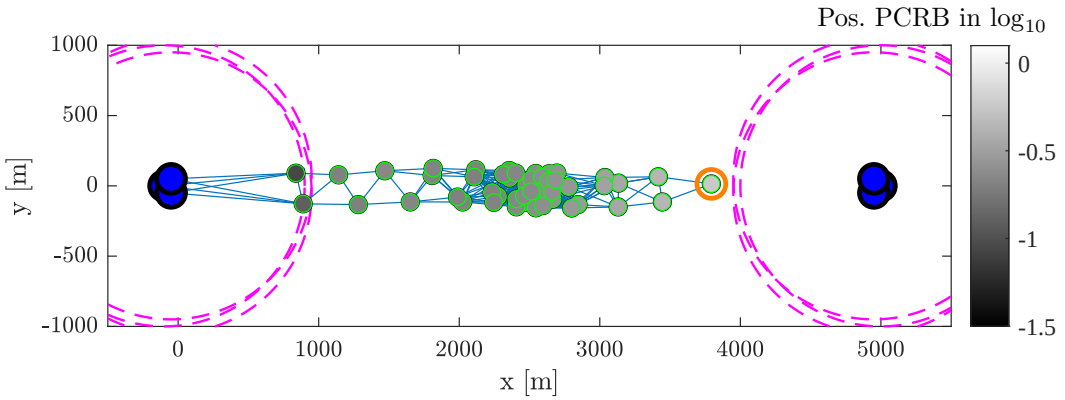

(a) *Without RF source at step 21,500*

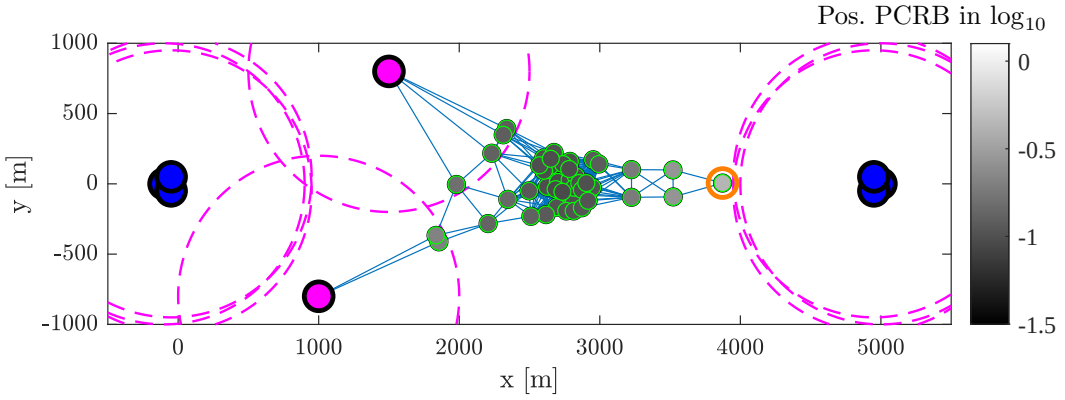

(b) *With 2 RF sources at step 22,500*

Figure 5.7. *BI seeking swarm control for swarm self- (and RF source in Figure 5.7b) localization w.r.t.* $\mathbb{G}$*: Similar scenario setup as in Figure 5.6, except the PCRBs of the swarm's positions are exploited for the position information seeking objectives instead of the CRBs. In Figure 5.7b two RF sources are added, whose positions are jointly estimated. The position PCRBs of the RF sources are not used as the control objectives. The RF sources are illustrated with magenta dots, with their measurement coverage shown as magenta circles. The colors of the agent dots indicate the value of their position PCRBs in logarithm.*

further extending its aperture, even though their positions need to be jointly estimated.

At last, we compare two BI seeking control scenarios with (Figure 5.10) and without (Figure 5.11) the support from additional RF sources.

In both scenarios, the BI seeking objective is set as the mixture of 10% agents information seeking and 90% gas source information seeking, i.e. $\mathbf{\Lambda}_p = 0.1\mathbf{\Lambda}_{\mathbf{p}_\mathcal{A}} + 0.9\mathbf{\Lambda}_{\mathbf{p}_{\text{gas}}}$. A goal approaching objective is included with the heterogeneous swarm control strategy. The maximum tolerated agents' position PCRBs constraint is applied. All nuisance parameters are considered as unknown. We also compare the position PCRBs of the agents, RF sources and the gas source with the estimation performances from the EKF. The gray scale colors on the nodes in Figure 5.10a and Figure 5.11a represent the position PCRBs of the nodes, while the ones in Figure 5.10b and Figure 5.11b indicate the absolute position error of the nodes at the same snapshot.

The formations in Figure 5.10a and Figure 5.11a share some similarities with the ones in Figure 5.7a and Figure 5.7b, respectively, due to similar goal approaching and agents BI seeking objectives. However, in Figure 5.10a and Figure 5.11a the swarm intends to expand its tangential aperture, which is due to the gas source BI seeking objective. Interestingly, in both Figure 5.10a and Figure 5.11a, the leader marked in orange is still in the front of the swarm, however, it is no longer in the leading position. It is due to the gas source BI seeking objective, which motivates the swarm to come closer to the gas source. As a consequence, the information seeking and goal approaching objectives do not generate contradictory preferable moving directions. Therefore, the heterogeneous swarm control strategy can not guarantee the leader to be at the leading position of the swarm. Last but not least, in Figure 5.10 the EKF performance coincides with the PCRBs. In Figure 5.11 the EKF performs generally worse than the PCRBs. It is due to an estimation bias of the RF sources introduced from the highly nonlinear measurement model. Despite the bias, EKF provides around one meter accuracy to the joint swarm self- and source localization in this challenge scenario, which is sufficient for the position-aware swarm control.

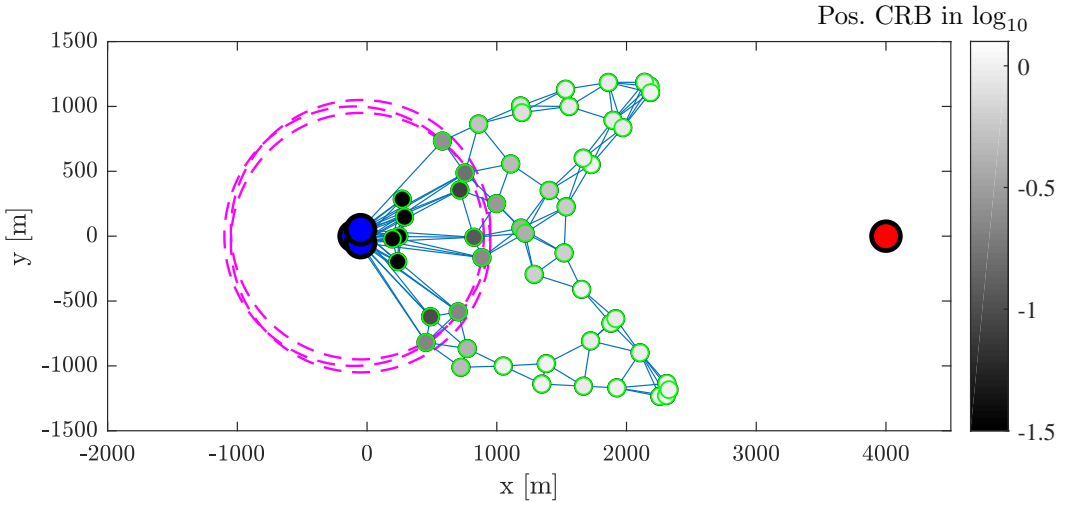

(a) *Without RF source*

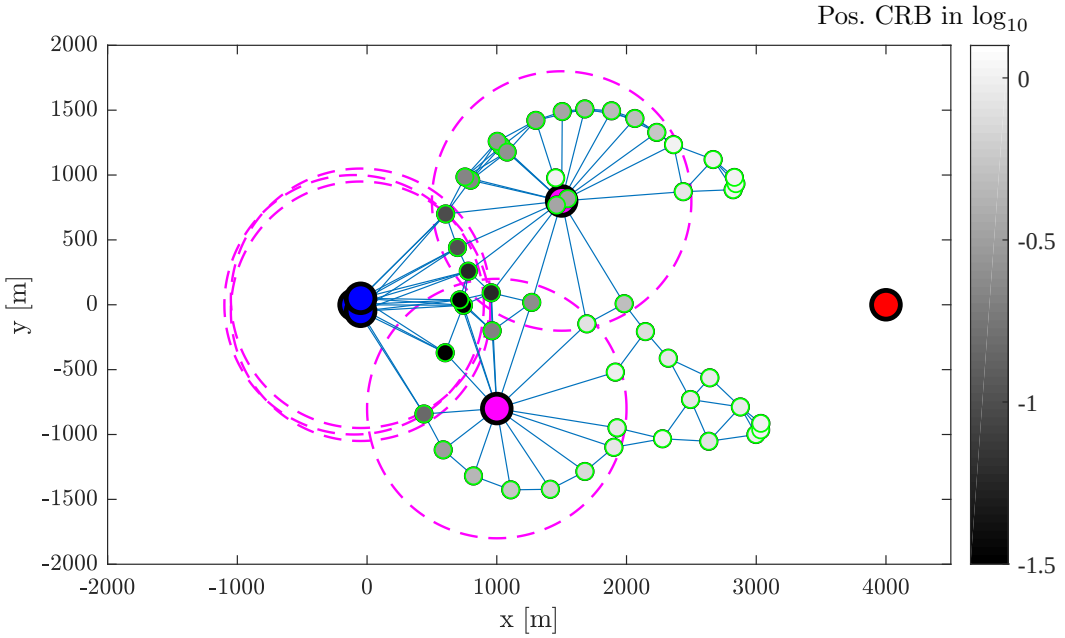

(b) *With 2 RF sources*

Figure 5.8. *FI seeking swarm control for swarm self- and source localization w.r.t.* $\mathbb{G}$*: Three beacons, shown as blue dots, are deployed at the mission base. Swarm aims to minimize the position CRB of a gas source, shown by the red dot, located 4 km away from the mission base. Similar as in Figure 5.7b, two RF sources are added in Figure 5.8b, whose positions are jointly estimated but the position CRBs are not used as the control objectives. Nuisance parameters are assumed to be known. Formations at time step 40,000 are shown. The colors of the agent dots indicate the value of their position CRBs in logarithm.*

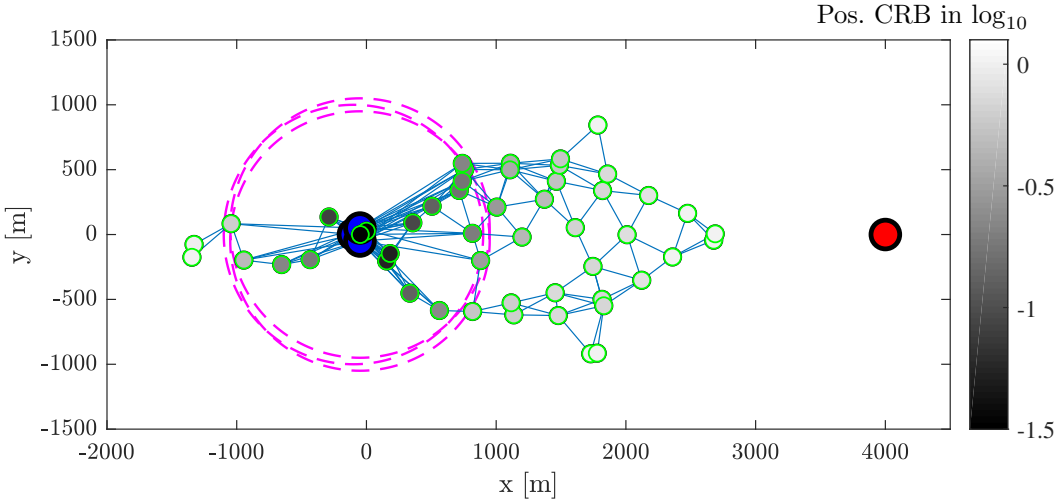

(a) *Without RF source*

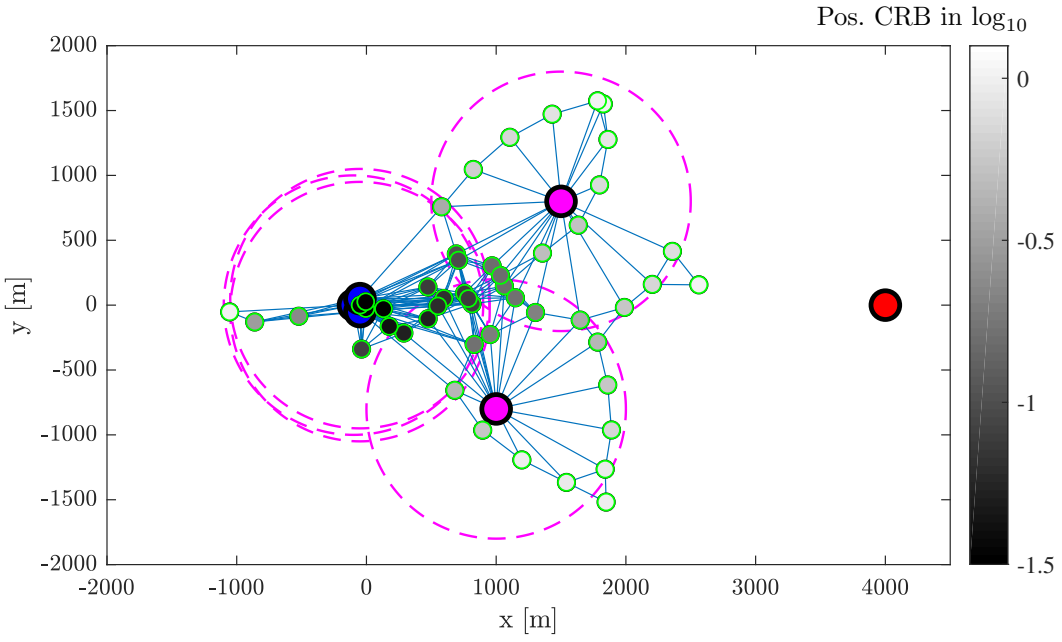

(b) *With 2 RF sources*

Figure 5.9. *FI seeking swarm control for swarm self- and source localization w.r.t.* $\mathbb{G}$*: Similar scenario setup as in Figure 5.8, except the nuisance parameters are assumed to be unknown.*

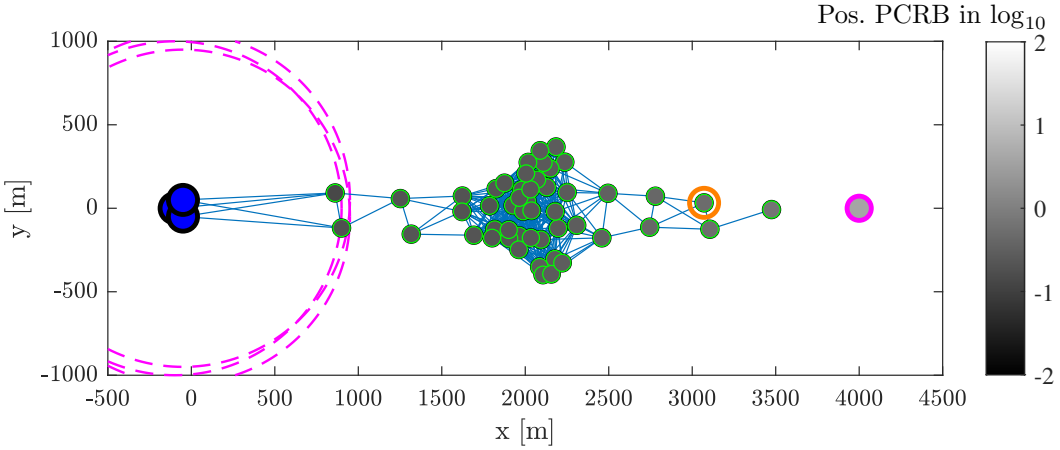

(a) *Position PCRBs at step 16,000*

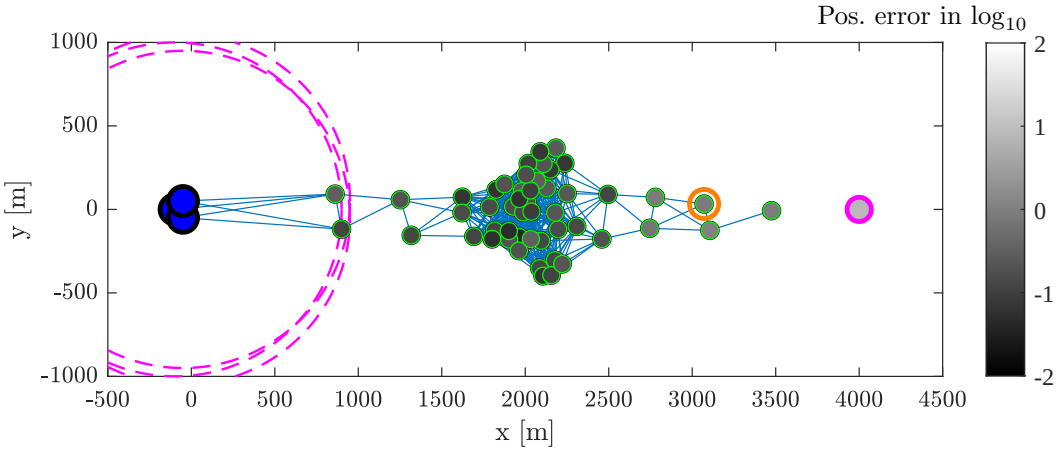

(b) *Localization error from EKF at step 16,000*

Figure 5.10. *BI seeking swarm control for swarm self- and source localization w.r.t.* $\mathbb{G}$*: Similar scenario setup as in Figure 5.9a. A heterogeneous swarm control strategy is applied, with the leader agent marked in orange. A mixture of swarm and gas position PCRBs is exploited as the position information seeking objectives. A goal approaching objective is added, where the swarm tries to approach the gas source in addition to localization. The nuisance parameters are assumed to be unknown. The colors of the agent and the source dots in Figure 5.10a and Figure 5.10b indicate the logarithmic value of their position PCRBs and their localization error from the EKF, respectively at the current step.*

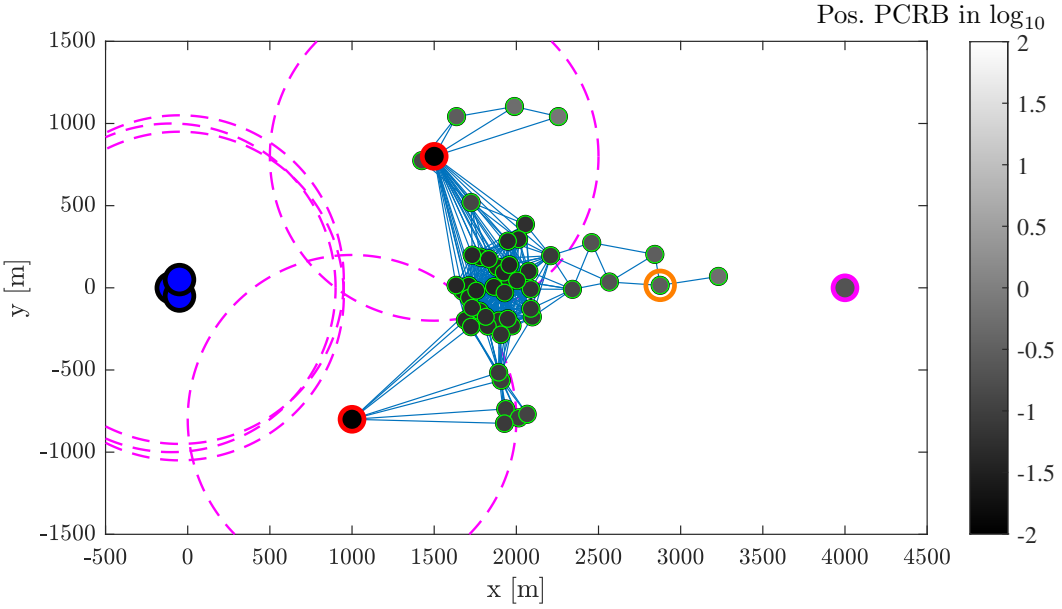

(a) *Position PCRB at step 16,000*

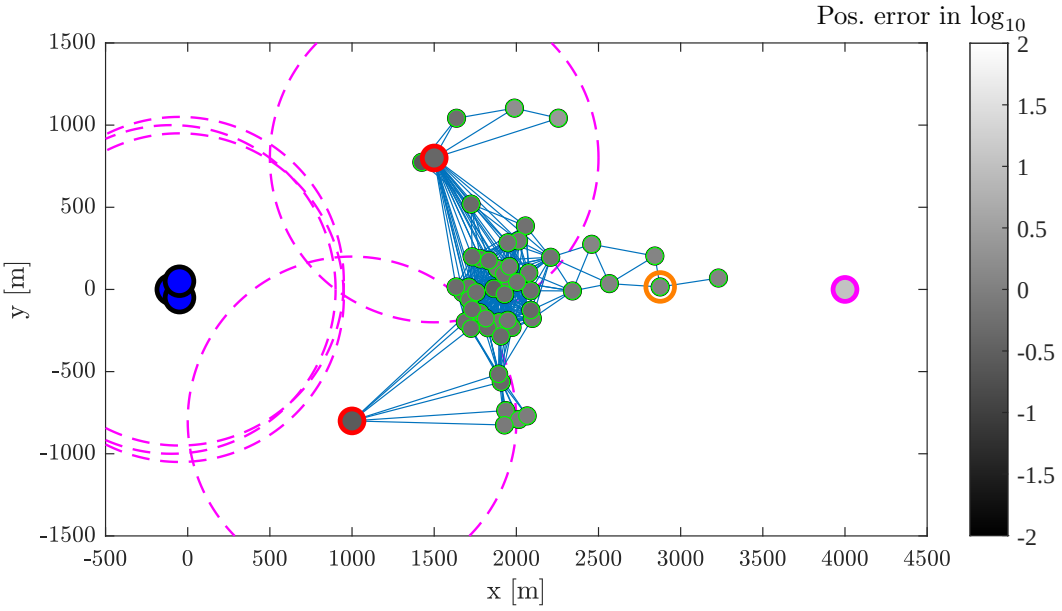

(b) *Localization error from EKF at step 16,000*

Figure 5.11. *Similar scenario setup as in Figure 5.10, except two RF sources are added for the joint localization. The RF sources' position PCRBs and the localization error are illustrated by the colors as well. The RF sources' position PCRBs is not exploited for control objectives.*

Chapter 6

Conclusion and Outlook

6.1 Conclusion

Robotic swarm is a promising system for a wide variety of sensing and exploration applications. Position awareness of the swarm itself and external entities is essential for the success of an autonomous swarm application, like future Mars swarm exploration. The implication of *position awareness* is threefold with three gradually increasing awareness levels, namely (1) awareness of position estimates, (2) awareness of position uncertainty, and (3) awareness of potential actions to enrich position information. The three position awareness levels are closely related to autonomous swarm navigation, including swarm self- and source localization corresponding to the first two levels, and swarm control corresponding to the third level. As a newly emerging technology, a thorough study of autonomous swarm navigation was still missing.

In this thesis, we have systematically studied the navigation problem of a general class of swarm, where generic signals are emitted from isotropic point emitters and observed by agents for navigation. Distance information between the emitter and the receiving agent could be in general inferred from either intensity features or propagation time features of the received signals. In particular w.r.t. the Mars swarm exploration mission considered in this thesis, the emitters are RF signal transmitters, such as agents in the swarm, beacons and RF sources, as well as a gas source. Features such as the carrier phases and symbol delays of the received RF signals and the gas concentration are exploited for swarm self- and source localization.

In comparison with traditional navigation systems, some distinguishing properties of swarm navigation systems are identified, such as non-trivial coordinate system, scalable topology, decentralization, collective behavior, coupling of localization and control, latency intolerance, etc. We have adequately investigated swarm navigation, partic-

ularly focusing on these properties. In this thesis, we covered both general swarm navigation theory, and an in-depth study on the specific swarm navigation system proposed for Mars exploration.

A formal generic swarm navigation definition was introduced. The theoretic potential of swarm localization were discussed, emphasizing on the interpretations of the reference systems, collective performance and scalability. Estimation theoretical tools, especially the Fisher information (FI) theory, are the core components throughout this thesis, not only in the theoretical analysis but also in the design of localization and control algorithms particularly suitable for swarm systems.

Concerning swarm self-localization, FI was interpreted with different forms of CRBs. A collaboration gain of the swarm self-localization has been proved to be proportional to the swarm's cardinality $|\mathcal{A}|$. The connectivity-ranging trade-off has been evaluated with ranging ZZB, which verifies the existence of an optimal RF measurement coverage for agents, balancing the connectivity and ranging accuracy for swarm self-localization.

A decentralized swarm self-localization algorithm dubbed DiPNet was proposed, exploiting the large cardinality property of the swarm. An agent's position was directly estimated from the received RF signal waveform, incorporating position uncertainty of neighboring nodes, with a low complexity multi-link fusion scheme. It was proved that the multipath and NLOS effects on DiPNet became insignificant for dense networks, due to the massive-link collective processing. Both simulations and experiments verified that DiPNet achieves a near-optimal performance with low complexity, superior to traditional two-step approaches. Therefore, it is particularly attractive for realtime swarm self-localization.

Considering swarm source localization, the swarm was collectively treated as a distributed large scale array. Geometrical interpretation of swarm source localization with different classes of observation has been investigated. Properties of source localization have been proved, which is useful to either design an optimal swarm formation for source localization, or verify the resulting swarm formation of the source position information seeking control. We decompose the swarm aperture into the perpendicular aperture towards the source and the radial aperture along the direction of the source. Source's AoA information can be inferred from the observations captured by the tangential aperture, independent of the nuisance parameters. In contrast, the source's distance estimation strongly depends on the type and knowledge of the nuisance parameters. If there is no nuisance parameter, the source distance information can be simply inferred from the distance related observation of individual links. If and only if the nuisance parameters are unknown and additive to the link distance, such as

the clock offset and the carrier phase offset of RF signals, the source distance is not observable from the radial aperture. The source distance can still be estimated with the tangential aperture, by observing the curvature of the spherical signal front, due to the isotropic source. We referred this technique to as curvature of arrival (CoA) based source localization, and proposed an algorithm exploiting the relation between the signal CoA and the source distance. The proposed algorithm was verified to be superior to the state of the art low complexity near field source localization algorithm. For other types of unknown nuisance parameters, such as the scaling and exponent factors of the gas source, source distance information is contained in the observations captured by both tangential and radial apertures.

Additionally, the mutual enhancement of swarm self-localization and source localization was addressed. Precise swarm position information is required for source localization. By collectively observing the source, a swarm's position information is further enriched.

Position aware swarm control was an other aspect of autonomous swarm navigation we investigated. Three swarm objectives have been introduced as examples, namely the goal approaching, the collision avoidance and the position information seeking. For goal approaching, only the first level of position awareness was required. For collision avoidance, the swarm needed to reach the second level of position awareness. Hence, not only the position estimates, but also the uncertainty of those estimates are crucial to collision avoidance objective. We designed a controller which limited the maximum probability of violation, assuming arbitrary distribution of agents' positions, given only the BIs of the agents. Position information seeking was the core component of the position aware swarm control. The position information qualities of the swarm itself as well as the sources were quantified by the FI for a snapshot based control and the BI for a Bayesian based control. Having derived analytically the closed-form expressions of the information gradients, control commands could be generated efficiently, allowing a large-scale swarm actively seeking position information. Position information could be flexibly chosen as either cost functions or constraints for swarm control, depending on the applications. As a result, the swarm actively adapted its formation to improve localization of itself and the sources, without losing track of other mission objectives. Unlike most of the traditional formation control methods, which focus on assembling and maintaining a predefined target formation, the position aware swarm control brings a justification to the swarm formation that emerges. The proposed position-aware swarm control concept has been verified in different scenarios of swarm exploration missions, such as self-localization, exploration area approaching, returning to mission base after exploration, gas source searching, etc.

As the final conclusion of the thesis, we proposed a generic concept of autonomous swarm navigation, which has been verified for a specific Mars swarm exploration system under investigation. More importantly, the concept can be generally adapted to a wide variety of swarm applications.

6.2 Outlook

Autonomous swarm navigation is an emerging interdisciplinary topic with proliferated applications. The work presented in this thesis helps us to gain some insight into the topic, instead of attempting to cover all the aspects exhaustively. A further investigation in the following directions may lead to a fruitful discovery:

1) Advanced models

   In order to obtain a fundamental understanding of swarm navigation system, abstract models have been widely assumed in this thesis. The extension to advanced models needs to be investigated. The agent's dynamic model can be extended with its attitude, velocity, acceleration, measurements from inertial sensors, and low level control loop. RF signals between nodes are emphasized through the thesis. Realistic channel models have been considered in the design and validation of DiPNet. The impacts of channel models on the fundamental limits of swarm navigation, CoA-based source localization, and swarm control deserve a further study. In addition, an advanced clock model should be considered, which may lead to challenges in swarm network synchronization. Besides of the RF signals, observations from other signals, like gas emission, with more sophisticated models can be considered.

2) Extension on optimal reference system

   Fundamentals in reference system of anchor-free localization has been addressed. It would be interesting to further extend the group motion constrained optimal reference system to Bayesian tracking, decentralized localization algorithm design and swarm control.

3) Decentralized information matrix estimation

   For the information seeking control, a full awareness of the estimated FIM or BIM entities is required. However, most of the BP based decentralized localization algorithms, like DiPNet proposed in this thesis, only approximate a partition of information at each node. A adequate study on decentralized calculating or approximating the entities of these information matrices is important in designing a fully decentralized swarm control algorithm.

Bibliography

[1] M. Ballerini *et al.*, "Interaction ruling animal collective behavior depends on topological rather than metric distance: Evidence from a field study," *Proceedings of the National Academy of Sciences*, vol. 105, no. 4, pp. 1232–1237, 2008.

[2] C. W. Reynolds, "Flocks, herds and schools: A distributed behavioral model," in *Proc. 14th Annu. Conf. Computer Graphics and Interactive Techniques*, ser. SIGGRAPH '87. New York, NY, USA: ACM, 1987, pp. 25–34.

[3] S. Johnson, *Emergence: The Connected Lives of Ants, Brains, Cities, and Software*, ser. Touchstone Book. Simon & Schuster, 2001.

[4] M. Moussaid, S. Garnier, G. Theraulaz, and D. Helbing, "Collective information processing and pattern formation in swarms, flocks, and crowds," *Topics in Cognitive Science*, vol. 1, no. 3, pp. 469–497, 2009.

[5] M. G. Hinchey, R. Sterritt, and C. Rouff, "Swarms and swarm intelligence," *IEEE Computer*, vol. 40, no. 4, pp. 111–113, Apr. 2007.

[6] S. Chung, A. A. Paranjape, P. Dames, S. Shen, and V. Kumar, "A survey on aerial swarm robotics," *IEEE Trans. Robot.*, vol. 34, no. 4, pp. 837–855, Aug. 2018.

[7] H. Hamann, *Swarm Robotics: A Formal Approach*, 1st ed. Springer Publishing Company, Incorporated, 2018.

[8] S. Li, R. Batra, D. Brown, H.-D. Chang, N. Ranganathan, C. Hoberman, D. Rus, and H. Lipson, "Particle robotics based on statistical mechanics of loosely coupled components," *Nature*, vol. 567, pp. 361–365, Mar. 2019.

[9] M. Bernard, K. Kondak, I. Maza, and A. Ollero, "Autonomous transportation and deployment with aerial robots for search and rescue missions," *J. Field Robot.*, vol. 28, no. 6, pp. 914–931, 2011.

[10] M. Dunbabin and L. Marques, "Robots for environmental monitoring: Significant advancements and applications," *IEEE Robot. Autom. Mag.*, vol. 19, no. 1, pp. 24–39, Mar. 2012.

[11] A. Seeni, B. Schfer, and G. Hirzinger, "Robot mobility systems for planetary surface exploration – state-of-the-art and future outlook: A literature survey," in *Aerospace Technologies Advancements*, T. T., Ed. London: InTech, Jan. 2010, pp. 189–208.

[12] A. Wedler *et al.*, "From single autonomous robots toward cooperative robotic interactions for future planetary exploration missions," in *Proc. Int. Astronautical Congr., IAC*. Bremen: International Astronautical Federation (IAF), Oct. 2018.

[13] P. van Vugt, A. Meijerink, and M. Bentum, "Calibration of the OLFAR space-based radio telescope using a weighted alternating least squares approach," in *2017 IEEE Aerospace Conference*, Mar. 2017, pp. 1–11.

[14] F. Mondada, L. M. Gambardella, D. Floreano, S. Nolfi, J. L. Deneuborg, and M. Dorigo, "The cooperation of swarm-bots: physical interactions in collective robotics," *IEEE Robot. Autom. Mag.*, vol. 12, no. 2, pp. 21–28, Jun. 2005.

[15] A. L. Christensen, R. O'Grady, and M. Dorigo, "From fireflies to fault-tolerant swarms of robots," *IEEE Trans. Evol. Comput.*, vol. 13, no. 4, pp. 754–766, Aug. 2009.

[16] E. Vassev, R. Sterritt, C. Rouff, and M. Hinchey, "Swarm technology at NASA: Building resilient systems," *IEEE IT Prof.*, vol. 14, no. 2, pp. 36–42, Mar. 2012.

[17] W. F. Truszkowski, M. G. Hinchey, J. L. Rash, and C. A. Rouff, "Autonomous and autonomic systems: A paradigm for future space exploration missions," *IEEE Trans. Syst., Man, Cybern. C*, vol. 36, no. 3, pp. 279–291, May 2006.

[18] N. R. Raz and M. Akbarzadeh-T., "Swarm-fuzzy rule-based targeted nano delivery using bioinspired nanomachines," *IEEE Trans. Nanobiosci.*, pp. 1–1, 2019.

[19] M. Schwager, B. J. Julian, M. Angermann, and D. Rus, "Eyes in the sky: Decentralized control for the deployment of robotic camera networks," *Proc. IEEE*, vol. 99, no. 9, pp. 1541–1561, Sep. 2011.

[20] M. Bajracharya, M. W. Maimone, and D. Helmick, "Autonomy for Mars rovers: Past, present, and future," *IEEE Computer*, vol. 41, no. 12, pp. 44–50, Dec. 2008.

[21] S. Engelen, E. Gill, and C. Verhoeven, "On the reliability, availability, and throughput of satellite swarms," *IEEE Trans. Aerosp. Electron. Syst.*, vol. 50, no. 2, pp. 1027–1037, Apr. 2014.

[22] W. Truszkowski, M. Hinchey, J. Rash, and C. Rouff, "NASA's swarm missions: The challenge of building autonomous software," *IEEE IT Prof.*, vol. 6, no. 5, pp. 47–52, Sep. 2004.

[23] H. Naseri and V. Koivunen, "Cooperative simultaneous localization and mapping by exploiting multipath propagation," *IEEE Trans. Signal Process.*, vol. 65, no. 1, pp. 200–211, Jan. 2017.

[24] C. Taylor, A. Rahimi, J. Bachrach, H. Shrobe, and A. Grue, "Simultaneous localization, calibration, and tracking in an ad hoc sensor network," in *2006 5th International Conference on Information Processing in Sensor Networks*, Apr. 2006, pp. 27–33.

[25] F. Meyer, H. Wymeersch, M. Fröhle, and F. Hlawatsch, "Distributed estimation with information-seeking control in agent networks," *IEEE J. Sel. Areas Commun.*, vol. 33, no. 11, pp. 2439–2456, Nov. 2015.

[26] B. Etzlinger, F. Meyer, F. Hlawatsch, A. Springer, and H. Wymeersch, "Cooperative simultaneous localization and synchronization in mobile agent networks," *IEEE Trans. Signal Process.*, vol. 65, no. 14, pp. 3587–3602, Jul. 2017.

[27] S. M. Kay, *Fundamentals of Statistical Signal Processing, Volume I: Estimation Theory*, 1st ed. Englewood Cliffs, N.J: Prentice Hall, 1993.

[28] Y. Shen, H. Wymeersch, and M. Win, "Fundamental limits of wideband localization, part II: Cooperative networks," *IEEE Trans. Inf. Theory*, vol. 56, no. 10, pp. 4981–5000, 2010.

[29] M. Z. Win, Y. Shen, and W. Dai, "A theoretical foundation of network localization and navigation," *Proc. IEEE*, vol. 106, no. 7, pp. 1136–1165, Jul. 2018.

[30] H. L. Van Trees, *Optimum Array Processing, Part IV*, ser. Detection, Estimation, and Modulation Theory / Harry L. Van Trees. New York: Wiley, 2002, no. 4.

[31] P. Tichavsky, C. H. Muravchik, and A. Nehorai, "Posterior Cramér-Rao bounds for discrete-time nonlinear filtering," *IEEE Trans. Signal Process.*, vol. 46, no. 5, pp. 1386 –1396, May 1998.

[32] H. Wymeersch, J. Lien, and M. Win, "Cooperative localization in wireless networks," *Proc. IEEE*, vol. 97, no. 2, pp. 427 –450, Feb. 2009.

[33] R. M. Buehrer, H. Wymeersch, and R. M. Vaghefi, "Collaborative sensor network localization: Algorithms and practical issues," *Proc. IEEE*, vol. 106, no. 6, pp. 1089–1114, Jun. 2018.

[34] J. J. Spilker Jr, P. Axelrad, B. W. Parkinson, and P. Enge, *Global positioning system: Theory and applications, Volume I.* American Institute of Aeronautics and Astronautics, 1996.

[35] B. W. Parkinson, P. Enge, P. Axelrad, and J. J. Spilker Jr, *Global positioning system: Theory and applications, Volume II.* American Institute of Aeronautics and Astronautics, 1996.

[36] R. M. Murray, "Recent research in cooperative control of multivehicle systems," *J. Dyn. Sys., Meas., Control*, vol. 129(5), pp. 571–583, 2007.

[37] K.-K. Oh, M.-C. Park, and H.-S. Ahn, "A survey of multi-agent formation control," *Automatica*, vol. 53, pp. 424–440, Mar. 2015.

[38] J. Shamma, *Cooperative Control of Distributed Multi-Agent Systems.* New York, NY, USA: Wiley-Interscience, 2008.

[39] W. Ren and Y. Cao, *Distributed Coordination of Multi-Agent Networks: Emergent Problems, Models, and Issues.* Springer Science & Business Media, Nov. 2010.

[40] W. Yu, G. Wen, G. Chen, and J. Cao, *Distributed Cooperative Control of Multi-Agent Systems.* John Wiley & Sons, May 2017.

[41] R. Olfati-Saber, "Flocking for multi-agent dynamic systems: Algorithms and theory," *IEEE Trans. Autom. Control*, vol. 51, no. 3, pp. 401–420, Mar. 2006.

[42] K. Oh and H. Ahn, "Formation control of mobile agents based on distributed position estimation," *IEEE Trans. Autom. Control*, vol. 58, no. 3, pp. 737–742, Mar. 2013.

[43] Y. Cai and Y. Shen, "An integrated localization and control framework for multi-agent formation," *IEEE Trans. Signal Process.*, vol. 67, no. 7, pp. 1941–1956, Apr. 2019.

[44] M. Ye, B. D. O. Anderson, and C. Yu, "Bearing-only measurement self-localization, velocity consensus and formation control," *IEEE Trans. Aerosp. Electron. Syst.*, vol. 53, no. 2, pp. 575–586, Apr. 2017.

[45] Y. Kim, G. Zhu, and J. Hu, "Optimizing formation rigidity under connectivity constraints," in *IEEE Conference on Decision and Control (CDC)*, 2010, pp. 6590–6595.

[46] F. Morbidi and G. L. Mariottini, "Active target tracking and cooperative localization for teams of aerial vehicles," *IEEE Trans. Control Syst. Technol.*, vol. 21, no. 5, pp. 1694–1707, 2013.

[47] J. N. Ash and R. L. Moses, "On the relative and absolute positioning errors in self-localization systems," *IEEE Trans. Signal Process.*, vol. 56, no. 11, pp. 5668–5679, Nov. 2008.

[48] J. Aspnes, T. Eren, D. K. Goldenberg, A. S. Morse, W. Whiteley, Y. R. Yang, B. D. O. Anderson, and P. N. Belhumeur, "A theory of network localization," *IEEE Trans. Mobile Comput.*, vol. 5, no. 12, pp. 1663–1678, Dec. 2006.

[49] M. Arulampalam, S. Maskell, N. Gordon, and T. Clapp, "A tutorial on particle filters for online nonlinear/non-Gaussian Bayesian tracking," *IEEE Trans. Signal Process.*, vol. 50, no. 2, pp. 174 –188, Feb. 2002.

[50] B. Ristic, S. Arulampalam, and N. Gordon, *Beyond the Kalman Filter - Particle Filters for Tracking Applications.* Artech House, 2004.

[51] S. Zhang, R. Raulefs, A. Dammann, and S. Sand, "System-level performance analysis for Bayesian cooperative positioning: From global to local," in *International Conference on Indoor Positioning and Indoor Navigation (IPIN).* IEEE, 2013, pp. 1–10.

[52] S. Mazuelas, A. Bahillo, R. M. Lorenzo, P. Fernandez, F. A. Lago, E. Garcia, J. Blas, and E. J. Abril, "Robust indoor positioning provided by real-time RSSI values in unmodified WLAN networks," *IEEE J. Sel. Topics Signal Process.*, vol. 3, no. 5, pp. 821–831, Oct. 2009.

[53] T. Wiedemann, D. Shutin, and A. J. Lilienthal, "Model-based gas source localization strategy for a cooperative multi-robot system—a probabilistic approach and experimental validation incorporating physical knowledge and model uncertainties," *Rob. Auton. Syst.*, 2019.

[54] M. Viberg, "Introduction to array processing," in *Array and Statistical Signal Processing*, ser. Academic Press Library in Signal Processing, A. M. Zoubir, M. Viberg, R. Chellappa, and S. Theodoridis, Eds. Boston: Elsevier, 2014, vol. 3, ch. 11, pp. 463–502.

[55] R. Pöhlmann, S. A. Almasri, S. Zhang, T. Jost, A. Dammann, and P. A. Hoeher, "On the potential of multi-mode antennas for direction-of-arrival estimation," *IEEE Trans. Antennas Propag.*, vol. 67, no. 5, pp. 3374–3386, May 2019.

[56] D. Dardari, A. Conti, U. Ferner, A. Giorgetti, and M. Z. Win, "Ranging with ultrawide bandwidth signals in multipath environments," *Proc. IEEE*, vol. 97, no. 2, pp. 404–426, Feb. 2009.

[57] I. Guvenc and C. Chong, "A survey on TOA based wireless localization and NLOS mitigation techniques," *IEEE Commun. Surveys Tuts.*, vol. 11, no. 3, pp. 107–124, rd 2009.

[58] E. Staudinger, S. Zhang, and A. Dammann, "Cramer-Rao lower bound for round-trip delay ranging with subcarrier-interleaved OFDMA," *IEEE Trans. Aerosp. Electron. Syst.*, vol. 52, no. 6, pp. 2961–2972, Dec. 2016.

[59] J. J. Caffery, *Wireless Location in CDMA Cellular Radio Systems.* Norwell, MA, USA: Kluwer Academic Publishers, 1999.

[60] M. Cobos, F. Antonacci, A. Alexandridis, A. Mouchtaris, and B. Lee, "A survey of sound source localization methods in wireless acoustic sensor networks," *Wirel. Commun. Mob. Com.*, vol. 2017, pp. 1–24, 2017.

[61] C. Rascon and I. Meza, "Localization of sound sources in robotics: A review," *Rob. Auton. Syst.*, vol. 96, pp. 184–210, 2017.

[62] N. Poiata, C. Satriano, J. P. Vilotte, P. Bernard, and K. Obara, "Multiband array detection and location of seismic sources recorded by dense seismic networks," *Geophys. J. Int.*, vol. 205, no. 3, pp. 1548–1573, 2016.

[63] C. Nicol, A. Ellery, B. Lynch, E. Cloutis, and G. de Croon, "Martian methane plume models for defining Mars rover methane source search strategies," *Int. J. Astrobiol.*, vol. 17, no. 3, pp. 228–238, 2018.

[64] A. J. Lilienthal, M. Reggente, M. Trincavelli, J. L. Blanco, and J. Gonzalez, "A statistical approach to gas distribution modelling with mobile robots - the Kernel DM+V algorithm," in *2009 IEEE/RSJ International Conference on Intelligent Robots and Systems*, Oct. 2009, pp. 570–576.

[65] M. Schmuker, V. Bahr, and R. Huerta, "Exploiting plume structure to decode gas source distance using metal-oxide gas sensors," *Sensors and Actuators, B: Chemical*, vol. 235, pp. 636–646, 2016.

[66] J. G. Proakis and M. Salehi, *Digital Communications*, 5th ed. Boston, Mass.: McGraw-Hill, 2008.

[67] S. Zhang, T. Jost, R. Pöhlmann, A. Dammann, D. Shutin, and P. A. Hoeher, "Spherical wave positioning based on curvature of arrival by an antenna array," *IEEE Wireless Commun. Lett.*, vol. 8, no. 2, pp. 504–507, Apr. 2019.

[68] J. Crank and E. Crank, *The Mathematics of Diffusion*, ser. Oxford science publications. Clarendon Press, 1979.

[69] T. Wiedemann, C. Manss, and D. Shutin, "Multi-agent exploration of spatial dynamical processes under sparsity constraints," *Auton. Agents Multi-Agent Syst.*, vol. 32, no. 1, pp. 134–162, Jan. 2018.

[70] H. Van Trees, *Detection, estimation, and modulation theory, Part I*, ser. Detection, Estimation, and Modulation Theory. Wiley, 1968.

[71] H. V. Poor, *An Introduction to Signal Detection and Estimation*. New York: Springer, 1994.

[72] P. Stoica and B. C. Ng, "On the Cramér-Rao bound under parametric constraints," *IEEE Signal Process. Lett.*, vol. 5, no. 7, pp. 177–179, Jul. 1998.

[73] Y. Shen and M. Z. Win, "Fundamental limits of wideband localization, part I: A general framework," *IEEE Trans. Inf. Theory*, vol. 56, no. 10, pp. 4956–4980, Oct. 2010.

[74] H. L. V. Trees and K. L. Bell, *Bayesian Bounds for Parameter Estimation and Nonlinear Filtering/Tracking*. Wiley-IEEE Press, 2007.

[75] J. Ziv and M. Zakai, "Some lower bounds on signal parameter estimation," *IEEE Trans. Inf. Theory*, vol. 15, no. 3, pp. 386–391, May 1969.

[76] D. Dardari and M. Z. Win, "Ziv-Zakai bound on time-of-arrival estimation with statistical channel knowledge at the receiver," in *Proc. IEEE Int. Conf. Ultra-Wideband*, Sep. 2009, pp. 624–629.

[77] K. L. Bell, Y. Steinberg, Y. Ephraim, and H. L. Van Trees, "Extended Ziv-Zakai lower bound for vector parameter estimation," *IEEE Trans. Inf. Theory*, vol. 43, no. 2, pp. 624–637, Mar. 1997.

[78] K. Zhang, Y. Shen, and M. Z. Win, "On the performance of map-aware cooperative localization," in *2016 IEEE International Conference on Communications (ICC)*, May 2016, pp. 1–6.

[79] V. M. Chiriac, A. M. Haimovich, S. C. Schwartz, and J. A. Dabin, "Performance bound for localization of a near field source," in *2009 Conference Record of the 43rd Asilomar Conference on Signals, Systems and Computers*, Nov. 2009, pp. 130–135.

[80] V. M. Chiriac, Q. He, A. M. Haimovich, and R. S. Blum, "Ziv–Zakai bound for joint parameter estimation in MIMO radar systems," *IEEE Trans. Signal Process.*, vol. 63, no. 18, pp. 4956–4968, Sep. 2015.

[81] H. L. Van Trees, *Detection, Estimation, and Linear Modulation Theory.* Hoboken, NJ: Wiley-Interscience, 2002.

[82] S. Zhang, S. Sand, R. Raulefs, and E. Staudinger, "Self-organized hybrid channel access method for an interleaved RTD-based swarm navigation system," in *Workshop on Positioning, Navigation and Communication, Dresden, Germany*, 2013.

[83] S. Zhang, E. Staudinger, S. Sand, R. Raulefs, and A. Dammann, "Anchor-free localization using round-trip delay measurements for martian swarm exploration," in *Proc. IEEE/ION Position, Location and Navigation Symp. - PLANS 2014*, May 2014, pp. 1130–1139.

[84] S. Zhang, E. Staudinger, T. Jost, W. Wang, C. Gentner, A. Dammann, H. Wymeersch, and P. A. Hoeher, "Distributed direct localization suitable for dense networks," *IEEE Trans. Aerosp. Electron. Syst.*, pp. 1–1, 2019.

[85] S. Zhang, M. Frohle, H. Wymeersch, A. Dammann, and R. Raulefs, "Location-aware formation control in swarm navigation," in *Proc. IEEE Globecom Workshops (GC Wkshps)*, Dec. 2015, pp. 1–6.

[86] P. Stoica and T. L. Marzetta, "Parameter estimation problems with singular information matrices," *IEEE Trans. Signal Process.*, vol. 49, no. 1, pp. 87–90, Jan. 2001.

[87] J. Lien, U. J. Ferner, W. Srichavengsup, H. Wymeersch, and M. Z. Win, "A comparison of parametric and sample-based message representation in cooperative localization," *International Journal of Navigation and Observation*, 2012.

[88] E. Staudinger and A. Dammann, "Round-trip delay ranging with OFDM signals-performance evaluation with outdoor experiments," in *2014 11th Workshop on Positioning, Navigation and Communication (WPNC)*, Mar. 2014, pp. 1–6.

[89] J. B. Lasserre, "A trace inequality for matrix product," *IEEE Trans. Autom. Control*, vol. 40, no. 8, pp. 1500–1501, Aug. 1995.

[90] A. Emmanuele, *Signal Design and Theoretical Bounds for Time-of-Arrival Estimation in GNSS Applications.* PhD Thesis, University of Pisa, 2012.

[91] P. Stoica and P. Babu, "The Gaussian data assumption leads to the largest Cramér-Rao bound [lecture notes]," *IEEE Signal Process. Mag.*, vol. 28, no. 3, pp. 132–133, May 2011.

[92] K. Meyberg and P. Vachenauer, *Höhere Mathematik 2: Differentialgleichungen · Funktionentheorie Fourier-Analysis · Variationsrechnung*, ser. Springer-Lehrbuch. Springer Berlin Heidelberg, 1991.

[93] C. A. Balanis, *Antenna Theory: Analysis and Design.* John Wiley & Sons, 2015.

[94] J.-P. Delmas, M. N. El Korso, H. Gazzah, and M. Castella, "CRB analysis of planar antenna arrays for optimizing near-field source localization," *Signal Processing*, vol. 127, pp. 117 – 134, Oct. 2016.

[95] A. Shahmansoori *et al.*, "Position and orientation estimation through millimeter-wave MIMO in 5G systems," *IEEE Trans. Wireless Commun.*, vol. 17, no. 3, pp. 1822–1835, Mar. 2018.

[96] Y. Han, Y. Shen, X. Zhang, M. Z. Win, and H. Meng, "Performance limits and geometric properties of array localization," *IEEE Trans. Inf. Theory*, vol. 62, no. 2, pp. 1054–1075, Feb. 2016.

[97] T. E. Tuncer and B. Friedlander, *Classical and Modern Direction-of-Arrival Estimation.* Boston: Academic Press, 2009.

[98] D. Waidelich, "The phase centers of aperture antennas," *IEEE Trans. Antennas Propag.*, vol. 28, no. 2, pp. 263–264, Mar. 1980.

[99] X. Song, D. Cvetkovski, W. Rave, E. Grass, and G. Fettweis, "Sequential channel equalization in strong line-of-sight MIMO communication," *IEEE Trans. Wireless Commun.*, vol. 18, no. 1, pp. 340–356, Jan. 2019.

[100] X. Yin *et al.*, "Scatterer localization using large-scale antenna arrays based on a spherical wave-front parametric model," *IEEE Trans. Wireless Commun.*, vol. 16, no. 10, pp. 6543–6556, Oct. 2017.

[101] E. Grosicki, K. Abed-Meraim, and Y. Hua, "A weighted linear prediction method for near-field source localization," *IEEE Trans. Signal Process.*, vol. 53, no. 10, pp. 3651–3660, Oct. 2005.

[102] J. Chen, X. Zhu, and X. Zhang, "A new algorithm for joint range-DoA-frequency estimation of near-field sources," *EURASIP Journal on Advances in Signal Processing*, vol. 2004, no. 3, p. 105173, Mar. 2004.

[103] K. Deng, Q. Yin, and H. Wang, "Closed form parameters estimation for near field sources," in *2007 IEEE International Symposium on Circuits and Systems*, May 2007, pp. 3251–3254.

[104] Y. Hsu, K. T. Wong, and L. Yeh, "Mismatch of near-field bearing-range spatial geometry in source-localization by a uniform linear array," *IEEE Trans. Antennas Propag.*, vol. 59, no. 10, pp. 3658–3667, Oct. 2011.

[105] P. R. Singh, Y. Wang, and P. Chargé, "Performance enhancement of approximated model based near–field sources localisation techniques," *IET Signal Processing*, vol. 11, no. 7, pp. 825–829, 2017.

[106] D. C. Popescu, M. Hedley, and T. Sathyan, "Posterior Cramér-Rao Bound for anchorless tracking," *IEEE Signal Process. Lett.*, vol. 20, no. 12, pp. 1183–1186, Dec. 2013.

[107] W. Wang, T. Jost, C. Mensing, and A. Dammann, "ToA and TDoA error models for NLoS propagation based on outdoor to indoor channel measurement," in *IEEE Wireless Communications and Networking Conference, 2009, WCNC*, 2009, pp. 1 – 6.

[108] Y. Zhu, A. Jiang, and H. K. Kwan, "ADMM-based sensor network localization using low-rank approximation," *IEEE Sensors J.*, vol. 18, no. 20, pp. 8463–8471, Oct. 2018.

[109] A. T. Ihler, J. W. Fisher, R. L. Moses, and A. S. Willsky, "Nonparametric belief propagation for self-localization of sensor networks," *IEEE J. Sel. Areas Commun.*, vol. 23, no. 4, pp. 809–819, Apr. 2005.

[110] N. Patwari, J. N. Ash, S. Kyperountas, A. O. Hero, R. L. Moses, and N. S. Correal, "Locating the nodes: Cooperative localization in wireless sensor networks," *IEEE Signal Process. Mag.*, vol. 22, no. 4, pp. 54–69, Jul. 2005.

[111] G. Mao, B. Fidan, and B. D. O. Anderson, "Wireless sensor network localization techniques," *Comput. Netw.*, vol. 51, no. 10, pp. 2529–2553, Jul. 2007.

[112] P. Closas and A. Gusi-Amigo, "Direct position estimation of GNSS receivers: Analyzing main results, architectures, enhancements, and challenges," *IEEE Signal Process. Mag.*, vol. 34, no. 5, pp. 72–84, Sep. 2017.

[113] P. Biswas and Yinyu Ye, "Semidefinite programming for ad hoc wireless sensor network localization," in *Third International Symposium on Information Processing in Sensor Networks, 2004. IPSN 2004*, Apr. 2004, pp. 46–54.

[114] L. Liao, J. Hightower, D. Fox, G. Borriello, and D. Schulz, "Bayesian filtering for location estimation," *IEEE Pervasive Comput.*, vol. 2, no. 03, pp. 24–33, Jul. 2003.

[115] C. Savarese, J. M. Rabaey, and K. Langendoen, "Robust positioning algorithms for distributed ad-hoc wireless sensor networks," in *Proceedings of the General Track of the Annual Conference on USENIX Annual Technical Conference*, ser. ATEC '02. Berkeley, CA, USA: USENIX Association, 2002, pp. 317–327.

[116] F. Meyer, O. Hlinka, and F. Hlawatsch, "Sigma point belief propagation," *IEEE Signal Process. Lett.*, vol. 21, no. 2, pp. 145–149, Feb. 2014.

[117] O. Hlinka, F. Hlawatsch, and P. M. Djuric, "Distributed particle filtering in agent networks: A survey, classification, and comparison," *IEEE Signal Process. Mag.*, vol. 30, no. 1, pp. 61–81, Jan. 2013.

[118] W. Gao, X. Chen, and J. Lu, "Cubature belief propagation for self-localization of wireless networks," in *2015 IEEE International Conference on Communications (ICC)*, Jun. 2015, pp. 6658–6662.

[119] G. Golub and V. Pereyra, "The differentiation of pseudo-inverses and nonlinear least squares problems whose variables separate," *SIAM Journal on Numerical Analysis*, vol. 10, no. 2, pp. 413–432, Apr. 1973.

[120] C. Gentner, S. Zhang, and T. Jost, "Log-PF: Particle filtering in logarithm domain," *Journal of Electrical and Computer Engineering*, vol. 2018, 2018.

[121] J. Selva, "Interpolation of bounded bandlimited signals and applications," *IEEE Trans. Signal Process.*, vol. 54, no. 11, pp. 4244–4260, Nov. 2006.

[122] M. Lashley, D. M. Bevly, and J. Y. Hung, "Performance analysis of vector tracking algorithms for weak GPS signals in high dynamics," *IEEE J. Sel. Topics Signal Process.*, vol. 3, no. 4, pp. 661–673, Aug. 2009.

[123] W. Wang, T. Jost, and A. Dammann, "Estimation and modelling of NLoS time-variant multipath for localization channel model in mobile radios," in *2010 IEEE Global Telecommunications Conference (GLOBECOM 2010)*, Dec. 2010, pp. 1–6.

[124] "WINNER II Deliverable D1.1.2: WINNER II Channel Models," Sep. 2007. [Online]. Available: http://www.ist-winner.org/deliverables.html

[125] S. Sand, *Hybridization with Localization Information from Wireless Communications Systems.* Dordrecht: Springer Netherlands, 2015, pp. 169–208.

[126] C. Gentner, S. Sand, and A. Dammann, "OFDM indoor positioning based on TDOAs: Performance analysis and experimental results," in *2012 International Conference on Localization and GNSS (ICL-GNSS).* IEEE, 2012, pp. 1–7.

[127] J. Fessler, A. O. Hero *et al.*, "Space-alternating generalized expectation-maximization algorithm," *IEEE Trans. Signal Process.*, vol. 42, no. 10, pp. 2664–2677, 1994.

[128] S. Zhang and R. Raulefs, "Multi-agent flocking with noisy anchor-free localization," in *11th International Symposium on Wireless Communications Systems (ISWCS)*, 2014, pp. 927–933.

[129] A. Guerra, D. Dardari, and P. M. Djurić, "Non-centralized navigation for source localization by cooperative UAVs," in *2019 27st European Signal Processing Conference (EUSIPCO)*, Sep. 2019.

[130] K. Dogancay, "UAV path planning for passive emitter localization," *IEEE Trans. Aerosp. Electron. Syst.*, vol. 48, no. 2, pp. 1150–1166, Apr. 2012.

[131] R. T. Haftka and Z. Gürdal, *Elements of Structural Optimization.* SPRINGER-SCIENCE+BUSINESS MEDIA, B.V., 1984.

[132] X. Chen and K. Zhou, "On the probabilistic characterization of model uncertainty and robustness," in *Proceedings of the 36th IEEE Conference on Decision and Control, 1997*, vol. 4, Dec. 1997, pp. 3816–3821 vol.4.

Appendix A

List of Acronyms and Abbreviations

1D	one-dimensional	57
2D	two-dimensional	13
3D	three-dimensional	23
5G	5^{th} generation mobile networks	25
a.k.a.	also known as	6
A2A	agent-to-agent	6
ADMM	alternating direction method of multipliers	88
AoA	angle of arrival	25
AoD	angle of departure	30
AWGN	additive white Gaussian noise	8
B2A	beacon-to-agent	16
B2B	beacon-to-beacon	16
BB	Bayesian bound	5
BCRB	Bayesian Cramér-Rao bound	33
BI	Bayesian information	10
BIM	Bayesian information matrix	33
BP	belief propagation	90
CBP	cubature belief propagation	91
CCI	conditional concavity indicator	101
CDF	cumulative distribution function	108
CIR	channel impulse response	89
CoA	curvature of arrival	10
CRB	Cramér-Rao bound	5
CSA	centro-symmetric array	62
DiPNet	direct particle filtering for decentralized network localization	10
DLR	German Aerospace Center	46
DPE	direct position estimation	88
DPF	distributed particle filtering	75
DRSS	differential received signal strength	25
EBIM	equivalent Bayesian information matrix	92
ECEF	Earth-centered, Earth-fixed	5

EFIM	equivalent Fisher information matrix	33
EKF	extended Kalman filter	41
EL	equivalent measurement likelihood	91
EM	expectation maximization	89
ENV	equivalent noise variance	95
ERII	equivalent ranging information intensity	89
ERV	equivalent ranging variance	93
FDD	frequency division duplexing	46
FI	Fisher information	5
FIM	Fisher information matrix	32
GNSS	global navigation satellite system	5
GPS	global positioning system	5
i.f.f.	if and only if	26
i.i.d.	independent and identically distributed	53
IFFT	inverse fast Fourier transform	96
ITS	intelligent transport systems	25
KF	Kalman filter	8
KLD	Kullback–Leibler divergence	91
LOS	line-of-sight	25
LS	least-square	88
LTE	long-term evolution	25
MAC	media access control layer	46
MAP	maximum *a posteriori*	19
MC	Monte Carlo	89
MIMO	multiple-input and multiple-output	64
ML	maximum likelihood	45
MMSE	minimum mean square error	19
MP	message passing	88
MPC	multipath component	25
MSE	mean square error	33
NASA	National Aeronautics and Space Administration	1
NBP	non-parametric belief propagation	91
NLOS	non-line-of-sight	10
ODE	ordinary differential equation	28
OFDM	orthogonal frequency-division multiplexing	25
OFDMA	orthogonal frequency-division multiple access	46
PBP	parametric belief propagation	91
PCO	pulse coupled oscillator	46
PCRB	posterior Cramér-Rao bound	31
PDE	partial differential equation	22
pdf	probability density function	19
PDoA	phase difference of arrival	25
PF	particle filter	19
PHY	physical layer	46
PLL	phase-locked loop	24
PoA	phase of arrival	30

PSD	power spectral density	23
PSGD	projected steepest gradient descent	116
PSK	phase-shift keying	99
RAT	radio access technology	46
RF	radio frequency	2
RII	ranging information intensity	35
RMSE	root mean square error	17
RSS	received signal strength	24
RTK	real-time kinematic	25
RTT	round trip time	25
s.t.	subject to	17
S2A	source-to-agent	6
SAGE	space-alternating generalized expectation-maximization	96
SCF	squared cross-correlation function	94
SDP	semi-definite programming	88
SLA	symmetric linear array	61
SLAM	simultaneous localization and mapping	5
SLAS	simultaneous localization and synchronization	5
SLAT	simultaneous localization and tracking	5
SLAX	simultaneous localization and any other parameter determination	6
SNR	signal to noise ratio	37
SPAWN	sum-product algorithm over a wireless network	90
SVD	singular value decomposition	48
TDMA	time-division multiple access	46
TDoA	time difference of arrival	22
ToA	time of arrival	24
ULA	uniform linear array	64
URA	uniform rectangular array	59
UWB	ultra-wide band	50
w.r.t.	with respect to	4
WGS84	world geodetic system 1984	5
WLAN	wireless local area network	25
WLS	weighted least-square	45
WSN	wireless sensor network	5
ZCRB	ZZB modified CRB	34
ZZB	Ziv-Zakai bound	31

Appendix B

List of Mathematical Notations

To avoid an overlong list, only the important notations are listed. The ones locally defined with limited usages in derivations are omitted.

$\mathbf{0}_{a\times b}$	matrix of zeros with dimension $a \times b$
$\mathbf{0}_a$	vector of zeros with length a
$\mathbf{0}$	vector or matrix of zeros
$\triangle^{\mathbf{b}}_{\mathbf{a}}\mathbf{c}$	second order partial derivative of $\mathbf{c}$ w.r.t. $\mathbf{b}$ and $\mathbf{a}$
$\triangleq$	is defined as
$\nabla_{\mathbf{a}}\mathbf{b}$	gradient of $\mathbf{b}$ w.r.t. $\mathbf{a}$
$\otimes$	Kronecker product
$\mathbf{1}_{a\times b}$	matrix of ones with dimension $a \times b$
$\mathbf{1}_a$	vector of ones with length a
$\mathbf{1}$	vector or matrix of ones
$\mathbf{A}^H$	Hermitian of $\mathbf{A}$
$\mathbf{A}^T$	transpose of $\mathbf{A}$
$\mathbf{A}^T$	transpose of $\mathbf{A}$
$\mathbf{A}^*$	complex conjugate of $\mathbf{A}$
$\mathbf{A}^\dagger$	Moore–Penrose pseudoinverse of $\mathbf{A}$
$\mathcal{A}$	agent set in complete network
$[\mathbf{A}]_{i,j}$	i^{th} row, j^{th} column element of $\mathbf{A}$
$\mathbf{A}_{<\mathbf{x}_1,\mathbf{x}_2>}$	sub-matrix of $\mathbf{A}$, whose rows correspond to vector $\mathbf{x}_1$ and columns correspond to vector $\mathbf{x}_2$
$\tilde{\mathcal{A}}_u$	agent set including $\mathbb{o}_u$ and its neighboring agents
$\mathcal{A}_u$	neighboring agent set of $\mathbb{o}_u$
A_{uv}	amplitude of a signal received by $\mathbb{o}_u$ and transmitted from $\mathbb{o}_v$
A_v	amplitude of a signal transmitted from $\mathbb{o}_v$
$\mathbb{A}^{(x_1x_2)}$	two dimensional coordinate system $\mathbb{A}$ with axes x_1 and x_2
$\mathcal{A}/a$	subset of $\mathcal{A}$ excluding element (or set) a
$\mathbf{a}^{(a_1:a_2)}$	variable a from time step a_1 to time step a_2
$a^{(+)}$	variable a at current time step
$\ddot{a}$	second derivative of variable a

$\dot{a}$	first derivative of variable a
a_g	scaling factor of gas source
$\bar{a}$	mean of a
$a^{(-)}$	variable a at last time step
$a_{uv,0}$	generic parameter a of the l^{th} MPC of the link between $\mathbb{o}_u$ and $\mathbb{o}_v$
$\mathbf{a}_u$	nuisance parameters of $\mathbb{o}_u$
α_{uv}	complex amplitude of signal transmitted from $\mathbb{o}_v$ and received by $\mathbb{o}_u$
α_{uv}	complex amplitude on link $\mathbb{e}_{uv}$
$\tilde{a}$	approximation of variable a
$\hat{a}$	estimation of variable a
$\|a\|$	Frobenius norm of variable a, where a can be scalar, vector and matrix
$\mathbf{a} \sim \mathcal{CN}(\mathbf{0}, \sigma^2)$	random variable(s) $\mathbf{a}$ is circularly-symmetric complex normally distributed with variance σ^2
$\mathbf{a} \sim \mathcal{N}(\boldsymbol{\mu}, \mathbf{C})$	random variable(s)$\mathbf{a}$ is normally distributed with mean $\boldsymbol{\mu}$ and covariance $\mathbf{C}$
$a \in (a_1, a_2]$	a belongs to the interval $(a_1, a_2]$, i.e. $a_1 < a \leq a_2$
$\mathbb{o}_u$	node u
$a_1 : a_2$	from time step a_1 to a_2
$\mathbb{B}$	swarm coordinate system defined by baseline
B	baseline of swarm
B_c	bandwidth of A2A links
$\mathcal{B}$	anchor set in complete network
B_s	bandwidth of B2A and RF S2A links
$\mathcal{B}_u$	neighboring beacon set of $\mathbb{o}_u$
$\tilde{\mathbf{b}}_{\mathcal{A}}$	unconstrained control command $\forall \mathbb{o}_u \in \mathcal{A}$
$\mathbf{b}_{\mathcal{A}}$	control command $\forall \mathbb{o}_u \in \mathcal{A}$
b_g	exponent factor of gas source
b_l	control command in l^{th} dimension
$b_u^{(k)}$	position belief of $\mathbb{o}_u$ at iteration k
b_{uv}	NLOS delay in addition to the LOS delay between $\mathbb{o}_u$ and $\mathbb{o}_v$, in meters
$\mathbf{b}_u$	control command for $\mathbb{o}_u$
β_c^2	effective bandwidth of A2A links
$\beta_{\max}$	maximum acceptable probability of collision avoidance violation
β_s^2	effective bandwidth of B2A and RF S2A links
β	IFFT interpolation factor for DiPNet
$\text{CRB}_0[d_{uv}]$	ranging CRB of link $\mathbb{l}_{uv}$ with full subcarrier occupation
$\text{CRB}[\mathbf{a}]$	CRB of variable $\mathbf{a}$
$\mathbb{C}$	swarm Cartesian coordinate system constrained by group motion
$\mathbf{C}_{uv}$	covariance matrix of vector $\mathbf{p}_{uv}$
C	gas concentration
$\mathbf{c}_{\mathcal{A}}^a$	gradient of a particular control objective function denoted as a w.r.t. $\mathbf{b}_{\mathcal{A}}$
$\mathbf{c}_{\mathcal{A}}$	gradient of control objective function w.r.t. $\mathbf{b}_{\mathcal{A}}$
c_l	gradient of control objective function on l^{th} dimension
$\mathbf{c}_u^a$	gradient of a particular control objective function denoted as a w.r.t. $\mathbf{b}_u$

$\mathbf{c}_u$	gradient of the control objective function w.r.t. $\mathbf{b}_u$
$\mathrm{cov}_{\mathbf{a}}[\cdot]$	covariance matrix calculated over particular pdf $p(\mathbf{a})$
$\mathrm{cov}[\cdot]$	covariance matrix
c	speed of light
$D_l(d)$	Dirichlet kernel, a.k.a. periodic sinc function
$\mathcal{D}_{\shortparallel}$	swarm's radial aperture to the source
$\mathcal{D}_{\perp}$	swarm's tangential aperture to the source
$\mathcal{D}$	swarm aperture
D_x	swarm aperture length in x-direction
D_y	swarm aperture length in y-direction
$\mathbf{D}_{\mathbf{a_2}\to\mathbf{a_1}}$	FI degradation of $\mathbf{a_1}$ due to an unknown variable $\mathbf{a_2}$
D	swarm's aperture size
$d_{\min}$	minimum tolerated distance of node pairs
d_{uv}	Euclidean distance between $\mathbb{o}_u$ and $\mathbb{o}_v$
d_u	d-coordinate of $\mathbb{o}_u$ in polar coordinate system $\mathbb{P}$
δ_u	clock offset of $\mathbb{o}_u$
$\mathrm{diag}\{\cdots\}$	diagonalization operator, arranging elements (scalars, vectors, or matrices) along the diagonal of a matrix
$\hat{d}_{uv}$	distance estimate between $\mathbb{o}_u$ and $\mathbb{o}_v$ from localization result
$\boldsymbol{\delta}$	control command projected on the tangent space of the activated constraints
$\mathcal{E}_0$	link set in complete network
$\mathcal{E}$	extended link set including $\mathcal{E}_0$ and virtual anchor-anchor links
$\mathcal{E}_u$	set of links to $\mathbb{o}_u$
$\mathrm{Exp}(a)$	pdf of exponential distribution with rate parameter a
$\mathbb{E}_a[\cdot]$	expectation operator w.r.t. variable(s) a
$\mathbf{e}_g$	directional vector of goal approaching objective
$\mathbb{e}_{uv}$	link from $\mathbb{o}_v$ to $\mathbb{o}_u$
ε_{uv}	absolute framework distance error of node pair $(\mathbb{o}_u, \mathbb{o}_v)$
$\boldsymbol{\varepsilon}_{\hat{\mathbf{d}}_{\mathcal{P}}}$	absolute difference between node pair distance of node set $\mathcal{P}$
$\varepsilon_{\hat{\mathbf{d}}_{\mathcal{P}}}$	framework distance RMSE of node set $\mathcal{P}$
$\varepsilon_{\max}$	maximum tolerated agent's position error
$\varepsilon_{\tilde{\mathcal{F}}_{\mathcal{P}}}$	average shape difference between frameworks $\tilde{\mathcal{F}}_{\mathcal{P}}$ and $\mathcal{F}_{\mathcal{P}}$ of node set $\mathcal{P}$
$\varepsilon(\mathbf{q}_{\mathcal{P}}, \mathbf{p}_{\mathcal{P}})$	generic metrics to indicate swarm localization performance
$\epsilon_{uv}(t)$	RF noise at time t on link $\mathbb{e}_{uv}$
$\boldsymbol{\epsilon}_{uv}$	RF noise samples on link $\mathbb{e}_{uv}$
$\boldsymbol{\varepsilon}_{\mathcal{T}_{\mathcal{P},\mathrm{opt}}(\mathbf{q}_{\mathcal{P}})}$	position error vector after the optimal affine transformation $\mathcal{T}_{\mathcal{P},\mathrm{opt}}$ of node set $\mathcal{P}$
$\boldsymbol{\varepsilon}_{\mathcal{T}_{\mathcal{P}}(\mathbf{q}_{\mathcal{P}})}$	position error vector after an affine transformation $\mathcal{T}_{\mathcal{P}}$ of node set $\mathcal{P}$
$\mathcal{F}_0$	directed extended framework composed of $\mathcal{G}_0$ and $\mathcal{E}_0$
$\mathcal{F}_u$	sub-framework composed of $\mathcal{G}_u$ and $\mathbf{p}_{\mathcal{N}_u}$
$\mathcal{F}$	undirected extended framework composed of $\mathcal{G}$ and $\mathcal{E}$
f_{c}	carrier frequency of A2A links
$f(d)$	cross-correlation of RF signal as a function of propagation distance d
$f(\mathbf{b}_{\mathcal{A}})$	generic cost function

$f_g(\mathbf{b}_\mathcal{A})$	goal approaching cost function
$f_p(\mathbf{b}_\mathcal{A})$	information seeking objective, as cost function
f_{sc}	subcarrier spacing
f_{s}	carrier frequency of B2A and S2A RF links
f_v	carrier frequency of RF signal transmitted from $\mathbb{o}_v$
$\mathcal{G}_0$	directed graph of the extended swarm network
$\mathbb{G}$	global coordinate system
$\mathcal{G}_u$	subgraph composed of $\mathcal{N}_u$ and $\mathcal{E}_u$
$\mathcal{G}$	undirected graph of the extended swarm network
γ	exponent coefficient of pathloss
$\mathbf{H}_\mathcal{A}$	overall geometry matrix of agent set $\mathcal{A}$
$\mathbf{H}_{\mathcal{L}_0}$	ranging geometry matrix
$h_{c,uv}(\mathbf{b}_\mathcal{A})$	collision avoidance constraint function
$\mathbf{h}(\mathbf{b}_\mathcal{A})$	generic constraint functions
$h_p(\mathbf{b}_\mathcal{A})$	information seeking objective, as constraint
$\mathbf{I}_{n\times n}$	identity matrix of size n
$\mathbf{I}$	identity matrix
$\tilde{\mathbf{I}}_\mathbf{a}$	EFIM of variable $\mathbf{a}$
$\mathbf{I}_\mathbf{a}^\mathbf{b}$	FIM of variable $\mathbf{a}$ in signal feature $\mathbf{b}$
$\mathbf{I}_{\mathbf{x}_1,\mathbf{x}_2}$	off-diagonal block in FIM representing the link between variables $\mathbf{x}_1$ and $\mathbf{x}_2$
$\mathbf{I}_\mathbf{a}$	FIM of variable $\mathbf{a}$
$\Im\{a\}$	imaginary part of variable a
ι_a^b	FI of a scalar variable a contained in variable b
$\tilde{\iota}_{d_{uv}}$	ERII of nodes distance d_{uv}
$\bar{\iota}_{d_{uv}}$	RII of nodes distance d_{uv} marginalized over $\mathbf{p}_u$ and $\mathbf{p}_v$
$\iota_{d_{uv}}$	RII of nodes distance d_{uv}
ι_a	FI of a scalar variable a
$\jmath$	imaginary unit
$\mathbf{J}_u$	EBIM of related to agent $\mathbb{o}_u$
$\mathbf{J}_\mathbf{x}$	Bayesian information matrix of $\mathbf{x}$
$\mathbf{J}_{u,v}$	sub-matrix of BIM corresponding to nodes $\mathbb{o}_u$ and $\mathbb{o}_v$
$\tilde{\mathbf{J}}_\mathbf{x}$	Bayesian information matrix of $\mathbf{x}$ after state transition before obtaining new measurements
K_s	number of iterations for SAGE based delay estimator
K_τ	number of iterations for correlation based delay estimator
K_{uv}	resource sharing factor
M_k	k^{th} empirical moment of the normalized agents' spatial distribution
κ_v	CoA of signal transmitted from node $\mathbb{o}_v$
$\mathcal{L}_0$	undirected edge set in extended swarm network
$\mathcal{L}_\mathcal{B}$	virtual undirected edges between beacons
$\mathcal{L}_{\text{all}}$	undirected edge set of virtual fully connected swarm network, excluding B2B edges
$\mathcal{L}$	undirected edge set in extended swarm network together with the virtual edges between beacons, i.e. $\mathcal{L} = \mathcal{L} \cup \mathcal{L}_\mathcal{B}$
L_{uv}	number of NLOS paths of link $\mathbb{l}_{uv}$

$\mathbf{\Lambda}_{\mathbf{p}_\mathcal{P}}$	weighing matrix for information seeking control, only including positions of a node subset $\mathcal{P}$
$\mathbf{\Lambda}^f$	weighing matrix for information seeking control as cost function
$\mathbf{\Lambda}^h$	weighing matrix for information seeking control as constraint
$\mathbf{\Lambda}$	weighing matrix for information seeking control
$\{\lambda_i(\mathbf{X}) : i = 1 \cdots n\}$	eigenvalues of $\mathbf{X}$ sorted in non-increasing order
$\lim_{a\to b}$	limit as a approaches b
$\mathrm{l.i.m.}_{a\to b}$	limit in the mean as a approaches b
$\mathbb{l}_{uv}$	unidirectional link between $\mathbb{o}_v$ and $\mathbb{o}_u$
$N_0/2$	PSD of noise
$\mathcal{N}_{uv}$	subcarrier set used for ranging at link $\mathbb{l}_{uv}$
N	number of samples(and subcarriers)
ω_c	angular carrier frequency of $A2A$ link
$\boldsymbol{\omega}_{\mathbf{p}_u}$	additive noise on control command $\mathbf{b}_u$ of agent $\mathbb{o}_u$
ω_sc	angular subcarrier spacing
ω_s	angular carrier frequency of $B2A$ and RF $S2A$ link
ω_v	angular carrier frequency of RF signal transmitted from $\mathbb{o}_v$
PCRB[$\mathbf{a}$]	PCRB of variable $\mathbf{a}$
P_a	point in space labeled as a
P_u	point in space where $\mathbb{o}_u$ is located
Φ_{uv}	carrier phase of the signal transmitted from $\mathbb{o}_v$ and received by $\mathbb{o}_u$
P	generic point in space
$\lvert\mathcal{P}\rvert$	cardinality of a set $\mathcal{P}$
ϕ_u	carrier phase offset of $\mathbb{o}_u$
$\tilde{p}(\mathbf{z}_{uv}\lvert\mathbf{p}_u, \mathbf{p}_v)$	equivalent measurement likelihood (EL)
$\mathbf{p}_\mathcal{P}$	coordinates of all nodes in generic set $\mathcal{P}$
$\mathbf{p}_a$	coordinates of point P_a in default coordinate system
$\mathbf{p}_g$	coordinates of destination of goal approaching objective
$\mathbf{p}_u^\mathbb{A}$	coordinates of $\mathbb{o}_u$ in a generic coordinate system $\mathbb{A}$
$\mathbf{p}_u$	coordinates of $\mathbb{o}_u$ in default coordinate system
$\mathbf{Q}(\mathbf{b}_\mathcal{A})$	covariance matrix of state transition noise
$Q(\cdot)$	Gaussian Q-function
$\mathbf{Q}_{\mathbf{p}_u}(\mathbf{b}_u)$	covariance matrix of position transition noise of agent $\mathbb{o}_u$
$\mathcal{Q}_u^{(k)}$	particle set of agent $\mathbb{o}_u$ at inner iteration k in DiPNet
$Q_u^{(q,k)}$	q^{th} particle of agent $\mathbb{o}_u$ at inner iteration k in DiPNet
Q	number of particles at agent $\mathbb{o}_u$ in DiPNet
$\mathbf{R}(\mathcal{F})$	rigidity matrix of framework $\mathcal{F}$
R_n	received symbol on OFDM subcarrier n
R	radius of the swarm aperture
$\mathbf{R}$	received symbols on all OFDM subcarriers
$\mathbb{R}_+$	positive number set
$\Re\{a\}$	real part of variable(s) a
$r_{uv}(t)$	received signal at time t at $\mathbb{o}_u$ through link $\mathbb{e}_{uv}$
$\mathbf{r}_{uv}$	received signal samples at $\mathbb{o}_u$ through link $\mathbb{e}_{uv}$
$\mathbf{r}_u$	received signals at $\mathbb{o}_u$ through all links

$\mathrm{rank}(\mathbf{A})$	rank of matrix $\mathbf{A}$
ρ_{uv}	ranging measurement between $\mathbb{o}_u$ and $\mathbb{o}_v$
$\mathcal{S}_{\mathrm{gas}}$	set of gas source
S_n	transmitted symbol on OFDM subcarrier n
$\mathcal{S}_{\mathrm{RF}}$	set of RF source
$\mathcal{S}$	set of source
$\mathbf{S}$	transmitted symbols on all OFDM subcarriers
$s_{uv}(t)$	transmitted signal at time t from $\mathbb{o}_v$ to $\mathbb{o}_u$
$\mathbf{s}_{uv}$	transmitted signal samples from $\mathbb{o}_v$ to $\mathbb{o}_u$
$\mathbf{s}_u$	transmitted signal from $\mathbb{o}_v$ to $\mathbb{o}_u$
$\tilde{\sigma}^2_{uv}$	equivalent noise variance
σ^2	variance of noise on control command normalized to step size
$\sigma^2_{v\to uv}$	position covariance of $\mathbb{o}_v$ projected to the measurement link $\mathbb{e}_{uv}$
σ^2_u	variance of RF noise at $\mathbb{o}_u$
ς	concavity indicator
T_{o}	observation time
T_{sa}	sampling period
$\mathcal{T}_{\mathrm{opt}}(\cdot)$	optimal affine transformation operator
$\mathcal{T}(\cdot)$	affine transformation operator
$\mathrm{Tr}[\mathbf{A}]$	trace of matrix $\mathbf{A}$
τ_{uv}	symbol delay of RF signal transmitted from $\mathbb{o}_v$ and received by $\mathbb{o}_u$
θ_{uv}	angle of of the link $\mathbb{e}_{uv}$
θ_u	θ-coordinate of $\mathbb{o}_u$ in polar coordinate system $\mathbb{P}$
$\mathcal{U}_{\mathcal{A}}$	feasible set of control command $\mathbf{b}_{\mathcal{A}}$ of agent set $\mathcal{A}$
$\mathcal{U}[a,b)$	pdf of uniform distribution within interval $[a,b)$
$\mathcal{U}$	feasible set of control command $\mathbf{b}_u$ of agent $\mathbb{o}_u$
$\mathcal{V}$	node set in complete network
$\tilde{\mathcal{V}}_u$	node set including $\mathbb{o}_u$ and its neighbors
$\mathcal{V}_u$	neighboring node set of $\mathbb{o}_u$
$\mathrm{var}[a]$	variance of variable a
$\mathrm{vec}\{\cdots\}$	vectorization operator, arranging elements (scalars or vectors) into a vector
$\mathbf{p}_u^{(q,k)}$	position of the q^{th} particle of agent $\mathbb{o}_u$ at inner iteration k in DiPNet
w_{g}	weight of goal approaching cost function
w_{p}	weight of information seeking cost function
$w_u^{(q,k)}$	weight of the q^{th} particle of agent $\mathbb{o}_u$ at inner iteration k in DiPNet
X_{uv}	LOS/NLOS indicator for link $\mathbb{l}_{uv}$
$\mathcal{X}$	set of nodes with unknown positions
$\mathbf{x}_{\mathcal{P}}$	state of nodes in generic node set $\mathcal{P}$
x_u	x-coordinate of $\mathbb{o}_u$ in Cartesian coordinate system $\mathcal{C}^{(xy)}$
y_u	y-coordinate of $\mathbb{o}_u$ in Cartesian coordinate system $\mathcal{C}^{(xy)}$
$\mathbb{Z}_+$	natural number set
$\mathrm{ZCRB}[\mathbf{p}_{\mathcal{A}}]$	ZZB modified agents' position CRB
$\mathrm{ZZB}[a]$	ZZB of variable a
$\tilde{\mathbf{z}}^{(+)}$	predicted measurements after potential movement
$\mathbf{z}_{\mathcal{P}}$	measurements of all links in set $\mathcal{P}$

$\mathbf{z}_{uv}$	generic measurement on link $\mathbb{e}_{uv}$
$\mathbf{z}_u$	generic measurement collected by $\mathbb{c}_u$

Appendix C

Mathematical Definitions & Derivations

C.1 FIM with Continuous Complex-valued Observations

We define sampling functions $\psi_i(t), \forall i = 1, \cdots, N$, with a sampling period of $T_{\text{sa}} = {}^1/_B = {}^{T_o}/_N$ as

$$\psi_i(t) = \begin{cases} 1/\sqrt{T_{\text{sa}}} & (i-1)T_{\text{sa}} \leq t < iT_{\text{sa}} \\ 0 & \text{else.} \end{cases} \tag{C.1}$$

The sampled signal is expressed as

$$r_{uv,i} = \int_0^{T_o} r_{uv}(t)\psi_i(t)\mathrm{d}t. \tag{C.2}$$

According to the Theory of Karhunen-Loève expansion [70], the continuous signal can be represented as

$$r_{uv}(t) = \underset{N\to\infty}{\text{l. i. m.}} \sum_{i=1}^{N} r_{uv,i}\psi_i(t), \tag{C.3}$$

where "l. i. m." denotes limit in the mean. The sampled signal $r_{uv,i}$ is a Gaussian distributed random variable with a variance of $\sigma_u^2 = N_0$ and a mean of

$$\mathbb{E}[r_{uv,i}] = s_{uv,i} = \frac{1}{\sqrt{T_{\text{sa}}}} \int_{(i-1)T_{\text{sa}}}^{iT_{\text{sa}}} s_{uv}(t)\mathrm{d}t. \tag{C.4}$$

According to estimation theory, the total FIM $\mathbf{I}_{\mathbf{x}}$ is the superposition of the FIMs from all the contributing links $\mathbb{e}_{uv} \in \mathcal{E}_0$, i.e.

$$
\begin{aligned}
\mathbf{I}_{\mathbf{x}} &= \sum_{\mathbb{e}_{uv}\in\mathcal{E}_0} \mathbf{I}_{\mathbf{x}}^{s_{uv}} \\
&\triangleq \lim_{N\to\infty} \frac{2}{N_0} \Re\{ \sum_{\mathbb{e}_{uv}\in\mathcal{E}_0} \nabla_{\mathbf{x}} \mathbf{s}_{uv}^{*} \nabla_{\mathbf{x}^T} \mathbf{s}_{uv} \} \\
&= \lim_{N\to\infty} \frac{2}{N_0} \Re\{ \sum_{\mathbb{e}_{uv}\in\mathcal{E}_0} \sum_{i=1}^{N} \nabla_{\mathbf{x}} s_{uv,i}^{*} \nabla_{\mathbf{x}^T} s_{uv,i} \} \\
&= \lim_{N\to\infty} \frac{2}{N_0 T_{\mathrm{sa}}} \Re\Big\{ \sum_{\mathbb{e}_{uv}\in\mathcal{E}_0} \sum_{i=1}^{N} \int_{(i-1)T_{\mathrm{sa}}}^{iT_{\mathrm{sa}}} \nabla_{\mathbf{x}} s_{uv}^{*}(t)\mathrm{d}t \int_{(i-1)T_{\mathrm{sa}}}^{iT_{\mathrm{sa}}} \nabla_{\mathbf{x}^T} s_{uv}(\tau)\mathrm{d}\tau \Big\} \\
&= \lim_{N\to\infty} \frac{2}{N_0} \Re\Big\{ \sum_{\mathbb{e}_{uv}\in\mathcal{E}_0} \sum_{i=1}^{N} \int_{(i-1)T_{\mathrm{sa}}}^{iT_{\mathrm{sa}}} \nabla_{\mathbf{x}} s_{uv}^{*}(t) \nabla_{\mathbf{x}^T} s_{uv}(t) \\
&\quad - \Big(\nabla_{\mathbf{x}} s_{uv}^{*}(t) - \frac{1}{T_{\mathrm{sa}}} \int_{(i-1)T_{\mathrm{sa}}}^{iT_{\mathrm{sa}}} \nabla_{\mathbf{x}} s_{uv}^{*}(\tau)\mathrm{d}\tau \Big) \Big(\nabla_{\mathbf{x}^T} s_{uv}(t) - \frac{1}{T_{\mathrm{sa}}} \int_{(i-1)T_{\mathrm{sa}}}^{iT_{\mathrm{sa}}} \nabla_{\mathbf{x}^T} s_{uv}(\tau)\mathrm{d}\tau \Big) \mathrm{d}t \Big\} \\
&= \lim_{N\to\infty} \frac{2}{N_0} \Re\Big\{ \sum_{\mathbb{e}_{uv}\in\mathcal{E}_0} \sum_{i=1}^{N} \int_{(i-1)T_{\mathrm{sa}}}^{iT_{\mathrm{sa}}} \nabla_{\mathbf{x}} s_{uv}^{*}(t) \nabla_{\mathbf{x}^T} s_{uv}(t)\mathrm{d}t \Big\} + \mathbf{0}^{+} \\
&\approx \frac{2}{N_0} \Re\Big\{ \sum_{\mathbb{e}_{uv}\in\mathcal{E}_0} \int_{0}^{T_o} \nabla_{\mathbf{x}} s_{uv}^{*}(t) \nabla_{\mathbf{x}^T} s_{uv}(t)\mathrm{d}t \Big\}, \qquad \text{(C.5)}
\end{aligned}
$$

which completes the derivation of (3.14). The term $\mathbf{0}^{+}$ denotes a negligible positive semi-definite matrix.

C.2 Condition of Non-Observable Source Distance

The condition of non-observable source distance from a 1D swarm colinear to the source is proved with the following equations arranged according to causality.

$$\det\left[\mathbf{I}_{\mathbf{x}_v}\right] = 0$$

$$\mathbb{E}_{\mathbf{p}_u^{\mathbb{P}}}\left[\iota_{g_{uv}}\left(\frac{\partial g_{uv}}{\partial d_v}\right)^2\right]\mathbb{E}_{\mathbf{p}_u^{\mathbb{P}}}\left[\iota_{g_{uv}}\left(\frac{\partial g_{uv}}{\partial a_v}\right)^2\right] - \mathbb{E}_{\mathbf{p}_u^{\mathbb{P}}}\left[\iota_{g_{uv}}\frac{\partial g_{uv}}{\partial d_v}\frac{\partial g_{uv}}{\partial a_v}\right]^2 = 0 \tag{C.6}$$

$$\mathbb{E}_{\mathbf{p}_u^{\mathbb{P}},\mathbf{p}_w^{\mathbb{P}}}\left[\iota_{g_{uv}}\iota_{g_{wv}}\left(\left(\frac{\partial g_{uv}}{\partial d_v}\frac{\partial g_{wv}}{\partial a_v}\right)^2 - \left(\frac{\partial g_{uv}}{\partial d_v}\frac{\partial g_{uv}}{\partial a_v}\right)\left(\frac{\partial g_{wv}}{\partial d_v}\frac{\partial g_{wv}}{\partial a_v}\right)\right)\right] = 0 \tag{C.7}$$

$$\mathbb{E}_{\{\mathbf{p}_u^{\mathbb{P}}:d_u>d_w\},\mathbf{p}_w^{\mathbb{P}}}\left[\iota_{g_{uv}}\iota_{g_{wv}}\left(\frac{\partial g_{uv}}{\partial a_v}\frac{\partial g_{wv}}{\partial d_v} - \frac{\partial g_{uv}}{\partial d_v}\frac{\partial g_{wv}}{\partial a_v}\right)^2\right] = 0 \tag{C.8}$$

$$\frac{\partial g_{uv}/\partial d_v}{\partial g_{uv}/\partial a_v} = \frac{\partial g_{wv}/\partial d_v}{\partial g_{wv}/\partial a_v}, \quad \forall u \neq w. \tag{C.9}$$

$$\frac{\partial g_{uv}/\partial d_{uv}}{\partial g_{uv}/\partial a_v} = \frac{\partial g_{wv}/\partial d_{uv}}{\partial g_{wv}/\partial a_v}, \quad \forall u \neq w. \tag{C.10}$$

It is straightforward to prove that the equality (C.10) is equivalent to (3.72).

C.3 Proof of Theorem 3.4.2

We apply the second-order Taylor expansion to d_{vu} at $d_u = 0$

$$d_{vu} \approx d_v - d_u\cos(\theta_u - \theta_v) + \frac{1}{2}\sin^2(\theta_u - \theta_v)d_u^2/d_v \tag{C.11}$$

$$\text{and define} \quad a_u \triangleq 1 - \frac{d_u^2\sin^2\theta_v}{2d_v^2} \quad \text{and} \quad b_u \triangleq \frac{d_u^2\sin\theta_v\cos\theta_v}{d_v}.$$

By exploiting the symmetry of SLAs, we can write

$$\sum_{\mathbb{o}_u\in\mathcal{A}}\nabla_{\mathbf{p}_v}d_{vu}\sum_{w=1}^{|\mathcal{A}|}\nabla_{\mathbf{p}_v^T}d_{vw} \approx \begin{pmatrix} \left(\sum\limits_{\mathbb{o}_u\in\mathcal{A}}a_u\right)^2 & \sum\limits_{\mathbb{o}_u\in\mathcal{A}}a_u\sum\limits_{\mathbb{o}_w\in\mathcal{A}}b_w \\ \sum\limits_{\mathbb{o}_u\in\mathcal{A}}a_u\sum\limits_{\mathbb{o}_w\in\mathcal{A}}b_w & \left(\sum\limits_{\mathbb{o}_u\in\mathcal{A}}b_u\right)^2 \end{pmatrix}$$

$$\text{and} \quad \sum_{\mathbb{o}_u\in\mathcal{A}}\nabla_{\mathbf{p}_v}d_{vu}\nabla_{\mathbf{p}_v^T}d_{vu} \approx \sum_{\mathbb{o}_u\in\mathcal{A}}\begin{pmatrix} a_u^2 & a_ub_u \\ a_ub_u & d_u^2\sin^2\theta_v + b_u^2 \end{pmatrix}.$$

The CRB of $\mathbf{p}_v$ can be derived as

$$\mathrm{CRB}[\mathbf{p}_v] \approx \frac{2N_0 d_v^2}{A_v^2|\mathcal{A}|D_\perp^4(M_4 - M_2^2)} \begin{pmatrix} d_v^{-4}/4 & \cot\theta_v d_v^{-3}/2 \\ \cot\theta_v d_v^{-3}/2 & \frac{D_\perp^{-2}M_2}{M_4 - M_2^2} + \cot^2\theta_v d_v^{-2} \end{pmatrix}^{-1}. \quad \text{(C.12)}$$

The CRB of AoA in (3.82) can be directly obtained by taking the second diagonal entity of (C.12). The distance CRB is derived by taking the first diagonal entity of (C.12)

$$\mathrm{CRB}[d_v] \approx \frac{8N_0 d_v^6}{A_v^2|\mathcal{A}|D_\perp^4(M_4 - M_2^2)}\Big(1 + \frac{(M_4 - M_2^2)\cot^2\theta_v}{(d_v/D_\perp)^2 M_2}\Big). \quad \text{(C.13)}$$

Equation (3.83) is obtained from (C.13) with the assumption $d_v \gg D_\perp$, which completes the proof.

C.4 Partial Derivatives for Joint Self- and Source Localization

The partial derivatives required for joint self- and source localization CRBs with a mixture of swarm Cartesian coordinate system $\mathbb{C}$ and the swarm polar coordinate system $\mathbb{P}$ can be written as

$$-\nabla_{\mathbf{x}_u}\tau_{uv} = \nabla_{\mathbf{x}_v}\tau_{uv} = \mathrm{vec}\{\cos\theta_{uv}, \sin\theta_{uv}, 1\}, \qquad \forall \mathbb{o}_u, \mathbb{o}_v \in \mathcal{A} \quad \text{(C.14)}$$

$$\nabla_{\mathbf{x}_u}\tau_{uv} = -\mathrm{vec}\{\cos\theta_{uv}, \sin\theta_{uv}, 1\}, \qquad \forall \mathbb{o}_u \in \mathcal{A}, \mathbb{o}_v \in \mathcal{S}_{\mathrm{RF}} \quad \text{(C.15)}$$

$$\nabla_{\mathbf{x}_v}\tau_{uv} = \mathrm{vec}\{\nabla_{\mathbf{p}_v^{\mathcal{P}}} d_{uv}, 1, 0\}, \qquad \forall \mathbb{o}_u \in \mathcal{A}, \mathbb{o}_v \in \mathcal{S}_{\mathrm{RF}} \quad \text{(C.16)}$$

$$\nabla_{\mathbf{x}_u}\phi_{uv} = \mathrm{vec}\{\cos\theta_{uv}, \sin\theta_{uv}, 1\}, \qquad \forall \mathbb{o}_u \in \mathcal{A}, \mathbb{o}_v \in \mathcal{S}_{\mathrm{RF}} \quad \text{(C.17)}$$

$$\nabla_{\mathbf{x}_v}\phi_{uv} = \mathrm{vec}\{-\nabla_{\mathbf{p}_v^{\mathcal{P}}} d_{uv}, 0, 1\}, \qquad \forall \mathbb{o}_u \in \mathcal{A}, \mathbb{o}_v \in \mathcal{S}_{\mathrm{RF}} \quad \text{(C.18)}$$

$$\quad \text{(C.19)}$$

where θ_{uv} is the angle of incoming signal $r_{uv}(t)$, w.r.t. the swarm coordinate system, and

$$\nabla_{\mathbf{p}_v^{\mathcal{P}}} d_{uv} = \mathrm{vec}\Big\{\frac{d_v - d_u\cos(\theta_v - \theta_u)}{d_{uv}}, \frac{d_u d_v \sin(\theta_v - \theta_u)}{d_{uv}}\Big\}. \forall \mathbb{o}_u \in \mathcal{A}, \mathbb{o}_v \in \mathcal{S}_{\mathrm{RF}} \quad \text{(C.20)}$$

C.5 Derivation of EBIM in (4.7)

The EBIM $\mathbf{J}_u$ can be formulated as

$$\mathbf{J}_u = \mathbf{J}_{(u,u)} - \mathbf{D}_u, \tag{C.21}$$

where $\mathbf{J}_{(u,u)}$ is defined in (4.11). The term $\mathbf{D}_u$ is the information degradation due to neighbor's uncertainty

$$\mathbf{D}_u \triangleq \sum_{\mathbb{o}_v \in \mathcal{A}_u} \mathbf{J}_{(u,v)}^T \mathbf{J}_{(v,v)}^{-1} \mathbf{J}_{(u,v)}, \tag{C.22}$$

$$\mathbf{J}_{(u,v)} = -\mathbb{E}_{\mathbf{p}_u,\mathbf{p}_v}\left[\iota_{d_{uv}} \mathbf{e}_{uv} \mathbf{e}_{uv}^T\right] \tag{C.23}$$

$$\mathbf{J}_{(v,v)} = \tilde{\mathbf{J}}_v^{(k-1)} + \mathbb{E}_{\mathbf{p}_u,\mathbf{p}_v}\left[\iota_{d_{uv}} \mathbf{e}_{uv} \mathbf{e}_{uv}^T\right]. \tag{C.24}$$

The superscript $(k-1)$ of $\tilde{\mathbf{J}}_v^{(k-1)}$ is omitted for simplicity. With the assumption of concentrated belief, the following approximation can be applied

$$\mathbb{E}_{\mathbf{p}_u,\mathbf{p}_v}\left[\iota_{d_{uv}} \mathbf{e}_{uv} \mathbf{e}_{uv}^T\right] \approx \bar{\iota}_{d_{uv}} \bar{\mathbf{e}}_{uv} \bar{\mathbf{e}}_{uv}^T. \tag{C.25}$$

Inserting C.23, (C.24) and C.25 into (C.22) and apply the Sherman-Morrison formula, the information degradation can be approximated as

$$\begin{aligned}
\mathbf{D}_u &\approx \sum_{\mathbb{o}_v \in \mathcal{A}_u} \bar{\iota}_{d_{uv}}^2 \bar{\mathbf{e}}_{uv} \bar{\mathbf{e}}_{uv}^T \left(\tilde{\mathbf{J}}_v^{-1} - \frac{\tilde{\mathbf{J}}_v^{-1} \bar{\iota}_{d_{uv}} \bar{\mathbf{e}}_{uv} \bar{\mathbf{e}}_{uv}^T \tilde{\mathbf{J}}_v^{-1}}{1 + \bar{\iota}_{d_{uv}} \sigma_{v \mapsto uv}^2} \right) \bar{\mathbf{e}}_{uv} \bar{\mathbf{e}}_{uv}^T \\
&= \sum_{\mathbb{o}_v \in \mathcal{A}_u} \bar{\iota}_{d_{uv}} \bar{\mathbf{e}}_{uv} \left(\bar{\iota}_{d_{uv}} \sigma_{v \mapsto uv}^2 - \frac{\bar{\iota}_{d_{uv}}^2 \sigma_{v \mapsto uv}^4}{1 + \bar{\iota}_{d_{uv}} \sigma_{v \mapsto uv}^2} \right) \bar{\mathbf{e}}_{uv}^T.
\end{aligned} \tag{C.26}$$

Plugging (C.26) into (C.21), the EBIM $\mathbf{J}_u$ is reformulated as

$$\mathbf{J}_u \approx \tilde{\mathbf{J}}_u^{(0)} + \sum_{\mathbb{o}_v \in \mathcal{A}_u} \left(\bar{\iota}_{d_{uv}} - \bar{\iota}_{d_{uv}}^2 \sigma_{v \mapsto uv}^2 + \frac{\bar{\iota}_{d_{uv}}^3 \sigma_{v \mapsto uv}^4}{1 + \bar{\iota}_{d_{uv}} \sigma_{v \mapsto uv}^2} \right) \bar{\mathbf{e}}_{uv} \bar{\mathbf{e}}_{uv}^T. \tag{C.27}$$

The expression in (4.7) is derived by simplifying (C.27), which completes the proof.

C.6 Derivation of SCF Expectation in (4.30)

$$
\begin{aligned}
&\mathbb{E}_{\mathbf{x}}\Big[\|\mathbf{r}^H\mathbf{s}(\tau)\|^2\Big] \\
=&\mathbb{E}_{\mathbf{x}}\Big[\|\Big(\sum_{l=0}^{L}\alpha_l^*\mathbf{s}(\tau_l)^H+\boldsymbol{\epsilon}^H\Big)\mathbf{s}(\tau)\|^2\Big] \\
=&\mathbb{E}_{\mathbf{x}}\Big[\sum_{l=0}^{L}\|\alpha_l^*\mathbf{s}(\tau_l)^H\mathbf{s}(\tau)\|^2\Big]+\mathbb{E}_{\mathbf{x}}\Big[\|\boldsymbol{\epsilon}^H\mathbf{s}(\tau)\|^2\Big] \\
&\underbrace{+\mathbb{E}_{\mathbf{x}}\Big[2\Re\{\sum_{l=0}^{L}\sum_{h>l}^{L}\alpha_l^*\alpha_h\mathbf{s}(\tau_l)^H\mathbf{s}(\tau)\mathbf{s}(\tau)^H\mathbf{s}(\tau_h)\}\Big]}_{①=0}+\underbrace{\mathbb{E}_{\mathbf{x}}\Big[2\Re\{\sum_{l=0}^{L}\alpha_l^*\mathbf{s}(\tau_l)^H\mathbf{s}(\tau)\mathbf{s}(\tau)^H\boldsymbol{\epsilon}\}\Big]}_{②=0}
\end{aligned}
\tag{C.28}
$$

$$
\begin{aligned}
=&\mathbb{E}_{\mathbf{x}}\Big[\mathrm{Tr}[N_0\mathbf{I}\mathbf{s}(\tau)\mathbf{s}(\tau)^H]\Big]+\mathbb{E}_{d_0,\theta}\Big[\mathbb{E}_{X|d_0}[\mathbb{E}_{P_0|d_0,X}[P_0]]\ \|\mathbf{s}(\tau_0)^H\mathbf{s}(\tau)\|^2\Big] \\
&+\mathbb{E}_{d_0,\theta}\Bigg[\mathbb{E}_{X|d_0}\Big[\mathbb{E}_{L,b|X}\Big[\sum_{l=1}^{L}\mathbb{E}_{P_l,\delta_l|d_0,X}[P_l\|\mathbf{s}(\tau_l)^H\mathbf{s}(\tau)\|^2]\Big]\Big]\Bigg].
\end{aligned}
\tag{C.29}
$$

We have used the fact that paths have independent channel gains α_l with uniformly distributed phases to prove the cross-terms ① and ② equal to zero. The sum of expectations over all MPCs in (C.29) can be replaced with the expectation over a single MPC, since the parameters of MPCs, i.e. P_l and δ_l, are i.i.d., i.e.

$$
\begin{aligned}
\mathbb{E}_{\mathbf{x}}\Big[\|\mathbf{r}^H\mathbf{s}(\tau)\|^2\Big] =&N_0\|\mathbf{s}\|^2+\mathbb{E}_{d_0}\Big[\underbrace{\mathbb{E}_{P_0|d_0}[P_0]}_{\bar{P}_0}\ \mathbb{E}_{\theta}[\|\mathbf{s}(\tau_0)^H\mathbf{s}(\tau)\|^2]\Big] \\
&+\mathbb{E}_{d_0}\Big[\underbrace{\mathbb{E}_{L|d_0}[L]}_{\bar{L}}\ \underbrace{\mathbb{E}_{P_l|d_0}[P_l]}_{\bar{P}_l}\ \mathbb{E}_{\delta_l,b|d_0}[\mathbb{E}_{\theta}[\|\mathbf{s}(\tau_l)^H\mathbf{s}(\tau)\|^2]]\Big].
\end{aligned}
\tag{C.30}
$$

C.7 Expectation of $\ddot{D}_l^2(\|\mathbf{p}_{u,0} - \mathbf{p}_v\|)$ over Exponentially Distributed δ_l and b

For an MPC in NLOS case

$$\begin{aligned}
&\mathbb{E}_{\delta_l,b;X=\mathrm{NLOS}}[\ddot{D}_l^2(\|\mathbf{p}_{u,0} - \mathbf{p}_v\|)] \\
=&\int_0^\infty \int_0^\infty a_{\mathbb{N}} a_{\mathbb{B}} \ddot{D}_l^2(\|\mathbf{p}_{u,0} - \mathbf{p}_v\|) e^{-a_{\mathbb{N}}\delta_l} e^{-a_{\mathbb{B}}b} \mathrm{d}\delta_l \mathrm{d}b \qquad \text{(C.31)} \\
=&\pi a_{\mathbb{N}} a_{\mathbb{B}} \sum_{n,m=-\frac{N-1}{2}}^{\frac{N-1}{2}} \frac{{\omega_{\mathrm{sc}}}^2 S_{mn}^2 \left(\tau_0 {\omega_{\mathrm{sc}}}^2 S_{mn}^2/c^2 - a_{\mathbb{N}} a_{\mathbb{B}} \tau_0 + a_{\mathbb{B}} + a_{\mathbb{N}}\right)/c^2}{\tau_0 \left({\omega_{\mathrm{sc}}}^2 S_{mn}^2/c^2 + {a_{\mathbb{N}}}^2\right) \left({\omega_{\mathrm{sc}}}^2 S_{mn}^2/c^2 + {a_{\mathbb{B}}}^2\right)}. \qquad \text{(C.32)}
\end{aligned}$$

For an MPC in LOS case, we can replace $a_{\mathbb{N}}$ by $a_{\mathbb{L}}$ and set $a_{\mathbb{B}} \to \infty$

$$\mathbb{E}_{\delta_l,b;X=\mathrm{LOS}}[\ddot{D}_l^2(\|\mathbf{p}_{u,0} - \mathbf{p}_v\|)] = \pi\left(\frac{a_{\mathbb{L}}}{\tau_0} - a_{\mathbb{L}}^2\right) \sum_{n,m=-\frac{N-1}{2}}^{\frac{N-1}{2}} \frac{S_{mn}^2 \omega_{\mathrm{sc}}^2}{S_{mn}^2 \omega^2 + a_{\mathbb{L}}^2 c^2}. \qquad \text{(C.33)}$$

C.8 Proof of Lemma 4.4.1

We first prove that local maxima of $h(\mathbf{p}_u)$ can only exist on the x-axis, by its contradiction. Assume there exists a local maximum at $\mathbf{p}_o = [x_o, y_o]^T$, where $y_o \neq 0$. The partial derivatives h_x and h_y of h, w.r.t. x_u and y_u can be expressed as

$$h_x = \frac{\partial g}{\partial d_u}\frac{x_u}{d_u} + \frac{\partial z}{\partial d_{uv}}\frac{x_u + d_0}{d_{uv}} = 0 \qquad \text{(C.34)}$$

$$h_y = \frac{\partial g}{\partial d_u}\frac{y_u}{d_u} + \frac{\partial z}{\partial d_{uv}}\frac{y_u}{d_{uv}} = 0. \qquad \text{(C.35)}$$

Since $y_o \neq 0$, from (C.35) we have

$$\frac{\partial z}{\partial d_{uv}}\frac{1}{d_{uv}} = -\frac{\partial g}{\partial d_u}\frac{1}{d_u}. \qquad \text{(C.36)}$$

Additionally we have ${}^{\partial g}/_{\partial d_u} < 0$, since $g(\mathbf{p}_u)$ is unimodal. Inserting (C.36) into (C.34), we get

$$h_x = -\frac{d_0}{d_u}\frac{\partial g}{\partial d_u} > 0. \qquad \text{(C.37)}$$

Hence $\mathbf{p}_o$ is not a stationary point of $h(\mathbf{p}_u)$, which contradicts to the assumption.

Then we apply the second derivative test with the following derivatives evaluated

at $\mathbf{p}_{ox} = [x_{ox}, 0]^T$

$$\begin{aligned}
&\frac{\partial d_{uv}}{\partial x_u} = \frac{x_u + d_0}{d_{uv}}, \ \frac{\partial d_u}{\partial x_u} = \frac{x_u}{d_u}, \ \frac{\partial d_{uv}}{\partial y_u} = \frac{\partial d_u}{\partial y_u} = 0, \\
&\frac{\partial^2 d_{uv}}{\partial y_u^2} = \frac{1}{d_{uv}}, \ \frac{\partial^2 d_u}{\partial y_u^2} = \frac{1}{d_u}, \\
&\frac{\partial^2 d_{uv}}{\partial x_u^2} = \frac{\partial^2 d_u}{\partial x_u^2} = \frac{\partial^2 d_{uv}}{\partial x_u \partial y_u} = \frac{\partial^2 d_u}{\partial x_u \partial y_u} = 0, \\
&h_{xy} = 0, \ h_{xx} = \frac{\partial^2 g}{\partial d_u^2} + \frac{\partial^2 z}{\partial d_{uv}^2}, \ h_{yy} = \frac{\partial g}{d_u \partial d_u} + \frac{\partial z}{d_{uv} \partial d_{uv}}.
\end{aligned}$$

Combining (C.35) and the assumption that $\mathbf{p}_{ox}$ is a local maximum point over x-domain, we can get

$$h_y = 0, \quad h_x = 0 \text{ and } h_{xx} < 0. \tag{C.38}$$

According to the second derivative test, $\mathbf{p}_{ox}$ would be a local maximum point of h, if and only if $h_{xx}h_{yy} - h_{xy}^2 > 0$, i.e., $h_{yy} < 0$. It can be shown after some algebra, that $h_{yy} < 0$ only if $x_{ox} > -d_0$, which completes the proof.

C.9 Proof of Theorem 4.4.1

The measurement function $z(x_u)$ can be substituted by the log-likelihood function of DiPNet

$$z(x_u) = \mathrm{SNR}_l D_l((x_u + d_0)/c)^2 / N. \tag{C.39}$$

In the case of $\delta > 0$, a natural number is defined as $\kappa = \lfloor B_c \delta / c \rfloor + 1 \in \mathbb{Z}_+$, where $x_\kappa = \delta - {}^{\kappa c}/_{B_c}$ is the κ^{th} zero point to the left of $z(x_u)$'s main peak. $\lfloor \cdot \rfloor$ denotes the floor operation. We further define $\gamma_{\kappa-1}$ as the $(\kappa-1)^{\text{th}}$ maximum point to the left of $z(x_u)$'s main peak, where $\gamma_0 = \delta$. According to the property of periodic sinc function, the value of $D_l((x_u + d_0)/c)^2$ monotonically increases from the origin to $\gamma_{\kappa-1}$, where it reaches a maximum. In the case of $\gamma_{\kappa-1} \geqslant 0$, the derivative $z_x(x_u)$ of z w.r.t. x_u satisfies

$$z_x(\gamma_{\kappa-1}) = 0 \text{ and } z_x(x_u) > 0, \quad \forall 0 \leqslant x_u < \gamma_{\kappa-1}. \tag{C.40}$$

Additionally by the definition of unimodality, the derivative $g_x(x_u)$ of g w.r.t. x_u fulfills

$$g_x(0) = 0 \text{ and } g_x(x_u) < 0, \quad \forall x_u > 0. \tag{C.41}$$

Combining (C.40) and (C.41), we can get for the derivative $h_x(x_u)$

$$h_x(0) > 0 \text{ and } h_x(\gamma_{\kappa-1}) < 0. \tag{C.42}$$

Therefore, there exists $x_{ox} \in (0, \gamma_{\kappa-1}]$, so that

$$\begin{aligned} h_x(x_u) &\geqslant 0, \forall x_u \in (0, x_{ox}] \\ h_x(x_u) &< 0, \forall x_u \in (x_{ox}, \gamma_{\kappa-1}], \end{aligned}$$

where the equality only holds at x_{ox}. According to Lemma 4.4.1, the maximum point of the belief is shifted from the origin to $\mathbf{p}_{ox}$, which introduces a bias to the belief $\|x_{ox}\| < \|\gamma_{\kappa-1}\| < \varrho_\kappa \triangleq \|\gamma_{\kappa-1} - x_\kappa\|$. The second inequality is obtained by the property of periodic sinc function that $\|x_{\kappa-1} - \gamma_{\kappa-1}\| < \|\gamma_{\kappa-1} - x_\kappa\|$. The upper bound ϱ_κ decreases with increasing κ from $\varrho_1 = {}^c\!/_B$ and quickly approaches its asymptotic value $\varrho_\infty = {}^c\!/_{2B_c}$. The proof can be extended to $-d_0 < \delta < 0$ and $\gamma_{\kappa-1} < 0$ in a similar manner, which completes the proof of Theorem 4.4.1.

C.10 Proof of Theorem 4.4.2

The measurement function $z(x_u)$ can be approximated by its second-order Taylor expansion $\tilde{z}(x_u)$ at $x_u = \gamma_{\kappa-1}$

$$\tilde{z}(x_u) = \frac{1}{2} \underbrace{z_{xx}(\gamma_{\kappa-1})}_{<0} (x_u - \gamma_{\kappa-1})^2 + \underbrace{z_x(\gamma_{\kappa-1})}_{=0} (x_u - \gamma_{\kappa-1}) + z(\gamma_{\kappa-1}). \tag{C.43}$$

The maximum point $\tilde{x}_{ox}$ of $g(x_u) + \tilde{z}(x_u)$ can be calculated with the equality of their derivatives

$$\begin{aligned} g_x(x_u) + \tilde{z}_x(x_u) &= -\frac{1}{\sigma_0^2} x_u + z_{xx}(\gamma_{\kappa-1})(x_u - \gamma_{\kappa-1}) = 0 \\ \tilde{x}_{ox} &= \frac{\gamma_{\kappa-1}}{1 - \frac{1}{\sigma_0^2 z_{xx}(\gamma_{\kappa-1})}}. \end{aligned} \tag{C.44}$$

With the property of the periodic sinc function, the derivatives of $z(x_u)$ and its Taylor expansion fulfill

$$0 \leqslant \|z_x(x_u)\| \leqslant \|\tilde{z}_x(x_u)\|, \tag{C.45}$$

where both equalities hold only for $x_u = \gamma_{\kappa-1}$. Therefore, the bias $\|x_{ox}\|$ of position belief $h(\mathbf{p}_u)$ is smaller than $\|\tilde{x}_{ox}\|$. Then we derive the derivatives of $z(x_u)$, simplifying

the periodic sinc function with the sinc function, and defining $\zeta = {}^{\omega_{\text{sc}}(\delta-\gamma_{\kappa-1})}/_{2c}$

$$z_x(\gamma_{\kappa-1}) \approx \frac{\omega_{\text{sc}}\text{SNR}_l \sin^2(N\zeta)}{c\zeta^2}\Big(\frac{1}{N\zeta} - \frac{\cos(N\zeta)}{\sin(N\zeta)}\Big) = 0,$$
$$z_{xx}(\gamma_{\kappa-1}) \approx \frac{\omega_{\text{sc}}^2\text{SNR}_l \sin^2(N\zeta)}{c^2\zeta^2}\Big(\frac{3}{2N\zeta^2} - \frac{N}{2} - \frac{2\cos(N\zeta)}{\zeta\sin(N\zeta)} + \frac{N\cos^2(N\zeta)}{2\sin^2(N\zeta)}\Big).$$

If $\|\delta\| < {}^{c}/_{B_c}$, $\kappa = 1$, i.e., $\zeta = 0$. The second derivative z_{xx} reaches its global minimum

$$\lim_{\zeta\to 0} z_{xx}(\gamma_{\kappa-1}) = -\frac{\omega_{\text{sc}}^2 N^3 \text{SNR}_l}{6c^2} = -\frac{1}{\text{CRB}_l} = -\frac{1}{\upsilon\sigma_0^2}.$$

The bias of position belief is bounded by

$$\|x_{ox}\| < \|\tilde{x}_{ox}\| = \frac{\|\delta\|}{1 + \frac{3c^2}{2\pi^2 N\text{SNR}_l B_c^2 \sigma_0^2}} = \frac{\|\delta\|}{1+\upsilon}. \tag{C.46}$$

If $\|\delta\| \geqslant {}^{c}/_{B_c}$

$$\begin{aligned} z_{xx}(\gamma_{\kappa-1}) \approx & \frac{\omega_{\text{sc}}^2\text{SNR}_l}{c^2\zeta^2}\Big(\frac{N\cos^2(N\zeta)}{2} - \frac{N\sin^2(N\zeta)}{2} - \frac{\sin^2(N\zeta)}{2N\zeta^2}\Big) \\ = & \frac{\omega_{\text{sc}}^2\text{SNR}_l}{c^2\zeta^2}\Big(\frac{N\cos(2N\zeta)}{2} - \frac{1-\cos(2N\zeta)}{4N\zeta^2}\Big) \\ > & -\frac{\omega_{\text{sc}}^2\text{SNR}_l}{2c^2\zeta^2}\Big(N + \frac{1}{N\zeta^2}\Big) = -\frac{2N\text{SNR}_l}{(\delta-\gamma_{\kappa-1})^2}\Big(1 + \frac{c^2}{\pi^2 B_c^2(\delta-\gamma_{\kappa-1})^2}\Big) \\ > & -\frac{2N\text{SNR}_l}{(\|\delta\|-\varrho_\kappa)^2}(1+\rho^2), \end{aligned} \tag{C.47}$$

where $\rho = {}^{c}/_{\pi B_c(\|\delta\|-\varrho_\kappa)}$. Therefore

$$\|x_{ox}\| < \|\tilde{x}_{ox}\| < \frac{\varrho_\kappa}{1 + \frac{\upsilon}{3\rho^2(1+\rho^2)}}. \tag{C.48}$$

We can combine (C.46) and (C.48), which completes the proof.

C.11 Partial Derivative of Weighted CRB

We define a notation $\mathbf{X}_{<uv>}$ as a sub-matrix of matrix $\mathbf{X}$, whose rows correspond to node $\mathbb{o}_u$ and columns correspond to node $\mathbb{o}_v$.

$$\begin{aligned} c_l =& \frac{\partial \mathrm{Tr}\left[\mathbf{\Lambda}^h \mathbf{I}^{-1}_{\mathbf{x}(+)}\right]}{\partial b_l} \\ =& -\mathrm{Tr}\left[\underbrace{\mathbf{I}^{-1}_{\mathbf{x}(+)}\mathbf{\Lambda}^h\mathbf{I}^{-1}_{\mathbf{x}(+)}}_{\mathbf{A}}\frac{\partial \mathbf{I}_{\mathbf{x}(+)}}{\partial b_l}\right] \qquad \text{(C.49)} \\ =& -\mathrm{Tr}\left[\sum_{\mathbb{e}_{uv}\in\mathcal{E}}\begin{pmatrix}\mathbf{A}_{<uu>} & \mathbf{A}_{<uv>}\\ \mathbf{A}_{<vu>} & \mathbf{A}_{<vv>}\end{pmatrix}\frac{\partial}{\partial b_l}\left(\mathbf{I}^{s_{uv}}_{\mathbf{x}_{uv}}+\mathbf{I}^{s_{vu}}_{\mathbf{x}_{uv}}\right)\right] - \mathrm{Tr}\left[\sum_{\mathbb{e}_{uv}\in\mathcal{E}}\mathbf{A}_{<uu>}\frac{\partial}{\partial b_l}\mathbf{I}^{s_{uv}}_{\mathbf{x}_u}\right], \qquad \text{(C.50)} \end{aligned}$$

where $\mathbf{x}_{uv} = \mathrm{vec}\{\mathbf{x}_u, \mathbf{x}_v\}$ and $\mathbf{I}^{s_{mn}}_{\mathbf{x}_c}$ is the information about $\mathbf{x}_c$ contained in the observation of s_{mn}, i.e.

$$\mathbf{I}^{s_{mn}}_{\mathbf{x}_c} \triangleq \begin{cases} \iota_{mn}\nabla_{\mathbf{x}_c}g_{mn}\nabla_{\mathbf{x}_c^T}g_{mn}, & \text{if } \mathbb{e}_{mn}\in\mathcal{E}_0 \\ \mathbf{0}, & \text{otherwise.}\end{cases}$$

A general term in (C.50) can be expressed analytically as

$$\begin{aligned} & -\mathrm{Tr}\left[\mathbf{A}_{op}\frac{\partial}{\partial b_l}\mathbf{I}^{s_{mn}}_{\mathbf{x}_c}\right] \\ =& -\mathrm{Tr}\Big[\mathbf{A}_{op}\Big(\frac{\partial\nabla_{\mathbf{x}_c}g_{mn}}{\partial b_l}\iota_{mn}\nabla_{\mathbf{x}_c^T}g_{mn}+\nabla_{\mathbf{x}_c}g_{mn}\frac{\partial\iota_{mn}}{\partial b_l}\nabla_{\mathbf{x}_c^T}g_{mn}+(\nabla_{\mathbf{x}_c}g_{mn})\iota_{mn}\frac{\partial\nabla_{\mathbf{x}_c^T}g_{mn}}{\partial b_l}\Big)\Big] \\ =& -\nabla_{\mathbf{x}_c^T}g_{mn}\mathbf{A}_{op}\frac{\partial\nabla_{\mathbf{x}_c}g_{mn}}{\partial b_l}\iota_{mn} - \nabla_{\mathbf{x}_c^T}g_{mn}\mathbf{A}_{op}\nabla_{\mathbf{x}_c}g_{mn}\frac{\partial\iota_{mn}}{\partial b_l} - \frac{\partial\nabla_{\mathbf{x}_c^T}g_{mn}}{\partial b_l}\mathbf{A}_{op}(\nabla_{\mathbf{x}_c}g_{mn})\iota_{mn} \\ =& -\frac{\partial\nabla_{\mathbf{x}_c^T}g_{mn}}{\partial b_l}(\mathbf{A}_{op}+\mathbf{A}_{op}^T)\nabla_{\mathbf{x}_c}g_{mn}\iota_{mn} - \nabla_{\mathbf{x}_c^T}g_{mn}\mathbf{A}_{op}\nabla_{\mathbf{x}_c}g_{mn}\frac{\partial\iota_{mn}}{\partial b_l}. \qquad \text{(C.51)} \end{aligned}$$

The partial derivative c_l can be formulated analytically by combining (C.50) and (C.51).

C.12 Partial Derivative of Collision Avoidance Objective

The derivative of $h_{c,uv}(\mathbf{b}_{\mathcal{A}})$ w.r.t. b_l, the l^{th} coefficient of $\mathbf{b}_u$, is expressed as

$$\frac{\partial h_{c,uv}(\mathbf{b}_{\mathcal{A}})}{\partial b_l} \tag{C.52}$$

$$= \frac{-d_{\min}}{\|\mathbf{C}_{uv}^{-1}\bar{\mathbf{p}}_{uv}\|} \frac{\partial \bar{\mathbf{p}}_{uv}^T \mathbf{C}_{uv}^{-2} \bar{\mathbf{p}}_{uv}}{\partial b_l} + \frac{\partial \bar{\mathbf{p}}_{uv}^T \mathbf{C}_{uv}^{-1} \bar{\mathbf{p}}_{uv}}{\partial b_l} \tag{C.53}$$

$$= \frac{-d_{\min}}{\|\mathbf{C}_{uv}^{-1}\bar{\mathbf{p}}_{uv}\|} \left(\bar{\mathbf{p}}_{uv}^T \frac{\partial \mathbf{C}_{uv}^{-2}}{\partial b_l} \bar{\mathbf{p}}_{uv} + 2\bar{\mathbf{p}}_{uv}^T \mathbf{C}_{uv}^{-2} \frac{\partial \bar{\mathbf{p}}_{uv}}{\partial b_l} \right) + \bar{\mathbf{p}}_{uv}^T \frac{\partial \mathbf{C}_{uv}^{-1}}{\partial b_l} \bar{\mathbf{p}}_{uv} 2\bar{\mathbf{p}}_{uv}^T \mathbf{C}_{uv}^{-1} \frac{\partial \bar{\mathbf{p}}_{uv}}{\partial b_l} \tag{C.54}$$

$$= \left(2\bar{\mathbf{p}}_{uv}^T \mathbf{C}_{uv}^{-1} - \frac{2d_{\min} \bar{\mathbf{p}}_{uv}^T \mathbf{C}_{uv}^{-2}}{\|\mathbf{C}_{uv}^{-1}\bar{\mathbf{p}}_{uv}\|} \right) \frac{\partial \bar{\mathbf{p}}_{uv}}{\partial b_l} + \left(\bar{\mathbf{p}}_{uv}^T \mathbf{C}_{uv}^{-2} - \frac{2d_{\min} \bar{\mathbf{p}}_{uv}^T \mathbf{C}_{uv}^{-3}}{\|\mathbf{C}_{uv}^{-1}\bar{\mathbf{p}}_{uv}\|} \right) \frac{\partial \mathbf{C}_{uv}}{\partial b_l} \bar{\mathbf{p}}_{uv}. \tag{C.55}$$

Additionally, we have

$$\frac{\partial \bar{\mathbf{p}}_{uv}}{\partial b_l} = \frac{\partial \mathbf{b}_u}{\partial b_l}, \tag{C.56}$$

and

$$\frac{\partial \mathbf{C}_{uv}}{\partial b_l} = \frac{\partial \mathbf{Q}_u}{\partial b_l} = \frac{\sigma^2 b_l}{\|\mathbf{b}_u\|} \mathbf{I}_{2\times 2}. \tag{C.57}$$

Finally we have the derivative of $h_{c,uv}(\mathbf{b}_{\mathcal{A}})$ w.r.t. $\mathbf{b}_u$ as expressed in (5.47), which completes the derivation.

Appendix D

List of Own Publications

D.1 Journal Publications

[J1] S. Zhang, R. Pöhlmann, T. Wiedemann, A. Dammann, H. Wymmeersch, and P. A. Hoeher, "Self-aware swarm navigation in autonomous exploration missions," *Proc. IEEE*, vol. 108, no. 7, pp. 1168–1195, 2020.

[J2] S. Zhang, E. Staudinger, T. Jost, W. Wang, C. Gentner, A. Dammann, H. Wymeersch, and P. A. Hoeher, "Distributed direct localization suitable for dense networks," *IEEE Trans. Aerosp. Electron. Syst.*, vol. 56, no. 2, pp. 1209–1227, 2020.

[J3] S. Zhang, T. Jost, R. Pöhlmann, A. Dammann, D. Shutin, and P. A. Hoeher, "Spherical wave positioning based on curvature of arrival by an antenna array," *IEEE Wireless Commun. Lett.*, vol. 8, no. 2, pp. 504–507, Apr. 2019.

[J4] U. Ulmschneider, S. Zhang, C. Gentner, and A. Dammann, "Multipath assisted positioning with transmitter visibility information (**under revision**)," *IEEE Access*, 2020.

[J5] A. Dammann, C. Gentner, R. Pöhlmann, R. Raulefs, E. Staudinger, U. Ulmschneider, M. Walter, and S. Zhang, "5G and beyond cooperative positioning – knowing "where is everything" (**under revision**)," *IEEE Access*, 2020.

[J6] M. Schuster *et al.*, "The ARCHES space-analogue demonstration mission: Towards heterogeneous teams of autonomous robots for collaborative scientific sampling in planetary exploration (**accepted**)," *IEEE Robot. Autom. Lett.*, 2020.

[J7] R. Pöhlmann, S. A. Almasri, S. Zhang, T. Jost, A. Dammann, and P. A. Hoeher, "On the potential of multi-mode antennas for direction-of-arrival estimation," *IEEE Trans. Antennas Propag.*, vol. 67, no. 5, pp. 3374–3386, May 2019.

[J8] C. Gentner, S. Zhang, and T. Jost, "Log-PF: Particle filtering in logarithm domain," *Journal of Electrical and Computer Engineering*, vol. 2018, 2018.

[J9] C. Gentner, R. Pöhlmann, M. Ulmschneider, T. Jost, and S. Zhang, "Positioning using terrestrial multipath signals and inertial sensors," *Mobile Information Systems*, vol. 2017, 2017.

[J10] E. Staudinger, S. Zhang, and A. Dammann, "Cramer-Rao lower-bound for round-trip delay ranging with subcarrier-interleaved OFDMA," *IEEE Trans. Aerosp. Electron. Syst.*, vol. 52, no. 6, pp. 2961 – 2972, Dec. 2016.

[J11] C. Gentner, T. Jost, W. Wang, S. Zhang, A. Dammann, and U.-C. Fiebig, "Multipath assisted positioning with simultaneous localization and mapping," *IEEE Trans. Wireless Commun.*, vol. 15, no. 9, pp. 6104–6117, Sep. 2016.

[J12] W. Wang, T. Jost, C. Gentner, S. Zhang, and A. Dammann, "A semi-blind tracking algorithm for joint communication and ranging with OFDM signals," *IEEE Trans. Veh. Technol.*, vol. 65, no. 7, pp. 5237–5250, Jul. 2016.

[J13] T. Andre, K. A. Hummel, A. P. Schoellig, E. Yanmaz, M. Asadpour, C. Bettstetter, P. Grippa, H. Hellwagner, S. Sand, and S. Zhang, "Application-driven design of aerial communication networks," *IEEE Commun. Mag.*, vol. 52, no. 5, pp. 129–137, May 2014.

[J14] R. Raulefs, S. Zhang, and C. Mensing, "Bound-based spectrum allocation for cooperative positioning," *Transactions on Emerging Telecommunications Technologies*, Jan. 2013.

D.2 Conference Publications

[C1] S. Zhang, R. Pöhlmann, and A. Dammann, "Heterogeneous network localization with a distributed phased array composed of cooperative vehicles," in *Proc. IEEE, EURASIP European Signal Processing Conference (EUSIPCO)*, A Coruña, Spain, Sep. 2019.

[C2] S. Zhang, R. Raulefs, and A. Dammann, "Localization-driven formation control for swarm return-to-base applicationn," in *Proc. IEEE, EURASIP European Signal Processing Conference (EUSIPCO)*, Budapest, Hungary, Aug. 2016.

[C3] S. Zhang, M. Fröhle, H. Wymeersch, A. Dammann, and R. Raulefs, "Location-aware formation control in swarm navigation," in *Proc. IEEE GLOBECOM Workshop on Wireless Networking, Control and Positioning for Unmanned Autonomous Vehicles (Wi-UAV), 2015*, San-Diego, California, USA, Dec. 2015.

[C4] S. Zhang, E. Staudinger, W. Wang, C. Gentner, A. Dammann, and E. Sandgren, "DiPLoc: Direct signal domain particle filtering for network localization," in *Proc. of ION GNSS+*, Tampa, Florida, USA, Sep. 2015.

[C5] S. Zhang and R. Raulefs, "Multi-agent flocking with noisy anchor-free localization," in *Proc. IEEE 11th International Symposium on Wireless Communications Systems (ISWCS)*, Barcelona, Spain, 2014.

[C6] S. Zhang, E. Staudinger, S. Sand, R. Raulefs, and A. Dammann, "Anchor-free localization using round-trip delay measurements for Martian swarm exploration," in *Proc. of IEEE ION PLANS*, Monterey, California, USA, May 2014.

[C7] S. Zhang, R. Raulefs, A. Dammann, and S. Sand, "System-level performance analysis for Bayesian cooperative positioning: From global to local," in *Proc. of International Conference on Indoor Positioning and Indoor Navigation (IPIN)*, Montbéliard - Belfort, France, Oct. 2013.

[C8] S. Zhang, S. Sand, R. Raulefs, and E. Staudinger, "Self-organized hybrid channel access method for an interleaved RTD-based swarm navigation system," in *Proc. of 10th Workshop on Positioning Navigation and Communication (WPNC)*, Dresden, Germany, Mar. 2013.

[C9] S. Zhang and R. Raulefs, "Improved particle filtering by exploring nomadic movements," in *Proc. IEEE 5th International Symposium on Communications, Control, and Signal Processing (ISCCSP)*, Rome, Italy, May 2012.

[C10] R. Pöhlmann, S. Zhang, A. Dammann, and P. A. Hoeher, "Manifold optimization based beamforming for DoA and DoD estimation with a single multi-mode antenna (**accepted**)," in *Proc. EURASIP 28th European Signal Processing Conf. (EUSIPCO)*, Amsterdam, The Netherlands, Jan. 2021.

[C11] M. J. Schuster *et al.*, "The ARCHES moon-analogue demonstration mission: Towards teams of autonomous robots for collaborative scientific sampling in Lunar environments," in *8th European Lunar Symposium*, Padua, Italy, May 2020, pp. 1–2.

[C12] R. Pöhlmann, S. Zhang, and A. Dammann, "In-field calibration of antennas or antenna arrays using wavefield modeling," in *Asilomar Conference on Signals, Systems, and Computers*, Pacific Grove, USA, Nov. 2019.

[C13] E. Staudinger, R. Pöhlmann, T. Wiedemann, S. Zhang, A. Dammann, and D. Shutin, "Swarm navigation and exploration for planetary surface missions: Experimental results," in *International Planetary Probe Workshop 2019*, Oxford, UK, Jul. 2019.

[C14] R. Raulefs, S. Zhang, and A. Dammann, "Unequal error protection for cooperative localization with message passing," in *Asilomar Conference on Signals, Systems, and Computers*, Pacific Grove, USA, 2018.

[C15] R. Pöhlmann, S. Zhang, A. Dammann, and P. A. Hoeher, "Fundamental limits for joint relative position and orientation estimation with generic antennas," in *Proc. EURASIP 26th European Signal Processing Conf. (EUSIPCO)*, Rome, Italy, Sep. 2018.

[C16] E. Staudinger, D. Shutin, C. Manss, A. Viseras, and S. Zhang, "Swarm technologies for future space exploration missions," in *Proc. 14th International Symposium on Artificial Intelligence, Robotics and Automation in Space (i-sairas)*, Jun. 2018.

[C17] R. Pöhlmann, S. Zhang, A. Dammann, and P. A. Hoeher, "Fundamental limits for joint relative position and orientation estimation," in *Proc. IEEE International Conference on Communications Workshops (ICC Workshops)*, Kansas City,, USA, May 2018.

[C18] R. Pöhlmann, S. Zhang, K. A. Yinusa, and A. Dammann, "Multi-mode antenna specific direction-of-arrival estimation schemes," in *Proc. IEEE 7th International Workshop on Computational Advances in Multi-Sensor Adaptive Processing (CAMSAP)*, Curacao, Dec. 2017.

[C19] R. Pöhlmann, S. Zhang, T. Jost, and A. Dammann, "Power-based direction-of-arrival estimation using a single multi-mode antenna," in *Proc. of the 14th Workshop on Positioning Navigation and Communications (WPNC)*, Bremen, Oct. 2017.

[C20] M. Walter, A. Dammann, T. Jost, R. Raulefs, and S. Zhang, "Waveform parameter selection for ITS positioning," in *Proc. of IEEE 76th Vehicular Technology Conference (VTC)*, Sydney, Australia, Jun. 2017.

[C21] D. Shutin and S. Zhang, "Distributed sparsity-based bearing estimation with a swarm of cooperative agents," in *Proc. IEEE Global Conference on Signal and Information Processing (GlobalSIP)*, Dec. 2016, pp. 555–559.

[C22] A. Dammann, T. Jost, R. Raulefs, M. Walter, and S. Zhang, "Optimizing waveforms for positioning in 5G," in *Proc. IEEE 17th International Workshop on Signal Processing Advances in Wireless Communications (SPAWC)*, Edinburgh, UK, Jul. 2016.

[C23] M. Arias, T. Jost, B. Gonzalez-Valdes, W. Wang, S. Zhang, M. Ulmschneider, and C. Gentner, "Statistical analysis of the radiation pattern of an antenna mounted on an aircraft," in *Proc. 10th European Conference on Antennas and Propagation (EuCAP)*, Davos, Switzerland, Apr. 2016.

[C24] R. Raulefs, A. Dammann, T. Jost, M. Walter, and S. Zhang, "The 5G localization waveform," in *Proc. ETSI Workshop on Future Radio Technologies focusing on Air Interfaces*, Sophia Antipolis, France, Jan. 2016.

[C25] A. Dammann, R. Raulefs, and S. Zhang, "On prospects of positioning in 5G," in *Proc. IEEE ICC - Workshop on 5G & Beyond - Enabling Technologies and Applications*, London, UK, Jun. 2015.

[C26] E. Staudinger, S. Zhang, A. Dammann, and C. Zhu, "Towards a radio-based swarm navigation system on Mars – key technologies and performance assessment," in *Proc. IEEE International Conference on Wireless for Space and Extreme Environments (WiSEE)*, Noordwijk, Netherlands, Oct. 2014.

[C27] W. Wang, R. Raulefs, T. Jost, A. Dammann, C. Gentner, and S. Zhang, "Ship-to-land broadband channel measurement campaign at 5.2 GHz," in *Proc. MTS/IEEE OCEANS*, St.John's, Canada, Sep. 2014.

[C28] C. Zhu, S. Zhang, A. Dammann, S. Sand, P. Henkel, and C. Günther, "Return-to-base navigation of robotic swarms in Mars exploration using DoA estimation," in *Proc. 55th International Symposium ELMAR*, Zadar, Croatia, Sep. 2013.

[C29] S. Sand, S. Zhang, M. Mühlegg, G. Falconi, C. Zhu, T. Krüger, and S. Nowak, "Swarm exploration and navigation on Mars," in *Proc. International Conference on Localization and GNSS (ICL-GNSS)*, Torino, Italy, Jun. 2013.

[C30] R. Raulefs, S. Zhang, C. Mensing, C. Ghali, and J. Hachem, "Dynamic cooperative positioning," *Proc. 11th European Wireless Conference*, Apr. 2011.

D.3 Book Chapters

[B1] M. Fröhle, T. Charalambous, H. Wymeersch, S. Zhang, and A. Dammann, "Formation control of multi-agent systems with location uncertainty," in *Multi-Technology Positioning*. Springer International Publishing, 2017.

[B2] M.-G. Di Benedetto, A. Cattoni, J. Fiorina, F. Bader, L. E. De Nardis, R. Raulefs, and S. Zhang, "Localization in cognitive radio networks," in *Cognitive Radio and Networking for Heterogeneous Wireless Networks*. Springer, 2015.